Limited Angle Ultrasound Tomography of the Compressed Breast

by

Rungroj Jintamethasawat

A dissertation submitted in partial fulfillment
of the requirements for the degree of
Doctor of Philosophy
(Biomedical Engineering)
in The University of Michigan
2018

Doctoral Committee:

Research Associate Professor Oliver D. Kripfgans, Co-Chair
Associate Professor Xueding Wang, Co-Chair
Professor Paul L. Carson
Professor Jeffery A. Fessler
Associate Professor Thomas F. Wenisch

Rungroj Jintamethasawat
rungroj@umich.edu
ORCID iD: 0000-0002-4222-0808

This dissertation is dedicated to all my family members who have provided me unconditional love and support.

ACKNOWLEDGEMENTS

First off all, I would like to express my deepest gratitude to my advisers, Prof. Oliver Kripfgans and Prof. Paul Carson for their considerable amount of time and patience in providing me invaluable comments and suggestions, even before I got into a doctoral program. Those have been very useful not only for my daily routine research but also for allowing me to improve problem-solving, communication, organization, and interpersonal skills that, I believe, are necessary for my prospective career and for every proactive step forward that I will pursue subsequently to fulfill my ambition to improve living standards in my home country.

I also sincerely thank Prof. Xueding Wang, Prof. Thomas Wenisch, and Prof. Jeffery Fessler, for serving on my dissertation committee. All feedback and comments I received especially during my qualification examination helped me realize the future trends of medical imaging and come up with better, more prioritized research plans. My appreciation is also extended to time and feedback from weekly meetings with Prof. Thomas Wenisch, and Prof. Chaitali Chakrabarti, regarding hardware design and algorithmic implementation, and Prof. Brian Fowlkes, Prof. Mitch Goodsitt, and Prof. Marilyn Roubidoux, regarding ultrasound imaging for breast cancer detection.

Working in Ultrasound Group has allowed me to be surrounded by many wonderful, open-minded people. My special thanks go to Dr. Yiying Zhu and Dr. Ashish Sahani for giving me useful advices and for relentlessly helping me overcome difficulties in both academic and non-academic situations. It is also entirely impossible to complete one of the research projects without Xiaohui Zhang's tremendous help and time in analyzing huge simulation datasets. In addition, I am sincerely grateful for generous help from Won-Mean Lee, Nneka Richards, Dr. Stephen Pinter, and Dr. Fong Ming Hooi in helping me with adjustments to the lab environments, setting up experiments, and teaching me basic English grammars and special scientific methods that are difficult to learn elsewhere. Last but not least, all other lab fellows, including Dr. Xiaofeng Liu, Dr. Alex Moncion, Kejie Chen, Dr. Ying Zhang, Dr. Yuxin Wang, Yunhao Zhu, and Qi You, have offered me blessing experience throughout my Ph.D. studies.

Most importantly, I sincerely thank all my family members for their endless amounts of love, encouragement, patience, and sacrification, both in physical and mental forms. I am also thankful for financial support from the Royal Thai Scholarship that has allowed me to pursue my M.S. and Ph.D. studies abroad and has given me opportunities to experience various aspects of the United States. The fact that parts of the income taxes from all Thais are allocated for my scholarship has also warranted my greatest empathy to their sacrification and patience. All these tremendous supports have undoubtedly led me to be more open to challenges and setbacks, and to have much clearer vision about actions needed to be done such that my country would directly benefit from them.

TABLE OF CONTENTS

CHAPTER

LIST OF FIGURES

Figure

LIST OF TABLES

<u>**Table**</u>

ABSTRACT

Limited Angle Ultrasound Tomography of the Compressed Breast

by

Rungroj Jintamethasawat

Co-Chairs: Oliver D. Kripfgans and Xueding Wang

X-ray mammography is widely accepted as the clinical standard for breast cancer screening and diagnosis. However, reflection mode ultrasound has been known to outperform x-ray in screening performance in dense breasts. With newer modes of ultrasound, acoustic properties of breast tissue, such as the speed of sound and attenuation coefficient distributions, can be extracted from captured ultrasound signals and used to characterize breast tissue types and contribute to detection and diagnosis of malignancy. The same is possibly true for optical absorption via photoacoustic imaging. Recently, we have developed a dual-sided ultrasound scanner that can be integrated with existing x-ray mammographic systems and acquire images in the mammographic view and compression. Transmission imaging for speed of sound and attenuation coefficient in this geometry is termed limited angle tomography, as the beams at frequencies yielding high resolution cannot transit the long axis of the compressed breast. This approach, ideally, should facilitate the co-registration and comparisons between images from three modalities discussed here (x-ray, ultrasound and photoacoustic) and increase diagnostic detection confidence. However, potential limitations inherent in limited angle tomography have received minimal exploration

up to this study, and existing imaging techniques developed for this approach are based on overly optimistic assumptions that hinder achievement of the desired image quality. This investigation of these problems should contribute valuable information to the validation and translation of the mammographically-configured, dual-sided ultrasound, or ultrasound and photoacoustic, scanner to the clinic.

This dissertation first aims to extensively identify possible sources of error resulting from imaging in the limited angle tomography approach. Simulation findings mapping parametric conditions reveal that image artifacts arising in reflection mode (B-mode) can be modulated or mitigated by ultrasound gels with adequate acoustic properties. In addition, sound speed imaging was performed determining the level of significance for several key sources of error. Results suggest that imaging in transmission mode is the most sensitive to transducer misplacement in the signal propagation direction. This misplacement, however, could be minimized easily by routinely calibrating transducer positions.

Next, this dissertation aims to advance speed of sound, attenuation, and photoacoustic image reconstruction algorithms for the limited angle tomography approach. This was done by utilizing both structural information of the imaged objects/tissues by means of the corresponding reflection mode images taken from the same imaging location, and a full acoustic modeling framework to account for complex acoustic interactions within the field of view. We have shown through simulations that both *a priori* information from reflection mode images and full acoustic modeling contribute to a noticeable improvement in the reconstructed images. Work done throughout the course of this dissertation should provide a foundation and insight necessary for improvements upon the existing dual-sided ultrasound scanner towards breast imaging in the clinic.

CHAPTER I

Introduction

1.1 Significance

According to the latest cancer statistics in 2018 [1], breast cancer has reportedly been the most frequently diagnosed incidence among all other diagnosed cancer types in the female population in the United States. Although breast cancer mortality rates have shown to decline in the last two decades, the latest statistics shows that breast cancer mortality still accounts for 14% of the total cancer mortality. More importantly, the recent statistics in 2015 [1] show that breast cancer is the most prevalent cause of cancer deaths in the group of young-to-middle-aged (20-59 years old) female adults. Such statistics represent significant loss of life and stress the importance of having medical diagnostic tools that enable early diagnosis of breast cancers.

Currently, x-ray mammography serves as the standard, non-invasive imaging solution for breast cancer diagnosis and screening. Despite wide clinical acceptance, x-ray mammography has crucial drawbacks. Its poor performance when imaging dense beasts, mostly found in young female adults, where early-stage cancers develop, hinders its ability to achieve early detection and screening. It furthermore suffers from ionizing radiation, that could cause potential harm to patients who are imaged repeatedly. However, alternative imaging modalities can be used to overcome these limitations, such as magnetic resonance imaging (MRI) and ultrasound. Although MRI provides superior image quality and is less prone to the dense tissues compared to the x-ray, the use of MRI in breast scanning is still not suitable for a screening process, primarily due to its long scanning time and high operational cost. On the other hand, ultrasound has become widespread and has been used as an adjunct to x-ray mammography, thanks to its ability to penetrate through dense breast tissue better than x-ray, where glandular tissue in dense breast tends to provide little contrast for x-ray photons as opposed to ultrasound signals [2]. Using ultrasound, in adjunct with x-ray, has shown to increase the overall detection sensitivity [3]–[5]. In addition, ultrasound is highly portable and requires substantially less operational cost compared to MRI and x-ray. Such advantages have encouraged several research groups to develop affordable and safe ultrasound imaging techniques whose performance are comparable to the existing x-ray mammography techniques. Our group has also developed mammographically-configured, automated, and dual-sided ultrasonic imaging, that is not only capable of acquiring the B-mode images in the same view as x-ray mammogram, but also capable of performing other advanced transmission mode imaging techniques [6]–[12].

The potential of using ultrasound in breast cancer detection and screening goes beyond conventional B-mode imaging, the most commonly-used technique nowadays to image breast tissue structures. The physics of propagating ultrasound waves, such as reflection, refraction, diffusion, and scattering, are strongly dictated by the underlying acoustic properties in the propagated media [13], [14]. As such, there have several attempts to extract those acoustic properties from the information contained in the received ultrasound signals. It has been shown by several studies that some acoustic properties, such as sound speed [7], [15]–[22], acoustic attenuation [8], [17]–[19], [21], [23]–[25], mass density [26], and mechanical elasticity [27]–[29], can be used to characterize breast tissue types such as fibroglandular, fat, cyst, and cancer.

Sound speed and acoustic attenuation are particularly of our interests, as they can be obtained directly from our dual-sided ultrasound scanner by means of transmission mode imaging, and these two properties provide attractive quantitative biomarkers that can help in the classification of breast tissue types [30]. For example, fat has the lowest sound speed, and cancer tends to have high sound speed and high attenuation. More interestingly, even though there is overlap among sound speed and attenuation of fibroadenoma, fibroglandular, and cyst, their distictive relationships between sound speed and attenuation could help in identifying these tissues. See Figure 1.1 for further illustration.

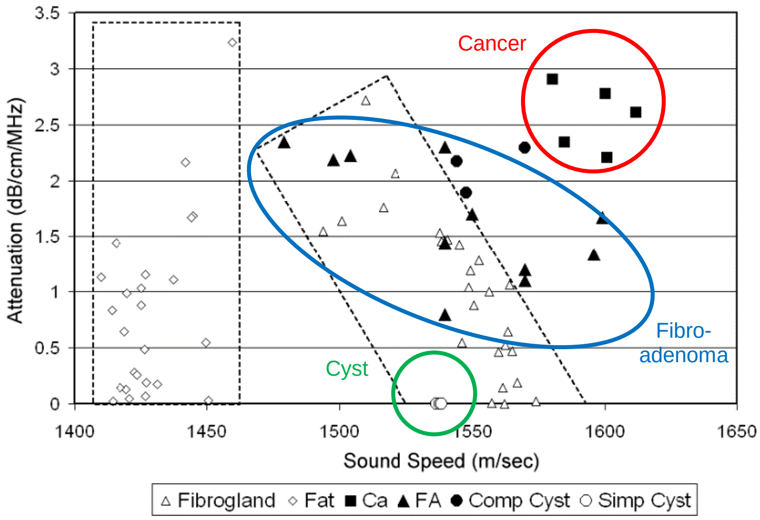

Figure 1.1: Distribution of speeds of sound and attenuation coefficients that can be used to characterize different tissue types (figure from [30]).

Several existing ultrasound systems have been specifically designed for sound speed and acoustic attenuation imaging and those systems have shown much success in imaging under clinical circumstances [17], [19]–[22], [31]–[36]. Their signal acquisition schemes are based on circular ultrasound arrays that transmit and receive signals with the patient's breast setup in a prone position. This is different from x-ray mammograms that acquire images in the compressed position of the breast. Coregistrations of images obtained from prone (ultrasound) and those from compressed (x-ray mammograms) cases, though possible, appear very challenging as they often require heavy task-specific parameter tuning [37], [38]. The ability to bridge this gap should make our cost-effective dual-sided scanner more preferable to clinicians who are already familiar with x-ray mammography. Figure 1.2 further shows a schematic representation of ultrasound scanner utilizing the circular ultrasound array geometry, versus our dual-sided ultrasound scanner utilizing two commercial linear ultrasound arrays, to demonstrate different breast compression levels.

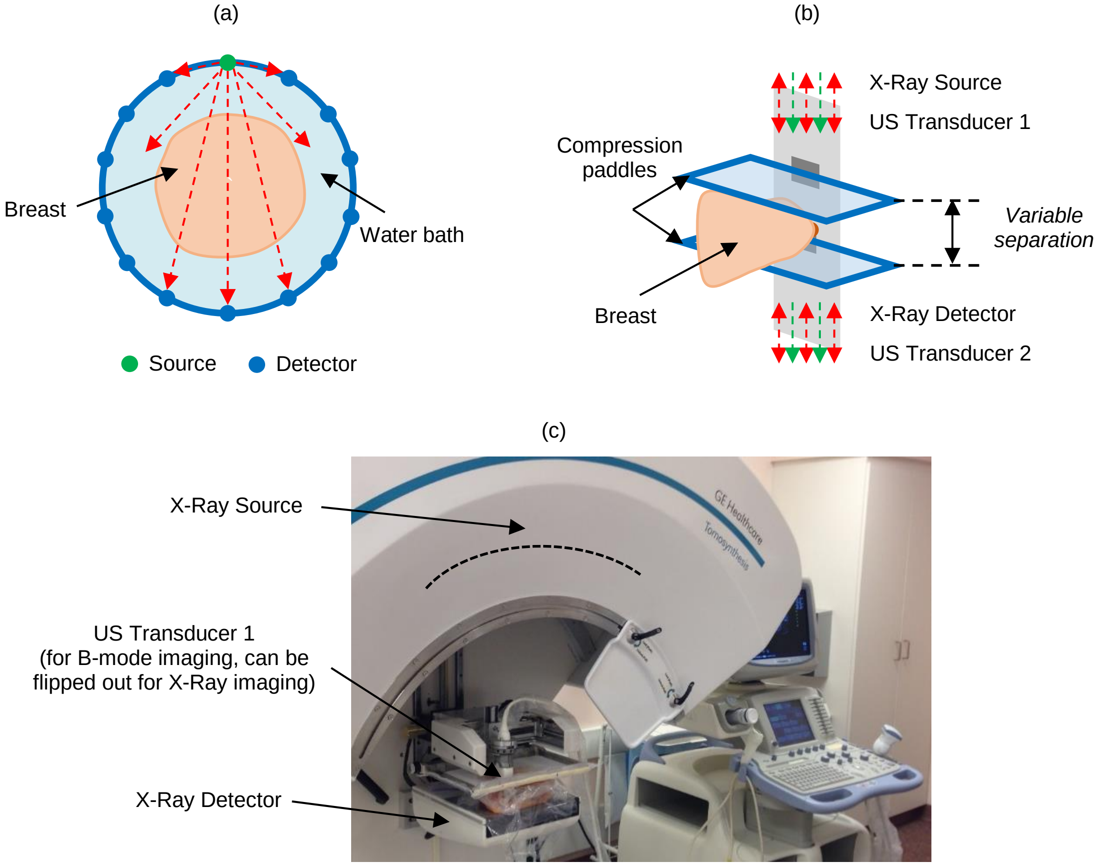

Figure 1.2: Schematic representation of (a) scanner in existing ultrasound systems utilizing the circular ultrasound array geometry, and (b) our dual-sided ultrasound scanner utilizing two commercial linear ultrasound arrays. Panel (c) shows the actual integration of ultrasound and x-ray tomosynthesis units.

For this reason, we have utilized our dual-sided ultrasound scanner for multimodality imaging in both transmission and reflection modes. The inherent limitation of our dual-sided scanner, in its lack of freedom to transmit and receive signals in any direction, has been overcome by the approach recently proposed by our former graduate student Dr. Hooi [7], [8], the use of already-available B-mode or x-ray images for guiding reconstructions. Still, our dual-sided ultrasound scanner has several areas that are left uninvestigated. First, it has been observed that breast tissue B-mode images, obtained in the mammographic or cranial-caudal view, are prone to artifacts appearing as shadow areas, where signal intensity drops. These artifacts occur due to the complex interactions between propagating ultrasound waves and intermediate tissues that distort the wave propagation patterns. Such aberrations not only decrease the signal-to-noise ratio in the shadow areas but also degrade the image reconstruction accuracy when segmentation is performed on those B-mode images. Most commonly such segmentation is performed to generate *a priori* information for later reconstructions of sound speed and acoustic attenuation images. Apart from mis-segmentations that are caused by aberrations (not only limited to shadow areas), the dual linear ultrasound arrays arranging, in the mammographic configuration, leads to a non-rigid system, where transducer positions are misplaced by forces, exerted by the compressed breast. Knowing the degrees of these effects on the reconstruction accuracy can give us insight into design considerations of ultrasound scanners and imaging couplants. Such insight then points to which factors are the most significant with respect to their influence on image reconstruction accuracy. Further considerations include the comparison of our existing ray-based reconstruction algorithms with more sophisticated approaches, not only with respect to reconstruction accuracy but also in terms for computational load and dataset size. Lastly, our existing dual-sided breast ultrasound scanner has not been utilized to its fullest diagnostic potential yet. By integrating additional imaging modalities with specialized processing algorithms, additional clinical information would potentially become available, thereby raising the significance of medical ultrasound and this imaging geometry.

1.2 Dissertation Outline

Throughout the course of this dissertation, we have performed detailed investigations to our dual-sided ultrasound scanner and developed various imaging algorithms suitable for this scanner to address the aforementioned issues. Such investigations and the concurrently developed imaging algorithms are studied in extensive simulation cases and datasets. We believe these will provide a solid foundation to *in-vivo* and clinical breast imaging in the future. The body of this dissertation is organized as follows:

Chapter II: We have demonstrated through simulations that shadow area artifacts, that manifest in B-mode images near the subareola region, can be minimized by using ultrasound couplant (coupling gel) that reduces the effective number of impedance mismatch layers within the image [39]. Our findings show that using a couplant with acoustic properties close to the breast skin can reduce spatial artifacts by 57.1% and 96.7%, in low (1 MHz) and high (4 MHz) frequency imaging, respectively.

Chapter III: We have investigated sources of inaccuracy that affect sound speed imaging as performed on our dual-sided ultrasound scanner and reconstructed based on bent-ray and limited angle transmission tomography developed in our group [6], [7], [40]. Each source of inaccuracy is classified as either mis-segmentation on *a priori* B-mode images or miscalibration due to non-rigid transducers. We have shown that simulated mis-segmentation in object size and their lateral location produced maximum sound speed errors of 6.3% within a 10 mm diameter change and 9.1% within a 5 mm spatial shift, respectively. More interestingly, axial translational miscalibration, which is the easiest type of inaccuracy to calibrate in most systems, happens to be the most significant inaccuracy (57.3% within a 5 mm shift).

Chapter IV: We have developed a waveform inversion algorithm for sound speed imaging on our dual-sided ultrasound scanner [9]. The algorithm can not only account for complex acoustic phenomena beyond the existing bent-ray based approach, but can also utilize *a priori* information from B-mode images and cope with image artifacts due to limited *a priori* constraints. Based on simulated reconstructions, using a waveform inversion algorithm provides at least 0.5% accuracy for the reconstruction of simple objects. In addition, when *a priori* information is not available, the reconstruction algorithm can recover fine structural details with minimal artifacts in both simple objects and more realistic, breast tissue-mimicking, phantoms.

Chapter V: We have developed an attenuation correction approach that takes into account the energy loss due to wave signals propagating out-of-plane and therefor missing the receiver [41]. This correction is suitable for attenuation imaging that employs bent-ray algorithms and commercial 1D ultrasound arrays. Three-dimensional waveform inversion algorithms and 2D ultrasound arrays cannot currently be attained due to limited resources. Simulation results show at least 30% more accuracy and 29% less deviation in the attenuation coefficient distribution within the imaged objects.

Chapter VI: We have revisited the waveform inversion algorithm presented in Chapter VI, and applied (modified) source encoding and compressed sensing techniques, to drastically accelerate reconstruction time as well as reduce dataset size. Given N as the number of active transducer elements, the improved reconstruction algorithm can reduce the computation up to a factor of N and dataset size up to a factor of 10, while still providing images comparable to the original waveform inversion algorithm.

Chapter VII: We have explored the possibility to combine algorithms developed for our dual-sided ultrasound system with an optical modality, namely photoacoustic tomography. Specifically, we have developed an image reconstruction algorithm that utilizes *a priori* information from assumed B-mode or B-flow image models. Through simulations, we have demonstrated, improved spatial accuracy as well as reduced noise in the reconstructed phototacoustic images. This holds, even when only one linear ultrasound array is used. Reconstructions on a realistically formed, simulated, breast phantom also suggest the feasibility to translate this technique to the clinic.

Chapter VIII: We summarize the dissertation and suggest possible improvements and future directions.

CHAPTER II

Acoustic Beam Anomalies in Automated Breast Imaging[1]

2.1 Introduction

In 2016, approximately 246,660 women in the United States were diagnosed to have breast cancer. Furthermore, out of all estimated new cancer cases, breast cancer accounts for 29% [42]. In fact, breast cancer is the most frequently diagnosed cancer in women. In the past decade, there has been great demand for ultrasound in the United States for breast cancer screening as a supplement of x-ray mammography, since ultrasound can detect unsuspected, mammographically occult cancer, especially in radiographically dense breasts that have a higher risk of developing breast cancer [3], [4], [43]. Also, several tissue acoustical properties obtained from received ultrasound signals such as speed of sound [7], [15]–[22], attenuation [8], [17]–[19], [21], [23]–[25], density [26], and elasticity [27]–[29] can be used for characterizing different tissue types as they tend to have different acoustic properties. The ability of ultrasonic imaging to characterize tissues, particularly the differentiation of malignant lesions from benign tissues, shows promise in decreasing the number of breast biopsies needed

---

[1] This chapter is published in *Journal of Medical Imaging*: R. Jintamethasawat, X. Zhang, P. L. Carlson, M. A. Roubidoux, and O. D. Kripfgans, "Acoustic Beam Anomalies in Automated Breast Imaging," *Journal of Medical Imaging*, vol. 4, pp. 4 -4 -10, 2017. doi: 10.1117/1.JMI.4.4.045001.

for adequate diagnosis [44].

Compared with x-ray, ultrasound beams undergo much more complex interactions with the tissues through which they propagate. In some cases, this interaction can alter the propagation patterns substantially [13], [14], [45]–[48]. Several studies have tried to extract tissue acoustic properties based on such interactions. To date, however, full-wave calculations have not been performed to study how the imaging anomalies at oblique incidence to the breast explored here arise and can be modified by the choice of coupling agents. Recently, it has been observed that in breast imaging, where images are acquired in the CC-view or in the mammographic view, the anomalies occur as parts of areas that have limited insonification, *i.e.*, signal dropout areas, and are located close to the papilla and the curved skin layer, where many malignant structures are found [49]–[51]. Figure 2.1 shows the signal dropout areas presented in three different B-mode images, acquired from three different patients using our mammography-configured automated ultrasound scanner developed in-house [6], [10], [11]. As can be seen, signal dropout areas occurring around the papilla could negatively result in misinterpretations in breast cancer diagnosis and substantially increasing further procedures for definitive diagnosis. Considering this, it is of particularly interest that automated ultrasonic imaging of the breast in the mammographic geometry, where the ultrasound signal goes through couplant and penetrates the skin at an angle (nonperpendicular direction), oftentimes misses much information of the subareolar tissues due to bending of the acoustic beam by refraction and reflection, leading to the low signal-to-noise ratio (SNR).

Here, we conduct finite-difference-time-domain (FDTD) simulations to investigate artifacts of ultrasound wave propagation in a simulated breast geometry with a curved skin layer under couplants with different acoustic impedances: commercial-gel-like, skin-like, and adipose-like. In addition, we investigate the characteristics of anomalies in the image as results of using the aforementioned couplants, as well as compare the

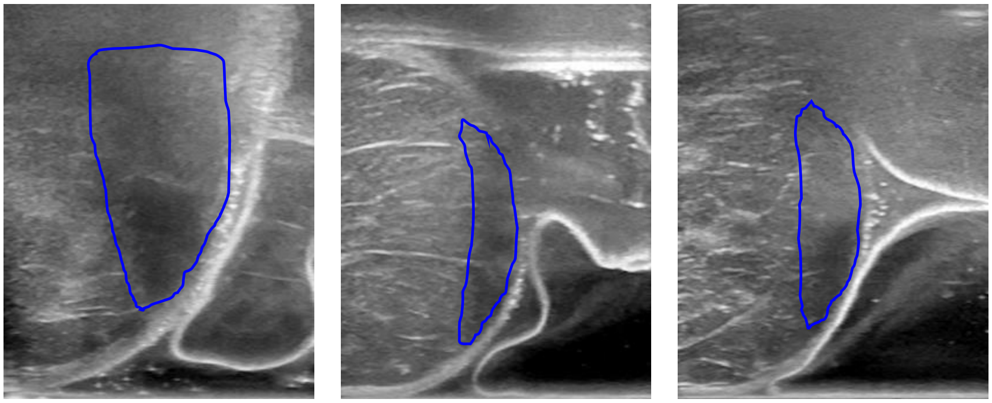

Figure 2.1: Clinical images of compressed female breasts acquired using a GE Logiq 9 ultrasound scanner (GE Healthcare, Milwaukee, Wisconsin) at 10 MHz. Each signal dropout area is enclosed by a manually segmented blue contour. Note that the imaging array is located at the bottom of the images.

imaging performance of each couplant. The findings of our study will provide detailed information about complex ultrasound signal interactions that occur during breast imaging, which could potentially be helpful for designing a couplant that minimizes these artifacts.

This paper is organized as follows: Section 2.2 describes the governing ultrasound wave equations, how the simulation environments were setup, and how the simulation datasets were acquired and processed. Section 2.3 demonstrates the characteristics of the anomalies resulting from using different couplants and provides an in-depth analysis of ultrasound wave interactions/propagation patterns under different circumstances. Finally, Section 2.4 provides a summary and possible future directions of our study.

2.2 Materials and Methods

2.2.1 Breast Geometry

The simulation breast phantom used for all studies consists of ultrasound couplant, skin, and adipose tissue, with their acoustical properties given in Table 2.1 and their geometry diagrammed in Figure 2.2. The dimensions of the field of view in the axial and lateral directions are 37.5 and 25 mm, respectively. The center of the field of view is located at (lateral, axial) = (0, 21.25) mm. The skin layer with a thickness of 2 mm [52], [53] corresponds to the enclosed boundaries that are defined as two elliptical arcs cocentered at (-12.5 -Δx, 37.5) mm, where Δx is the lateral shift of the transducer, and with half major axes of 31 and 33 mm and half minor axes of 18 and 20 mm. By means of Δx, lateral beams are simulated by varying Δx from 0 to 8 mm. The bottom of the numerical breast is bulged and supported by a transducer with an aperture size of 16.74 mm, and surface curvature is defined as an arc of 30-mm radius circle centered at (0, 31.3) mm, mimicking lateral focusing. Note that the curved transducer represents the linear transducer with a focus at the center of curvature, (0, 31.3) mm.

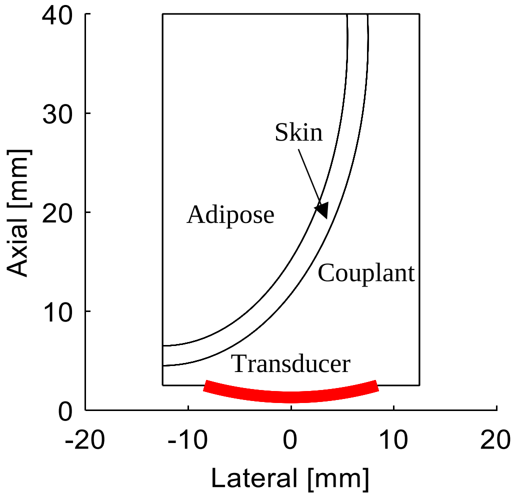

Figure 2.2: Simulated breast geometry consisting of couplant, skin, and adipose tissue.

Table 2.1: Acoustical properties of simulated breast tissues and couplant.

Acoustical properties per tissue/material	Skin	Gel	Adipose
Speed of sound (m/s)	1060	1490	1450
Density (kg/m^3)	1060	1060	900
Dynamic Viscosity (Pa s)	0.5	0	0.5
Bulk viscosity (Pa s)	0.5	0	0.5

Table 2.2: Constants used for simulating wave propagation.

Governing constant	Value
Initial pressure (p_0)	101325 Pa
Pulse delay (t_0)	3 μs
Maximum inward acceleration (a_0)	10000 m/s^2

2.2.2 Wave Propagation Theory

The wave propagation in lossy viscous media with respect to any given time t can be described by the following equation [13]:

$$\frac{1}{\rho c^2}\frac{\partial^2 p}{\partial t^2} + \nabla \cdot \left[-\frac{1}{\rho}\nabla p + \frac{1}{\rho c^2}\left(\frac{4\mu}{3} + \mu_B\right)\frac{\partial \nabla p}{\partial t}\right] = 0, \tag{2.1}$$

where p is the total pressure that is dependent on the given speed of sound c, density ρ, dynamic viscosity μ, and bulk viscosity μ_B. The initial conditions for Equation 2.1 are given as $p = p_0$ and $\frac{\partial p}{\partial p} = 0$ at $t = 0$, where p_0 is the initial pressure (see Table 2.2).

The transmitted pressure from the transducer can be modeled as the inward acceleration of the mesh element whose direction is normal to the transducer surface (red curve in Figure 2.2) and points toward the simulation domain. This can be written as:

$$\mathbf{n} \cdot \left(-\frac{1}{\rho}\nabla p \right) = a_n \tag{2.2}$$

where p is the transmitted pressure, $\mathbf{n}$ is the normal vector of the transducer surface, and a_n is the inward acceleration. The inward acceleration pulse with respect to the lateral location x is given by a sinusoidal acceleration tapered by a Gaussian function and transducer apodization window:

$$a_n(x) = a_0 H(x) e^{-[(t-t_0)1.25f_0]^2 \sin(2\pi f_0 t)}, \tag{2.3}$$

where f_0 is the center frequency and $H(x)$ is the Hamming window defining transducer apodization. The additional parameters a_0 and t_0 are given in Table 2.2.

In addition, to minimize reflections from the simulation domain boundaries, the following radiation boundary conditions are modeled:

$$-\mathbf{n_b} \cdot \left(-\frac{1}{\rho} \nabla p_b \right) + \frac{1}{\rho} \left(\frac{1}{c} \frac{\partial p_b}{\partial t} \right) = Q_i \tag{2.4a}$$

$$Q_i = \frac{1}{\rho} \left(\frac{1}{c} \frac{\partial p_i}{\partial t} \right) + \mathbf{n_b} \cdot \frac{1}{\rho} \nabla p_i \tag{2.4b}$$

$$p_i = e^{\left(\frac{t - x/c}{0.01} \right)^2}, \tag{2.4c}$$

where p_i is the incident pressure field, $\mathbf{n_b}$ is the normal vector of the boundary, Q_i is the acceleration of incidence field in the direction of $\mathbf{n_b}$ on the domain boundaries, x is the lateral location, and p_b is the pressure radiated out of the boundary to cancel reflections caused by simulation domain boundaries.

2.2.3 Simulation Parameters and Assumed Properties

The simulation studies were conducted using center frequencies of 1 and 4 MHz, each with three different choices of couplants. Such three couplants mimicked acoustical properties, *i.e.*, speed of sound, density, and viscosity of commercial gel couplant [54], [55] skin [56] and adipose tissue [21], [57], [58]. To achieve an attenuation coefficient of $\alpha = 0.6$ dB/cm/MHz, the dynamic and bulk viscosity of 0.5 Pa s was applied in skin and adipose studies.

The simulation domain was divided into meshes, where the mesh size was primarily determined by the medium's speed of sound, the used imaging frequency, and a factor that adjusts the mesh size in terms of a fraction of the local wavelength, called spatial sampling rate (SSR). Such parameters are given in Table 2.3. The maximum growth of neighboring meshes with respect to the given mesh is controlled by the maximum element growth rate. Furthermore, the maximum mesh size is controlled by the curvature factor: the mesh size must not exceed the curvature radius of the given geometric boundary, multiplied by the curvature factor. The parameters that constrain the change of mesh size and maximum mesh size allowed with respect to the geometric boundary curvature are given in Table 2.4.

The simulation was performed using the COMSOL multiphysics program V4.2 (COMSOL, Inc., Burlington, Massachusetts), which models wave propagation via the FDTD approach.

Table 2.3: Mesh properties used for 1 and 4 MHz simulation studies. Note that for computational time feasibility at higher frequency, the SSR per wave cycle was reduced to expand the maximum grid size limit.

Mesh property per center frequency f_0	$f_0 = 1$ MHz	$f_0 = 4$ MHz
Temporal sampling rate per wave cycle (TSR)	6	11
SSR per wave cycle	6	4
Maximum SSR per wave cycle ($\mathrm{SSR}_{\max}$)	11	11
Maximum element size	$c/(f_0\mathrm{SSR})$	
Minimum element size	$c/(f_0\mathrm{SSR}_{\max})$	

Table 2.4: Mesh properties used for different materials. To avoid aliasing due to spatial undersampling caused by higher speed of sound, note that the maximum element growth rate and the curvature factor in regions representing skin-like material were set to have slightly lower values than those in regions representing gel-like and adipose-like materials. Lowering these properties for gel-like and adipose-like materials, however, does not yield any accuracy improvement.

Mesh property per material	Skin-like	Gel-like	Adipose-like
Maximum element growth rate	1.1	1.3	1.3
Curvature factor	0.2	0.3	0.3

2.2.4 Simulations

2.2.4.1 Wavefront image generation

To visualize the beam patterns and progression across all simulation times (from 0 to 30 s with the step sizes of 0.25 s for 1 MHz studies and 0.0625 s for 4 MHz studies), all wavefronts from all simulation times were superimposed on the same simulation domain. Specifically, the superimposed image, *i.e.*, the wavefront image, was generated by the following: for any given grid point on the simulation domain, the pressure value was set to the one with the highest absolute value among all simulation times at the same grid point location, *i.e.*, max-hold in time. Note that, from now on, we will define this superimposing procedure as max-hold method. Note that, before performing the max-hold operation, a median filter with a patch size of 0.75 mm 0.75 mm was applied as some (<0.1% by area) of the simulated signals were artifacts with unusually high amplitude.

Twenty-one wavefront images were generated from 21 datasets corresponding to 21 different lateral beam positions. Specifically, the beam was moved laterally from 0 to 8 mm by 0.4 mm increments, thus simulating an image with a 400 μm lateral beam spacing.

2.2.4.2 Determining imaging beam deflections

The imaging beam deflection, *i.e.*, the directional change of the wave from the original propagation direction due to an acoustic impedance mismatch at the interface of two adjacent media, is determined by the wavefront by the most dominant beam refracted after traversing the interface. The most dominant beam is defined as the one with the highest spatial average positive peak pressure over the chosen positive wave peaks on the beam. The following paragraph explains how this average positive peak pressure is determined.

Since it is difficult to determine the most dominant beam *a priori*, several beams were initially considered. Then, for each such beam, the positive wave peaks were localized and the average pressure amplitude of the positive wave peaks was assessed. Only the peak locations from the beam with the highest average pressure amplitude were used to determine the beam propagation direction. Simple linear regression was employed to estimate the line-fitting lateral location of the particular peak given its axial location, and the calculated slope was used for calculating the deflection angle (see Figure 2.3 for illustration of the deflection angle). The same procedure was repeated three times on the same beam, and the average of three deflection angles was calculated. For each type of couplant, the average deflection angle was also calculated as the average of all deflection angle magnitudes among all transducer lateral shifts.

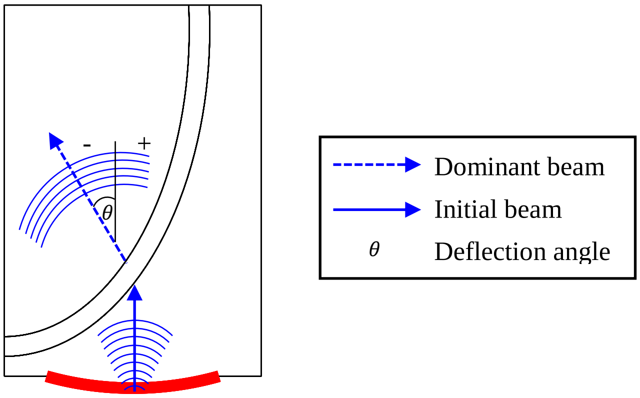

Figure 2.3: Beam deflection caused by acoustic impedance mismatch at the interface between two different media. The deflection angle θ can be obtained by calculating the difference between the directions of the initially propagated beam (solid line) and the deflected beam that has the highest spatial average positive peak pressure (dashed line). Figure labels and annotations are omitted for more clarity; see Figure 2.2 for annotations.

2.2.4.3 Determining signal dropout areas

To demonstrate the effects of signal dropout appearing over a wide range of imaging locations, 21 wavefront images reflecting shifts of 0 to 8 mm were first converted to positive values by the absolute operation ($|\cdot|$) and were then superimposed using the max-hold method. The field-of-view range of the final image containing the signal dropout area was set to 4 to 12 mm laterally and 5 to 40 mm axially, with the uniform resolution of 0.05 mm (see Figure 2.2 for dimension details). Since there is a mismatch between the spatial distribution of pressure mesh point in wavefront images and the signal dropout area image, the pressure mesh point in the 2-D plane was interpolated onto a rectlinear grid via the scattered interpolation method.

The resulting image is the max-hold superimposed pressure distribution from all lateral beam locations showing the signal dropout. The signal dropout area was enclosed by an isocontour whose amplitude was measured by 3 dB down from the minimum of two maximum signal pressures on the cross-section signal profile obtained at the top of the image (greatest axial depth). These two maximum points correspond to the maximum values on two signal profile segments separated by skin layers; see Figure 2.4 for illustration. Once the isocontour of the signal dropout area was determined, the enclosed area was calculated; the minimum, maximum, and average values of all field points within the signal dropout area were also determined.

Note that the propagated signal was attenuated by $\alpha = 0.6$ dB/cm/MHz. For this reason, a time gain compensation (TGC) technique was applied to equalize the attenuated signal with depth. Knowing that the assuming propagation medium has a homogeneous speed of sound of c and a homogeneous linear attenuation of α, the correction factor V at the time t is given as:

$$V(t) = e^{\frac{tc\alpha f_0}{8.686}} \tag{2.5}$$

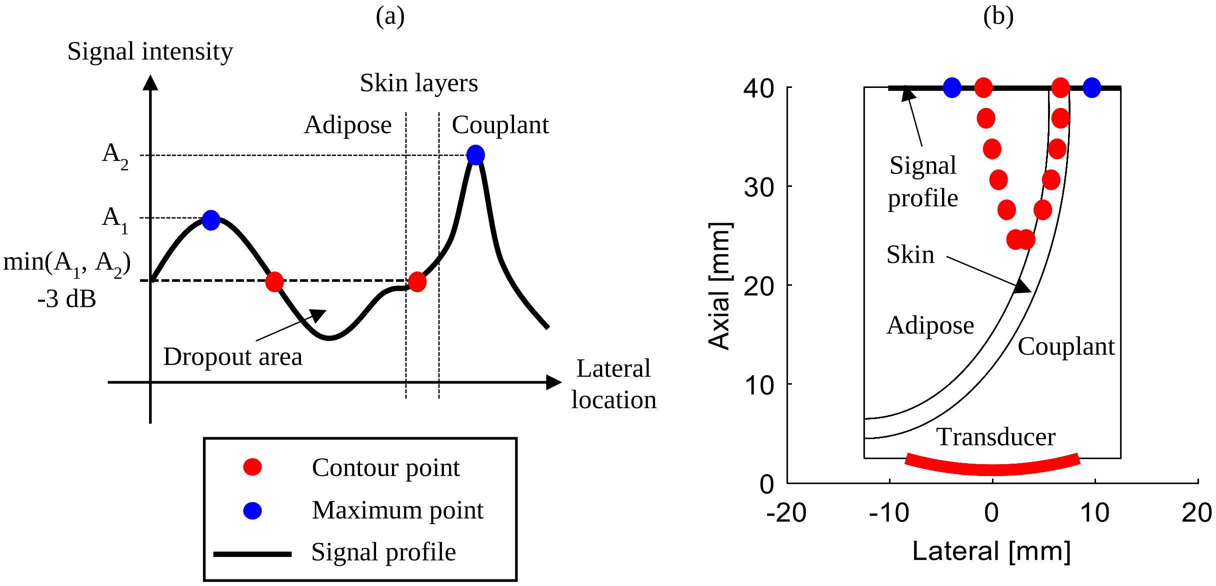

Figure 2.4: (a) Illustration of a signal profile corresponding to the horizontal cross section of the signal dropout area image at the greatest axial depth (40 mm). Two maximum signal pressures on the profile are marked as blue dots. The signal profile under the thick black dashed line represents part of the signal dropout area. All contour points (red) constitute the isocontour of the signal dropout area shown in (b) and Figure 2.7

2.3 Results and Discussion

2.3.1 Deflections of the Transmitted Beams

Figure 2.5 shows examples of beam refraction patterns that occur when the beam transverses the interface between couplant, skin, and breast tissue. Refraction is a function of the local impedance mismatch, the boundary geometry (function of the lateral beam position), and the center frequency. The refracted beam with the highest average pressure amplitude, *i.e.*, the most dominant beam, is marked by a red trace. Figure 2.6 shows the corresponding deflection angle of the most dominant beam, with respect to a vertical path, at both center frequencies, the three couplants, and the 21 beam positions. Note that, due to unresolved technical issues, the simulation at 6.4 mm lateral beam position and 4 MHz center frequency could not be accomplished. The range of 0 to 8 mm was chosen because it is the range over which the artifacts due to the beam deflections are noticeable for the typical breast shape commonly found in clinical settings and chosen for the simulation. Also, the center frequencies of 1 and 4 MHz were chosen because there is a major transition of beam propagation behavior: between these two frequencies, increasing the center frequency from 1 to 4 MHz narrows the beam, which is then able to funnel within the skin layer. Positive deflection angles denote the wave refraction toward the positive lateral direction (*i.e.*, to the right side, see Figure 2.3 for illustration), and negative deflection angles denote the wave refraction toward the negative lateral direction. In general, the deflection curves generated from 1 and 4 MHz datasets (Figures 2.6(a) and 2.6(b), respectively) have somewhat similar characteristics; in the beam shift range of 0 to 1.6 mm, the beams deflect into the breast adipose tissue, and in the range of 4.4 to 8 mm, the beams deflect away from the breast. However, the center frequency seems to play a role in how beams are deflected outside the mentioned ranges. This effect can be seen from both Figures 2.5 and 2.6(b) when commercial-gel-like or adipose-like couplant is used and the center frequency is set to 4 MHz. The beam appears to funnel within the skin layer. This effect, however, does not appear with the lower, 1 MHz, center frequency. This could be explained by the fact that the beam-focusing capability is enhanced when a higher frequency is used, *i.e.*, a narrower beam width is realized and therefore most of its energy can be confined and funneled within the skin layer.

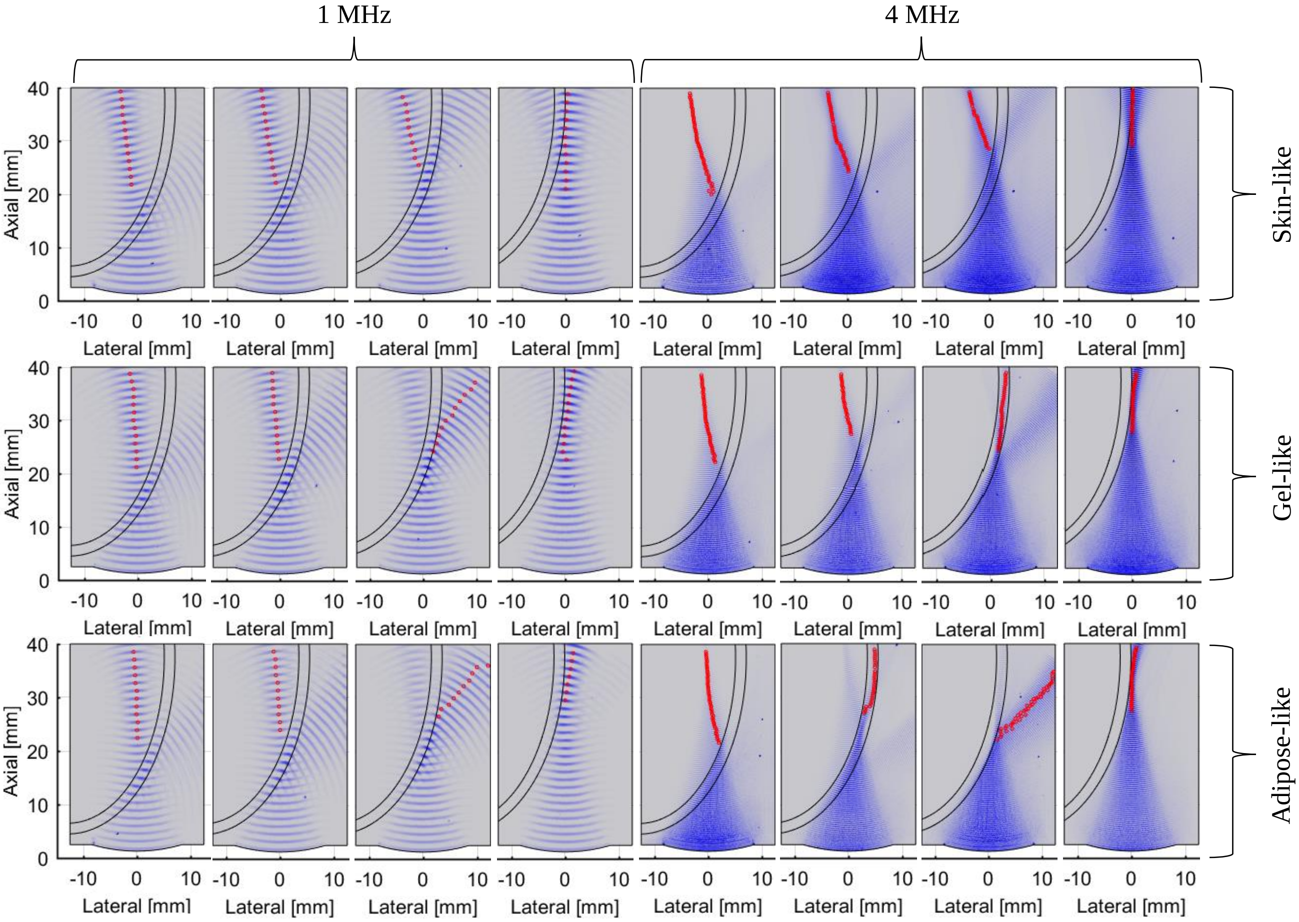

Figure 2.5: Wave propagation pattern as a result of different couplants, beam lateral positions, and two center frequencies. The resultant images are grouped by center frequency and couplant name. For each group, four images from left to right represent wave propagation patterns obtained at lateral beam positions of 0.4, 2.0, 4.0, and 7.6 mm, respectively.

Also, as expected, using the skin-like couplant results in the least amount of beam deflection. However, if the most dominant beam lies inside the breast tissue, the skin

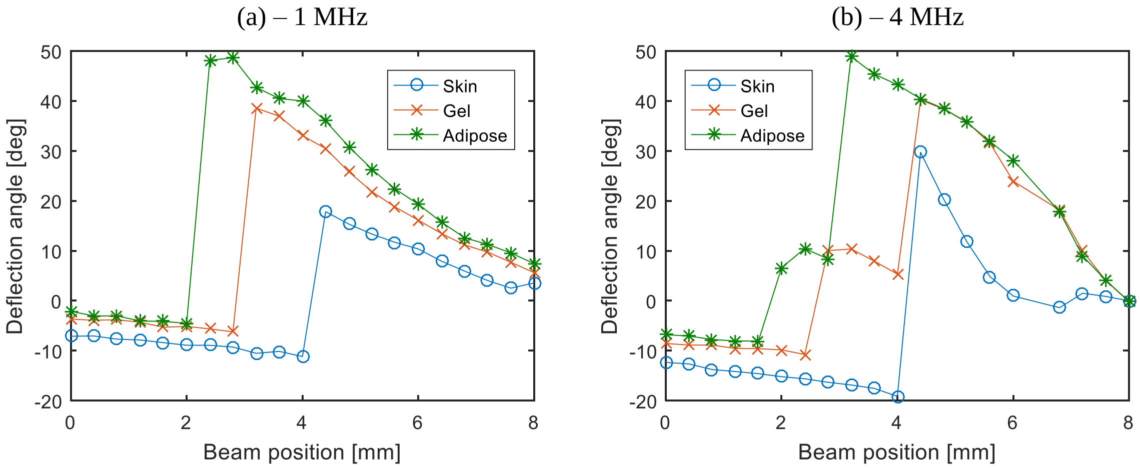

Figure 2.6: Deflection angle of the most dominant beam as a result of different couplants and lateral beam positions. (a) and (b) correspond to the used center frequencies of 1 and 4 MHz, respectively. Two important aspects to note at a particular lateral transducer shift are (1) for beam position not >4 mm, the skinlike couplant will cause the greatest negative deflection, slightly greater than commercial-gel-like and adipose-like couplants, the direction causing signal dropout in the breast. There is less positive deflection for beam position >4 mm with the skin-like coupling, but that angle is basically irrelevant and (2) using the higher center frequency results in more complex beam deflection patterns, especially with the commercial-gel-like and adipose-like couplants.

like couplant will cause the greatest negative deflection compared with commercial-gel-like and adipose-like couplants for both 1 and 4 MHz center frequencies, as can be seen from Figure 2.6. This could be explained as the beam traveling through the skin-like couplant will deflect only at the interface between the inner skin layer and the adipose tissue in the breast, and, since the adipose tissue has a lower speed of sound than the skin, this refraction will cause the beam to deflect to the left side (negative angle). On the other hand, using either the commercial-gel-like or the adipose-like couplant that has lower speed of sound than skin will initially cause the beam to deflect to the right side when the beam is hitting the outer skin layer. Note that this deflection, in turn, causes a greater incidence angle of the beam at the interface between the inner skin layer and the adipose tissue than the same incidence angle resulted from using the skin-like couplant, thus making the final beam bend less toward the left side. On the other hand, when the adipose-like couplant is used, it is important to note that the beam deflections in the breast seem to be greater toward the positive direction than those resulted from using commercial-gel-like couplant. The lower speed of sound of adipose tissue causes the greater positive deflection angle of the beam at the outer skin layer. The greater the positive deflection angle at the outer skin layer, the greater the positive incidence angle at the interface between the inner skin layer and adipose tissue, and this greater incidence angle will cause the final beam to bend more toward the right.

2.3.2 Areas of Signal Dropouts

Figure 2.7 shows the results of signal dropout area in the simulated breast using various couplants. The signal dropout area characteristics (size, minimum, maximum, and average of all pressure samples in the signal dropout area) are given in Table 5 and the box plots in Figure 2.8. As can be seen from both Figures 2.7-2.8 and Table 2.5, both the center frequency and the couplant affect the size and the signal intensity in

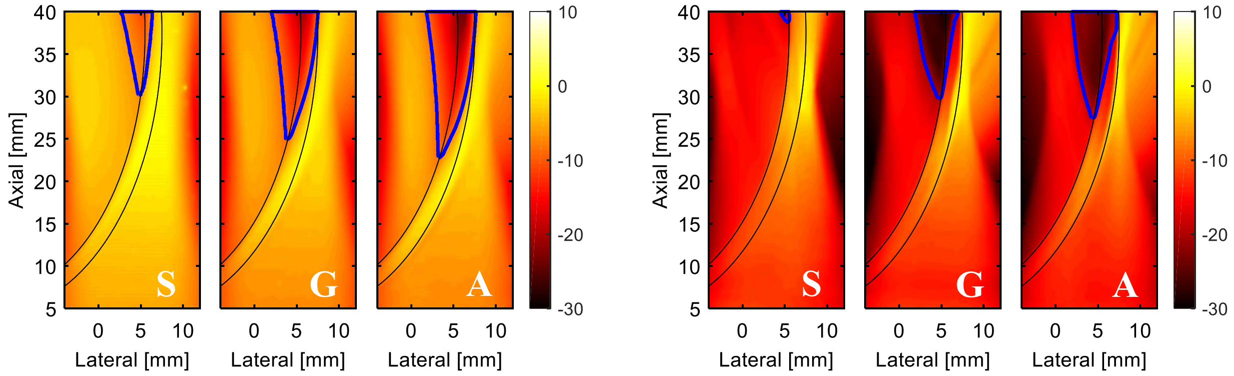
(a) – 1 MHz, 40 dB range

(b) – 4 MHz, 40 dB range

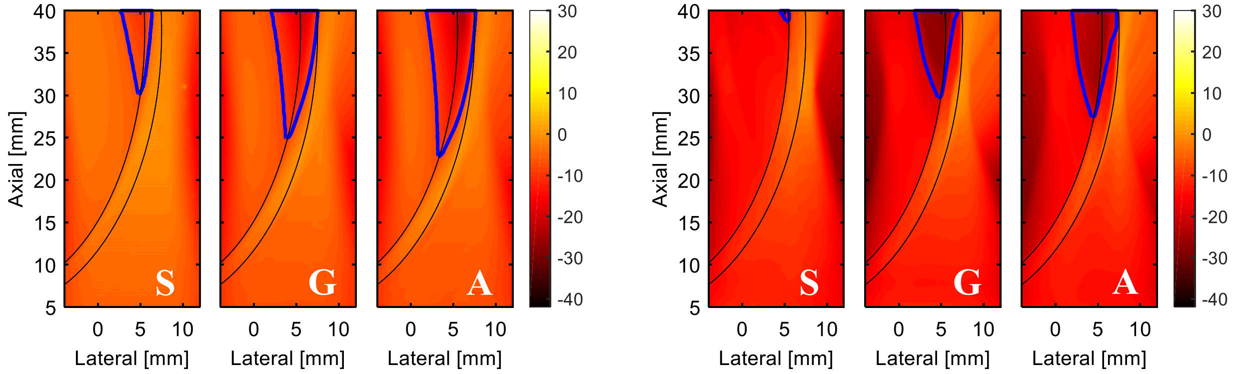
(c) – 1 MHz, 72 dB range

(d) – 4 MHz, 72 dB range

Figure 2.7: Clinical images of compressed female breasts acquired using a GE Logiq 9 ultrasound scanner (GE Healthcare, Milwaukee, Wisconsin) at 10 MHz. Each signal dropout area is enclosed by a manually segmented blue contour. Note that the imaging array is located at the bottom of the images.

Table 2.5: The properties of signal dropout area as results of using different couplants and center frequencies.

Center frequency	1 MHz			4 MHz		
Coupling material	Skin-like	Gel-like	Adipose-like	Skin-like	Gel-like	Adipose-like
Average absolute deflection angle (deg)	9.0	14.6	20.6	12.0	15.1	20.3
Dropout area (mm^2)	21.0	49.0	62.0	1.00	30.0	41.0
Minimum signal intensity in dropout area (dB)	11.1	20.5	23.7	20.0	28.4	25.7
Maximum signal intensity in dropout area (dB)	6.54	8.54	8.33	18.4	20.6	18.6
Average signal intensity in dropout area (dB)	8.03	12.0	12.7	19.1	24.7	22.5

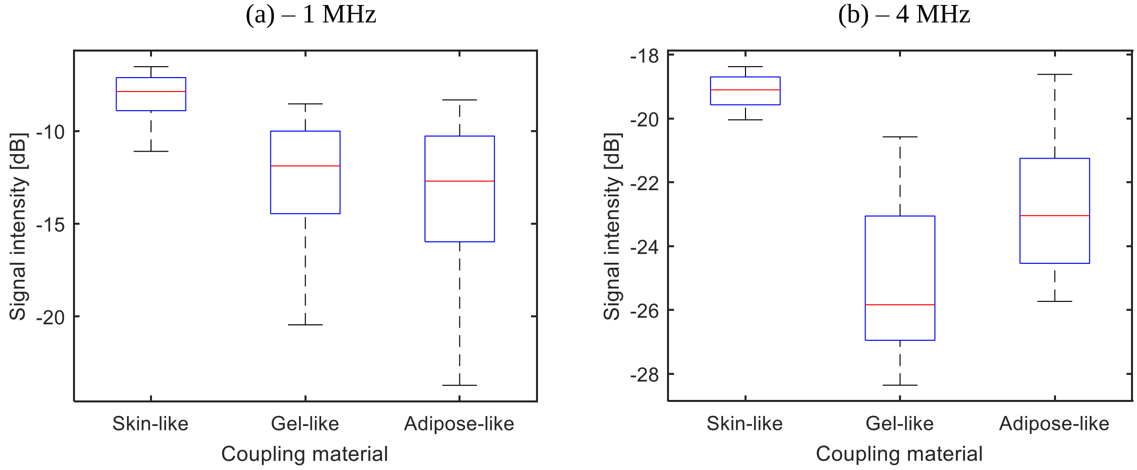

Figure 2.8: Box plots of signal intensity in dropout area, as results of using (a) 1 MHz and (b) 4 MHz center frequencies.

the dropout area.

When using the higher imaging frequency (4 MHz), the propagated beam will be narrower and allow for better spatial resolution, but higher attenuation due to higher frequency can cause a weaker average signal intensity in the dropout area, as suggested by Table 5 and Figure 2.8. Straightforward solutions to compensate for the signal loss are to increase TGC or overall gain (see Section 2.2.4.3 for more details) or to increase the dynamic range. Unfortunately, neither solution is capable of mitigating the signal dropout area. The TGC technique is only able to recover the signal loss due to the attenuation but not the refraction due to the impedance mismatch at the interface between two media. Increasing the dynamic range helps visualize the image regions with low intensity as demonstrated in Figure 2.7, but it is impractical in situations of low SNR.

It is observed that, to decrease the size of the signal dropout area, it may be better to choose an appropriate couplant instead of pursuing the aforementioned solutions.

Couplants affect the signal dropout area characteristics due primarily to phase interference resulting from the speed of sound and acoustic impedance mismatches. As can be seen, both Figure 2.7 and Table 2.5 suggest that the skin like couplant results in the smallest signal dropout area, followed, in order, by the increasingly lower speed of sound commercial ultrasound gel and adipose-like couplants. In addition, it is interesting to note that the area of the signal dropout seems to be related to the average absolute deflection angle obtained across all beam lateral shifts. As can be seen from Table 2.5, the average absolute deflection angle with the three couplants follows the same order as the area of the signal dropout. The reason for using skin-like couplant resulting in the smallest signal dropout area is obviously not only the reduction of one effective interface but also the reduction of absolute speed of sound difference with the skin, which causes a more advantageous refraction result. Note that we have not attempted to make an empirical or analytical fit to these results, as details of the effects will vary in a complex way depending on the particular geometry and acoustic properties of the tissues.

Furthermore, as can be seen from Table 2.5 and Figure 2.8, when a skin-like couplant is used, the average signal intensity in the dropout area is greater and the range of signal intensity in the dropout area is narrower than those obtained when using a gellike or adipose-like couplant. This could be attributed to the reduction in acoustic impedance mismatch that helps ablate overall beam deflection as a result of using the skin-like couplant. Thus, it suggests that using the couplant that minimizes the acoustic impedance mismatch not only improves the signal intensity within the dropout area but also helps eliminate the circumstances where low and high intensity areas appear closely to each other and might confuse radiologic interpretations. The advantages of replacing the gel with a skin-like couplant will be more noticeable in pulse-echo imaging, where round-trip wave propagation occurs as opposed to the one-way wave propagation simulated in this paper.

It is also expected that, for frequencies lower than 1 MHz, the signal intensity within the dropout area will increase due to reduced attenuation; thus, the artifacts will diminish. For frequencies higher than 4 MHz, the dropout areas should appear similar to those of the 4 MHz case as beam deflection patterns will be similar for 4 MHz and above.

The use of relatively low frequencies in the range of transmission tomography systems, compared with the usual 8 to 15 MHz of manual breast imaging, was necessary for computational efficiency. However, the results at frequencies differing by a factor of three give some suggestions of trends at higher frequencies.

2.4 Conclusions

This paper has demonstrated how acoustic impedance mismatch between coupling material, human skin, and subcutaneous breast tissues leads to some of the anomalies seen in imaging, such as during automated whole breast ultrasound and transmission tomography, where the transducers are not always directly in contact with the skin. These anomalies manifest themselves as signal dropout areas, or shadows, inside the breast when the imaging beam transverses the skin at a fairly steep angle (40 deg to 60 deg). This would be particularly important in the subareolar region, where cancer is relatively common near the skin [52], [53]. The simulations showed that reducing the acoustic impedance mismatch between skin and couplant decreases the area of and signal intensity loss in the signal dropout area. Even though only 1 and 4 MHz frequencies were used in the simulations, we expect that this main conclusion will still hold for diagnostic frequencies, as we have seen similar types of artifacts in clinical images, as shown in Figure 2.1. Despite that subcutaneous fat was always assumed beneath the skin, in rare other cases, the subareolar region located close to the skin might also have a speed of sound close to that of the skin. Therefore, similar, possibly increased, artifacts could also be expected around that region, and using couplant with skin-like acoustic properties could then mitigate such artifacts.

Design of an ultrasound couplant with acoustic properties close to those of breast skin might not be trivial. One of these possibilities might be to utilize an ethanolwater mixture with a 17% concentration by weight, which has been shown to provide a speed of sound close to that of breast skin (1605 to 1610 ms) and provide a negligible temperature coefficient of speed of sound in the range of room to body temperatures. However, control of the volatility of the ethanol might be needed. Modest reduction in the temperature of the breast and couplant would also reduce the speed of sound contrast in the breast and resulting artifacts, but there are clear limitations related to patient comfort.

It was observed that using the skin-like couplant could cause slightly greater beam deflection within the breast, but this increase in deflection is outweighed by the considerable decrease in the signal dropout area compared with using commercial ultrasound or adipose-like gel.

When performing compound imaging in a breast freely suspended in a coupling medium, without having transmission data and doing three-dimensional (3-D) full-wave migration, this type of analysis would potentially allow the exclusion of erroneous data from compound summations. One might also include some refracted wave data after approximate corrections for the expected bending of wavefronts. The surface of the skin should be tracked in 3-D in the images performed up to the image being formed to make these corrections in, eventually, real-time interpolations of a more extensive set of data than that provided here. This correction should result in much improved image quality at distances of up to several centimeters from the skin.

Short of full-wave migration imaging, wave migration calculations in a limited volume might be performed to allow corrections around recognizable and segmentable internal structures for which reasonable estimates of the speed of sound could be made [59]–[61]. This could strongly reduce shadows at the edges of structures with smooth borders, such as suspensory ligaments, cysts, and fibroadenomas, revealing possible diagnostic information about poorly seen distal borders and providing more information about the attenuation properties of the tissues of the smooth-walled masses themselves, independent of their speed of sound differences with the surrounding material [8], [25]. Shadow reduction might be less with the majority of invasive carcinomas, those having very diffuse borders.

CHAPTER III

Error Analysis of Speed of Sound Reconstruction in Ultrasound Limited Angle Transmission Tomography[1]

3.1 Introduction

A leading application of ultrasound transmission tomography (UTT) is breast cancer screening and diagnosis [17], [21], [22], [62]–[68]. Our approach has been to adapt UTT to work in the same geometry as x-ray mammography and the similar digital breast tomosynthesis (DBT) to facilitate use of the dual modality information that, in the dense breast, is highly complementary. MRI can also be used to distinguish normal and cancerous masses, but it is limited by high imaging cost and the current necessity of intravenous contrast agent [3], [4].

Most successful ultrasound transmission tomography systems for breast imaging involve suspending the breast in a water tank and using a rotating transducer array or a ring-like transducer array. The latter allows the wave signal to be transmitted from and received by elements in any direction in the image plane. While work has

---

[1] This chapter is published in *Ultrasonics*: R. Jintamethasawat, W.-M. Lee, P. L. Carson, F. M. Hooi, J. B. Fowlkes, M. M. Goodsitt, R. Sampson, T. F. Wenisch, S. Wei, J. Zhou, C. Chakrabarti, and O. D. Kripfgans, "Error Analysis of Speed of Sound Reconstruction in Ultrasound Limited Angle Transmission Tomography," In press.

progressed on registering ultrasound with mammography acquired in a different geometry [37], in practice this registration is still quite difficult. Recently, Hooi and Carson [7] showed that two stationary linear transducer arrays, configured for limited angle transmission imaging, (Figure 3.1) have promise in delivering information similar to that of full-aperture ultrasound transmission tomography, by utilizing B-mode image segmentation to define areas of relatively homogeneous tissues. This segmentation information is necessary because otherwise, with just pulse transit time data between two opposed linear arrays, there is minimal information on the location of tissue boundaries lying parallel to the transducers. This lack of complete information thus results in limited-angle vertical artifacts. The advantages of limited angle tomography include use of established clinical transducers, shorter path lengths, that in turn allow higher frequency imaging, and potential combination with photoacoustics or x-ray mammography or tomosynthesis [6], [10], [11], [37], [69].

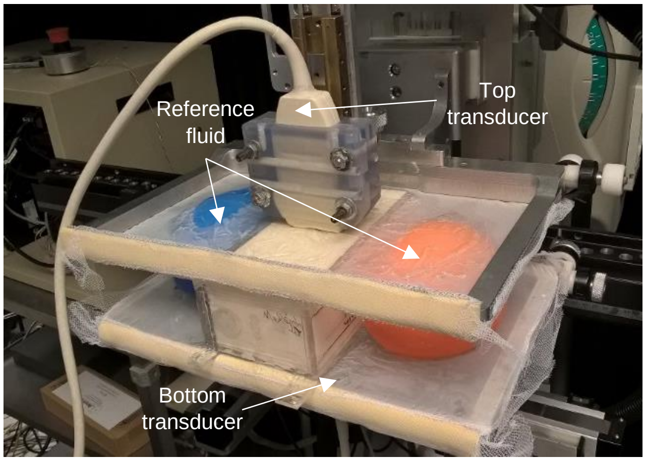

Figure 3.1: Breast-mimicking phantom compressed between two mesh paddles, imaged by two axially opposing ultrasound transducers operating in reflection and transmission mode. Inside the lateral balloons on the sides is a reference fluid for transducer position calibration. The system is named the Breast Light and Ultrasound Combined Imaging (BLUCI) system.

SOS images of small lesions and larger structures in a challenging tissue-mimicking phantom (Madsen, Madison, WI), reconstructed by limited angle transmission tomography previously proposed in [7], are shown in Figure 3.2 along with their corresponding true SOS image (Figure 3.2(d)) and B-mode images (Figure 3.2(a)-(b)). This phantom has the same geometry as the one shown in [7] but has different SOS contrast. With help from segmentation information obtained from B-mode images (Figure 3.2(c)), the reconstructed SOS image shown in Figure 3.2(f) appears more accurate than that shown in Figure 3.2(e), where segmentation information was not utilized. The greatest SOS error in Figure 3.2(f) was -1.4%, in the 5 mm, hypoechoic, spherical simulated mass on the left hand side. Our generation of the research scanner (Verasonics, Kirkland, WA) employed for individual RF channel data in the transmission measurements provided inferior B-mode images and algorithms. Thus, the main homogeneous regions in Figure 3.2(b) were segmented by overlaying the corresponding B-mode image from a separate scan in the same compression using a Logiq 9 scanner (GE Healthcare, Milwaukee, WI) (Figure 3.2(a)). Other factors necessitating use of the Logiq 9 scanner included the higher frequency of GE's M12L transducer (9 MHz) compared to the L7-4 (5 MHz) transmission imaging arrays (ATL/Philips, Bothell, WI) used with the Verasonics scanner. The resulting manually-segmented regions are shown in Figure 3.2(c), and note that advanced automated segmentation methods can potentially be used to delineate tissue regions with reasonably homogeneous SOS.

Our earlier work in limited-angle SOS imaging [7] was performed with a rigid system, without the possibility of flexible positioning, that is now offered in the Breast Light and Ultrasound Combined Imaging (BLUCI) system. There are, however, strong spatial and weight constraints for transducers and translators that are added to BLUCI and correspondingly to a commercial mammographic or DBT system. When scanning in contact with the breast and flexible compression membrane, forces and torque are exerted on the transducers. These make it difficult to meet rigidity criteria imposed by the extreme sensitivity of SOS reconstructions to relative positions of the two transducers. Moreover, as illustrated earlier in Figure 3.2, B-mode images can be used to provide *a priori* information to aid the SOS reconstruction and improve its accuracy. However, the SOS reconstruction does rely on the given enclosing boundary and other segmentation information, thus it is crucial to understand the effects of inaccurate mis-segmentation.

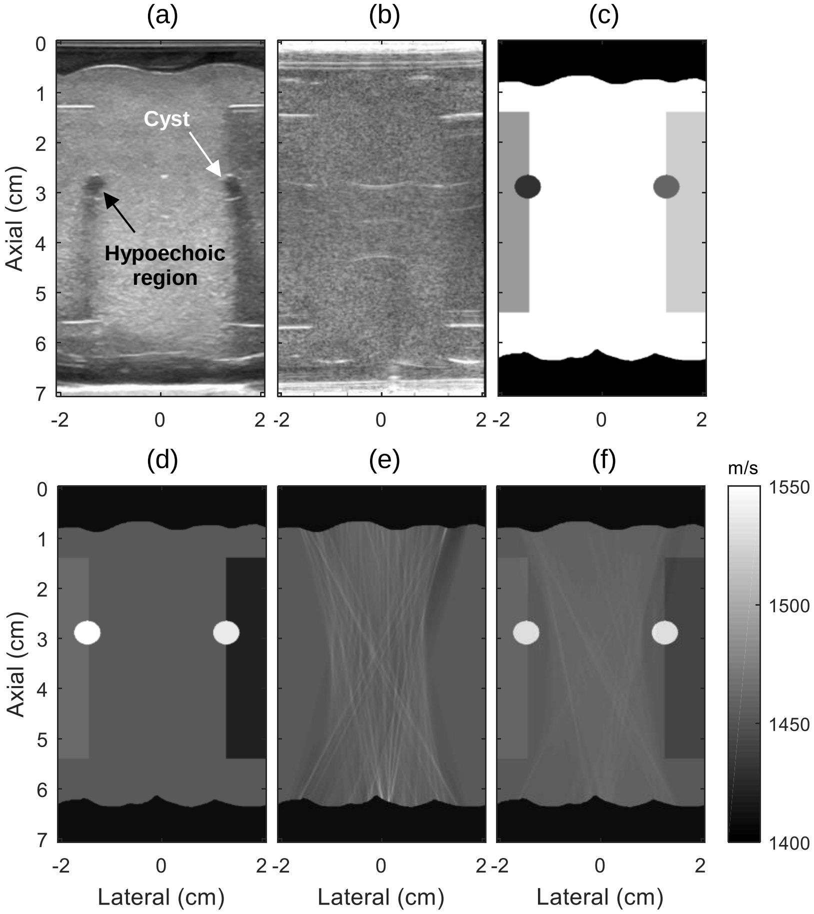

Figure 3.2: (a) B-mode image of a tissue-mimicking phantom obtained from a commercial ultrasound system, used mainly for guiding segmentation on (b). (b) B-mode image of the same phantom obtained from a research ultrasound system. (c) Image of segmented regions. (d) Known, true speed of sound image. (e) and (f) reconstructed speed of sound images without and with guidance from segmentation, respectively. The speed of sound of two enclosing wavy layers at the top and bottom was fixed at 1409 m/s for the reconstruction.

3.2 Materials and Methods

3.2.1 System Descriptions and Specifications

Our Breast Light and Ultrasound Combined Imaging (BLUCI) [6], [10] system consists of two linear array transducers mounted above and below two mammographic-style mesh compression paddles in positioning carriages, as illustrated in Figure 3.1. The coupling between breast, paddles, and transducers is achieved by using bubble free ultrasound gel (Sonotech, Bellingham, WA). The reference fluid in the side balloons is used for transducer position calibration. The positioning carriages can move the transducers in the lateral-elevational 2D space with 2 µm step size (Parker, Rohnert Park, CA). Concurrently, in absence of external forces, arising from the compression paddles and the transducer apertures touching the paddle/skin, the distance between the transducers is kept constant.

The system is interfaced with a Verasonics V-1 (Verasonics, Kirkland, WA) research ultrasound system (ATL/Philips, Bothell, WI, with two ATL L7-4 linear arrays), to acquire raw radiofrequency (RF) data of regions shown in Figure 3.2. A Logiq 9 scanner (GE Healthcare, Milwaukee, WI) with M12L transducers are used to acquire high quality B-mode images.

For tomographic RF data acquisition, an ultrasound wave is transmitted from one element in the transmit array and received by all elements of the opposite array. Thus, for an L7-4 linear array with 128 elements, a total of 128×128 RF traces are collected, though signals from the most oblique angles are of poor signal-to-noise ratio and cannot be used because of the limited directivity of the transducer elements. The main lobe is up to ±17 deg from the central axis. B-mode images are also obtained from the top and bottom transducers to allow boundary identification of objects and background regions to merge with this M12L image for segmentation.

The SOS image reconstruction algorithm for limited angle ultrasound tomography as proposed by [7], adopts the inversion algorithm in [70] and the approaches in [17], [71]. The proposed reconstruction problem can be formulated via minimizing the following cost function S with respect to the given vectorized slowness (inverse SOS) $\mathbf{m}$:

$$2S(\mathbf{m}) = \big(g(\mathbf{m}) - \mathbf{d}\big)^T \mathbf{C}_{\mathbf{D}}^{-1} \big(g(\mathbf{m}) - \mathbf{d}\big) + \big(\mathbf{m} - \mathbf{m_a}\big)^T \mathbf{C}_{\mathbf{M}}^{-1} \big(\mathbf{m} - \mathbf{m_a}\big) \tag{3.1}$$

Vectors $\mathbf{d}$ and $g(\mathbf{m})$ represent measured and simulated time of flight (TOF). The operator g converts the given slowness vector $\mathbf{m}$ to the simulated TOF vector, which can be accomplished by Multistencils Fast Marching Methods (MSFM) [72]. Variances of individual measured TOFs can be modeled via the diagonal matrix $\mathbf{C_D}$. *A priori* information, usually from B-mode segmentation of regions of similar tissues, is included in the second term on the right hand side of Equation 3.1, through assigning initial guesses of the slowness image $\mathbf{m_a}$ and through defining the variances of reconstructed slowness pixels and their correlations in $\mathbf{C_M}$. The initial estimate of the slowness image, $\mathbf{m_a}$, can be assigned as a uniform slowness. $\mathbf{C_M}$ can be defined by the correlation coefficient ρ_k of region k and the standard deviation σ of the reconstructed slowness. For pixels i and j, $\mathbf{C_M}$ is more specifically defined as $C_{M_{ij}}$. If $i \neq j$ and i and j belong to the same region, then $C_{M_{ij}} = \rho_k \sigma^2$. If $i = j$, then $C_{M_{ij}} = \sigma^2$ and otherwise $C_{M_{ij}} = 0$.

The conjugate gradient method was employed to iteratively minimize the cost function in Equation 3.1. For every image reconstruction done in this paper, the pixel size was set to $0.25\lambda \times 0.25\lambda$, where λ was the wavelength. Such pixel size was chosen to ensure that it was well within the resolution limit [73] while keeping the computational complexity tractable. The slowness distribution was assumed as Gaussian, whose mean and standard deviation were set to the initial estimate of the slowness image ($\mathbf{m_a}$) and 4.8×10^{-5} s/m, respectively. This definition allowed the slowness to vary from 6.19×10^{-4} to 7.15×10^{-4} s/m, corresponding to an approximated SOS range of 1400 to 1615 m/s, which includes normal breast tissue, fatty tissue, fibroadenoma, and cancer[17]. Similarly, the TOF distribution was assumed as Gaussian with its mean centered at the measured TOF ($\mathbf{d}$) and standard deviation of 50 ns, *i.e.* the signal jitter at 20 MHz, which was also used to populate the diagonal entries of $\mathbf{C_D}$. The initial slowness image ($\mathbf{m_a}$) was set to a homogeneous SOS map obtained from averaging all rays normal to the transducer arrays. Intra region correlation coefficients (ρ_k) were set to 0.01, based on previous studies [7], to allow enough degree of freedom for the reconstructed slowness to recover object profiles along the axial direction. For large homogeneous background, the correlation coefficient was set to 0, as it was thought that its estimated initial SOS was likely close to the true SOS. The reconstruction algorithm was run for up to five iterations and was stopped earlier if the ratio of the residual (L1 norm of $\big(g(\mathbf{m}) - \mathbf{d}\big)$ in Equation 3.1) of the current iterations, to the 1st iteration was converging and was less than a pre-specified threshold.

Investigations using simulations are described in Section 3.2.2 and some of those results were validated by physical experiments that are described in Section 3.2.3. All the simulations and image reconstruction were performed using MATLAB (MathWorks, Natick, MA).

3.2.2 Simulations

Simulation studies were aimed to investigate misalignment effects under controllable settings and magnitudes. The simulation setup consisted of two artificial linear array transducers (ATL L7-4, Table 3.1). Transducer elements were assumed to be transmit/receive points rather than areas and have unlimited directivity. A SOS image can be reconstructed from 1) the input TOF vector ($\mathbf{d}$) consisting of first arrival times of all transmit-receive element pairs, 2) the assumed positions of the receive transducer elements relative to the transmit transducer elements, and 3) the assumed segmented regions-of-interest (ROI) of the B-mode image used for constructing $\mathbf{C_M}$. The input TOF vector was generated by multistencils fast marching methods described in [72], given the correct speed of sound image and the transmit element location as the inputs. Unless stated otherwise, the input TOF vector $\mathbf{d}$ was noise-free. All simulated misalignment magnitudes are shown in Table 3.2.

Table 3.1: Simulation control variables used for transducer modeling

Simulation Parameter	Value
Number of transducer elements	128
Transducer center frequency	5 MHz center frequency 4 to 7 MHz nominal frequency
Transducer element spacing	300 µm
Separation between the two transducers	60 mm

Table 3.2: Types and magnitudes of misalignments/miscalibrations for simulation and experimental studies

Simulation Parameter	Value
Segmentation size (r)	Scenario A: -10 to 10 mm with 2 mm step Others: -5 to 5 mm with 1 mm step
Segmentation axial (d_1) and lateral (d_2) displacements	-5 to 5 mm with 1 mm step
Transducer axial (d_1), lateral (d_2), and elevational (d_3) displacements	-5 to 5 mm with 1 mm step
Transducer rotations about elevational (θ) and axial (α) axes	-10 deg to 10 deg with 2 deg step

3.2.2.1 Pre-Study: effect of noise on measurements

In practice, noise in the acquired signals, besides mis-segmentations and miscalibrations, may contribute to the errors in the reconstruction. As such, it is important to investigate how much its effect is on the reconstruction errors before proceeding to other studies. To do so, three background Gaussian noise levels were generated by three Gaussian distributions with zero mean and following standard deviations: 1, 2, and 3 percent of the average of TOF as obtained from all rays normal to the arrays.

For each noise level, three noise realizations were generated, and the mean SOS errors, within the background and object regions for each noise realization, were calculated. The final SOS mean and standard deviation for each noise level were calculated.

3.2.2.2 Effects of segmentation inaccuracy

Segmentation inaccuracies can occur for either the objects of interest (*i.e.*, masses) or other tissues, and their effects on reconstructed SOS images were assessed. We investigated segmentation inaccuracies on a single cylindrical target in the following scenarios:

- Scenario A - Effects of segmentation errors due to incorrect size (r in Figure 3.3(a)) or location (d_1 and d_2 in Figure 3.3(b)) of the target ROI segment, for a simulated cylindrical target placed at the center of the imaging field (refer to Table 3.2 for misalignment magnitudes). The reconstruction was repeated for cylinders of 6, 9, 12, and 15 mm diameter. Such sizes were chosen as they represent early stage tumor size. The assigned cylinder and background SOS were 1606 and 1492 m/s, respectively.

- Scenario B - Same as A but for six combinations of cylinder SOS of 1434, 1550, and 1606 m/s and background SOS of 1492 and 1515 m/s. Note that the object SOS of 1550 m/s and background SOS of 1515 m/s were assigned based on those of tumors and fibroglandular tissue in the breasts of middle-aged women [17], [59] and all other parameters were chosen to represent clinical imaging. The cylinder was chosen to be 12 mm diameter.

- Scenario C - Effects of segmentation errors in a simulated 12-mm diameter cylindrical target placed off-center in the imaging field. The cylinder and background SOSs were 1606 and 1492 m/s, respectively. The reconstruction was repeated for four different cylinder positions placed at 4 and 8 mm from the center of the imaging field in the axial and lateral directions, respectively.

- Scenario D - Effects of segmentation errors due to incorrect size or location of a nearby object (r in Figure 3.3(c)). The nearby object was a rod with elliptical cross-section. Both cylinder (12 mm diameter) and rod were placed 11.25 mm axially from the center of the imaging field. Inaccurate segmentation was simulated for the rod, whose SOS was set to 1434 and 1550 m/s for low and high SOS contrast, and whose cross-sectional half major axis was set to 7 and 13 mm. Its half minor axis was fixed at 6 mm and the background had a SOS of 1492 m/s. The rod's SOS was computed as the mean SOS within the rod's misaligned ROI and the cylinder's SOS was computed as the mean SOS within the cylinder's ROI.

3.2.2.3 Effects of array miscalibration

We simulated array miscalibration errors by displacing the receive and transmit array centers in the axial, lateral, and elevational directions, and rotating the receive array about elevational and axial axes (Figures 3.3(d) and (e), see Table 3.2). Studies of array miscalibration were executed according to Scenarios A-C, respectively.

Elevational translations and axial rotations result in shifts of most element pairs in the elevational direction and, thus violate the planar imaging assumption. To continue considering this problem as planar in the simulations, we created new virtual image planes that were not coplanar with the original image plane. For the axial rotations, this virtual plane was where the misaligned receive array and the given transmit element lay. This is possible as the transmit/receive elements are point sources and receivers. The cylinder's cross-section was projected into the imaging plane.

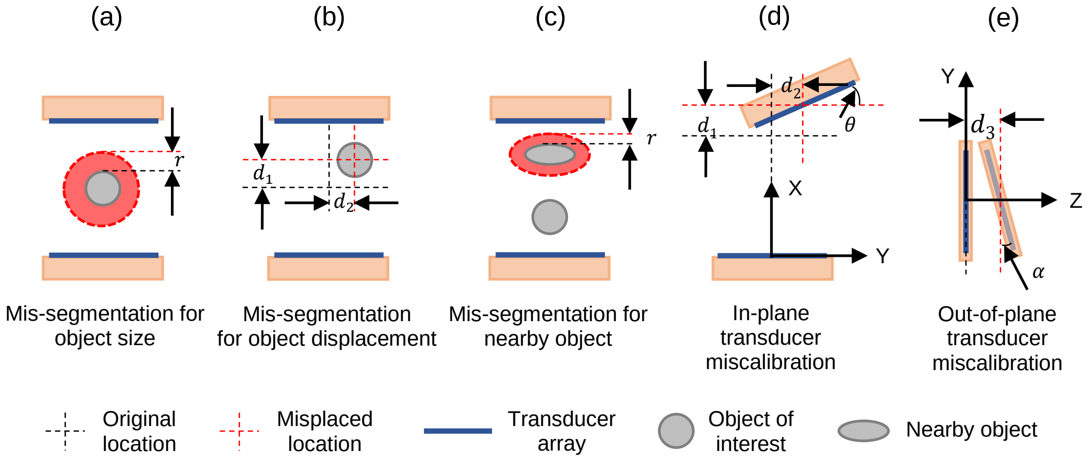

(a) Mis-segmentation for object size

(b) Mis-segmentation for object displacement

(c) Mis-segmentation for nearby object

(d) In-plane transducer miscalibration

(e) Out-of-plane transducer miscalibration

Figure 3.3: (a)-(c) Studied error types in object segmentation. (a) r corresponds to a diameter change in segmentation. d_1 and d_2 in (b) correspond to the axial and lateral shift in segmentation, respectively. (c) Mis-segmentation of nearby object size. (d)-(e) Studied types of relative transducer miscalibration: d_1, d_2, in (d) and d_3 in (e) correspond to axial, lateral and elevational translation miscalibrations, respectively. θ in (d) and α in (e) correspond to elevational and axial rotation miscalibrations. The image plane origates at the transmit element.

3.2.3 Physical Phantom Experiments

The experiments were performed on the BLUCI system as described in Section 3.2.1. The paddles and scanning system were rotated 90 deg from a mammographic cranial-caudal (CC) to a lateral view to facilitate placement of a 6 cm thick polyethylene bag (69 µm wall thickness, Ziploc, SC Johnson, Racine, WI) filled with deionized water and held between the two mesh paddles (Figure 3.4). The two transducers were first aligned to be coplanar by pulse echo measurements from a flat plate and then in transmission mode in the calibration liquid. Then, in-plane calibration was performed according to [74] to correct all in-plane miscalibrations and warrant the desired transducer separation.

Effects of segmentation inaccuracy (r in Figure 3.3(a) and d_1, d_2 in Figure 3.3(b)) were assessed paralleling Scenario A in Section 3.2.2.2. Similarly, effects of array miscalibration were assessed paralleling translational miscalibrations (d_1, d_2 in Figure 3.3(d) and d_3 in Figure 3.3(e)) as described in Section 3.2.2.3. The miscalibrations in the elevational and lateral directions were achieved by moving both transducers in opposite directions via the micro-positioning motors. Axial miscalibration was adjusted manually and observed using an analog displacement gauge dial (±0.001 inches, Mitutoyo America, Aurora, Illinois 60502). Table 3.2 provides all relevant mis-segmentation and miscalibration magnitudes. One cylindrical target with 13-mm diameter was imaged with cylinder and background SOS of 1606 and 1492 m/s, respectively. Simulation reconstructions of the same cylinder were performed for direct comparison to the physical experiments.

The input TOF vector $\mathbf{d}$ was generated by extracting arrival times of all received RF traces via the Akaike Information Criterion (AIC) picker [75] that is robust to superpositions of direct and refracted waves. Since the experiments were performed in a low attenuation medium (water), the limited directivity within ±17 deg from the central axis was not taken into account, meaning all RF traces from all transmit-receive element pairs were acquired. The covariance matrix $\mathbf{C_M}$ was generated from dual-sided B-mode image segmentation. Top and bottom images were spliced using cubic spline interpolation [10].

The cylindrical target (polyethylene wall) was filled within an ethanol-water solution with a constant SOS in the range of 20-35 °C. Ethanol-water is an excellent calibration liquid thanks to its ability to provide a wide range of SOS in human biological tissues [76] when varying the ethanol concentration [77].

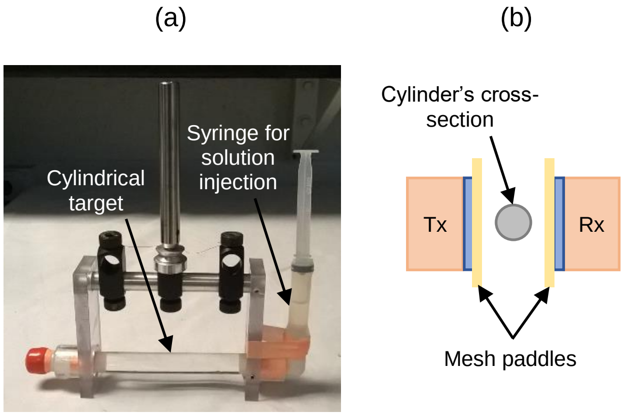

Figure 3.4: (a) Horizontal cylindrical target filled with ethanol-water solution. It was also contained in a Ziploc water bag. The transducers were positioned between two compression paddles and transducers of the BLUCI scanning system as illustrated in (b) and Figure 3.1.

The SOS of a given ethanol-water solution can be measured using a system described by Selfridge [78] (Figure 3.5) and consisting of two single-element focused transducers transmitting broadband pulses at 5 MHz center frequency, placed facing each other inside a water tank and mounted on digital Vernier calipers with ±10 µm accuracy. The SOS of ethanol-water solutions was measured along the central axis of a 10.3 mm thick PVC ring, whose windows were sealed with 10 µm thick Saran wrap (Saran, SC Johnson, Racine, WI). The acquired RF traces were cross-correlated [79], [80] to extract TOFs determined by the AIC picker method [75].

Water-ethanol solution SOS was measured for each concentration from 10% to

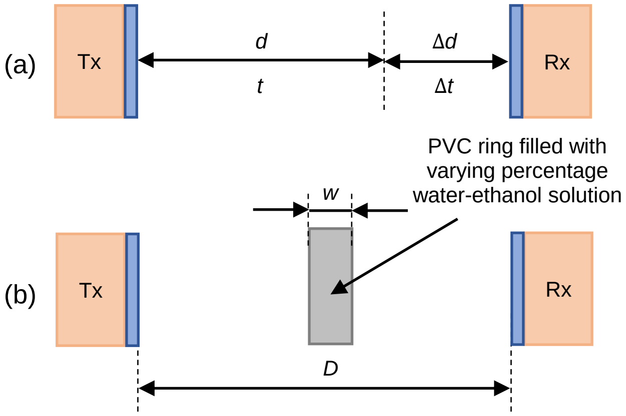

Figure 3.5: (a) Setup for SOS data acquisition as described by Selfridge [78]. The SOS of water (surrounding medium) was calculated from differences in TOFs (Δt) and transducer separations (Δd). (b) Setup for SOS measurement of the sample solution in a short PVC pipe with thickness w (10.3 mm) and $D \approx 15 - 20$ mm. Two signal acquisitions, one without the sample in the path and another with, allow the SOS calculation of varying percentage water-ethanol solution.

90% vol/vol at 23±0.3 °C ($N = 12$, 10% point steps, ±0.1 °C). Means and standard deviations were compared to the literature [77], [81], [82]. Literature results not based on volume concentrations were converted by using the Alcohol and Tobacco Tax and Table Bureau (TTB) software [83], [84]. Linear interpolation was applied where necessary. Furthermore, we measured solution SOS at five additional concentrations of 16, 17, 18, 19, and 20% vol/vol and at four additional temperatures of 20, 25, 30, and 35 °C, to confirm stability over these ranges ($N = 12$) [77].

3.3 Results

3.3.1 Speed of Sound Measurement of Ethanol-Water Solutions

The measured SOSs are plotted in Figure 3.6 in comparison to published results [77], [81], [82]. The maximum measured standard deviation is 3.8 m/s at 10% vol/vol concentration and hence small compared to the absolute scale with the published data, suggesting that it is acceptable to use our velocimetry apparatus.

Table 3.3 shows ethanol-water solution speed of sound at finer stepped ethanol concentrations and ambient temperatures ($N = 4$ each). As shown, a volume concentration of 17%, corresponding to the SOS of 1606 m/s, has the smallest standard deviation, suggesting that SOS is least dependent on temperature at this concentration. This finding is consistent with the results in the literature at 23 °C and 17% vol/vol [77], [81], [82].

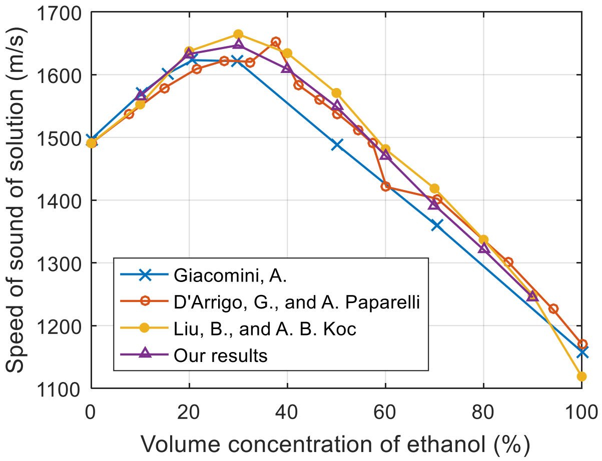

Figure 3.6: Comparison of our SOS measurements of a 23 °C ethanol-water solution with published data. For each concentration, 12 measurements were used to calculate the mean SOS. Note: Error bars on our data points are smaller than the plot symbol.

Table 3.3: Measured speed of sound of ethanol-water solutions at different ethanol concentrations and ambient temperatures (in m/s). Standard deviation of measurements across different temperatures ($N = 4$) is also given.

Temperature (°C±0.1 °C)	Concentration (% vol/vol±0.5% vol/vol)				
	16	17	18	19	20
20	1597	1608	1609	1630	1623
25	1605	1606	1604	1615	1624
30	1603	1606	1614	1610	1617
35	1600	1610	1608	1612	1615
Standard dev. SOS ($N = 4$)	3.5	1.9	4.1	9.1	4.4

3.3.2 Pre-Study: Effect of Noise on Measurements

The calculated regional (object, background) mean [standard deviation] SOS, for 1, 2, and 3 percent Gaussian noise levels, is (1575 [2.0], 1497 [1.4]), (1572 [3.9], 1496 [2.6]), and (1566 [5.5], 1496 [3.2]) m/s, respectively, corresponding to (-1.9, 0.4), (-2.1, 0.3), and (-2.5, 0.3) percent SOS error with respect to the correct SOS ($N = 3$).

3.3.3 Effects of Object Segmentation Inaccuracy

Figure 3.7 shows the calculated reconstruction error of an object in Scenario A, *i.e.*, SOS error of the simulated object (1606 m/s) mis-segmentation in background (1492 m/s). Maximum object SOS errors from incorrect segmentation are 6.3% within 10 mm object diameter change and 9.1% within 5 mm lateral shift. By comparison, an axial shift in the segmentation produces a 2.6% error within 5 mm shift.

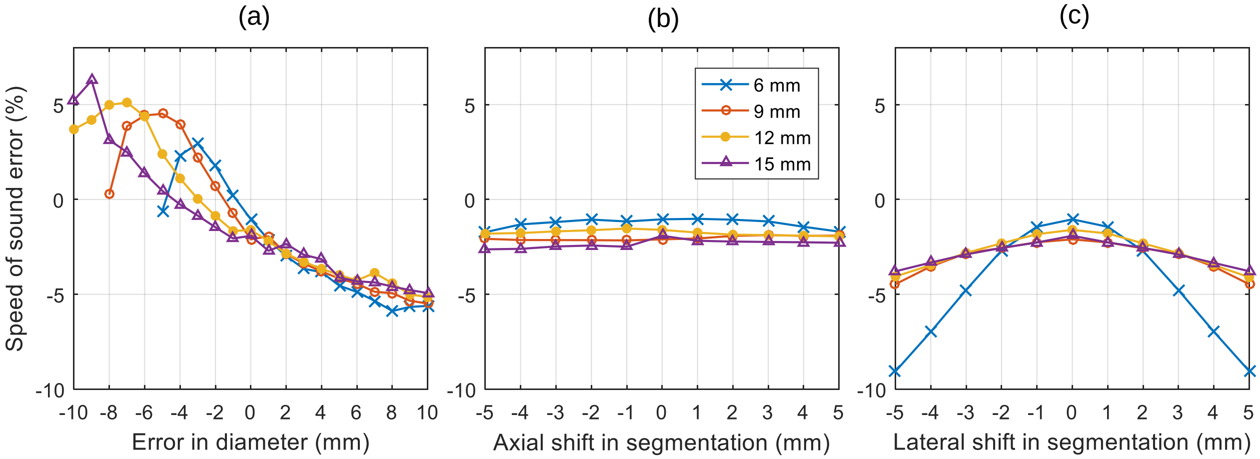

Figure 3.7: SOS error in objects of +7.6% actual SOS contrast and four different diameters, for mis-segmentations of (a) object size, (b) axial location, and (c) lateral location.

The effects of segmentation errors in Scenario B, *i.e.*, for different SOS contrast between object and background ($\text{SOS}_{\text{object}}$-$\text{SOS}_{\text{background}}$), are shown in Figure 3.8. As can be seen, higher contrast magnitude leads to higher SOS error.

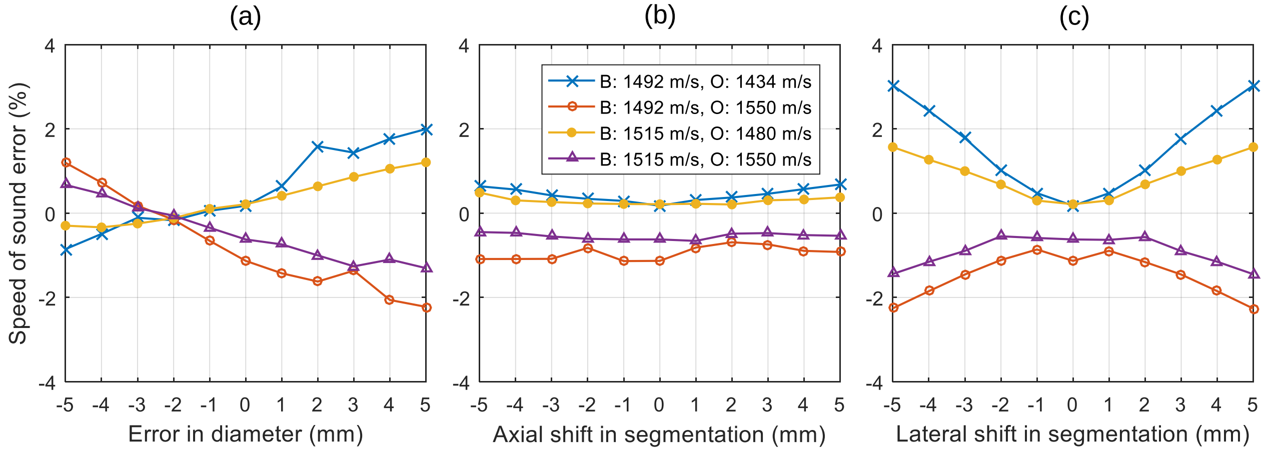

Figure 3.8: SOS error in objects of 12 mm actual diameter with varying object (O) to background (B) SOS contrasts. Shown are object mis-segmentations in: (a) size, (b) axial location, and (c) lateral location.

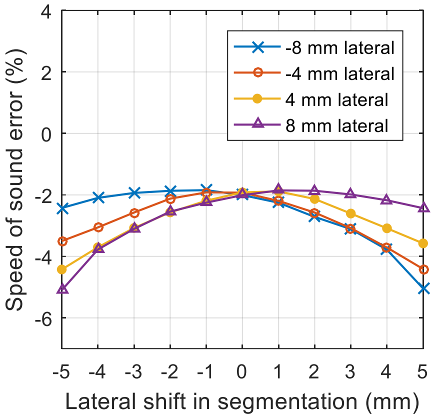

Figure 3.9: SOS error in 12 mm diameter objects of +7.6% actual SOS contrast at four actual locations laterally off the image center, as a function of lateral mis-segmentation.

According to studies performed in Scenario C, a lateral shift in segmentation was the only case with a dependence between lateral object location and SOS error. Note that the results obtained by varying the axial object location are not shown here due to indistinguishable SOS errors. Beyond the -1.9% bias present in all shifts, Figure 3.9 shows that the SOS error, for a reasonable 2 mm, or greater 5 mm, lateral segmentation displacement, is about -1% and -3%, respectively. That is over the range of cases studied where the actual object is placed within 8 mm laterally from the center.

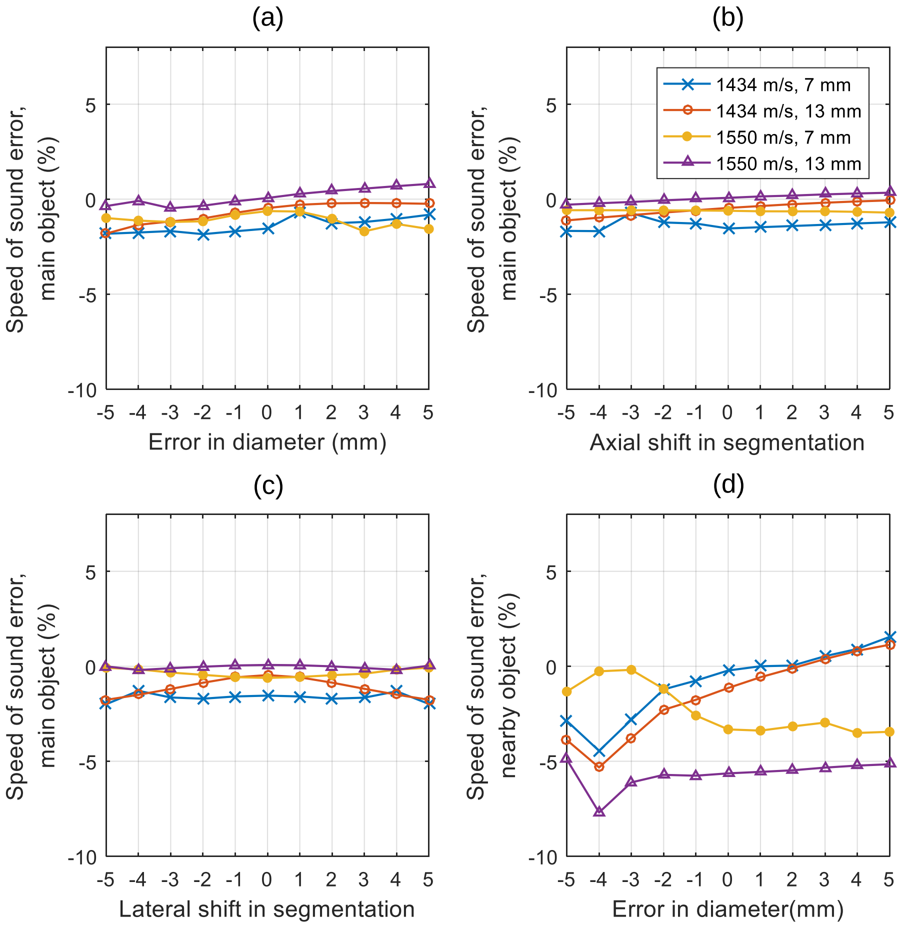

Figure 3.10: SOS errors in object of interest due to mis-segmentation of secondary object in acoustic path (See Figure 3.3(c)) (a)-(c). Mis-segmentation of the secondary object: (a) size, (b) axial location, and (c) lateral location. (d) Errors in SOS of the secondary object due to mis-segmentation of its size.

Effects of segmentation errors regarding a nearby object (Scenario D) are shown in Figure 3.10. SOS errors in the mis-segmented ROI are greater than those induced in the main object of interest. Comparison of Figures 3.10(a) and (d) shows the difference in error between the object of interest and the nearby object, respectively. Also, note that in panel (d) the SOS error trends similar to the blue curves ('-x') shown in Figure 3.8(a), which possess the same SOS contrast with respect to background.

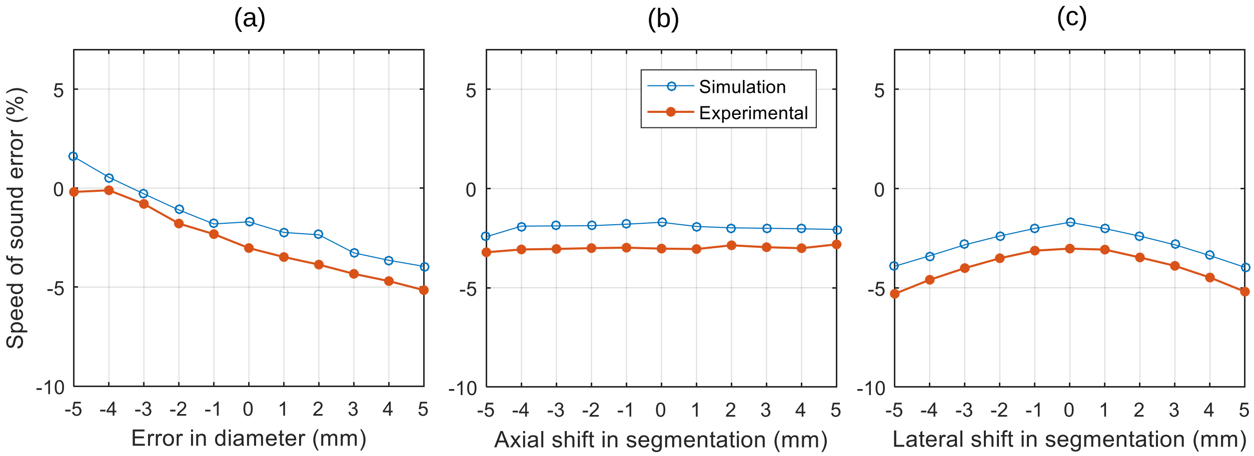

Figure 3.11: SOS error in objects obtained from reconstructions of simulated and physical cylinders with 13 mm radius, shown for mis-segmentation of object in (a) size, (b) axial location and (c) lateral location.

Experimental and paired simulation results are shown in Figure 3.11. Both results show essentially the same changes in SOS error as a function of segmentation error.

3.3.4 Effects of Array Miscalibration

Simulated SOS errors due to translational and rotational array miscalibrations are shown in Figures 3.12-3.14 for Scenarios A-C, respectively. Refer to the definition of each scenario in Section 3.2.2.2 for more details.

Figure 3.12 indicates that the calculated object SOS is most sensitive to transducer translational miscalibration in the axial direction (maximum error of 57.3% within 5 mm shift), followed by rotational calibration about elevational axis (maximum error of 8.4% within 10 deg change) and translational miscalibration in the lateral direction (maximum error of 5.0% within 5 mm shift). Moreover, Figure 3.12(d) indicates that the error resulting from axial rotational miscalibration is insignificant.

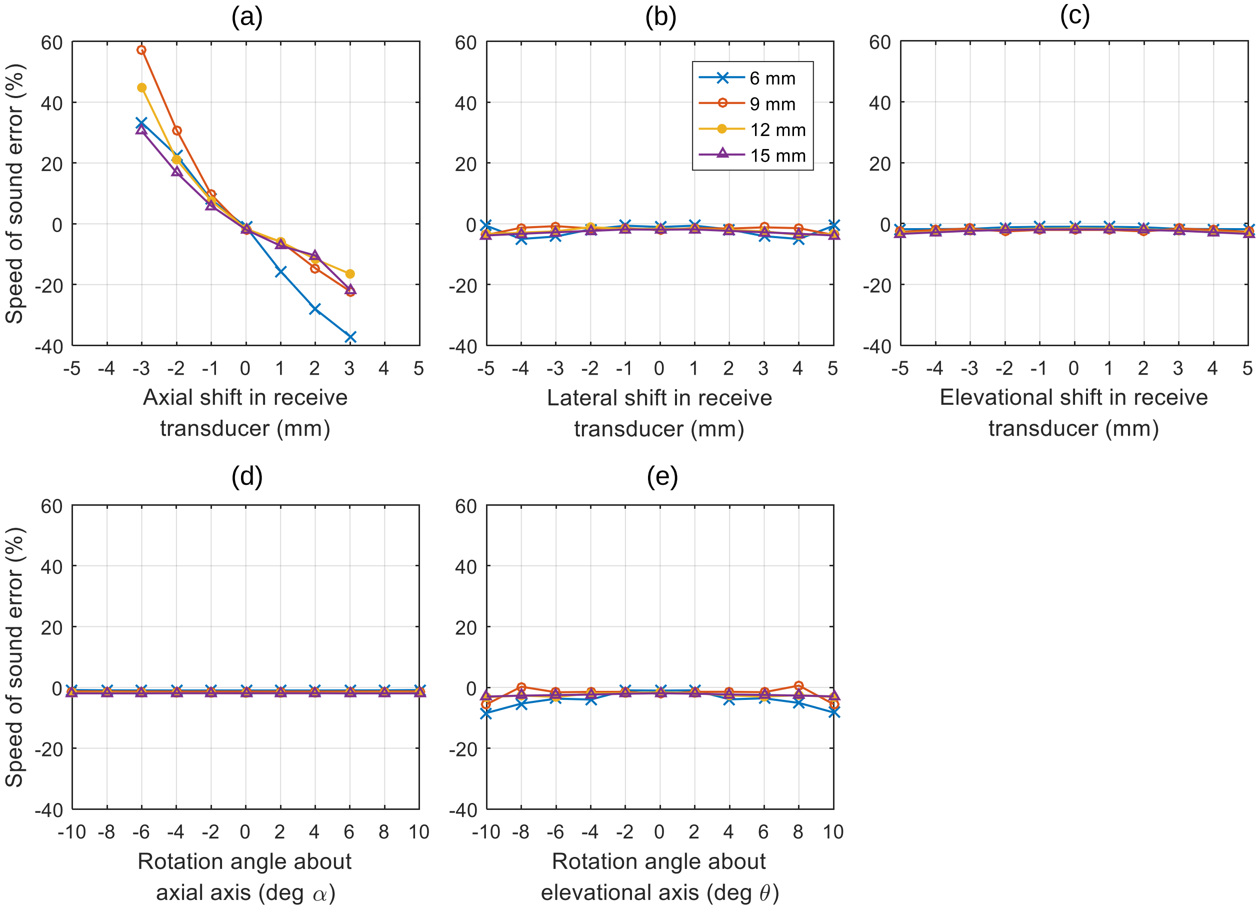

Figure 3.12: SOS error in objects of +7.6% actual SOS contrast and four different diameters, for transducer translational miscalibration along: (a) axial, (b) lateral, and (c) elevational, and (d) for transducer rotational miscalibration about the axial and (e) the elevational axes.

In addition, simulation results in Figure 3.13 show that SOS errors depend on contrast. SOSs of negative contrast objects seem to be slightly more sensitive to transducer array displacements than SOSs of positive contrast objects. Figure 3.14 further shows that reconstruction errors are dependent on the actual lateral object location in the presence of elevational rotational miscalibration. Note that the results obtained by varying the axial object location are not shown here due to indistinguishable SOS errors.

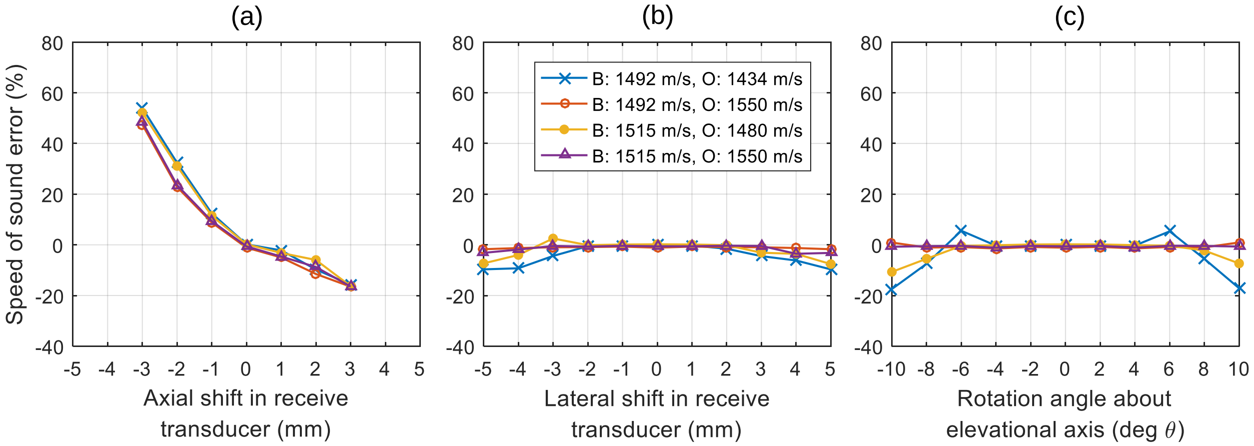

Figure 3.13: SOS error in objects of 12 mm actual diameter with varying object (O) to background (B) SOS contrasts. Receive transducer translational miscalibration in (a) axial and (b) lateral directions, and (c) transducer rotational miscalibration about the elevational axis.

Comparison between experimental and simulation results are shown in Figure 3.15. Both simulation and experimental error curves show a qualitatively similar change in SOS error.

3.4 Discussion

3.4.1 Pre-Study: Effect of Noise on Measurements

The calculated object and background SOS and their statistics at different noise levels suggest that our reconstruction algorithm is robust in the presence of bias-free, noisy TOF input (means and standard deviations change insignificantly with changing noise level). This robustness can be attributed to the correlation coefficient that strengthens the SOS homogeneity within the same tissue region. Also, it is

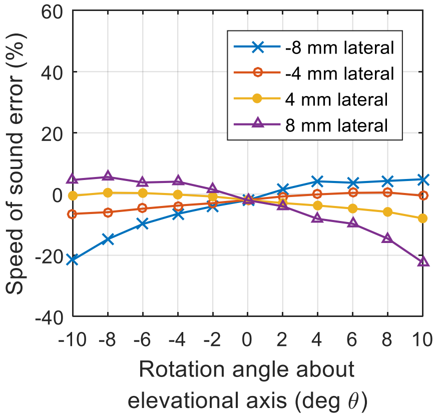

Figure 3.14: SOS error in 12 mm diameter objects of +7.6% actual SOS contrast at four actual locations laterally off the image center, for rotational miscalibration of the receive transducer about the elevational axis.

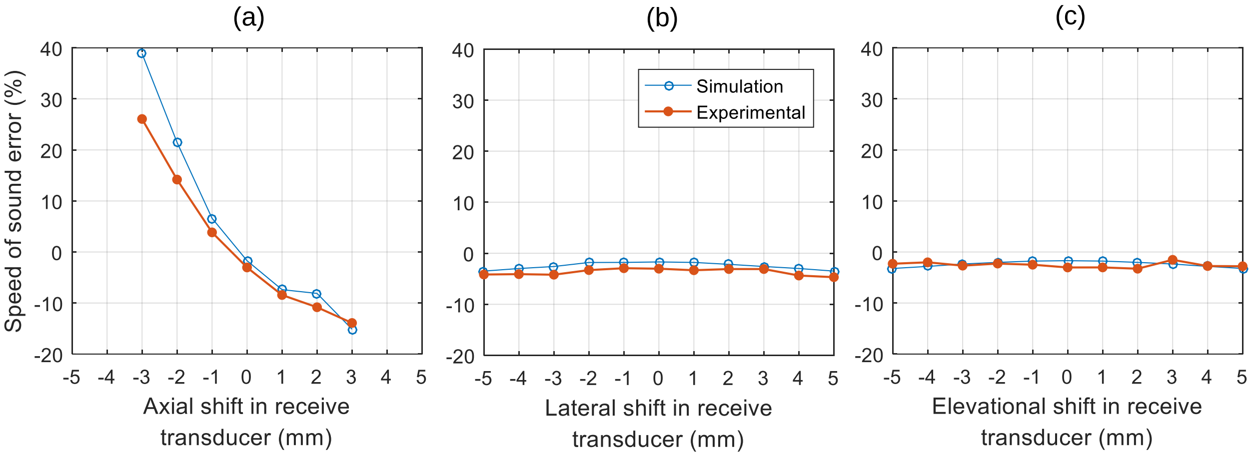

Figure 3.15: SOS error in objects obtained from reconstructions of simulated and physical cylinders with 13 mm radius. Receive transducer translational miscalibrations in: (a) axial, (b) lateral, and (c) elevational directions are shown.

important to note that the errors in the background region are small compared to the object region. This is because the SOS value set to the initial estimate of the slowness image $\mathbf{m_a}$ is already close to the background's true SOS. As the background region is much bigger than the object region, its contribution to the cost S in Equation 3.1 is elevated. This is true even if the correlation coefficient of the background pixel is set to a finite value. As such, it is much easier for the object pixel to update than those of the background and thus being more prone to noise.

3.4.2 Effects of Object Segmentation Inaccuracy

Changing size or location (Scenario A) of a segmented ROI affects the amount of signal penetrating its interior and therefore the cost S in Equation 3.1. The SOS pixel (background and object) thereby need to be adjusted to keep the cost S low. Therefore, reconstructions are more prone to incorrect object size and lateral location than to axial location. The same holds for Scenario C (Figure 3.9). Changing the lateral location of the actual object affects the amount of signal penetrating the actual object far more noticeably than changing the axial location. Therefore, different lateral object locations utilize different amounts of helpful TOF information for reconstruction and lead to different SOS errors.

As explained in Section 3.4.1, it is much easier for object pixel to update than for background pixel. Therefore we can see why the object's SOS function (Figure 3.7(a)) is approximately hyperbolic, where the calculated SOS becomes more sensitive to ROI shrinkage than expansion. Errors due to mis-segmentation of object size were mostly transferred to the object's segmented ROI, and the smaller diameter ROIs need to change their SOS more to accommodate these errors. The same explanation applies to the plot in Figure 3.7(c), which shows that the SOS reconstruction error is most sensitive to errors in the segmentation of the smallest object (6 mm).

Nevertheless, in Figure 3.7(a), there is a deviation from a hyperbolic shape of the curves when the segmented ROI diameter is too small (*e.g.*, <-3 mm for a 6 mm diameter object). This is due to the too small ROI size, where the difference in the SOS image from the initial guess causes a relatively small penalty in the data cost term in Equation 3.1, *i.e.*, $\big(g(\mathbf{m})-\mathbf{d}\big)^T \mathbf{C}_{\mathbf{D}}^{-1}\big(g(\mathbf{m})-\mathbf{d}\big)$, compared to the penalty in the model cost term, *i.e.*, $\big(\mathbf{m}-\mathbf{m_a}\big)^T \mathbf{C}_{\mathbf{M}}^{-1}\big(\mathbf{m}-\mathbf{m_a}\big)$, thereby preventing the reconstruction algorithm from further updating the SOS image.

The reason that higher contrast magnitude leads to higher SOS error, as shown in Figure 3.8, is similar to that already described above. Specifically, the reconstruction needs to achieve a trade-off between calculating the SOS image, whose corresponding simulated TOF vector is close to the measured TOF vector, and concurrently preventing the final SOS image from diverging too much from the SOS image included into the model cost term. The reconstructed object and background SOS image, whose actual SOS contrast is high, makes the model cost term high and causes the reconstruction to put more effort in decreasing the SOS contrast. The SOS contrast decrease then in turn generates a larger SOS error.

Figure 3.10 shows that in the two-object imaging case, the SOS error tends to appear more in the mis-segmented object than in the correctly-segmented object. This occurs because forcibly inducing the SOS error in the correctly-segmented region greatly changes the data cost term and the overall cost S. On the other hand, inducing the SOS error in the mis-segmented region is easier because its SOS can be adapted to maintain the average SOS across the image such that the data cost term is not over-penalized. Therefore, introducing the SOS error within the mis-segmented region seems to be the most effective way to decrease the overall cost term.

Note that in Figures 3.7-3.10, there is a DC offset of -1.9% in absence of any mis-segmentation. In some cases this can be attributed to the reconstruction assumptions for the initial SOS image as well as the geometries of structures of interest (see Section 3.2.1). Due to the model cost term in Equation 3.1, approaching the correct

SOS image, that is far from the initial image, can be challenging because doing so would increase the model cost term. Using an average SOS as the initial SOS image, however, could be too pessimistic because, in clinical or phantom applications, one could quickly determine an initial SOS image based on any straight-ray reconstruction approach [85], which yields better initial guesses that are closer to the true SOS image, thus giving more accurate reconstruction results.

Figure 3.11 shows similar SOS error trends between the simulation and experimental results. Since the same reconstruction algorithm was employed in both cases, this provides confirmation of the experimental methods except for a larger bias in the experimental results. The additional -3.0% SOS error bias in the experimental results as seen in Figures 3.11 and 3.15 could be attributed to several reasons. First, the alcohol concentration in the tube might decrease due to alcohol leaking out of the tube when left in the water bag during temperature stabilization ($\approx$ 3 hours). The decreased alcohol concentration changes the SOS of the ethanol-water solution as supported by Figure 3.6. Second, it might also be possible that the temperature of the water in the Ziploc bag changed during the experiments. Third, the recorded RF traces are compromised due to diffraction and scattering effects. The accuracy of extracted TOF using the AIC picker method is thus potentially degraded. Finally, it is possible, although unlikely, that the transducer separation changed when the support of the cylindrical tube was mounted to the compression paddles on the dual-sided BLUCI scanner.

3.4.3 Effects of Array Miscalibration

Misplacing the transducer position and orientation mainly affects the data cost term in Equation 3.1, *i.e.*, $\big(g(\mathbf{m})-\mathbf{d}\big)^T \mathbf{C}_\mathbf{D}^{-1}\big(g(\mathbf{m})-\mathbf{d}\big)$. This occurs because transducer miscalibrations induce change in the simulated TOF vector $g(\mathbf{m})$, which can result in greater SOS error, most dominantly in the axial direction. This similarly explains why reconstruction errors are most sensitive to the lateral object location in the presence of rotational miscalibration about the elevational axis (see Figure 3.14). This rotation creates laterally distributed axial shifts.

The reason that objects with negative contrast seem to be more sensitive to miscalibrations, than objects with positive contrast, as shown in Figure 3.13, could be attributed to the wave refraction that occurs at the interface between two media with different SOSs. There, the wave travels a longer distance in the negative contrast cylindrical object than in the positive contrast object, given the same angle of incidence. This results in a greater SOS error.

As shown in Figures 3.12-3.15, the two factors resulting in the greatest SOS reconstruction errors are miscalibration in the axial direction and elevational rotational miscalibration. Therefore, these need to be more carefully controlled to ensure an acceptable level of reconstruction accuracy. For example, according to Figure 3.12, to discriminate a 6-15 mm wide fat inclusion at 1440 m/s from background fibroglandular tissue at 1515 m/s in vivo [57], [58], [63], [67] (relative contrast of approximately 75 m/s), the allowable axial translational miscalibration to resolve the SOS contrast is 0.43 mm. The allowable elevational rotational miscalibration is 5.9 deg. For discriminating cancer and fibroadenomas, greater accuracy and maximum contrast are desired, as the contrast is modest and there is some overlap of the SOS distributions. Given SOSs of surrounding fibroadenomas and 6-15 mm wide cancer as 1515 and 1550 m/s, respectively [17], the allowable axial translational miscalibration and elevational rotational miscalibration would instead be 0.20 mm and 2.8 deg, respectively. We have not investigated the SOS errors due to miscalibrations happening in parallel yet, however, it should be possible to obtain the worst-case SOS error by simply summing up the SOS errors due to individual miscalibrations.

3.5 Conclusions

This paper demonstrates the degree to which our previously proposed SOS reconstruction algorithm for ultrasound limited angle tomography is dependent on *a priori* information such as segmentation of structures in the B-mode images and calibration of transducer placements relative to each other. Axial translational and elevational rotational requirements are non-trivial but doable with careful calibrations. The calculated SOS is most sensitive to mis-segmentations in size and lateral location of the segmented ROI and will benefit from B-mode enhancements.

The SOS reconstruction of a complex tissue-mimicking phantom, shown in Figures 3.1-3.2, suggests that good discrimination of fairly complex tissues can be attained given accurate segmentation and transducer alignment. There are several possibilities suggesting that both mis-segmentations and miscalibrations can be minimized in imaging in the future. For example, with emerging ultrasound signal processing and beamforming techniques, and advances in ultrasound image segmentation [38], [59], [60], we expect it is possible to overcome difficulties in blurry tissue identification and obtain segmentation that farther improves SOS image reconstruction. In addition, in a system with the transducers contacting a nonrigid paddle in contact with the breast, the transducers should extend beyond the breast for real time calibration, as shown in Figure 3.2.

All technical findings reported in this paper could be applicable to any future design of a limited-angle transmission ultrasound system in the mammographic geometry utilizing two long transducers and a bent-ray SOS reconstruction algorithm. Full wave inversion approaches, on the other hand, could be more sensitive to the misalignments, as their reconstruction algorithms usually rely on the mismatch between the whole simulated and measured signals rather than the less-fluctuating, smoother mismatch between the simulated and measured pulse arrival times. Nonetheless, our findings have demonstrated that with proper ultrasound system design, calibration, and good reflection mode images, SOS imaging with a limited-angle transmission ultrasound system and a bent-ray SOS reconstruction algorithm appears feasible.

CHAPTER IV

Waveform Inversion for Limited-Angle Breast Ultrasound Tomography with Decoupled *A Priori* Information and Artifact Suppression[1]

4.1 Introduction

Breast ultrasound tomography has shown promise in delivering similar information as x-ray due to similar contrasts of breast tissues appearing in images from these two imaging modalities [62]. In addition, thanks to complex interactions between ultrasound and breast tissue, several acoustic properties, such as sound speed, attenuation, and elasticity can be extracted from the received ultrasound signals. Sound speed has gained much attention in a past decade, as it can be used to characterize breast tissue types such as fibroglandular, fat, cyst, and cancer [30].

Most image acquisition techniques for sound speed reconstruction image the breast, suspended in a temperature-controlled water bath [15], [17], [20]–[22], [34], [63], [68], [86]–[89]. The signal acquisition then begins by using opposed transducer elements in array to sequentially transmit signals by one or more transducer elements and receive

---

[1] This chapter is published in *Proceedings of SPIE*: R. Jintamethasawat, Y. Zhu, O. D. Kripfgans, J. Yuan, M. M. Goodsitt, and P. L. Carson, "Limited Angle Breast Ultrasound Tomography with *A Priori* Information and Artifact Removal," in *Proc. SPIE*, vol. 10139, 2017, pp. 10139 -10139 -12. doi: 10.1117/12.2253911.

signals using all transducer elements of the array. The arrays are often multiple linear, convex linear, or 2D planar arrays, or circular or cylindrical arrays. Even though these techniques give reasonably accurate sound speed images due to the ability to transmit and receive the signal in any direction within a coronal plane or the aperture of a 2D receiver array, imaging in this prone position results in views that differ from those obtained from mammography, the current x-ray reference-standard. This can cause difficulties for radiologists to compare images from ultrasound and mammography. There have been attempts that try to co-register ultrasound sound speed and mammography images, but they often require heavy task-specific parameter tuning [37], [38].

As such, we recently proposed a combined mammography scanner for x-ray and ultrasound acquisition in the same view, location, and compression [6], [10]. However, acquiring the ultrasound signal in the mammographic geometry poses challenges in tomographic image reconstruction as the signal can be obtained at the top and bottom of the patient breast only, resulting in incomplete acquisition. This limited-angle ultrasound tomography introduces dominant artifacts that can severely degrade image clarity and accuracy. Fortunately, recent works have shown that by using also-available B-mode images, one can improve the reconstruction accuracy and reduce artifacts by including delineations of the tissues of interest via segmentation [7], [64]. Such delineations provide the homogeneity assumption that pixels in the same segmented region belong to the same tissue type and should have similar characteristic values, such as sound speed.

In the meantime, it has been shown that waveform inversion techniques are able to realistically retrieve both acoustic tissue properties and their boundaries despite their high computational burden [20], [22], [33], [90], suggesting that they could be utilized when tissue delineation information is not available. The popularity of waveform inversion techniques has also increased in recent years thanks to the increase in computational capability. However, despite better reconstruction accuracy, waveform inversion techniques still suffer from the limited-angle artifacts. Accuracy improvement and artifact reduction are key factors for enhancing breast screening performance [10], [91]–[94], yet none of the existing approaches utilize *a priori* B-mode segmentation information and simultaneously suppress artifacts.

Here, we propose a sound speed imaging algorithm that both utilizes *a priori* segmentation information from existing B-mode data and suppresses reconstruction artifacts. This approach decouples the overall reconstruction into two sub-problems that can be solved separately: (1) *a priori* information inclusion and (2) artifact suppression [95], [96]. Each sub-problem can be solved individually, thereby decoupling the combined optimization scheme. The first sub-problem can, for example, be solved by any standard gradient-descent method. The second can be accomplished by total-variation (TV) regularization based on the fast split Bregman method that overcomes non-differentiability [97]. The reconstructions are primarily based on a waveform inversion approach.

Details about the related theory and reconstruction algorithm implementation are described in the Materials and Methods section. Results and their analysis are described in the Results and Discussion section, respectively. The Conclusions section summarizes our study and provides future directions.

4.2 Materials and Methods

4.2.1 Dual-Sided Ultrasound Scanner

Figure 4.1(a) illustrates an idealized dual-sided research ultrasound scanner. It consists of two linear transducer arrays imaging from top and bottom of the patient breast, which is compressed by two polyethelyne mesh paddles. This is similar to our experimental dual sided ultrasound scanner, which is built on a used mammography system, but no longer has the x-ray detector attached [69]. In the complete system schematized in Figure 4.1(a), the x-ray and ultrasound image the breast in the same view, location, and compression, allowing very good co-registration.

A schematic of the ultrasound system is given in Figure 4.1(b), showing the plane for a coronal image of the breast. For each sound speed image reconstruction slice, the signal acquisition sequentially transmits from each element and, on each transmit, receives signal by all elements on both arrays. Note that all image reconstructions performed in this paper are based on simulation studies using a simulated scanner as diagrammed here.

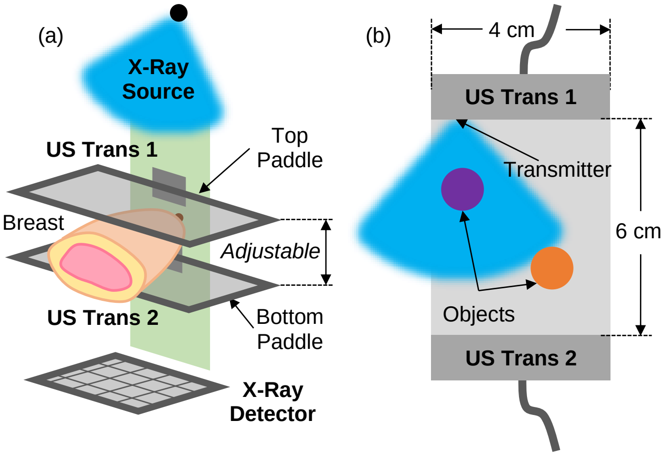

Figure 4.1: (a) Schematic representation of a combined dual-sided ultrasound and x-ray scanner, allowing both x-ray and ultrasound images to be acquired in the same view. (b) Schematic representation of simulated dual-sided ultrasound scanner used in this work, imaging embedded objects.

4.2.2 Ultrasound Propagation Modeling

4.2.2.1 Time-of-flight-based modeling

The time-of-flight (TOF), or first-arrival time of a wave in heterogeneous sound speed media $m(\mathbf{r}) : \mathbb{R}^2 \rightarrow \mathbb{R}^+$ can be modeled over space $r \in \mathbb{R}^2$ by solving the following Eikonal equation:

$$\|\nabla \mathbf{T}(\mathbf{r})\|_2 m(\mathbf{r}) = 1, \quad \mathbf{T}(\mathbf{r_0}) = 0, \tag{4.1}$$

where m and $\mathbf{T}$ are the speed and first-arrival time of the wave as a function of location r, and r_0 is the wave propagation origin. The Multistencils Fast Marching Method (MSFM) [72] was utilized to solve Equation 4.1 with high accuracy (negligible in breast imaging application) and fast computation time.

4.2.2.2 Wave-based modeling

Wave propagation in lossless heterogeneous sound speed media $m(\mathbf{r}) : \mathbb{R}^2 \to \mathbb{R}^+$ can be modeled over time $t \in [0, T]$ and space $r \in \mathbb{R}^2$ by the following second-order partial derivative equation [14]:

$$\nabla^2 p(\mathbf{r}, t) - \frac{1}{m^2(\mathbf{r})} \frac{\partial^2}{\partial t^2} p(\mathbf{r}, t) = \frac{\partial}{\partial t} s(\mathbf{r}, t), \tag{4.2}$$

where $s(\mathbf{r}, t) : \mathbb{R}^2 \times \mathbb{R}_0^+ \to \mathbb{R}$ and $p(\mathbf{r}, t) : \mathbb{R}^2 \times \mathbb{R}_0^+ \to \mathbb{R}$ are the time-and-space-dependent source pulse and acoustic wave pressure, respectively. The initial conditions are given by $p(\mathbf{r}, 0) = p_t(\mathbf{r}, 0) = 0$.

With space-dependent attenuation $\alpha(\mathbf{r}) : \mathbb{R}^2 \to \mathbb{R}_0^+$ included, wave propagation can be equivalently expressed by the following three first-order coupled equations [14], [98], [99]:

$$\frac{\partial}{\partial t} \mathbf{u}(\mathbf{r}, t) = -\frac{1}{\rho_0(\mathbf{r})} \nabla p(\mathbf{r}, t) \tag{4.3a}$$

$$\frac{\partial}{\partial t} \rho(\mathbf{r}, t) = \rho_0(\mathbf{r}) \big(- \nabla \cdot \mathbf{u}(\mathbf{r}, t) + \int\limits_0^t s(\mathbf{r}, t') dt' \big) \tag{4.3b}$$

$$p(\mathbf{r}, t) = m^2(\mathbf{r}) \left[1 - \tau(\mathbf{r}) \frac{\partial (-\nabla^2)^{\frac{y}{2}-1}}{\partial t} - \eta(\mathbf{r}(-\nabla^2)^{\frac{y+1}{2}-1}) \right] \rho(\mathbf{r}, t), \tag{4.3c}$$

where $\mathbf{u}(\mathbf{r}, t) : \mathbb{R}^2 \times \mathbb{R}_0^+ \to \mathbb{R}^2$ and $\rho(\mathbf{r}, t) : \mathbb{R}^2 \times \mathbb{R}_0^+ \to \mathbb{R}$ are the time-and-space-dependent particle velocity and density, respectively. The initial conditions are given by $p(\mathbf{r}, 0) = \mathbf{u}(\mathbf{r}, 0) = 0$. The attenuation coefficient is included in terms $\tau(\mathbf{r}) : \mathbb{R}^2 \to \mathbb{R}_0^+$ and $\eta(\mathbf{r}) : \mathbb{R}^2 \to \mathbb{R}_0^+$ defined as:

$$\tau(\mathbf{r}) = -2\alpha(\mathbf{r})m(\mathbf{r})^{y-1} \tag{4.4a}$$

$$\eta(\mathbf{r}) = 2\alpha(\mathbf{r})m(\mathbf{r})^{y} \tan\left(\frac{\pi y}{2}\right), \tag{4.4b}$$

where y denotes the acoustic attenuation power law exponent.

In this paper, wave propagation is computed by utilizing a k-space pseudospectral method [100], [101] that benefits from low memory and time step requirements.

4.2.3 Image Reconstruction Theory

4.2.3.1 Basic reconstruction algorithm

The sound speed reconstruction problem can be considered as the least-square minimization between the measured data vector $\mathbf{d}$ and simulated data vector $g(\mathbf{m})$:

$$E(\mathbf{m}) = \big(\mathbf{d} - g(\mathbf{m})\big)^T \mathbf{C_D}^{-1} \big(\mathbf{d} - g(\mathbf{m})\big) \tag{4.5}$$

Given the number of elements in each linear array as N, the measured and simulated data vectors can be either a collection of concatenated time-of-flights of all $(2N)^2$ transmit-receive pairs ($\begin{bmatrix} t_{11} & \dots & t_{1(2N)} & t_{21} & \dots & t_{2(2N)} & \dots & t_{(2N)1} & \dots & t_{(2N)(2N)} \end{bmatrix}^T$ where t_{ij} denotes the time-of-flight from i^{th} transmit element to j^{th} receive element) or a collection of concatenated recorded pressure traces of all $(2N)^2$ transmit-receive pairs ($\begin{bmatrix} p_{11} & \dots & p_{1(2N)} & p_{21} & \dots & p_{2(2N)} & \dots & p_{(2N)1} & \dots & p_{(2N)(2N)} \end{bmatrix}^T$ where p_{ij} denotes the time-domain pressure trace transmitted by i^{th} element and recorded by j^{th} element). The data covariance matrix $\mathbf{C_D}$ is used for adjusting contributions of individual data or correlations between pairs of data. $\mathbf{C_D}$ is set to an identity matrix if all data have equal contribution.

The reconstruction techniques utilizing time-of-flight data and assuming wave propagation direction as a bent-ray are usually classified as bent-ray inversion approach, and those using pressure trace data are classified as the waveform inversion approach.

4.2.3.2 Reconstruction using *a priori* information and artifact suppression

By adding two additive regularization terms to Equation 4.5 , the sound speed reconstruction problem can account for *a priori* information and it can suppress artifacts:

$$E(\mathbf{m}) = \big(\mathbf{d} - g(\mathbf{m})\big)^T \mathbf{C}_\mathbf{D}^{-1} \big(\mathbf{d} - g(\mathbf{m})\big) + \big(\mathbf{m} - \mathbf{m_a}\big)^T \mathbf{C}_\mathbf{M}^{-1} \big(\mathbf{m} - \mathbf{m_a}\big) + \lambda \|\mathbf{Em}\|_{TV} \quad (4.6)$$

The regularization term $\big(\mathbf{m} - \mathbf{m_a}\big)^T \mathbf{C}_\mathbf{M}^{-1} \big(\mathbf{m} - \mathbf{m_a}\big)$ allows us to include the *a priori* segmentation data from corresponding B-mode and/or x-ray image [70]. The correlated pixels within the same segmented region have similar sound speed. The correlation strength can be set through the covariance matrix $\mathbf{C_M}$ such that pixels i and j correlate with the positive correlation coefficient ρ_k such that $\mathbf{C_M}_{ij} = \rho_k \sigma^2$. Confidence in correlation scales with ρ_k. Note that $\mathbf{C_M}_{ij} = 0$ for any independent pixels i and j and $\mathbf{C_M}_{ii} = \sigma^2$. This term also allows us to set the initial sound speed guess through the term $\mathbf{m_a}$. Usually, for bent-ray inversion approaches, $\mathbf{m_a}$ is set to a homogeneous background sound speed, and for waveform inversion approaches, $\mathbf{m_a}$ is set to the sound speed that results from a bent-ray inversion approach.

The regularization term $\lambda\|\mathbf{Em}\|_{TV}$ includes the total-variation (TV) $\|\mathbf{m}\|_{TV}$ and can be written as:

$$\|\mathbf{m}\|_{TV} = \sum_i \sum_j \sqrt{\left(\nabla_x m_{ij}\right)^2 + \left(\nabla_y m_{ij}\right)^2}, \tag{4.7}$$

where ∇_x and ∇_y denote gradients in axial and lateral directions, and m_{ij} denotes the sound speed of pixel at the i^{th} axial and j^{th} lateral location. Specifically, this term measures the difference between two adjacent pixels, and thus increases with artifacts. Inversely, artifacts can be suppressed by minimizing $\|\mathbf{m}\|_{TV}$. However, note that there is an abrupt change of pixel values around tissue boundaries. Those pixels could contribute to high gradient magnitudes and are likely to be suppressed during the minimization of Equation 4.7. For this reason, the diagonal weight matrix $\mathbf{E}$ is introduced to keep track of boundary pixel. For any pixel m_{ij} in an image with size $M = M_1 \times M_2$, we define $E_{(i-1)M_2+j,(i-1)M_2+j}$ as:

$$E_{(i-1)M_2+j,(i-1)M_2+j} = \exp\left(- \left(\left(\nabla_x m_{ij}\right)^2 + \left(\nabla_y m_{ij}\right)^2 \right) / \sigma_e \right), \tag{4.8}$$

where σ_e scales inversely with the level of edge preservation in m_{ij} during the minimization of Equation 4.7 [102]. However, this method is a trade-off between edge preservation and artifact suppression. The notation E here is made distinct from E in Equations 4.5 and 4.6, by a subscript $(i-1)M_2 + j, (i-1)M_2 + j$ that denotes the element value at the $((i-1)M_2 + j)^{th}$ row and column of $\mathbf{E}$.

4.2.3.3 Solving the reconstruction problem

One of the difficulties in solving the reconstruction problem in Equation 4.6 is that the objective function consists of both differentiable (the first two terms in Equation 4.6) and non-differentiable (the TV term in Equation 4.6) terms with respect to sound speed in the image $\mathbf{m}$. We chose to avoid solving the TV-regularized problem by directly applying a gradient-based optimization. Instead, we solved the proposed reconstruction problem by decoupling the minimization problem into two sub-problems as mentioned above.

We first introduced the auxiliary variable $\mathbf{u}$ to the objective function in Equation 4.6 and replaced the term $\mathbf{m_a}$ with $\mathbf{u}$:

$$E(\mathbf{m},\mathbf{u}) = \big(\mathbf{d} - g(\mathbf{m})\big)^T \mathbf{C_D^{-1}} \big(\mathbf{d} - g(\mathbf{m})\big) + \big(\mathbf{m} - \mathbf{u}\big)^T \mathbf{C_M^{-1}} \big(\mathbf{m} - \mathbf{u}\big) + \lambda \|\mathbf{Eu}\|_{TV} \tag{4.9}$$

Note that Equation 4.9 can be solved by alternately minimizing the objective functions $E_1(\mathbf{m})$ and $E_2(\mathbf{u})$ with respect to individual variables $\mathbf{m}$ and $\mathbf{u}$ until the solution converges or another desired end-point is reached [95], [96]:

$$E_1(\mathbf{m}) = \big(\mathbf{d} - g(\mathbf{m})\big)^T \mathbf{C_D^{-1}} \big(\mathbf{d} - g(\mathbf{m})\big) + \big(\mathbf{m} - \mathbf{u}\big)^T \mathbf{C_M^{-1}} \big(\mathbf{m} - \mathbf{u}\big) \tag{4.10}$$

$$E_2(\mathbf{u}) = \big(\mathbf{m} - \mathbf{u}\big)^T \mathbf{C_M^{-1}} \big(\mathbf{m} - \mathbf{u}\big) + \lambda \|\mathbf{Eu}\|_{TV}. \tag{4.11}$$

Since Equation 4.10 contains just differentiable terms, it can be minimized by any conventional (conjugate) gradient-based method [7], [64], [70]. Specifically, the steepest descent vector $\gamma_{\mathbf{m}}$ evaluated at $\mathbf{m}$ (not the same as gradient, see [70] and Section 4.3.1 for more details) is first calculated as:

$$\gamma_{\mathbf{m}} = \mathbf{C_M} \mathbf{G_m^*} \big[\mathbf{C_D^{-1}} \big(g(\mathbf{m}) - \mathbf{d}\big)\big] + \mathbf{m} - \mathbf{u}, \tag{4.12}$$

where $\mathbf{G_m}$ is the Fréchet derivative of g evaluated at $\mathbf{m}$ [103]. The adjoint of $\mathbf{G_m}$, $\mathbf{G_m^*}$, provides mapping from data space to model space.

In the bent-ray inversion reconstruction, $\mathbf{G_m}$ is defined as a pathlength matrix, where $G_{m_{2(i-1)N+j,k}}$ represents the path length fraction in the k^{th} pixel, of the wave that is transmitted by the i^{th} element and received by the j^{th} element (N denotes the number of elements on each linear array). $\mathbf{G_m^*}$ then be written as the Hermitian transpose of $\mathbf{G_m}$.

In the full-wave inversion, $\mathbf{G^*_m}$ can be first computed analytically in the continuous domain through the adjoint-state method [103]–[105]. It can be shown that for single-transmit event:

$$\mathbf{G^*_{m,sin}}[h]\Bigg|_{\mathbf{r'}} = \frac{2}{m^3(\mathbf{r'})}\int\limits_0^T q(\mathbf{r'}, T-t)\frac{\partial^2}{\partial t^2}p(\mathbf{r'}, t)dt, \tag{4.13}$$

for any continuous pressure $h(\mathbf{r}, t)$ and location $\mathbf{r'}$. $p(\mathbf{r}, t)$ and $q(\mathbf{r}, t)$ denote the simulated pressure field and the corresponding adjoint field. The adjoint field can be computed using the same wave propagation equation as Equation 4.2 or 4.3 for lossless and lossy media, except for the source term, $s(\mathbf{r}, t)$, is replaced by its timed-reversed version $h(\mathbf{r}, T-t)$.

Suppose that $d_i(\mathbf{r}, t)$ and $p_i(\mathbf{r}, t)$ are the measured and simulated pressure fields transmitted by i^{th} element. Also, assume that the acquired pressure samples are independent and have equal variance σ_D^2, that is, $\mathbf{C_D}$ can be expressed as $\mathbf{C_D} = \sigma_D^2\mathbf{I}$, where $\mathbf{I}$ is an identity matrix. Now, if the adjoint field $q_i(\mathbf{r}, t)$ is simulated by the source given as $h_i(\mathbf{r}, t) = \sigma_D^2\sum_{j=1}^{2N}\big(p_i(\mathbf{r_{Rj}}, t) - d_i(\mathbf{r_{Rj}}, t))\big)$, where $\mathbf{r_{Rj}}$ denotes the location of the j^{th} receiver, it can be easily seen that:

$$\mathbf{G^*_{m,mul}}[h_1, h_2, ..., h_{2N}] = \sum_{i=1}^{2N}\mathbf{G^*_{m,sin}}[h_i] \tag{4.14}$$

gives rise to the adjoint operator for multi-transmit event and is equivalent to $\mathbf{G^*_m}\big[\mathbf{C_D^{-1}}\big(g(\mathbf{m})-\mathbf{d}\big)\big]$ in discrete domain, calculated as:

$$\begin{aligned}\mathbf{G^*_m}\big[\mathbf{C_D^{-1}}\big(g(\mathbf{m}) - \mathbf{d}\big)\big]\Bigg|_{\mathbf{r_d}} &= \frac{2\sigma_D^2}{m^3(\mathbf{r_d})}\sum_{i=1}^{2N}\sum_{k=2}^{K-1}\big(q_i(\mathbf{r_d}, T-k\Delta t)(p_i(\mathbf{r_d}, (k+1)\Delta t) \\ &\qquad -2p_i(\mathbf{r_d}, k\Delta t) + p_i(\mathbf{r_d}, (k-1)\Delta t))\big)/\Delta t^2\end{aligned} \tag{4.15}$$

for an image with pixels $\mathbf{r_1}, \mathbf{r_2}, ..., \mathbf{r_M}$. $T = K\Delta t$ is the time duration of simulation. Note that another scaling factor Δt in Equation 4.15 is needed to convert from unit of time in continuous domain to unit of sample in discrete domain.

The sound speed image at the $(n+1)^{th}$ iteration, $\mathbf{m}^{n+1}$ is then given by:

$$\mathbf{m}^{n+1} = \mathbf{m}^n - \alpha_{n+1}\mathbf{v}^{n+1} \tag{4.16a}$$

$$\mathbf{v}^{n+1} = \gamma_{\mathbf{m}}^n - \beta_{n+1}\mathbf{v}^n. \tag{4.16b}$$

The vectors $\mathbf{v}^i, i = 1, 2, ..., (n+1)$ are chosen to form conjugate bases for Krylov subspaces [106]. This can be achieved by choosing the parameter β_n according to the Polak and Ribiére formula:

$$\beta_{n+1} = \frac{< \mathbf{C_M^{-1}}(\gamma_{\mathbf{m}}^{n+1} - \gamma_{\mathbf{m}}^n), \gamma_{\mathbf{m}}^{n+1} >}{< \mathbf{C_M^{-1}}\gamma_{\mathbf{m}}^n, \gamma_{\mathbf{m}}^n >}. \tag{4.17}$$

The step length α_n that minimizes the objective function at the n^{th} iteration is given by [70], [74]:

$$\alpha_{n+1} = \frac{(\mathbf{v}^{n+1})^T\mathbf{C_M^{-1}}\gamma_{\mathbf{m}}^{n+1}}{(\mathbf{G_m}\mathbf{v}^{n+1})^T\mathbf{C_D^{-1}}(\mathbf{G_m}\mathbf{v}^{n+1}) + (\mathbf{v}^{n+1})^T\mathbf{C_M^{-1}}\mathbf{v}^{n+1}}. \tag{4.18}$$

Equation 4.11 that consists of a convex, differentiable term $(\mathbf{m}-\mathbf{u})^T\mathbf{C_M^{-1}}(\mathbf{m}-\mathbf{u})$ and non-differentiable term $\lambda\|\mathbf{Em}\|_{TV}$ can be solved by the fast-split Bregman method [97]. Specifically, the objective function in Equation 4.11 can be equivalently expressed by two additional auxiliary variables and two additional equality constraints:

$$\begin{gathered}\underset{\mathbf{u},\mathbf{d_x},\mathbf{d_y}}{\arg\min}\left\{\lambda\|(\mathbf{d_x},\mathbf{d_y})\|_2 + \big(\mathbf{m}-\mathbf{u}\big)^T\mathbf{C_M^{-1}}\big(\mathbf{m}-\mathbf{u}\big)\right\} \\ \text{subject to} \quad \mathbf{d_x} = \mathbf{E}\nabla_x\mathbf{u} \quad \text{and} \quad \mathbf{d_y} = \mathbf{E}\nabla_y\mathbf{u},\end{gathered} \tag{4.19}$$

where $\|(\mathbf{d_x},\mathbf{d_y})\|_2 = \sum_i\sum_j\sqrt{\big(d_{x_{ij}}\big)^2 + \big(d_{y_{ij}}\big)^2}$ and i, j denote pixels i and j in the image. Note that from Equation 4.8, $\mathbf{E}$ depends on $\mathbf{m}$, and this dependency makes the optimization unnecessarily complicated. Varying $\mathbf{E}$ in every iteration shows an insignificant difference compared to operating with a fixed $\mathbf{E}$. To simplify the computation, $\mathbf{E}$ was precomputed based on the most current image $\mathbf{m}$ from Equation 4.10 and treated as a constant matrix throughout the subsequent optimization of Equation 4.11.

Rewriting from Equation 4.19 as unconstrained problem yields:

$$\begin{aligned}\arg\min_{\mathbf{u},\mathbf{d_x},\mathbf{d_y}} \Big\{ &\lambda\|(\mathbf{d_x},\mathbf{d_y})\|_2 + \big(\mathbf{m}-\mathbf{u}\big)^T \mathbf{C}_{\mathbf{M}}^{-1}\big(\mathbf{m}-\mathbf{u}\big) + \\ &\alpha\|\mathbf{d_x} - \mathbf{E}\nabla_x\mathbf{u} - \mathbf{b_x}\|_2^2 + \alpha\|\mathbf{d_y} - \mathbf{E}\nabla_y\mathbf{u} - \mathbf{b_y}\|_2^2 \Big\}.\end{aligned} \tag{4.20}$$

Choosing $\lambda \to \infty$ enforces stronger equality constraints in Equation 4.20, but this will prevent the Bregman iteration from converging properly due to increasing likelihood of ill-posedness [97]. For this reason, we set $\alpha = \lambda/2$. Furthermore, the proof in [97] shows that any arbitrary value of $\lambda > 0$ can lead to convergence.

Additional terms, $\mathbf{b_x}$ and $\mathbf{b_y}$ are updated at each minimization iteration based on the following Bregman iterations scheme [97]:

$$\begin{aligned}\mathbf{b}_{\mathbf{x}}^{j+1} &= \mathbf{b}_{\mathbf{x}}^{j} + (\mathbf{E}\nabla_x\mathbf{u}^{j+1} - \mathbf{d}_{\mathbf{x}}^{j+1}) \\ \mathbf{b}_{\mathbf{y}}^{j+1} &= \mathbf{b}_{\mathbf{y}}^{j} + (\mathbf{E}\nabla_y\mathbf{u}^{j+1} - \mathbf{d}_{\mathbf{y}}^{j+1}).\end{aligned} \tag{4.21}$$

Solving Equation 4.20 then can be accomplished by further decomposing it into two sub-problems:

$$\mathbf{u}^{j+1} = \arg\min_{\mathbf{u}} \Big\{ \big(\mathbf{m}-\mathbf{u}\big)^T \mathbf{C}_{\mathbf{M}}^{-1}\big(\mathbf{m}-\mathbf{u}\big) + \alpha\|\mathbf{d}_{\mathbf{x}}^{j} - \mathbf{E}\nabla_x\mathbf{u} - \mathbf{b}_{\mathbf{x}}^{j}\|_2^2 + \alpha\|\mathbf{d}_{\mathbf{y}}^{j} - \mathbf{E}\nabla_y\mathbf{u} - \mathbf{b}_{\mathbf{y}}^{j}\|_2^2 \Big\} \tag{4.22}$$

$$\left(\mathbf{d}_{\mathbf{x}}^{j+1},\mathbf{d}_{\mathbf{y}}^{j+1}\right)=\underset{\mathbf{d}_{\mathbf{x}},\mathbf{d}_{\mathbf{y}}}{\arg\min}\left\{\lambda\|\mathbf{d}_{\mathbf{x}},\mathbf{d}_{\mathbf{y}}\|_2+\|\mathbf{d}_{\mathbf{x}}-\mathbf{E}\nabla_x\mathbf{u}^{j+1}-\mathbf{b}_{\mathbf{x}}^j\|_2^2+\|\mathbf{d}_{\mathbf{y}}-\mathbf{E}\nabla_y\mathbf{u}^{j+1}-\mathbf{b}_{\mathbf{y}}^j\|_2^2\right\}. \tag{4.23}$$

Note that all terms in the objective function in Equation 4.22 are differentiable and we employed the simple steepest-descent method to solve Equation 4.22, *i.e.*:

$$\mathbf{u}^{j+1,n+1}=\mathbf{u}^{j+1,n}-\mu\gamma_{J(\mathbf{u})}\big|_{\mathbf{u}^{j+1,n}}, \tag{4.24}$$

where $J(\mathbf{u})$ and $\nabla J(\mathbf{u})$ can be written as:

$$\begin{aligned}J(\mathbf{u})&=\big(\mathbf{m}-\mathbf{u}\big)^T\mathbf{C}_{\mathbf{M}}^{-1}\big(\mathbf{m}-\mathbf{u}\big)+\alpha\|\mathbf{d}_{\mathbf{x}}^j-\mathbf{E}\nabla_x\mathbf{u}-\mathbf{b}_{\mathbf{x}}^j\|_2^2+\alpha\|\mathbf{d}_{\mathbf{y}}^j-\mathbf{E}\nabla_y\mathbf{u}-\mathbf{b}_{\mathbf{y}}^j\|_2^2\\ \gamma_{J(\mathbf{u})}&=2\big(\mathbf{m}-\mathbf{u}\big)-2\alpha\mathbf{C}_{\mathbf{M}}\mathbf{E}\nabla_x^T(\mathbf{d}_{\mathbf{x}}^j-\mathbf{b}_{\mathbf{x}}^j-\mathbf{E}\nabla_x\mathbf{u})-2\alpha\mathbf{C}_{\mathbf{M}}\mathbf{E}\nabla_y^T(\mathbf{d}_{\mathbf{y}}^j-\mathbf{b}_{\mathbf{y}}^j-\mathbf{E}\nabla_y\mathbf{u}).\end{aligned} \tag{4.25}$$

$\mathbf{d}_{\mathbf{x}}$ and $\mathbf{d}_{\mathbf{y}}$ in Equation 4.23 can also be solved using a generalized shrinkage formula [107]:

$$\begin{aligned}\mathbf{d}_{\mathbf{x}}^{k+1}&=\max\left(s^k-\frac{\lambda}{2\alpha},0\right)\frac{\mathbf{E}\nabla_x\mathbf{u}^k+\mathbf{b}_{\mathbf{x}}^k}{s^k}\\ \mathbf{d}_{\mathbf{y}}^{k+1}&=\max\left(s^k-\frac{\lambda}{2\alpha},0\right)\frac{\mathbf{E}\nabla_y\mathbf{u}^k+\mathbf{b}_{\mathbf{y}}^k}{s^k},\\ \text{where}\quad s^k&=\sqrt{\|\mathbf{E}\nabla_x\mathbf{u}^k+\mathbf{b}_{\mathbf{x}}^k\|_2^2+\|\mathbf{E}\nabla_y\mathbf{u}^k+\mathbf{b}_{\mathbf{y}}^k\|_2^2}.\end{aligned} \tag{4.26}$$

The whole reconstruction algorithm utilizing *a priori* information and artifact suppression is summarized in Table 4.1.

Table 4.1: Algorithmic description of the proposed reconstruction algorithm.

```
Initialize: $\mathbf{u}^0 = \mathbf{m}^0 = \mathbf{m_a}$ and $k = 0$
Output: $\mathbf{m}^{k+1}$

while ($k < K$)
    Solve Equation 4.10 to get $\mathbf{m}^{k+1}$
    if $\|\mathbf{m}^{k+1} - \mathbf{m}^k\|_2 > \text{TOL1}$
        return $\mathbf{m}^{k+1}$
    end
    Assign $\mathbf{d}_\mathbf{x}^0 = \mathbf{d}_\mathbf{y}^0 = \mathbf{b}_\mathbf{x}^0 = \mathbf{b}_\mathbf{y}^0 = \mathbf{0}$
    Assign $j = 0$ and $\mathbf{u}^{k,0} = \mathbf{u}^k$
    while(true)
        Solve Equation 4.22 to get $\mathbf{u}^{k,j+1}$
        Solve Equation 4.23 to get $\mathbf{d}_\mathbf{x}^{j+1}$ and $\mathbf{d}_\mathbf{y}^{j+1}$
        Update $\mathbf{b}_\mathbf{x}^{j+1}$ and $\mathbf{b}_\mathbf{y}^{j+1}$ using Equation 4.21
        if $\|\mathbf{u}^{k,j+1} - \mathbf{u}^{k,j}\|_2 > \text{TOL2}$
            break; // breaks when $j = q$
        end
    $j \leftarrow j + 1$
    end
    $\mathbf{u}^{k+1} = \mathbf{u}^{k,q}$
    $k \leftarrow k + 1$
end
```

4.2.4 Simulated Experiments

4.2.4.1 Field-of-view simulation configurations

The simulated field-of-view had a physical size of 6 cm in the axial direction and 4 cm in the lateral direction and was discretized by a square grid of $h = 312.5\,\mu\text{m}$ spacing. Two transducers with 40 point-like elements were placed within the field-of-view (top and bottom sides), with the inner padding of 1.5 grid spacings on all sides. Also, the first and last 6 columns in the image where transducer elements were located were excluded from the analysis due to lack of stability. The acoustic attenuation was set to 0.75 dB/cm/MHz$^{\text{-y}}$ with the power law exponent of $y = 1.5$, representing average frequency dependence of attenuation in breast tissue [108].

4.2.4.2 Input data generation

Input pressure datasets were generated using the k-Wave toolbox [109], with inputs given as true sound speed, mass density, and source pulse, where the latter was modeled as a 0.5 MHz sinusoidal waveform tapered by a Gaussian envelope centered at 13.7 µs and a 2 times standard deviation width of 2 µs. The peak amplitude of the input pressure was 1 a.u. The pressure traces were sampled at 17.1 MHz for 110 µs, resulting in 1,878 samples for each trace. Therefore, given the one-transmit-all-receive scheme, the resulting pressure dataset had a size of 80 × 80 × 1,878 samples.

4.2.4.3 Reconstruction settings

For the image reconstruction with *a priori* information algorithm (subproblem (1)), instead of leaving the algorithm to run until the incremental sound speed changed by a specified threshold (TOL1 in Table 4.1), we found it more desirable to fix the maximum number of iterations allowed and inspect the resulting values. By our observation, the maximum numbers of iterations for converging reconstruction were

15 and 20 for bent-ray and waveform inversion approaches, respectively. Running reconstruction algorithms for more than the given maximum numbers of iterations did not make any significant difference (the magnitude of the steepest descent in Equation 4.12 at the 20th iteration is within 5% of the magnitude of the steepest descent at the 1st iteration. However, if the the artifact suppression algorithm was activated, the maximum number of iterations was set to 5 instead and K in the outermost loop (line 1 in Table 4.1) was set to 3 so that the image was updated 20 times in total. For the artifact suppression algorithm (subproblem (2)), TOL2 was set to 0.0001 and the maximum number of iterations was set to 100.

The correlation coefficient ρ_k, was applied for all reconstructions, and was set to 0 if *a priori* segmentation information was not utilized. The default positive TV regularization parameter λ in Equation 4.6 was set to 10^{-8}. The parameter σ_e in Equation 4.8 was set to 1,024 s^{-2}. $\mathbf{C_D}$ was set to $\sigma_D^2\mathbf{I}$ where $\sigma_D = 50$ ns for bent-ray inversion and 10^{-2} a.u. for waveform inversion, respectively. The sound speed pixel standard deviation σ was set to 10,000 m/s to allow large variation of pixel values, and was constrained to $\mathbb{R}^+$. The initial sound speed was set to $\mathbf{u}$ and for the bent-ray inversion approach, $\mathbf{u}$ was set to be homogeneous at background sound speed. Subsequently, the bent-ray inversion result was then used as the initial image $\mathbf{u}$ for waveform inversion.

4.2.4.4 Simulation studies

The following studies were conducted to investigate accuracy, convergence behavior, and tolerance to noise and *a priori* segmentation uncertainty:

1. Noiseless reconstructions

   Sound speed images of several numerical phantoms were reconstructed from noiseless input datasets, using different reconstruction configurations. Those phantoms were basic cylinders (Figures 4.3- 4.4), two numerical breast phantoms similar to the Karmanos Cancer Institutes physical breast phantom (Figure 4.8) (Detroit, MI), and a numerical breast phantom similar to the physical Madsinh breast phantom (Figure 4.9) (Madsen, Madison, WI). For the basic cylinders in Figure 4.3, reconstruction accuracy and contrast-to-noise ratio (CNR) were also assessed. CNR between region R and background B is defined as:

$$CNR_R = |\mu_R - \mu_B|/(\sqrt{\sigma_R^2 + \sigma_B^2}), \tag{4.27}$$

where μ and σ denote sound speed mean and standard deviation.

2. Noisy reconstructions

   True sound speed and density distributions of the numerical Madsinh breast phantom were corrupted by a zero-mean Gaussian noise with 2 times standard deviation width equal to 4% of the maximum absolute amplitude of the received pressure signal. A waveform inversion approach without *a priori* information was employed.

3. Effects of regularization parameter λ on artifact suppression

   The regularization parameter λ in Equation 4.6 was varied in 7 logarithmic steps from 10^{-9} to 10^{-7} and applied to reconstructed images of basic cylinders obtained from the waveform inversion approach without *a priori* information. Images were obtained at 20^{th} iteration from the image reconstruction with *a priori* information sub-problem. The CNR of each region was calculated for each value of λ.

4. Effects of uncertain segmentation on reconstruction error

   Segmentation of real tissues could be prone to uncertainty of tissue boundaries, especially near distal borders of fibrous invasive cancers, these could be blurry or distorted due to aberration, speckle and electronic noise. The segmentation uncertainty was investigated in the reconstructions of a single cylinder (42 grid points diameter), placed in the center of a field of view. The uncertainty was defined as a finite-thickness zone centered around the circumference of the cylinder with the correlation coefficient ρ_k set to 0, as shown in Figure 4.2. Three different zone thicknesses, $2h$, $4h$, and $6h$, were assigned (h denotes grid spacing) and two sets of reconstructions utilizing different correlation coefficients ($\rho_k = 0.0005$ and $\rho_k = 0.005$) were performed for each. The sound speed error was calculated within the actual object region for each reconstruction case.

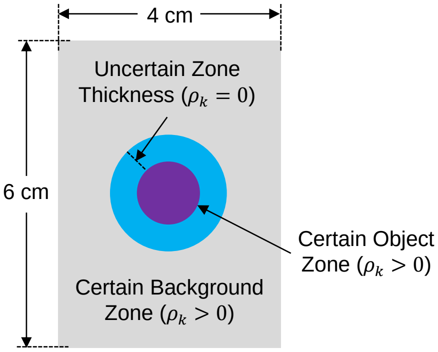

Figure 4.2: Demonstration of how segmentation uncertainty can be handled by defining a circular border with correlation coefficient $\rho_k = 0$ for uncertain boundaries. All other regions whose segmentation is known to be accurate (zones of certain background and object) can have $\rho_k > 0$.

4.3 Results and Discussion

4.3.1 Noiseless Reconstructions

Figure 4.3(a) shows the actual, assumed sound speed image of two, 1 cm diameter cylinders placed diagonally. Figures 4.3(b)-(e) show the corresponding reconstruction results obtained from different reconstruction techniques and correlation coefficients, ρ_k, as labeled in the figure. True sound speed and density are given in Table 4.2. Calculated sound speed and CNR are given in Table 4.3.

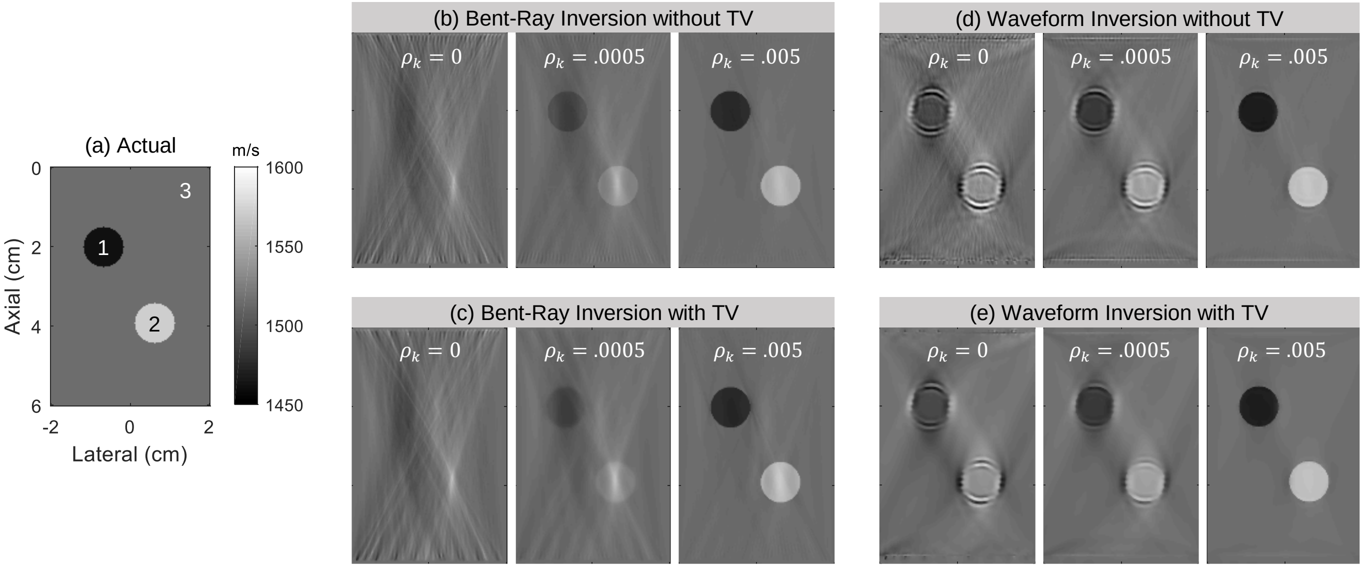

Figure 4.3: Sound speed reconstructions of two cylinders placed diagonally in the image. The true configuration is shown in (a). Bent-ray inversion results are shown in the left column (a, c) and waveform inversion results are shown in the right column (d, e). The bottom row (c, e) includes total-variation (TV) to suppress artifacts, whereas the top row (b, d) does not. Three correlation coefficients ρ_k are used for three levels of use of *a priori* spatial information: 0, 0.0005, and 0.005.

Table 4.2: Assumed acoustic properties for imaged structures shown in Figure 4.3. Region 1, 2, and 3, are top left cylinder, bottom right cylinder and background, respectively.

Region	1	2	3
Sound Speed (m/s)	1460	1570	1515
Mass Density (kg/m^3)	900	1200	1000

Table 4.3: Calculated sound speed (top row) and CNR (bottom row) of regions 1 and 2 shown in Figure 4.3, obtained using the reconstruction techniques as listed in Figure 4.3. Each row value corresponds to the respective correlation coefficient ρ_k.

Reconstruction method	Region	
	1	2
BR without TV	(2.72, 2.21, 1.06) (1.6, 3.6, 13.0)	(-2.92, -2.23, -1.06) (0.7, 2.0, 8.1)
BR with TV	(2.73, 2.27, 1.06) (1.6, 3.0, 11.3)	(-2.84, -2.32, -1.00) (0.8, 1.6, 5.4)
WI without TV	(2.18, 1.63, 0.55) (1.4, 3.0, 12.7)	(-1.98, -1.42, -0.44) (1.1, 2.6, 12.7)
WI with TV	(2.24, 1.70, 0.66) (1.9, 3.9, 12.2)	(-2.10, -1.60, -0.58) (1.6, 3.8, 12.7)

As can be seen from Figure 4.3 and Table 4.3, calculated sound speed accuracy and distinct, accurate object borders scale with the correlation coefficient ρ_k. This applies to all reconstruction techniques shown in the figure and is not surprising since larger ρ_k enforces stronger correlation and thus homogeneity of speed of sound values within the delineated regions. As such, if segmented regions are strongly homogeneous, applying high ρ_k should result in substantial improvement in calculated sound speed distributions as well as mean values.

Waveform inversion also improves sound speed accuracy and object geometry features as it can address higher order effects such as diffraction and multiple reflections. Without TV regularization sound speed errors in regions 1 and 2 were reduced by (0.54, 0.58, 0.51)%, and (0.94, 0.81, 0.62)% for correlation coefficients of ρ_k = (0, 0.0005, 0.005), respectively, compared to those of bent-ray inversion approach (see Table 4.3).

Moreover, for small or zero ρ_k, the waveform inversion approach unveils geometric features much better than bent-ray (Figure 4.3 and Table 4.3). This suggests that the waveform inversion approach could potentially help to overcome situations with the limited *a priori* information, as is the case when confidence in segmentation homogeneity is low. Despite this clear advantage of the waveform inversion approach, limited angle artifacts arise in conjunction with small ρ_k. In this circumstance, the TV regularization term in Equation 4.6 will have a large value, and the reconstruction algorithm will attempt to minimize this term. This effect can be seen as the increase of CNR in Table 4.3 when applying TV regularization to the waveform inversion approach. As a result, TV regularization is most effective when ρ_k is low, as higher ρ_k inherently reduces artifacts. In addition, note that changes in calculated sound speed due to artifact suppression are negligible although artifact suppression does alter sound speed variation.

The reconstruction of the presented two cylinders was investigated further by changing their orientation and one's size. Two cylinders were placed in the lateral center of the field of view and one of them was enlarged so that the larger cylinder acoustically shadowed the smaller cylinder. Two reconstruction cases were performed for two configurations: larger cylinder with positive sound speed contrast relative to background and bottom cylinder (Figure 4.4(a)), and larger cylinder with negative sound speed contrast (Figure 4.4(b)).

Reconstruction results are shown in panels (c)-(f). Shadowing effects can be observed by intrusion of high sound speed values at the side of cylindrical wall facing the high contrast cylinder. With no *a priori* information, $\rho_k = 0$ (Figures 4.4(c) and (d) left), the bent ray reconstructions are almost unrecognizable and in the waveform inversion image (e), vertical ambiguity artifacts intrude noticeably from the high speed cylinder into the low speed one. At zero and low ρ_k, waveform inversion is, again superior to bent ray reconstruction. Use of the nonzero correlation coefficient values, as well as TV, improve the waveform inversion results. Artifact suppression becomes crucial in reducing noise and improving CNR in low ρ_k settings. Specifically, for $\rho_k = 0$ and no TV, the CNRs of regions (1, 2) are (1.0, 0.6) and (1.2, 0.5) for cases 1 and 2, respectively. By applying TV regularization, the CNRs of these regions

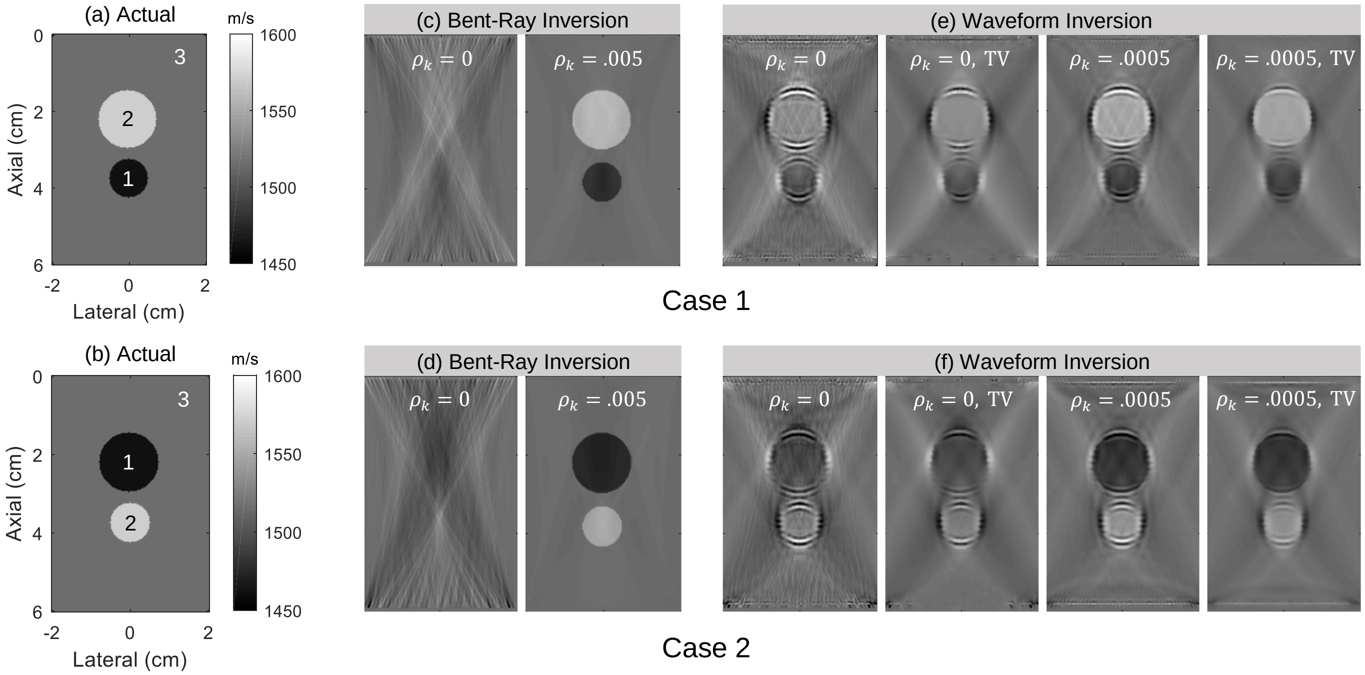

Figure 4.4: Sound speed reconstructions of two cylinders with different sizes placed vertically. (a) and (b) Assumed objects with the sound speed contrast of (a) reversed in (b), *i.e.*, case 1 and case 2, respectively. Results from each reconstruction technique are shown in (c)(f) with the names of the technique given in the group titles. (c), (e) were obtained from reconstructions of (a), and (d), (f) from reconstructions of (b). The correlation coefficient ρ_k and use of TV are overlaid on the images.

increase to (1.4, 0.7) and (1.5, 0.7), which reflects an improvement of (40, 16.7)% and (25, 40)% for cases 1 and 2, respectively. This is further demonstrated visually by the corresponding line graph cross-sections for the waveform inversion approach ($\rho_k = 0$), shown in Figure 4.5. High sound speed fluctuations around the boarder of the objects are visible and likely result from an ill-posed reconstruction setting.

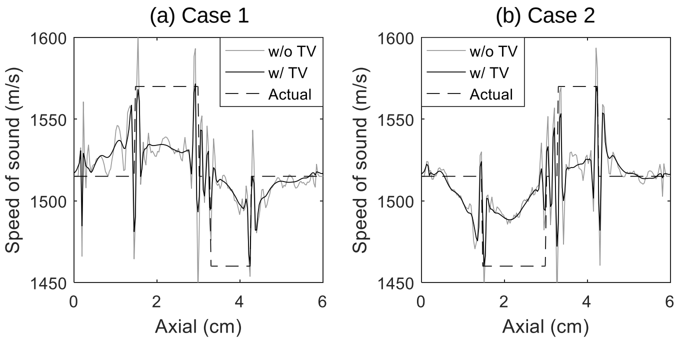

Figure 4.5: Line graph cross-sections (a and b) of the reconstructed sound speed for cylinder contrasts as defined in Figure 4.4 (a and b), obtained with and without TV regularization. The reconstructions are based on waveform inversion with no *a priori* information, *i.e.* $\rho_k = 0$.

However, as described earlier, for large ρ_k, it is unnecessary to utilize waveform inversion reconstruction and TV regularization for artifact suppression. Figures 4.4(c) and (d) and cross-section plot in Figure 4.6 show that when $\rho_k = 0.005$ is applied, not only the reconstruction accuracy is improved, but also the artifacts are significantly reduced. The accuracy of bent-ray inversion using large ρ_k (*e.g.* 0.005) could surpass that of waveform inversion using low ρ_k (*e.g.* 0.0005 or 0) (Figure 4.4), in situations in which the segmentation of homogeneous regions is accurate. The reconstruction results using the waveform inversion approach with $\rho_k = 0.005$ are not shown in Figure 4.4 as they provide very similar results as those of bent-ray inversion approach with the same ρ_k (Figures 4.4(c) and (d) right).

Reconstruction convergence can be verified by monitoring the magnitude of the steepest descent (SD) vector ($\gamma_{\mathbf{m}}$ in Equation 4.12), which should decrease for increas-

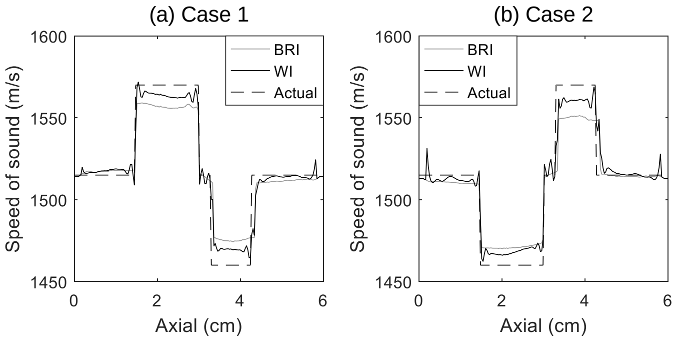

Figure 4.6: Line graph cross-section plots (a and b) of reconstructed sound speed with *a priori* information for cylinders as defined in Figure 4.4 (a and b). The reconstructions utilize bent-ray and waveform inversion but no TV regularization. The correlation coefficient ρ_k is set to 0.005.

ing iterations. The normalized SD is shown in Figure 4.7(a). Note that nonzero correlation coefficients lead to variations of the SD at approximately the first 10 iterations. In contrast, the normalized magnitude of the data term gradient ($\mathbf{G}_{\mathbf{m}}^{*}\left[\mathbf{C}_{\mathbf{D}}^{-1}\left(g(\mathbf{m})-\mathbf{d}\right)\right]$ in Equation 4.15) these variations are less noticeable (Figure 4.7(b)). This is attributed to the SD vector, whose direction is not necessarily the same as direction of the gradient. Specifically, altering ρ_k induces directional change of the SD vector due to structural change of the covariance matrix $\mathbf{C_M}$. Note that this process is also necessary because it allows the sound speed image to be updated according to the *a priori* constraints. This is not the case for the gradient direction, which is independent from the covariance matrix $\mathbf{C_M}$.

More complex phantom reconstructions are shown in Figure 4.8 and Figure 4.9. The first one is based on the numerical Karmanos Cancer Institute breast phantom with reduced breast size and sound speed of glandular tissue (region 2) replaced by the sound speed of coupling gel (region 7). The latter one is based on the physical Madsinh breast phantom [6]. The corresponding true sound speed and mass density for each region are given in Tables 4.4 and 4.5. Note that in all reconstructions of the second phantom, the fatty layer sound speed was fixed to avoid sound speed

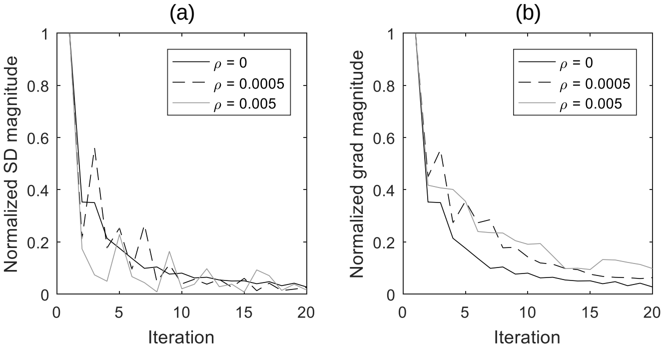

Figure 4.7: Magnitude of two possible measures of convergence: (a) Normalized steepest descent of total cost term (SD) and (b) normalized gradient of data cost term (grad). Both are plotted versus iteration number and for three correlation coefficients.

reconstruction ambiguity that arises in horizontal layers. This is a limitation of limited angle reconstructions without use of *a priori* information.

Table 4.4: Assumed acoustic properties of each region in numerical Karmanos Cancer Institute breast phantom.

Region	1	2	3, 4	5, 6
Speed of sound (m/s)	1600	1515	1470	1550
Density (kg/m^3)	1000	1000	1000	1000

Table 4.5: Assumed acoustic properties of each region in numerical Madsinh breast phantom.

Region	1	2	3	4	5	6
Speed of sound (m/s)	1409	1461	1421	1537	1552	1452
Density (kg/m^3)	1000	1000	1000	1200	1200	1000

Similar to the simple phantom studies, reconstruction accuracy and object geometry is enhanced by including *a priori* segmentation data or replacing the bent-ray inversion approach with waveform inversion. As can be seen from Figures 4.8 and 4.9, accurate segmentation reduces sound speed error and limited angle artifacts for both approaches. However, the bent-ray resolution limit (the first Fresnel zone) is larger than that of waveform inversion, which allows waveform inversion to better recover

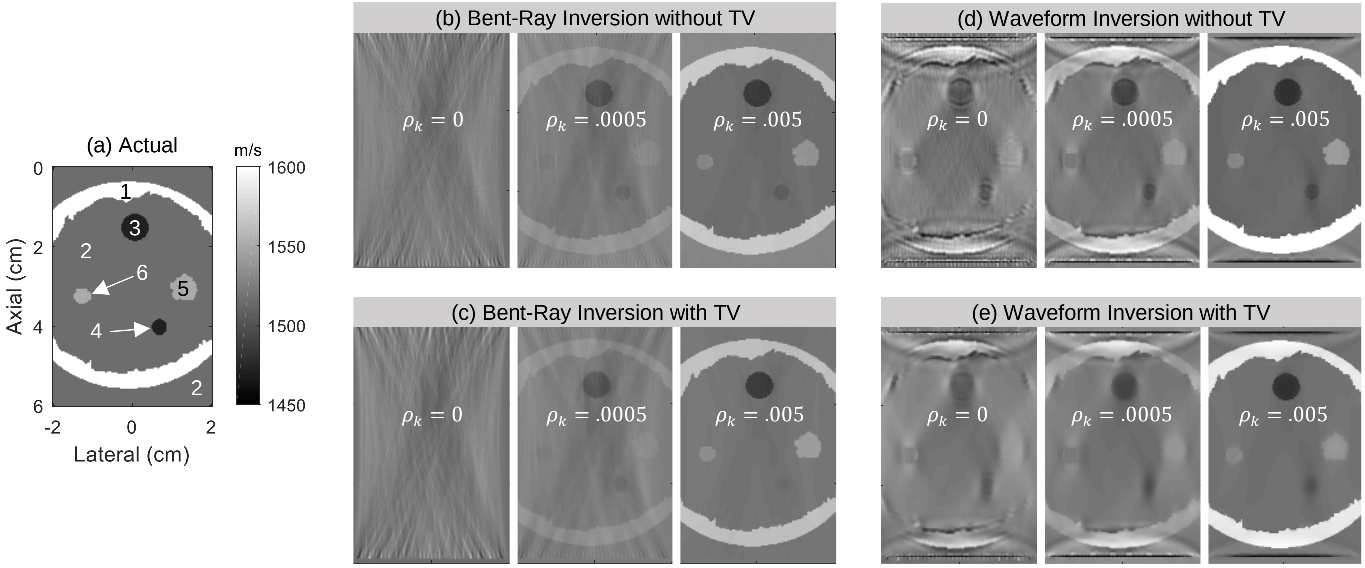

Figure 4.8: Sound speed reconstructions using the numerical Karmanos Cancer Institute breast phantom. Initial, assumed, configuration is shown in (a). Results are shown in image groups (b) (e). Different reconstruction techniques are labeled. TV denotes total-variation used for artifact suppression. Use of *a priori* information, by means of the correlation coefficient ρ_k, is labeled on each image. Regions 1-7 are: skin layer (1), glandular tissue (2), large (3) and small (4) fat nodules, large (5) and small (6) tumors, and gel couplant (7).

small object geometries even for low segmentation homogeneity. This is demonstrated as the high-contrast cancer nodule (region 6) appears more like a low-contrast object bent-ray inversion results (Figure 4.8, $\rho_k = 0$ or 0.0005). Still, even if waveform inversion approach is employed, small features could be smoothed out by the TV regularization, making them look more blurry. The effects of using different regularization parameters on the reconstructed images will be further discussed in Section 4.3.3.

Note that even though TV regularization has shown to suppress granular limited angle artifacts due to low ρ_k, as demonstrated in Figures 4.8 and 4.9, its performance in suppressing large artifacts is limited. Figures 4.9(b)-(e) show an example of a large negative contrast artifact located in the middle of the image. This becomes more noticeable for lower ρ_k. Such negative contrast artifacts can arise from high-contrast streaking artifacts extending out of two lesions (region 5 and 6) diagonally. These streaking artifacts can reduce the sound speed around the center of the image, thus causing a large negative contrast artifact. However, if the segmentation confidence is high enough, one could still apply high ρ_k to suppress this artifact.

4.3.2 Noisy Reconstructions

Figure 4.10 shows the waveform inversion reconstruction results of the numerical Madsinh breast phantom, using input pressure traces containing Gaussian noise. Images from Figure 4.10(a) and CNR values show that applying higher ρ_k results in both accuracy improvement and artifact reduction. However, for low or zero ρ_k, segmentation homogeneity is not enforced strongly, thus Gaussian noise in the input pressure traces is noticeably manifested as grainy artifacts in the images. Applying TV regularization therefore leads to effective artifact suppression for low or zero ρ_k, *e.g.* $\rho_k = 0$ (panel b).

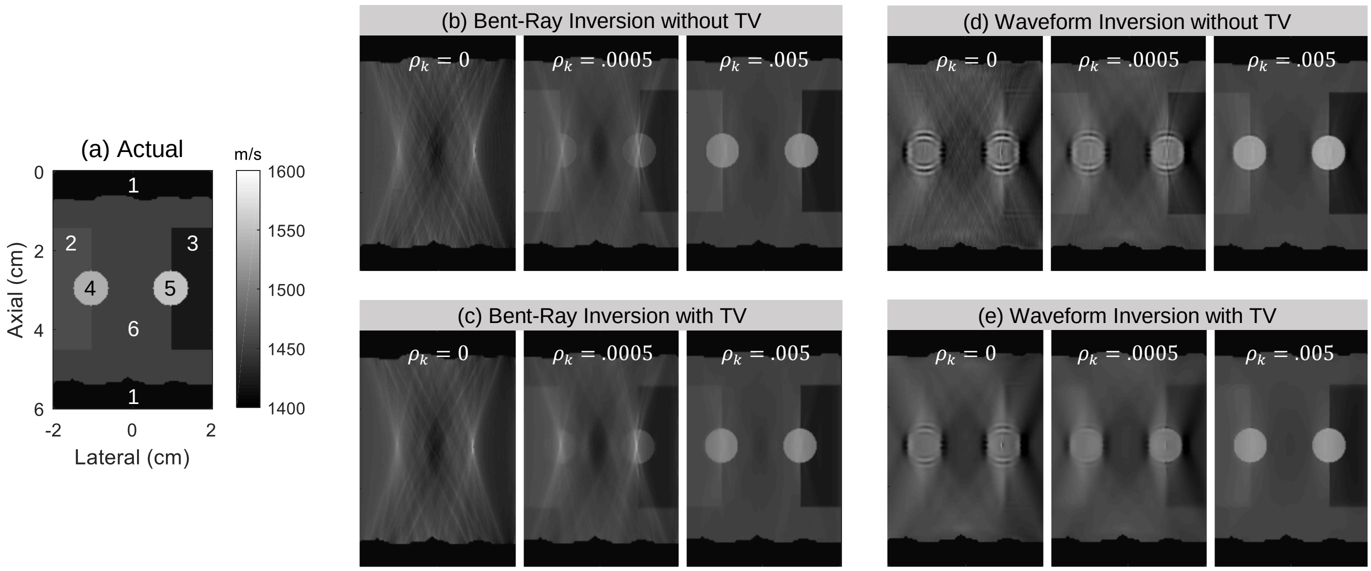

Figure 4.9: Sound speed reconstructions of the numerical Madsinh breast phantom. The initial, assumed, configuration is shown in (a). Results are shown in groups (b) (e) with reconstruction techniques as labeled. TV denotes total-variation and is used for artifact suppression. Use of *a priori* information, by means of the correlation coefficient ρ_k, is labeled on each image. Regions 1-6 are: skin layers (1), high-speed glandular tissue (2), high-speed fat (3), cysts (4)-(5), and medium-speed glandular tissue (6).

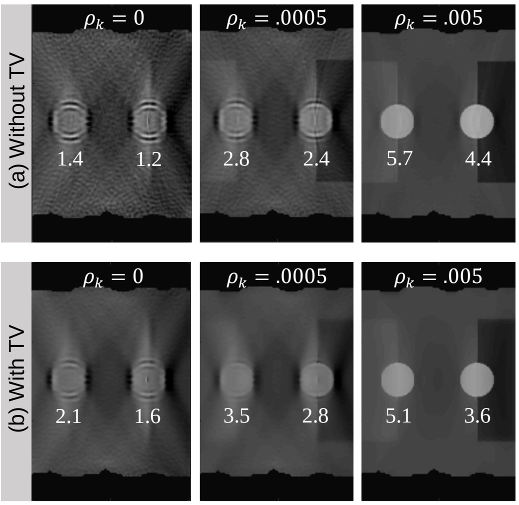

Figure 4.10: Waveform inversion based sound speed reconstructions using the numerical Madsinh breast phantom (Figure 4.9(a)) with added Gaussian noise. Results without and with total variation (TV) are shown in image groups (a) and (b), respectively. TV denotes total-variation used for artifact and noise suppression. The correlation coefficient ρ_k implementing *a priori* information and the CNR value are labeled on top and bottom of each image, respectively.

4.3.3 Effects of Regularization Parameter λ on Artifact Suppression

Figure 4.11 shows waveform inversion results of the numerical Madsinh breast phantom without *a priori* information ($\rho_k = 0$) and with different TV regularization parameters ($\lambda > 0$). The corresponding CNRs for each λ are given in Figure 4.12. Increasing λ tends to decrease artifacts and improve CNR. Higher λ yields a higher penalty term $\lambda\mathbf{E}\|\mathbf{m}\|_{TV}$ in Equation 4.6. However, in order to keep the total cost value $E(\mathbf{m})$ low, the artifacts in the image need to be further suppressed such that the value of $\|\mathbf{m}\|_{TV}$ will decrease. Note that large λ can cause noticeable image blurring. Therefore the choice of λ is a trade-off between CNR improvement and blurring.

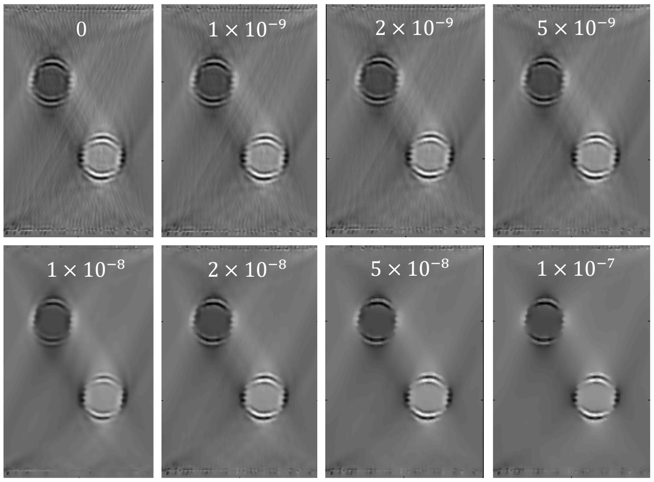

Figure 4.11: Waveform inversion based sound speed reconstructions in a cylinder phantom as shown in Figure 4.3(a). While no *a priori* information is used ($\rho_k = 0$), the TV regularization parameter λ for artifact suppression is logarithmically increased.

4.3.4 Effects of Uncertain Segmentation on Reconstruction Results

Figure 4.13 shows calculated sound speeds obtained from different uncertainty zone (zone with $\rho_k = 0$) thicknesses and *a priori* correlation coefficients ρ_k. Note that using higher confidence of segmentation homogeneity (higher ρ_k) can help reduce

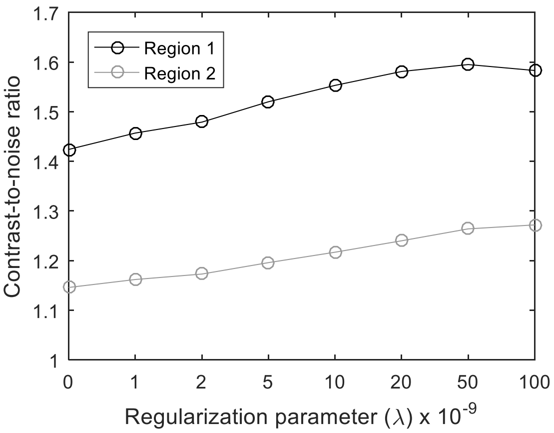

Figure 4.12: CNR as a function of the TV regularization parameter λ in the cylinder phantom shown in Figure 4.11. The region number is equivalent to that in Figure 4.3(a), *i.e.* top left and bottom right are 1 and 2, respectively.

the speed of sound error. However, the uncertain segmentation around the object boundary induces the modest object's speed of sound error as shown in Figures 4.13(a) and (b), and the speed of sound error increases when the uncertainty zone thickness increases. The positive contrast object in general brings down the calculated object's speed of sound as seen from Figure 4.13(a) and vice versa as seen from Figure 4.13(b). This could be explained by the fact that most sources or the error due to segmentation uncertainly are transferred and absorbed by the uncertainty zone. Such errors can be observed when the object's speed of sound is calculated from all pixels within the combined certain object zone and uncertainty zone (see Figure 4.13(c) for positive contrast object and Figure 4.13(d) for negative contrast object). The reason that the uncertainty zone can absorb most errors is because of its correlation coefficient ρ_k that is set to 0, thus allowing the most flexibility and heterogeneity of pixels within that uncertainty zone.

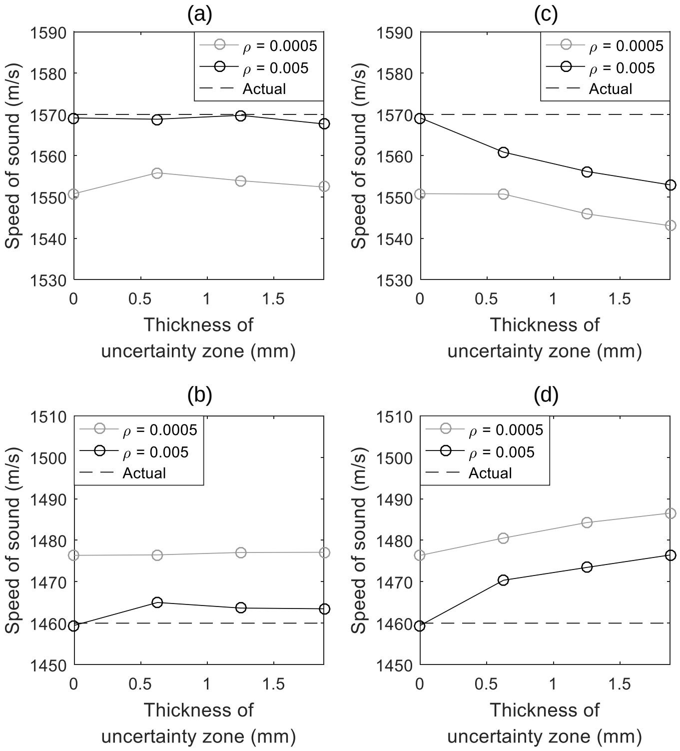

Figure 4.13: Sound speed estimation errors due to uncertainly zone (zone with $\rho_k = 0$) representing segmentation uncertainty, obtained from different uncertainty zone thicknesses and correlation coefficients ρ_k of 0.0005 and 0.005. The sound speeds of positive and negative contrast objects, calculated within the certain object zone only, are shown in (a) and (b). The sound speeds of positive and negative contrast objects, calculated within the combined certain object zone and uncertainty zone, are shown in (c) and (d).

4.4 Conclusions

Spatially reconstructing ultrasound tissue sound speed in the limited-angle tomography setting results in significant image artifacts and degrades speed of sound accuracy, as the limited information in the acquired signals introduces strong ill-posedness in the reconstruction problem.

This work has shown that both *a priori* segmentation data and waveform inversion are capable of providing the structural boundary information around heterogeneous interfaces, thus are able to resolve object geometry features and improve reconstruction accuracy. In addition, in most clinical imaging cases where*a priori* segmentation data is not available or ambiguous, waveform inversion could potentially be employed together with artifact suppression to reduce the heterogeneities introduced by the limited angle imaging geometry.

Despite the extensive simulation results presented in this work, it is worthwhile to note that the reconstructions could have been performed more realistically by the following approaches: First, the imaging probe impulse response should be modeled with bandwidth limitations. Second, cross-talk between adjacent transducer elements should be modeled and thus removed by trimming the beginning of each rf-signal. Third, given adequate computational resources, physical experiments should be performed to validate the feasibility in clinical imaging within complicated geometries and using higher imaging frequencies (as high as 10 MHz for current clinical breast scanning).

The proposed reconstruction algorithm demonstrates that applying *a priori* segmentation and waveform inversion, or both, show promise in using ultrasound to image breast in the same view as x-ray mammography that is currently considered as the clinical standard. This allows easier comparison of images from two modalities and thus delivering better breast cancer detection and screening performance.

CHAPTER V

3D Corrections for Reconstruction of Bulk Tissue Attenuation Coefficients[1]

5.1 Introduction

Ultrasound attenuation imaging has recently received much attention in breast imaging for cancer detection, as the localized attenuation coefficient has shown to be a good discriminator among various breast tissue types [23], [24], [30], [57], [110]–[112]. Despite the fact that shadows in B-mode images can be caused by ultrasound reflectors dispersing the beam, the full history of ultrasound breast imaging has recommended scrutinizing tissues causing shadows as possible cancers [113]–[115]. Several studies suggest that tissue regions with high attenuation coefficients and high sound speed are more likely to be cancer [16], [17], [19], [21], [30]–[32], [57], [110], [111], [116]. However, obtaining accurate attenuation coefficient images can be more challenging than obtaining sound speed images [36], [117]–[119]. This results from the several overlapping factors, such as geometric spreading, refraction, diffraction, and scattering, that deflect the energy away from the receivers, usually by amounts dependent on the angle of incidence to a sound speed gradient. This, usually coherent, scattering depends on a tissues properties relative to that of its surroundings, as

---

[1] This chapter is submitted: R. Jintamethasawat, O. D. Kripfgans, J. B. Fowlkes, and P. L. Carson, "3D Corrections for Reconstruction of Bulk Tissue Attenuation Coefficients."

opposed to attenuation caused by interactions in the tissue itself. We call the measure of this attenuation that is representative of a given tissue, the bulk attenuation coefficient. This is distinguished from absorption coefficient of that tissue, representing only the energy absorbed locally in the tissue, but not the local scatter.

Existing breast attenuation coefficient image reconstruction algorithms can be divided into 2 categories: (a) bent-ray based approaches that approximate the ultrasound signal propagation path as a ray whose bending represents refraction [8], [16], [17], [31], [118]; and (b) waveform based approaches that utilize the received signal within a larger context [18], [19], [21], [30], [32], [35], [111], [120]–[122]. Even though bent-ray based approaches do not offer the detailed image resolution and fidelity of waveform based approaches, they are still attractive as they demand less computational power and are more robust with respect to ill-conditioned reconstructions [21], [32], [36], [117]–[119]. Unfortunately, most of the bent-ray based approaches only remove the geometric spreading effect by acquiring an additional non-attenuating water dataset and determining the received signal energy (or amplitude, spectrum, etc.) difference between it and the tissue dataset [8], [16], [17], [25], [31], [116]–[118]. Other effects, such as acoustic impedance mismatch between adjacent tissue types, *i.e.*, boundary effects, still remain, thus resulting in received energy and reconstructions dependent on the differences between tissues as well as the desired attenuation as a property of each individual tissue type. Such effects become more severe when boundary scattering is directed out of the imaging plane. Note that even though waveform based approaches can eliminate geometric spreading and boundary effects, the forward solvers need to be able to capture all of the wave propagation physics. Thus, 3D full-wave propagation modeling is required to simulate signals that travel in 3D space. Failure to comply with such requirements will lead to inaccurate attenuation coefficient image reconstructions and yield severe artifacts [32], [35], [36], [118], [119].

To compromise between the clinical demand for rapid and cost-efficient breast cancer diagnosis and that of superior image quality, we propose a hybrid attenuation coefficient image reconstruction algorithm that utilizes a waveform propagation simulation for 3D attenuation correction and a subsequent bent-ray scheme for 2D image reconstruction.

Two-dimensional bent-ray based reconstruction is fast compared to its waveform-based counterpart. Three-dimensional attenuation correction (*i.e.* the removal of geometric spreading and boundary effects) is obtained by only 2 forward solver runs (total) for signal propagation computation in lossless media. In contrast, the majority of iterative waveform inversion algorithms require *at least* 2 forward solver runs (per iteration), namely one for the wave fields and another one for adjoint fields.

The proposed attenuation correction is done under the assumption that a good sound speed distribution of the imaged volume has been reconstructed. Similar attenuation correction techniques have been proposed previously for pulse-echo imaging in the spectral domain [123], [124]. However, those techniques only account for refraction. Other attenuation coefficient image reconstruction algorithms [8], [25] account for refraction and diffraction and are more closely related to our 3D work. The importance of this extension is to account for possible beam refraction or scattering out of the detector apertures at major boundaries. This paper is organized as follows: Section 5.2 explains the related acoustic theory, the proposed attenuation correction method and the proposed image reconstruction method. A series of simulation study parameters and techniques is also given in this section. The associated results and their analyses are given in Section 5.3. Section 5.4 provides a summary, conclusions, and future directions of study.

5.2 Materials and Methods

5.2.1 Signal Acquisition

Scanning systems typically utilize either ring arrays or opposed linear arrays. The signal acquisition is accomplished by sequentially transmitting from a single or virtual transducer element and receiving signal by all transducer elements on the ring array if a ring array is used, or on all elements of the opposing linear array, if two opposed linear arrays are used. Regardless of the transducer type, note that the transmitted signal can be refracted and diffracted both in-plane and out-of-plane primarily due to the sound speed mismatch between two media as shown in Figure 5.1 [13], [14].

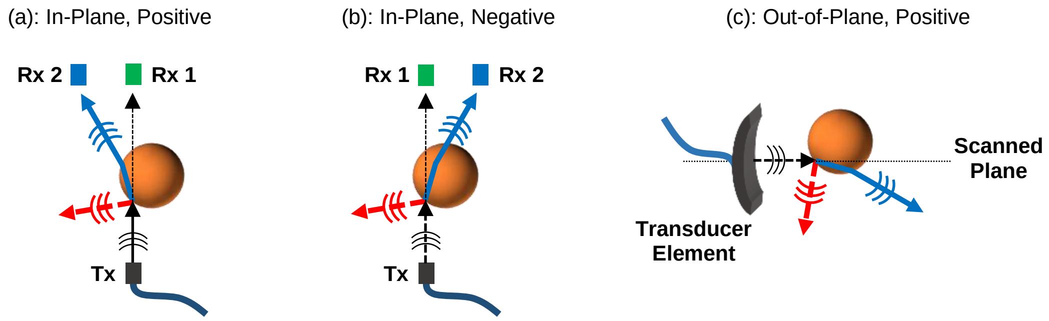

Figure 5.1: Refracted acoustic ray path (blue solid bold arrow) and reflected ray path (red dashed bold arrow) due to sound speed and impedance differences, respectively, at the interface between two media, occurring in-plane (a), (b) and out-of-plane (c). Changes in beam propagation direction from the assumed directions (black thin dashed arrow) are illustrated for cases where the imaged object has positive (a), (c) or negative (b) sound speed contrast relative to the background. Tx and Rx 1 denote active transmit element and opposed receive element, respectively, and Rx 2 denotes a neighboring receive element.

5.2.2 Wave Propagation Modeling

5.2.2.1 Full-wave modeling

Acoustic wave propagation in a 3D medium with heterogeneous sound speed $c(\mathbf{r}) : \mathbb{R}^3 \rightarrow \mathbb{R}^+$ and attenuation coefficient $\alpha(\mathbf{r}) : \mathbb{R}^3 \rightarrow \mathbb{R}_0^+$ can be modeled over time $t \in [0, T]$ and space $r \in \mathbb{R}^3$ by the following three first-order coupled equations [14], [98], [99]:

$$\frac{\partial}{\partial t}\mathbf{u}(\mathbf{r}, t) = -\frac{1}{\rho_0(\mathbf{r})}\nabla p(\mathbf{r}, t) \tag{5.1a}$$

$$\frac{\partial}{\partial t}\rho(\mathbf{r}, t) = \rho_0(\mathbf{r})\big(-\nabla \cdot \mathbf{u}(\mathbf{r}, t) + \int\limits_0^t s(\mathbf{r}, t')dt'\big) \tag{5.1b}$$

$$p(\mathbf{r}, t) = c^2(\mathbf{r})\left[1 - \tau(\mathbf{r})\frac{\partial(-\nabla^2)^{\frac{y}{2}-1}}{\partial t} - \eta(\mathbf{r}(-\nabla^2)^{\frac{y+1}{2}-1})\right]\rho(\mathbf{r}, t), \tag{5.1c}$$

where $s(\mathbf{r}, t) : \mathbb{R}^3 \times \mathbb{R}_0^+ \rightarrow \mathbb{R}$ is the source pressure, $\mathbf{u}(\mathbf{r}, t) : \mathbb{R}^3 \times \mathbb{R}_0^+ \rightarrow \mathbb{R}^3$ is the particle velocity, $p(\mathbf{r}, t) : \mathbb{R}^3 \times \mathbb{R}_0^+ \rightarrow \mathbb{R}$ is the acoustic wave pressure or pressure trace, and $\rho(\mathbf{r}, t) : \mathbb{R}^3 \times \mathbb{R}_0^+ \rightarrow \mathbb{R}^+$ and $\rho_0(\mathbf{r}) : \mathbb{R}^3 \rightarrow \mathbb{R}_0^+$ are the object density and background density, respectively. The terms $\tau(\mathbf{r})$ and $\eta(\mathbf{r})$ include the attenuation coefficient as:

$$\tau(\mathbf{r}) = -2\alpha(\mathbf{r})c(\mathbf{r})^{y-1} \tag{5.2a}$$

$$\eta(\mathbf{r}) = 2\alpha(\mathbf{r})c(\mathbf{r})^y \tan\big(\frac{\pi y}{2}\big), \tag{5.2b}$$

where y denotes the power law exponent for the attenuation coefficient. In this paper, the three first-order coupled acoustic equations were solved via a k-space pseudospectral method for the sake of low memory usage and adequate numerical stability [109].

This paper utilizes full-wave modeling for simulating non-attenuating signals for energy correction (Section 5.2.3) as well as for generating simulated tissue datasets used as input pressure traces used for bent-ray based reconstructions (Section 5.2.5).

5.2.2.2 Bent-ray modeling

An alternative and simpler wave propagation modeling approach is based on ray theory [46], [125]. It models the propagation of a single point on the wavefront as a bent-ray, rather than a continuous wavefront. All points on the same wavefront are assumed to have the same phase.

The first-arrival time, *i.e.*, time-of-flight (TOF), of the wavefront at the location $\mathbf{r_0}$ can be calculated by solving the following Eikonal equation:

$$\|\nabla\mathbf{T}(\mathbf{r})\|_2 c(\mathbf{r}) = 1, \quad \mathbf{T}(\mathbf{r_0}) = 0, \tag{5.3}$$

where $\mathbf{T}$ represents the calculated TOF map, whose gradient direction $\nabla\mathbf{T}$ (*i.e.* receiver towards source) resembles the propagation path. While employing a 3D full-wave forward model for attenuation correction, this paper utilizes the bent-ray modeling for the inverse, 2D sound speed and attenuation image reconstructions.

5.2.3 Attenuation Correction

Receive signal attenuation (absorption and scattering effects), denoted as a, can be obtained from energy loss of a received signal propagating through the heterogeneous attenuation and sound speed distribution consisting of simulated object(s) and surrounding background E_o, compared to the non-absorbing and homogeneous background medium E_b. The attenuation is given as:

$$a = 10\log_{10}(E_b) - 10\log_{10}(E_o) = 10\log_{10}(\frac{E_b}{E_o}). \tag{5.4}$$

The energy of a given signal $s(t)$, acquired from time t_1 to t_2, can be obtained from the time integral of the Hilbert transform of $s(t)$:

$$E = \int_{t_1}^{t_2} |H(s(t))|^2 dt, \tag{5.5}$$

where E denotes the total signal energy of the signal $s(t)$ and H denotes the Hilbert transformation operator.

Note that Equation 5.4 only allows for correcting signal energy loss due to geometric spreading resulting from the unknown actual path lengths. Thus, the calculated attenuation does not accurately represent the actual energy loss, due to refraction or diffraction effects that usually occur in media with heterogeneous sound speed and on oblique interfaces between media.

As illustrated in Figure 5.1, refraction and scattering can occur both in-plane (a)-(b) and out-of-plane (c), often causing energy to miss or inappropriately hit the detectors compared to that in propagating through homogeneous sound speed media [25]. Figures 5.1(a) and (b) specifically illustrate in-plane positive and negative sound speed contrast refraction effects. The object with positive sound speed contrast (a) causes the beam to diverge away from the object, here as an energy shift from Rx 1 to Rx 2, thus changing the resulting recorded attenuation. Similarly, the object with negative sound speed contrast (b) causes the beam to refract towards the inside of the object. Note that elevational spreading can lead to out-of-plane refraction and diffraction effects, as shown in Figure 5.1(c), and thus signal energy loss.

Fortunately, it is possible to account for the signal loss that is due to a tissues impedance and speed of sound differences with its surroundings, resulting in the loss that is a property of the tissue itself. Similar to Equation 5.4, the corrected attenuation is written as:

$$a_c = a - a_s, \tag{5.6}$$

where a is the overall attenuation. a_c is the corrected attenuation due only to the tissue absorption and scattering within bodies of relatively homogeneous tissue. a_s is the attenuation due to refraction, reflection and diffraction at macroscopic gradients in sound speed or acoustic impedance. Given that the object delineations and their corresponding sound speed distributions are known *a priori*, it is possible to calculate a_s from two simulated pressure datasets: one from full-wave propagation simulation in a homogeneous background medium, and another from full-wave propagation simulation in non-absorbing media with heterogeneous *a priori* sound speed distribution. Specifically, a_s is calculated as:

$$a_s = 10\log_{10}(E_{b,s}) - 10\log_{10}(E_{o,s}) = 10\log_{10}(\frac{E_{b,s}}{E_{o,s}}), \tag{5.7}$$

where $E_{o,s}$ is the simulated 3D receive signal energy that includes out-of-plane signal loss due to heterogeneous *a priori* sound speed. It is computed as a wave that is propagating through the non-absorbing object(s), thereby yielding relative signal loss due to out-of-plane refraction and diffraction. $E_{b,s}$ is the simulated receive signal energy propagating through the homogeneous background medium. Equations 5.1a-5.1c can be utilized to compute a_s, with the background attenuation $\alpha(\mathbf{r}) = 0$ for all $\mathbf{r} \in \mathbb{R}^3$.

5.2.4 Reconstruction of Attenuation Coefficient Images

Radiofrequency pressure trace datasets acquired from ultrasound scanners can be used for reconstructing both sound speed and attenuation coefficient images. Image reconstruction can be regarded as the minimization of an objective function shown in Equation 5.8 with respect to the vectorized slowness $\mathbf{s}$ (inverse of sound speed $\mathbf{c}$) and attenuation coefficient $\boldsymbol{\alpha}$:

$$
\begin{aligned}
(\mathbf{s}, \boldsymbol{\alpha}) = \arg\min_{\mathbf{s},\boldsymbol{\alpha}} \Big\{ & \big(\mathbf{d_{sos}} - g_{sos}(\mathbf{s})\big)^T \mathbf{C}^{-1}_{\mathbf{D,sos}} \big(\mathbf{d_{sos}} - g_{sos}(\mathbf{s})\big) \\
& + \big(\mathbf{d_{att}}(\mathbf{s}) - g_{att}(\boldsymbol{\alpha}, \mathbf{s})\big)^T \mathbf{C}^{-1}_{\mathbf{D,att}} \big(\mathbf{d_{att}}(\mathbf{s}) - g_{att}(\boldsymbol{\alpha}, \mathbf{s})\big) \\
& + \big(\mathbf{s} - \mathbf{s_0}\big)^T \mathbf{C}^{-1}_{\mathbf{M,sos}} \big(\mathbf{s} - \mathbf{s_0}\big) + \big(\boldsymbol{\alpha} - \boldsymbol{\alpha_0}\big)^T \mathbf{C}^{-1}_{\mathbf{M,att}} \big(\boldsymbol{\alpha} - \boldsymbol{\alpha_0}\big) \Big\}.
\end{aligned}
\tag{5.8}
$$

Let N be the number of data from all transmit-receive element pairs, $\mathbf{d_{sos}}$ and $g_{sos}(\mathbf{s})$ denote the measured and simulated time-of-flight vectors of all these pairs, such that $\mathbf{d_{sos}} = [t_1, t_2, \ldots, t_N]^T$, where t_i denotes the i^{th} pair time-of-flight. $\mathbf{d_{att}}(\mathbf{s})$ and $g_{att}(\mathbf{s}, \boldsymbol{\alpha})$ denote the measured and simulated transmit-receive element pair attenuation vectors, such that $\mathbf{d_{att}}(\mathbf{s}) = [a_1(\mathbf{s}), a_2(\mathbf{s}), \ldots, a_N(\mathbf{s})]^T$, where $a_i(\mathbf{s})$ denotes the attenuation associated with the i^{th} pair and also depends on slowness $\mathbf{s}$ if attenuation correction is applied according to Equation 5.7. The measured attenuation $\mathbf{d_{att}}$, obtained from the input pressure dataset, can be calculated either from Equation 5.4 to obtain the uncorrected attenuation or from Equation 5.6 to obtain the corrected attenuation.

In this paper, we utilize the computationally efficient bent-ray modeling for 2D image reconstructions. Simulated time-of-flight can be first calculated via the Eikonal equation in Equation 5.3, with inputs $\mathbf{s}$ and $\mathbf{T}$. Bilinear interpolation is performed to approximate $\mathbf{T}$ for receive elements whose locations do not coincide with the simulation grid. Solving Equation 5.3 for all transmit locations, we get $g_{sos}(\mathbf{s})$. In addition, the propagation path l_{sr} from a transmit element s to the receive element r can be calculated by ray tracing along the TOF map gradient, $\nabla\mathbf{T}$, *i.e.* from r to s. Once l_{sr} is computed, the simulated attenuation can be computed by integrating the local attenuation along the propagation path:

$$
\int_{l \in l_{sr}} \alpha(l) dl. \tag{5.9}
$$

One can also write Equation 5.9 in a discrete matrix form as:

$$g_{att}(\boldsymbol{\alpha}, \mathbf{s}) = \mathbf{L}(\mathbf{s})\boldsymbol{\alpha}, \tag{5.10}$$

where $\mathbf{L}(\mathbf{s})$ is the $N \times M$ path length matrix whose i^{th} row corresponds to the path length distribution in all image pixels for the i^{th} transmit-receive element pair. Note, that the path length matrix $\mathbf{L}$ also on the vectorized slowness $\mathbf{s}$ depends.

In addition, Equation 5.8 allows us to introduce noise in TOF and attenuation measurements through the covariance matrices $\mathbf{C_{D,sos}}$ and $\mathbf{C_{D,att}}$ [70]. Similarly, the slowness and attenuation coefficient covariance can be set through the matrices $\mathbf{C_{M,att}}$ and $\mathbf{C_{M,att}}$. Initial guesses can be set through the terms $\mathbf{s_0}$ and $\boldsymbol{\alpha}_\mathbf{0}$. *A priori* geometric object features are included by weighting solutions with correlated values in the objects pixels. Specifically, suppose ρ_M is the assumed (*a priori*) correlation between two pixels from the same object type, for any given pixels i and j, $C_{M_{ij}} = \rho_M \sigma^2$, if pixels i and j are within the same object type but $C_{M_{ij}} = 0$, if they are not. Note that $C_{M_{ii}} = \sigma^2$ for any pixel i, where the assumed variance of the individual pixels is σ^2.

Assuming that dispersion can be neglected and sound speed does not depend on the attenuation coefficient, we can obtain the slowness $\mathbf{s}$ first from Equation 5.11 and then the attenuation coefficient $\boldsymbol{\alpha}_\mathbf{0}$ from Equation 5.12:

$$\mathbf{s} = \arg\min_{\boldsymbol{\theta}} \left\{ \big(\mathbf{d_{sos}} - g_{sos}(\boldsymbol{\theta})\big)^T \mathbf{C}^{-1}_{\mathbf{D,sos}} \big(\mathbf{d_{sos}} - g_{sos}(\boldsymbol{\theta})\big) + \big(\boldsymbol{\theta} - \mathbf{s_0}\big)^T \mathbf{C}^{-1}_{\mathbf{M,sos}} \big(\boldsymbol{\theta} - \mathbf{s_0}\big) \right\} \tag{5.11}$$

$$\boldsymbol{\alpha} = \arg\min_{\boldsymbol{\theta}} \Big\{ \big(\mathbf{d_{att}}(\mathbf{s}) - g_{att}(\boldsymbol{\theta}, \mathbf{s})\big)^T \mathbf{C}_{\mathbf{D},\mathbf{att}}^{-1} \big(\mathbf{d_{att}}(\mathbf{s}) - g_{att}(\boldsymbol{\theta}, \mathbf{s})\big) + \big(\boldsymbol{\theta} - \boldsymbol{\alpha_0}\big)^T \mathbf{C}_{\mathbf{M},\mathbf{att}}^{-1} \big(\boldsymbol{\theta} - \boldsymbol{\alpha_0}\big) \Big\}. \tag{5.12}$$

Note that the minimizer of Equation 5.12, , is calculated analytically as:

$$\boldsymbol{\alpha} = \boldsymbol{\alpha_0} + \mathbf{C}_{\mathbf{M},\mathbf{att}} \mathbf{L}(\mathbf{s})^T \big(\mathbf{L}(\mathbf{s}) \mathbf{C}_{\mathbf{M},\mathbf{att}} \mathbf{L}(\mathbf{s})^T + \mathbf{C}_{\mathbf{D},\mathbf{att}}\big)^{-1} \big(\mathbf{d_{att}}(\mathbf{s}) - g_{att}(\boldsymbol{\alpha_0}, \mathbf{s})\big). \tag{5.13}$$

However, we found empirically that updating the attenuation coefficient image at every iteration, after the path length matrix $\mathbf{L}$ is computed, results in an image with less artifacts. For this reason, we chose to reconstruct the attenuation coefficient image based on an iterative approach. Specifically, for each iteration, the attenuation coefficient image is updated based on the current path length matrix $\mathbf{L}$ that is concurrently obtained from the TOF map $\mathbf{T}$, and $\mathbf{T}$ is simulated from the current slowness image.

The minimization problem is facilitated by the conjugate gradient method, similar to the approaches described in [8], [64], [70]. To do so, the steepest descent vectors for slowness and attenuation coefficient images, $\boldsymbol{\gamma_s}$ and $\boldsymbol{\gamma_\alpha}$, are first derived as:

$$\begin{aligned} \boldsymbol{\gamma_s} &= \mathbf{C}_{\mathbf{M},\mathbf{sos}} \mathbf{L}(\mathbf{s})^T \big[\mathbf{C}_{\mathbf{D},\mathbf{sos}}^{-1} \big(g_{sos}(\mathbf{s}) - \mathbf{d_{sos}}\big)\big] + \mathbf{s} - \mathbf{s_0} \\ \boldsymbol{\gamma_\alpha} &= \mathbf{C}_{\mathbf{M},\mathbf{att}} \mathbf{L}(\mathbf{s})^T \big[\mathbf{C}_{\mathbf{D},\mathbf{att}}^{-1} \big(g_{att}(\mathbf{s}, \boldsymbol{\alpha}) - \mathbf{d_{att}}(\mathbf{s})\big)\big] + \boldsymbol{\alpha} - \boldsymbol{\alpha_0}. \end{aligned} \tag{5.14}$$

The slowness and attenuation coefficient images at the $(n+1)^{th}$, $\mathbf{s}^{n+1}$ and $\boldsymbol{\alpha}^{n+1}$, are then given by:

$$\begin{aligned} \mathbf{s}^{n+1} &= \mathbf{s}^{n} - p_{\mathbf{s},n+1}\mathbf{v}_{\mathbf{s}}^{n+1} \quad \text{and} \quad \boldsymbol{\alpha}^{n+1} = \boldsymbol{\alpha}^{n} - p_{\boldsymbol{\alpha},n+1}\mathbf{v}_{\boldsymbol{\alpha}}^{n+1} \\ \text{where} \quad \mathbf{v}_{\mathbf{s}}^{n+1} &= \gamma_{\mathbf{s}}^{n} - \beta_{\mathbf{s},n+1}\mathbf{v}_{\mathbf{s}}^{n} \quad \text{and} \quad \mathbf{v}_{\boldsymbol{\alpha}}^{n+1} = \gamma_{\boldsymbol{\alpha}}^{n} - \beta_{\boldsymbol{\alpha},n+1}\mathbf{v}_{\boldsymbol{\alpha}}^{n}. \end{aligned} \tag{5.15}$$

Parameters $\beta_{\mathbf{s}}$ and $\beta_{\boldsymbol{\alpha}}$, are chosen according to Polak and Ribière's formula such that the vectors in the sets $\left\{\mathbf{v}_{\mathbf{s}}^{i}\right\}_{i=1}^{n+1}$ and $\left\{\mathbf{v}_{\alpha}^{i}\right\}_{i=1}^{n+1}$ form conjugate bases for the Krylov subspaces [106]:

$$\beta_{\mathbf{s},n+1} = \frac{< \mathbf{C}_{\mathbf{M,sos}}^{-1}(\gamma_{\mathbf{s}}^{n+1} - \gamma_{\mathbf{s}}^{n}), \gamma_{\mathbf{s}}^{n+1} >}{< \mathbf{C}_{\mathbf{M,sos}}^{-1}\gamma_{\mathbf{s}}^{n}, \gamma_{\mathbf{s}}^{n} >} \quad \text{and} \quad \beta_{\boldsymbol{\alpha},n+1} = \frac{< \mathbf{C}_{\mathbf{M,att}}^{-1}(\gamma_{\boldsymbol{\alpha}}^{n+1} - \gamma_{\boldsymbol{\alpha}}^{n}), \gamma^{n+1} >}{< \mathbf{C}_{\mathbf{att}}^{-1}\gamma_{\boldsymbol{\alpha}}^{n}, \gamma_{\boldsymbol{\alpha}}^{n} >}. \tag{5.16}$$

The optimal step length can be obtained analytically by the following equations:

$$\begin{aligned} p_{\mathbf{s},n+1} &= \frac{(\mathbf{v}_{\mathbf{s}}^{n+1})^{T}\mathbf{C}_{\mathbf{M,sos}}^{-1}\gamma_{\mathbf{s}}^{n+1}}{(\mathbf{L}^{n}\mathbf{v}_{\mathbf{s}}^{n+1})^{T}\mathbf{C}_{\mathbf{D,sos}}^{-1}(\mathbf{L}^{n}\mathbf{v}_{\mathbf{s}}^{n+1}) + (\mathbf{v}_{\mathbf{s}}^{n+1})^{T}\mathbf{C}_{\mathbf{M,sos}}^{-1}\mathbf{v}_{\mathbf{s}}^{n+1}} \\ p_{\boldsymbol{\alpha},n+1} &= \frac{(\mathbf{v}_{\boldsymbol{\alpha}}^{n+1})^{T}\mathbf{C}_{\mathbf{M,att}}^{-1}\gamma_{\boldsymbol{\alpha}}^{n+1}}{(\mathbf{L}^{n}\mathbf{v}_{\boldsymbol{\alpha}}^{n+1})^{T}\mathbf{C}_{\mathbf{D,att}}^{-1}(\mathbf{L}^{n}\mathbf{v}_{\boldsymbol{\alpha}}^{n+1}) + (\mathbf{v}_{\boldsymbol{\alpha}}^{n+1})^{T}\mathbf{C}_{\mathbf{M,att}}^{-1}\mathbf{v}_{\boldsymbol{\alpha}}^{n+1}}. \end{aligned} \tag{5.17}$$

The reconstruction algorithm for sound speed and attenuation coefficient images are summarized in Table 5.1. Note that this algorithm also can be used to reconstruct sound speed images separately.

5.2.5 Simulation Studies

Attenuation coefficient image reconstructions using both uncorrected and corrected attenuation maps were performed on 3 different numerical 3D phantoms. Both ring and linear arrays with finite-aperture line sources, shown in Figures 5.2(a) and (b)-(d), were utilized for reconstructions. The phantoms, where each is imaged by a pair of linear arrays, are illustrated in Figures 5.2(b)-(d). The transducer and imaging

Table 5.1: Algorithmic description of the proposed reconstruction algorithm.

```
Inputs: $\mathbf{d_{sos}}$, $\mathbf{d_{att}}$, $k = 0$, $\beta_{\mathbf{s},0} = \beta_{\boldsymbol{\alpha},0} = 0$, $\mathbf{v}_{\mathbf{s}}^0 = \mathbf{v}_{\boldsymbol{\alpha}}^0 = 0$
while ($k < K$)
    Solve Equation 5.3 to get TOF map $\mathbf{T}^k$ and $g_{sos}(\mathbf{s}^k)$
    Obtain $\mathbf{L}^k$ from $\nabla\mathbf{T}^k$
    Obtain $\gamma_{\mathbf{s}}^k$ and $\gamma_{\boldsymbol{\alpha}}^k$ from Equation 5.14
    if ($k > 0$) obtain $\beta_{\mathbf{s},k+1}$ and $\beta_{\boldsymbol{\alpha},k+1}$ from Equation 5.16
    if ($k > 0$) obtain $\mathbf{v}_{\mathbf{s},k+1}$ and $\mathbf{v}_{\boldsymbol{\alpha},k+1}$ from Equation 5.15
    Obtain $p_{\mathbf{s},k+1}$ and $p_{\boldsymbol{\alpha},k+1}$ from Equation 5.17
    Sound speed and attenuation coefficient images
    Obtain $\mathbf{s}^{k+1}$ and $\boldsymbol{\alpha}^{k+1}$ from Equation 5.15
    Enforce 0 to negative-valued pixels
    $k \leftarrow k + 1$
end
Return $(\mathbf{s}^K)^{-1}$ and $\boldsymbol{\alpha}^K$
```

configurations are given in Table 5.2. In this paper, the k-Wave Toolbox [109] was utilized for 3D full-wave propagation modeling, *i.e.*, for generating input datasets and non-attenuating datasets described shortly. Input wave traces were generated with known sound speed, attenuation, and density distributions. Time-of-flight was extracted for each trace using the Akaike information criterion (AIC) as described in [75] and then used to reconstruct the 2D sound speed image. In addition, input wave traces were used to obtain the attenuation map (vectorized as $\mathbf{d_{att}}$) that was later used as the input for reconstruction of the 2D attenuation images. If attenuation correction was applied, an additional *non-attenuating* (zero attenuation coefficient) dataset was also simulated given *a priori* volumes with sound speed and density. The uncorrected and corrected attenuation datasets were calculated based on Equations 5.4 and 5.6, respectively. Note that the wave propagation modeling done here assumed the correct, heterogeneous density distribution, but even without this knowledge, only modest reflection and scattering should be present due to the low-contrast density.

Two-dimensional sound speed and attenuation reconstructions utilized bent-ray modeling and assumed point-like transducer elements. The 2D TOF map $\mathbf{T}$ and the

Table 5.2: Simulation parameters for 3D full-wave propagation modeling. Note that for imaging the numerical breast-mimicking phantom, the field-of-view size is slightly expanded in the elevational direction to fully capture all spherical masses.

Parameter		Value
Array size		Ring array: 4.8 cm diameter Linear array: 4.87 cm axial separation, 3.88 cm aperture size
Array element height		6 cm
Array center frequency		2 MHz
Source pulse		2 MHz sinusoidal waveform tapered by a Gaussian envelope centered at 6.4 µs and with a standard deviation of 0.5 µs
Total number of array elements		Ring array: 80 Linear array: 40 each
Field-of-view size	Spherical-object	Ring array: 5 cm×5 cm×1.35 cm (240×240×65 voxels) Linear array: 5 cm×4 cm×1.35 cm (240×192×65 voxels)
	Breast	Linear array: 5 cm×4 cm×1.77 cm (240×192×85 voxels)

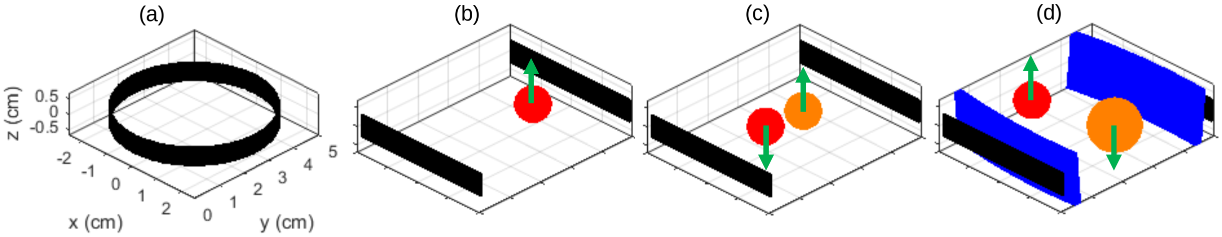

Figure 5.2: The geometries of ring (a) and linear (b)-(d) transducer arrays, and three different 3D numerical objects (b)-(c), shown in isometric view. For compactness, only axis labels for ring array and only phantoms imaged by linear arrays are shown. Objects shown in (b), (c), and (d) are single sphere, two spheres, and breast-mimicking phantom. The arrows on spherical objects indicate their directions away from the image plane. The acoustic properties of all regions within the field-of-view for single sphere, two spheres, and breast-mimicking phantom imaging cases are given in Tables 5.4, 5.5, and 5.6, respectively.

corresponding ray geometries encoded in the path length matrix $\mathbf{L}$ can be accurately obtained using Multistencils Fast Marching Methods (MSFM) [72]. The reconstruction parameters are given in Table 5.3. In addition, after the attenuation coefficient image was updated at each iteration, zero was assigned to all image pixels whose values were negative to enforce the non-negativity constraint on the attenuation coefficient.

Note that even though the correlation coefficient of the background region can be positive since all pixels within the background region should have very similar acoustic properties, we chose to assign zero because of two reasons: First, we initialized both sound speed and attenuation coefficient image guesses with the actual sound speed and attenuation coefficient of background, thus pixels in the background region should be updated very slightly, resulting in background homogeneity and little correlation with the coefficient value. In practice, with known locations of transducer elements, the background sound speed estimate can be obtained through signal travel times for

Table 5.3: Simulation geometry for 2D image reconstruction. Note that the field-of-view size was automatically determined during the reconstruction based on the array geometry in Table 5.2, thus resulting in different field-of-view sizes for ring and linear arrays.

Parameter		Value
Total number of array elements		Ring array: 80 Linear array: 40 each
Field-of-view size		Ring array: 302×302 grids Linear array: 306×249 grids
Number of iterations (K in Table 5.1)		5
$\mathbf{C_{M,sos}}$	Correlation coefficient (ρ_M)	0.005 (except 0 for the background)
	Standard deviation (σ)	0.048 µs/mm
$\mathbf{C_{M,att}}$	Correlation coefficient (ρ_M)	0.005 (except 0 for the background)
	Standard deviation (σ)	11 dB/cm
$\mathbf{C_{D,sos}}$	Correlation coefficient (ρ_M)	0
	Standard deviation (σ)	0.05 µs
$\mathbf{C_{D,att}}$	Correlation coefficient (ρ_M)	0
	Standard deviation (σ)	0.1 dB

all transmit-receive element pairs, and the estimate of the background attenuation can be obtained through signal amplitude decreases for all transmit-receive element pairs. Second, the steepest vectors in Equation 5.14 are only optimal for very small update steps and performing updates with steps that are too big could sometimes result in divergence rather than convergence [70]. Setting the correlation coefficient to zero makes $\mathbf{C_{M,sos}}$ and $\mathbf{C_{M,att}}$ more like a scaled identity matrix. This in turn makes the steepest descent vectors in Equation 5.14 more like gradient vectors. We also found empirically that this results in faster convergence. Although it is not the scope of this paper, using a preconditioning matrix in the optimization problem might also result in faster convergence [70].

Four studies were performed to reconstruct 2D attenuation coefficient images, one each for the three single slice cases of: a single sphere, two spheres, and the numerical breast-mimicking phantom, as well as one single sphere multi slice case. Their details are provided as follows:

5.2.5.1 Single slice reconstructions of a single sphere

The 4.2-mm radius spherical object of Figure 5.2(b) is placed at $(x, y, z) = (4.2, 33.4, 2.4)$ mm, *i.e.*, it is also placed out of the axial-lateral image plane 1/2 radius (2.4 mm) elevationally. The actual acoustic properties (sound speed, density, and attenuation) are given in Table 5.4. Note that there are two sets of actual sound speed and density assigned to the object, as we would like to investigate the effects of sound speed contrast (the difference between object and background) on the efficiency of attenuation correction.

Beam patterns (whose value at a given location is equal to the maximum pressure amplitude at that location over the propagation time) and attenuation maps are presented prior to the reconstruction results to illustrate the beam distortion due to sound speed heterogeneity and image object geometries, as well as to illustrate how the effects on estimated attenuation can be corrected. The beam propagation patterns transmitted from a single finite-aperture line source element are shown for positive and negative sound speed relative to background and 2 different views (axial-lateral and axial-elevational). The beam was transmitted by element 16 (the element index starts from $x = 2$ cm) on the linear array that was located at $y = 5$ cm and passed through the center of the sphere. For attenuation maps, note that only maps of wave traces in the positive direction are presented for the sake of brevity, *i.e.* transmitted from $y = 0$ cm and received by $y = 5$ cm. The indices of transmit and receive arrays start at $x = -2$ cm and $x = 2$ cm, respectively.

Table 5.4: Acoustic properties (sound speed, density, and attenuation) of all regions shown in Figure 5.2(b). Two sound speed and density sets were used for generating positive- and negative-contrast sound speed datasets.

Region	(Sound Speed, Density)	Attenuation Coefficient
Red	(1460 m/s, 900 kg/m^3) or (1570 m/s, 1200 kg/m^3)	3.5 dB/cm/MHz
Background	(1515 m/s, 1000 kg/m^3)	0 dB/cm/MHz

All reconstructed images along with their corresponding cross-sectional plots are presented. The bias for each reconstructed slice was also computed by subtracting the mean reconstructed object attenuation coefficient in that slice from the actual object attenuation coefficient. The corresponding root-mean-square deviation from the mean (RMSD) of the pixel attenuation coefficient was also computed after the bias was subtracted from all pixels. The decrease of absolute bias and RMSD, as a result of applying attenuation correction, was calculated for all object regions and is presented in Section 5.3.

In addition, radial plots of the actual and the reconstructed attenuation coefficient images were generated and compared. A radial plot shows the average attenuation coefficient over a given radial profile averaged across all radial angles. The radial profile of a given radius r is defined by the mean reconstructed image values along the perimeter of a circle with said radius r, and whose center coincides with the center of the spherical object. The attenuation coefficients along the given perimeter were uniformly sampled with 0.2 grid spacing steps (41.7 µm), and bilinear interpolation was performed where necessary.

5.2.5.2 Single slice reconstructions of two spheres

Figure 5.2(c) shows two 4.2-mm radius spherical objects imaged by linear arrays. The red and orange spherical objects are placed at (x, y, z) = (-3.2, 21.8. -2.4) mm and (3.2, 28.2. 2.4) mm, respectively. Note that both spherical objects are placed at 1/2 radius (2.4 mm) away from the axial-lateral image plane but on the opposite sides of the image plane. Both spheres have different attenuation coefficients yet the same sound speed. Their actual acoustic properties as well as those of background are given in Table 5.5. For the same reason as mentioned earlier, there are two sets of actual sound speed and density assigned to the object. All reconstructed images along with their corresponding projection plots are presented. The decrease of absolute bias and RMSD, as a result of the attenuation correction, was calculated for all object regions and is presented in Section 5.3.

Table 5.5: Acoustic properties (sound speed, density, and attenuation) of all regions shown in Figure 5.2(c). Two sound speed and density sets were used for generating positive- and negative-contrast sound speed datasets.

Region	(Sound Speed, Density)	Attenuation Coefficient
Red	(1460 m/s, 900 kg/m^3) or (1570 m/s, 1200 kg/m^3)	3.5 dB/cm/MHz
Orange	(1460 m/s, 900 kg/m^3) or (1570 m/s, 1200 kg/m^3)	1.5 dB/cm/MHz
Background	(1515 m/s, 1000 kg/m^3)	0 dB/cm/MHz

5.2.5.3 Single slice reconstructions in the numerical breast-mimicking phantom

Figure 5.2(d) shows the 3D numerical breast-mimicking phantom imaged by linear arrays. The breast phantom consists of a 2.1-mm think skin enclosing the 4.2-mm radius spherical cancer and a 6.3-mm radius spherical cyst. Masses are located away from the image plane by half their radius, such that the axial-lateral image plane lies between the two masses and is 2.4 mm away from the cancer ($z = 2.4$ mm) and 3.15 mm away from the cyst ($z = -3.15$ mm). The curved skin layer is defined by all voxels in $S_1 \cap S_2$, where sets S_1 and S_2 are defined as:

$$\begin{aligned} S_1 &= \left\{(x,y,z) \in \mathbb{R}^3 : \left(\frac{x-25}{22.9}\right)^2 + \left(\frac{y-28.3}{64.6}\right)^2 + \left(\frac{z-53.3}{85.4}\right)^2 \leq 1\right\} \\ S_2 &= \left\{(x,y,z) \in \mathbb{R}^3 : \left(\frac{x-25}{20.8}\right)^2 + \left(\frac{y-28.3}{62.5}\right)^2 + \left(\frac{z-53.3}{83.3}\right)^2 \leq 1\right\}. \end{aligned} \tag{5.18}$$

All actual acoustic properties are given in Table 5.6. All reconstructed images along with their corresponding cross-section plots are presented. The decreas of absolute bias and RMSD, as a result of the attenuation correction, was calculated for all object regions and is presented in Section 5.3.

Table 5.6: Acoustic properties (sound speed, density, and attenuation) of all tissues in the numerical breast-mimicking phantom shown in Figure 5.2(d). Note that the exponent term of 1.5 will be used as the power law exponent in Equation 5.2.

Region	(Sound Speed, Density)	Attenuation Coefficient
Red (cancer)	(1570 m/s, 1200 kg/m^3)	2.8 dB/cm/MHz$^{1.5}$
Orange (cyst)	(1540 m/s, 1200 kg/m^3)	0.5 dB/cm/MHz$^{1.5}$
Blue (skin)	(1600 m/s, 1200 kg/m^3)	2.5 dB/cm/MHz$^{1.5}$
Background	(1515 m/s, 1200 kg/m^3)	0.75 dB/cm/MHz$^{1.5}$

5.2.5.4 Multi slice reconstructions of a single sphere: performance evaluation

The single sphere shown in Figure 5.2(b) was imaged again by both linear and ring arrays, but the transducer(s) were moved elevationally with four increments of one (0.833 mm) grid spacing to acquire multiple 2D image slices comprising the 3D attenuation coefficient image of the top half of the sphere. In addition, the effects of imperfect *a priori* sound speed distribution used for the attenuation correction on the reconstruction accuracy were evaluated and compared to those obtained via attenuation correction using the actual (accurate) *a priori* sound speed distribution. The sound speed bias b was computed for each slice by subtracting the mean reconstructed object sound speed in that slice from the actual object sound speed. Then this bias was used to create two imperfect *a priori* sound speeds, specifically a 1x biased (b) as well as 2x biased ($2b$) sound speed. Generally, object sound speed reconstruction biases towards the background sound speed, *i.e.* it underestimates the contrast. See Table 5.1 for more details about sound speed image reconstruction.

5.3 Results

5.3.1 Single Slice Reconstructions of a Single Sphere

Figures 5.3(a)-(d) show the beam patterns transmitted from a single finite-aperture line source element and propagating laterally but not elevationally through the center of the spherical object. The beam patterns were investigated for positive and negative object sound speed contrast and refraction effects are visible. Figure 5.3(a) (positive contrast) shows signals deflecting away from the spheres surface, and the opposite occurs in Figure 5.3(b) (negative contrast). These effects result in signal distortion at the receive array elements. Effects of out-of-plane refraction, are shown in Figures 5.3(c) and (d).

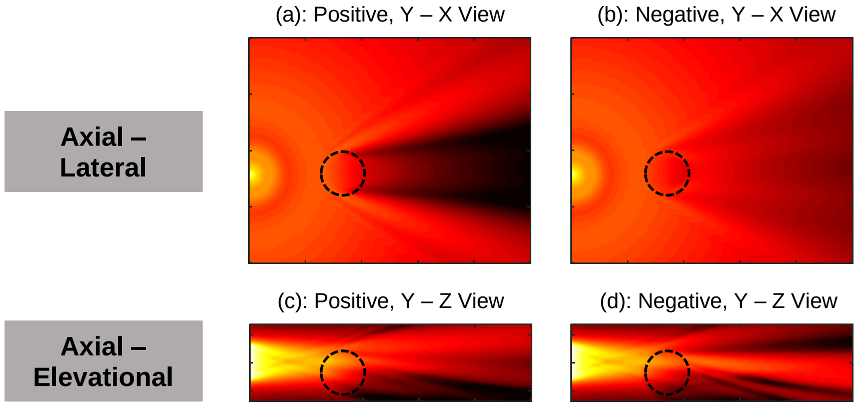

Figure 5.3: Beam patterns for positive and negative contrast of sphere in the axial-lateral (a), (b) and axial-elevational (c), (d) planes, illuminating the sphere shown in Figure 5.2(b). The sound source is a single element at approximately $(x, z) = (0.4, 0)$ cm. Images are shown on a [-40, 0] dB scale.

Figure 5.4 shows that for the case of imaging a sphere of positive sound speed contrast, its penumbra displays higher attenuation in the uncorrected attenuation map (Figure 5.4(a)) than in the corrected attenuation map (Figure 5.4(c)). For negative sound speed contrast, the beam tends to deflect towards the center of the sphere as shown in Figure 5.3(b). This contributes to the signal loss around the object border, Figure 5.4(d). The calculated boundary attenuation map (Figures 5.4(b) and (e)) is subtracted from the full effects map (Figures 5.4(a) and (d)) to produce the corrected attenuation maps (Figures 5.4(c) and (f)).

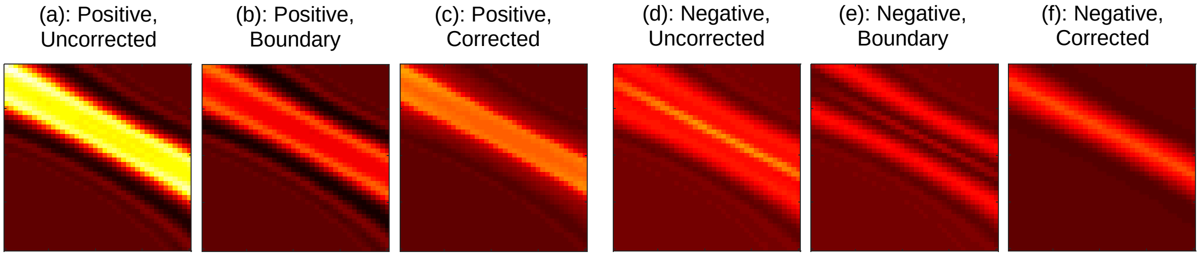

Figure 5.4: Attenuation maps of all transmit-receive element pairs obtained from simulated imaging a single sphere arranged as shown in Figure 5.2(b), with different sound speed contrasts. Attenuation of the i^{th} transmit and j^{th} receive pair can be obtained from the value at the j^{th} row and i^{th} column of the map. (a), (d) are attenuation maps affected by all acoustic effects. (b), (e) Attenuation maps affected by refraction and scattering around the object boundary. (c), (f) Attenuation maps with boundary effects removed. All images are windowed to [-2, 13] dB.

Corresponding 2D reconstruction slices for opposed linear arrays are shown in Figure 5.5. The effects of sound speed contrast seen around the object border are partially corrected in Figures 5.5(b) and (c) in the positive and negative contrast cases, respectively. For the sake of compactness, note that the corresponding 2D reconstruction slices for the ring array are presented here only as thumbnails, but their improved bias and RMSD are shown in Table 5.7 with values normalized by the center frequency, given in Table 5.2.

The horizontal cross-sections and radial plots of all reconstruction scenarios, shown in the top and bottom rows of Figures 5.6(a)-(d) and 5.6 (e)-(h), illustrate the spatial character of the attenuation correction. As can be seen from Figure 5.6, horizontal cross-sections and radial plots show less object edge artifacts and overall bias if attenuation correction is applied to obtain the bulk tissue attenuation coefficient. In

Table 5.7: Numbers outside parentheses: Calculated bias and RMSD (dB/cm/MHz) within a single sphere, obtained from 2D reconstructions with corrected attenuation map for positive and negative sound speed contrast of objects with the background. Numbers insides parentheses: Corresponding percent decreases of the absolute bias and RMSD with respect to uncorrected reconstructions.

Linear Transducer				Ring Transducer			
Positive		Negative					
Bias	RMSD	Bias	RMSD	Bias	RMSD	Bias	RMSD
-0.52 (75)	0.76 (31)	-0.95 (41)	0.27 (29)	-0.06 (98)	0.96 (31)	-0.44 (57)	0.19 (49)

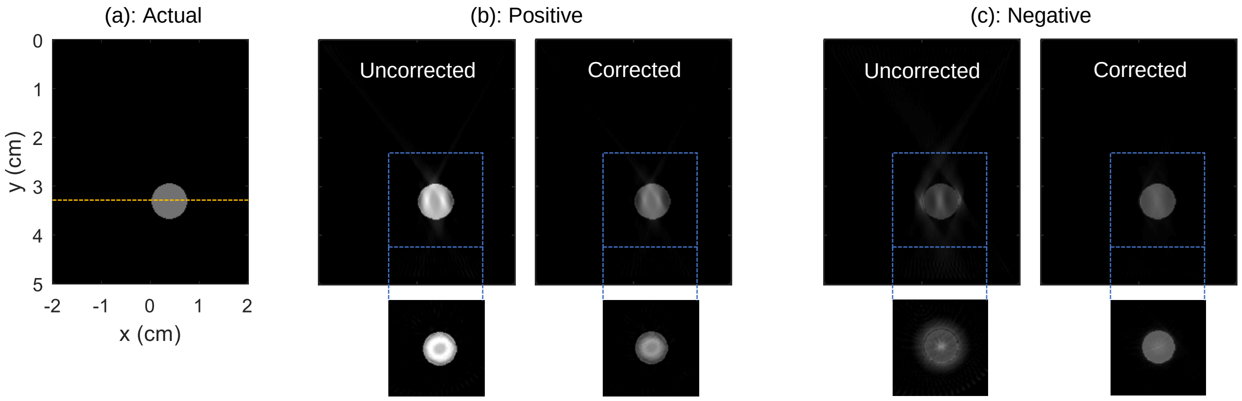

Figure 5.5: Attenuation coefficient reconstruction in 2D, of a single sphere (Figure 5.2(b)), displayed on a [0, 8] dB/MHz/cm dynamic range. Full-size images (top row) were reconstructed with opposed linear arrays and their corresponding thumbnails (bottom row) were reconstructed with ring array. The actual attenuation coefficient distribution is shown in (a) and Table 5.4. Reconstructed images in (b) and (c) correspond to the sphere with sound speed of 1570 and 1460 m/s, respectively. The yellow dashed line in (a) represents the location of cross-sections shown in Figure 5.5.

addition, for radial plots, note the more frequent overshoots for data obtained using uncorrected attenuation maps.

5.3.2 Single Slice Reconstructions of Two Spheres

Figure 5.7 shows the reconstructed attenuation coefficients of two spherical objects, when imaged using two linear arrays (Figure 5.2(c)). The corresponding ring array results are shown as thumbnails. This challenging imaging situation with multiple objects, broken symmetry, and uncorrected attenuation maps leads to even more noticeable errors. The observed distortions can be explained with reasoning similar to the previous cases, *i.e.* refracted waves due to positive and negative sound speed contrast. Using attenuation map correction, the reconstruction results show significant accuracy improvement and artifact reduction in all cases of sound speed contrast and array geometries. Such improvements can also be seen in diagonal projections shown

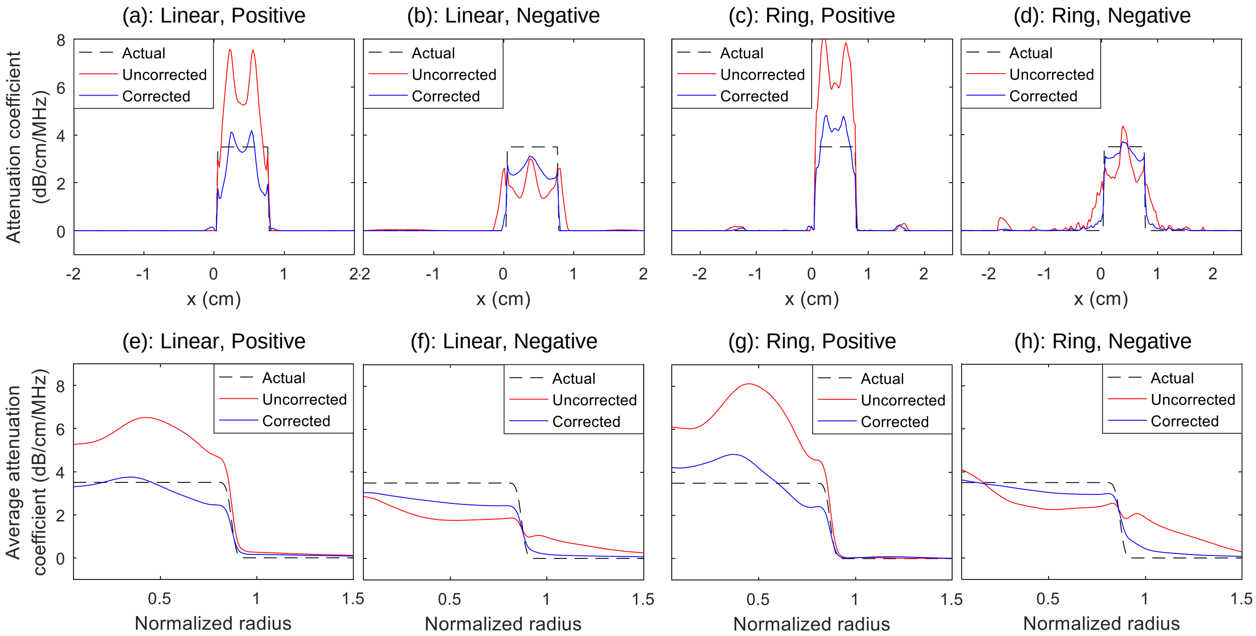

Figure 5.6: Horizontal cross-sections of 2D reconstructed attenuation coefficient images of spherical object shown in Figure 5.5. (e)-(h) Radial plots of 2D reconstructed attenuation coefficient images of spherical object with respect to normalized radius (the ratio of perimeter radius to the spherical radius). Horizontal cross-sections and radial plots are obtained from reconstructions with various scenarios indicated in the figure legends and the group titles, and are compared to those of the actual 2D attenuation coefficient image.

in Figure 5.8. Calculated bias and RMSD values are given in Table 5.8. Note that the negative sound speed contrast, low attenuation coefficient (orange) sphere, using the uncorrected attenuation map, results in zero-valued pixels almost everywhere in the spherical region. This occurs because those pixels are forced by the non-negativity constraint to have zero values (see Line 10 of Table 5.1), thus leading to larger homogeneity and therefore lower RMSDs than those obtained from the corresponding reconstructions using the corrected attenuation map.

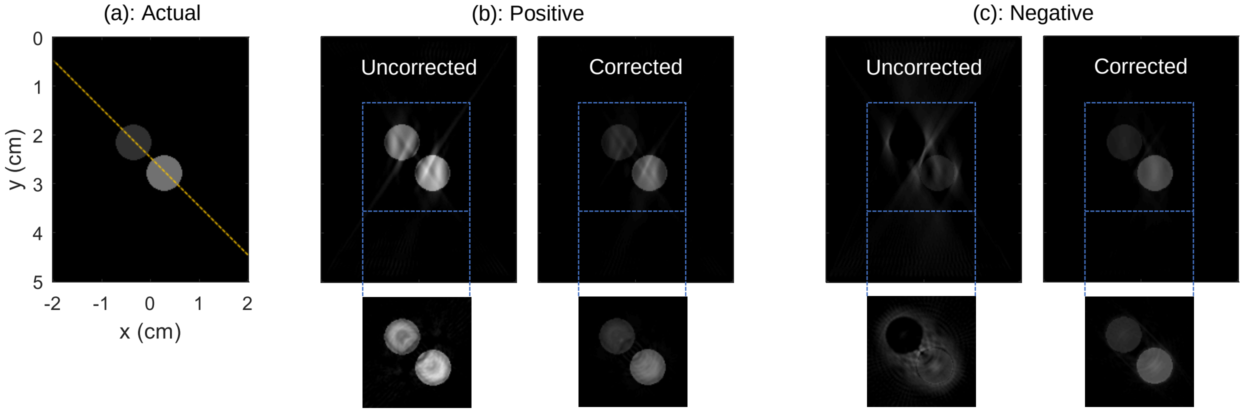

Figure 5.7: Attenuation coefficient reconstruction in 2D, of two spheres (Figure 5.2(c)), displayed on a [0, 8] dB/MHz/cm dynamic range. Full-size images (top row) were reconstructed with opposed linear arrays. Their corresponding thumbnails (bottom row) were reconstructed using the ring array geometry. Actual attenuation coefficients are shown in (a) and Table 5.5. Reconstructed images in (b) and (c) correspond to the spheres with sound speeds of 1570 and 1460 m/s, respectively. The diagonal dashed line in (a) represents the location of projections shown in Figure 5.8.

5.3.3 Single Slice Reconstructions in a Numerical Breast-Mimicking Phantom

Figure 5.9 shows a reconstructed 2D center slice, *i.e.* $z = 0$, of the attenuation coefficients in the numerical breast-mimicking phantom using opposed linear

Table 5.8: Numbers outside parentheses: Calculated bias and RMSD (dB/cm/MHz) within individual spheres, obtained from 2D reconstructions with corrected attenuation map for positive and negative sound speed contrast objects. Numbers insides parentheses: Corresponding percent decrease of absolute bias and RMSD with respect to uncorrected reconstructions. Note: Refer to Figure 5.2(c) for color coding.

Region	Linear Transducer				Ring Transducer			
	Positive		Negative		Positive		Negative	
	Bias	RMSD	Bias	RMSD	Bias	RMSD	Bias	RMSD
Red	-0.75 (30)	0.69 (44)	-1.14 (54)	0.25 (34)	-0.55 (62)	0.51 (53)	-0.89 (54)	0.19 (46)
Orange	-0.32 (83)	0.26 (70)	-0.55 (63)	0.10 (-150)	-0.11 (95)	0.24 (73)	-0.22 (85)	0.09 (0)

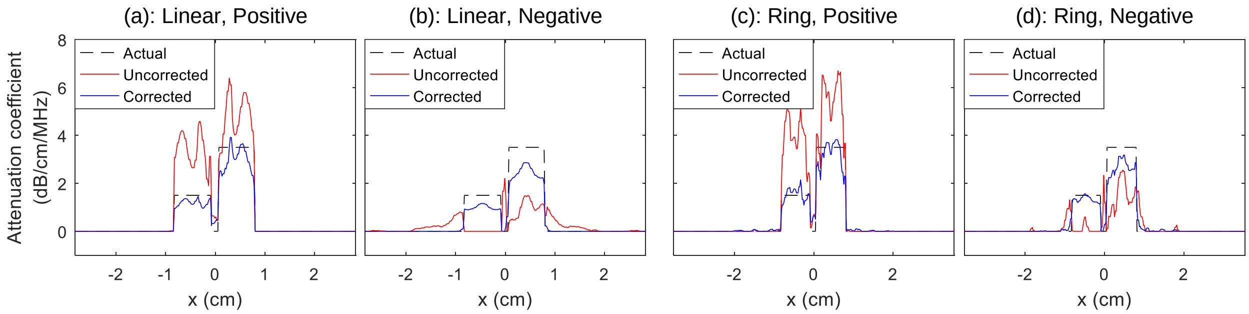

Figure 5.8: (a)-(d) Diagonal projections of 2D reconstructed attenuation coefficient images of spherical objects shown in Figure 5.7. They were obtained from reconstructions with various scenarios indicated in the figure legends and the group titles, and are compared to the actual 2D attenuation coefficient distribution.

arrays, under positive and negative sound speed contrast and attenuation map input (corrected and uncorrected). The values of calculated bias and RMSD are given in Table 5.9. Not surprising, using corrected attenuation maps, one improves the reconstruction accuracy and reduces artifacts, for the same reasons presented in Sections 5.3.1 and 5.3.2 and [25].

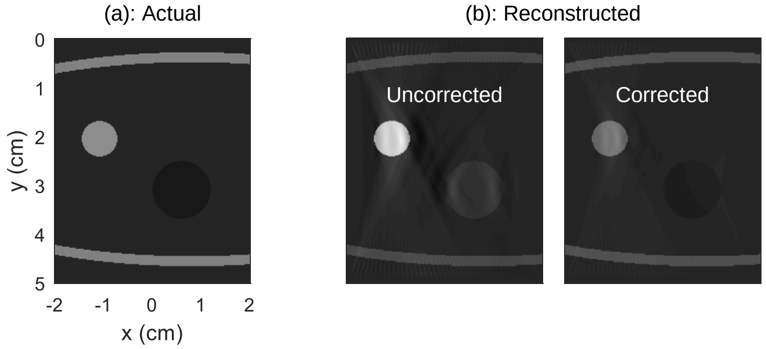

Figure 5.9: Attenuation coefficient reconstruction in 2D using a numerical breast-mimicking phantom (Figure 5.2(d)), imaged with opposed linear arrays. Images are shown for a dynamic range of [0, 5] dB/cm/MHz$^{1.5}$. The actual attenuation coefficient distribution is shown in (a) and Table 5.6.

Table 5.9: Numbers outside parentheses: Calculated bias and RMSD (dB/cm/MHz$^{1.5}$) within three tissue types, obtained from 2D reconstructions with corrected attenuation maps for positive and negative sound speed contrast objects relative to background. Numbers insides parentheses: Corresponding percent decreases of the absolute bias and RMSD with respect to uncorrected reconstructions. Note: Refer to Figure 5.2(d) for color coding.

Region	Bias	RMSD
Red (Cancer)	-0.58 (51)	0.19 (47)
Orange (Cyst)	0.13 (76)	0.02 (80)
Orange (Cyst)	-0.28 (81)	0.02 (80)

5.3.4 Multi Slice Reconstructions of a Single Sphere: Performance Evaluation

Figure 5.10 shows the calculated attenuation coefficients of a single sphere, obtained from linear and ring array 2D reconstructions at 5 elevational slice positions. Object sound speed was given *a priori*. Sound speed results and biases are shown in Table 5.10.

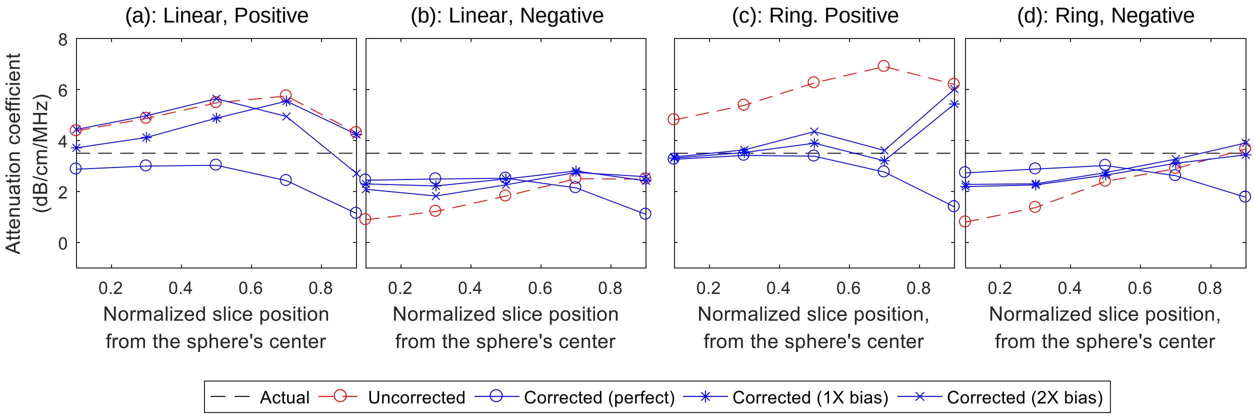

Figure 5.10: Calculated attenuation coefficients of a single sphere as a function of normalized slice position (*i.e.* absolute elevational coordinate divided by the sphere radius) obtained under 4 combined conditions of transducer type and sound speed contrast. The types of input attenuation maps and *a priori* sound speed are indicated in the legends. For comparison, the actual attenuation coefficient is shown as a black dashed line.

Table 5.10: Calculated sound speed (m/s) of a single sphere, obtained from linear and ring array 2D reconstructions at 5 elevational slices. The absolute slice position is in units of the sphere radius. Positive and negative refer to the sound speed contrast with respect to the background sound speed. Sound speed bias (m/s) is given in parentheses.

Normalized Slice Position	Linear Transducer		Ring Transducer	
	Positive	Negative	Positive	Negative
0.1	1541 (-29)	1467 (7)	1568 (-2)	1468 (8)
0.3	1539 (-31)	1475 (15)	1567 (-3)	1475 (15)
0.5	1534 (-36)	1479 (19)	1563 (-7)	1480 (20)
0.7	1522 (-48)	1482 (22)	1546 (-24)	1472 (12)
0.9	1517 (-53)	1485 (25)	1533 (-37)	1480 (20)

The corrected attenuation coefficient, as obtained by either perfect (no bias, solid line, 'o' of Figure 5.10) or by realistic (1x) bias (solid line, '*') *a priori* sound speed distribution, is more accurate than that obtained from the uncorrected attenuation data (dashed line, 'o'). However, this is not generally the case.

It is true for both contrasts and all slice reconstruction for normalized elevational displacements less than 0.7 (Figures 5.10(a) and (c)). For objects of negative contrast, increasing *a priori* sound speed bias is as detrimental to the calculated attenuation coefficient profile as the loss of proper attenuation correction. However, the same trend does not apply to positive-contrast reconstructions using linear arrays and an attenuation map corrected by *a priori* sound speed with 2x bias (solid line, 1'x'). This occurs because adding large bias flips the objects sound speed contrast from positive to negative, and thus leading to the wrong *a priori* assumption. Note that bias is always towards the background speed. Therefore, 1x bias will still result in the same contrast type, but 2x bias will flip for example from positive to negative contrast.

Note that for normalized slice positions greater than 0.5, there might be circumstances where applying attenuation correction yields a lower than actual attenuation coefficient. This could be attributed to following two reasons.

First, when the object is imaged at an oblique angle, it is important to note that the transmitted beam will have an elevational beam profile that interacts asymmetrically with the object boundary. Appropriate modelling requires the use of a finite-aperture line source, which we did not do here, as we used point sources. This effect becomes more dominant when the incidence angle increases, even when using corrected attenuation maps.

Second, when the sphere is imaged farther from its center, the sphere's cross-section becomes too small for the bent-ray reconstruction algorithm to handle. This limitation is caused by the width of the first Fresnel zone in the bent-ray scheme that dictates the image resolution limit [73]. Specifically, features smaller than the width of the first Fresnel zone cannot be accurately reconstructed by bent-ray algorithms. This limitation is further demonstrated in Table 5.10 where the sound speed bias is observed to be more fluctuating (ring array and negative-contrast sphere) or increasing (for all other cases) with increasing slice position off center.

From the analysis above, it is suggested that the attenuation correction performance is optimum when the elevational incidence angle between beam and the normal to the object surface is 30 degrees or less, which corresponds here to a normalized slice position of 0.5 and less. Moreover, using realistic values as *a priori* object sound speeds (1x bias and less) seems to be sufficient for the attenuation correction approach as presented here.

5.4 Conclusions

We proposed a reconstruction algorithm for imaging bulk tissue attenuation coefficients that utilizes bent-ray inversion for fast 2D image reconstructions and 3D full-wave simulation for signal energy correction. The results show improved accuracy thanks to an attenuation correction that only requires 2 sets of 3D simulated full-wave pressure datasets (and only 1 set, if a pressure wave propagation dataset in the assumed homogeneous background medium is simulated beforehand). Although the reconstruction results with attenuation correction might not be as accurate as those from 3D waveform inversion algorithms, they should be more accurate than those from 2D waveform inversion algorithms that lack the ability to account for out-of-plane and other missed detector acoustic effects. The reconstruction time should be much less than 3D and even 2D waveform inversion algorithms as well, which positions our method as a promising tool for clinical use.

If the mass density distribution of the imaged region is known, or can be estimated *a priori*, it can be incorporated into the attenuation correction to better model the acoustic impedance mismatch between adjacent interfaces. Alternatively, one can estimate the density by assuming that it is approximately proportional to the sound speed. Nonetheless, note that both accurate density and sound speed might not be required, as density inhomogeneity affects the wave propagation pattern much less than sound speed changes. It was demonstrated in the Results and Discussion section that the attenuation correction should still be able to provide robust and acceptable results if (a) the error of *a priori* sound speed is modestly biased (1x or less) due to inaccurate sound speed reconstructions and (b) the beam incidence angle is finite but smaller than 30 degrees.

The degree to which the true attenuation coefficient can be recovered depends on the quality of sound speed and impedance imaging.

Future directions include 3D bent-ray image reconstructions to account for out-of-plane wave propagation effects and physical experiments using clinical arrays and a physical breast-mimicking phantom. In addition, our simulation studies currently do not account for the transducer responses (frequency response, spatial response, directivity, etc.) that exist in clinical arrays [74]. In practice, those responses could alter the received signal and negatively affect the reconstructions, thus it is worthwhile to model those responses in future experiments as well.

CHAPTER VI

Acceleration and Data Reduction Methods for Full-Wave Ultrasound Tomography

6.1 Introduction

The ability to image dense breasts non-radiatively and high portability are the striking advantages that has led ultrasound to become the complementary imaging modality for the clinical standard x-ray mammography. Sound speed is one of the useful acoustic properties that not only correlates well with tissue mass density [62], but can also be used to characterize different breast tissue types, therefore allowing for detection of potential malignancies [30].

Recently, waveform inversion approaches have received much attention in the field of sound speed imaging of breast tissues. This is due to the fact that waveform inversion approaches [20]–[22], [36], [126] can take into account complex acoustic phenomena that occur in the tissues, such as diffraction and scattering effects, as opposed to the bent-ray based approaches [17], [63], [89] that can only account for acoustic refraction. Since waveform inversion approaches are usually much more computationally demanding as opposed to bent-ray based approaches, several research groups have been proposing alternative reconstruction methods, such as source encoding [22], [127]–[129] and dataset batching approaches [122], [130], to drastically decrease the computational demand (usually between 1 and 2 orders of magnitude).

Apart from the attempts to accelerate waveform inversion algorithms, other research groups have explored possibilities to reduce the input data size required for image reconstruction, especially for B-mode imaging with 2D transducer arrays. [131], [132] However, to our surprise, data reduction in breast ultrasound sound speed tomography is still left unexplored, and there are only a few attempts in seismology for this [133], [134] based on the compressed sensing technique. To our belief, decreasing the acquired dataset size is crucial as it could potentially help in reducing the required storage, simplifying the designs of acquisition components, and most importantly, streamlining the acquisition and image reconstruction processes towards real-time imaging in the future.

Here, we develop a waveform inversion approach that utilizes both source encoding and compressed sensing techniques, thereby enabling significant reduction in both reconstruction time and dataset size. Compressed sensing [135], though recently discovered, has been proven to be highly successful in various fields, including image reconstructions such as in magnetic resonance imaging (MRI) [136] and seismology with sparse (reduced) datasets [133], [134]. We have applied compressed sensing in this work, through a sparse regularization technique, that could help to mitigate image artifacts arising from the limited dataset size. In addition, the source encoding algorithm was modified according to [130] to allow for multiple encoding vectors to be used at once. This modification results in a slight computational increase but has shown to reduce the cross-talk artifacts due to source encoding and improve the overall image quality, especially when the dataset size is large enough, *i.e.* contains sufficient information.

This work is organized as follows: Section 6.2 reviews the related background and provides details on how the simulation studies were implemented. Simulation findings and their corresponding discussion are given in Section 7.3. Section 7.4 provides a summary of this paper and introduces potential future directions.

6.2 Materials and Methods

6.2.1 Dual-Sided Breast Ultrasound Scanner

Figure 6.1 shows a schematic representation of the simulated breast ultrasound scanner. It consists of two transducer arrays placed on the opposite side of each other, where each array has N transmit-receive elements. Each scanning acquisition is accomplished by transmitting the signal from one element and then receiving the signal by all elements from both the same and the opposite sides. Note that the transducers here cannot be rotated freely, thus the signal acquisition direction is limited.

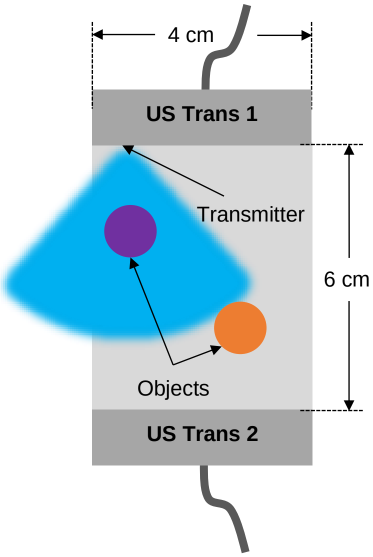

Figure 6.1: Schematic representation of the dual-sided ultrasound scanner simulated in this work. Unlike other tomographic systems, this system is a limited angle tomography system as transmit and receive apertures are available for less than 2π angle.

Given that all transmit elements are used for signal acquisition, we can see that the total number of pressure traces is $(2N)^2$, *i.e.* scales up quadratically with increasing

N. This can be problematic especially when the number of transmit elements N is large, since both more storage and computational power are required. Please refer to Section 6.3.1 for analysis of storage and computational requirements.

6.2.2 Image Reconstruction

6.2.2.1 General least-square optimization problem

Given N as the number of transducer elements, sound speed image reconstructions can, in the simplest form, be regarded as minimizing the L2-norm of the difference between the recorded pressure traces and simulated pressure traces, denoted as E, with respect to the sound speed [70], [104], [105], *i.e.*:

$$E(\mathbf{m}) = \sum_{i=1}^{2N} \|g(\mathbf{m}; \mathbf{s_i}) - \mathbf{d_i}\|_2^2, \tag{6.1}$$

where $\mathbf{d_i}$ and $g(\mathbf{m}; \mathbf{s_i})$ denote the recorded and simulated vectors of pressure traces with respect to the vectorized sound speed $\mathbf{m}$ and source $\mathbf{s_i}$, written as $\begin{bmatrix} p_{i1} & \dots & p_{i(2N)} \end{bmatrix}^T$. p_{ij} denotes the time-domain pressure trace transmitted by the i^{th} element and received by the j^{th} element. The operator g represents the acoustic wave propagation modeling, with a source pulse originated at the location of the transmit element, and initial conditions defined as $p(\mathbf{r}, t) = 0$ and $\partial/\partial t p(\mathbf{r}, t) = 0$, for $p(\mathbf{r}, t)$ being the modeled pressure field. The source pulse was designated to be the same as the actual source pulse excited from an actual physical transducer element.

Typically, minimizing Equation 6.1 can be achieved by iteratively updating $\mathbf{m}$ using a gradient-based optimization method, *i.e.* for iteration j, $\mathbf{m}$ is updated by the following scheme:

$$\mathbf{m}^{j+1} = \mathbf{m}^j - \alpha \nabla E(\mathbf{m}^j) \tag{6.2a}$$

$$\nabla E(\mathbf{m}^j) = \sum_{i=1}^{2N} \mathbf{G}^*\big(g(\mathbf{m}^j;\mathbf{s_i}) - \mathbf{d_i}\big), \tag{6.2b}$$

where $\nabla E(\mathbf{m}^j)$ denotes the gradient evaluated at $\mathbf{m}^j$. $\alpha_j > 0$ denotes the step length that can be determined by either trial and error or line-search techniques. $\mathbf{G}$ represents the linearized operator of g, and $\mathbf{G}^*$ is the corresponding adjoint operator of $\mathbf{G}$. It has been shown in several work that $\mathbf{G}^*$ can be solved efficiency by a technique called adjoint-state method [104]. Specifically, suppose that Δt and L are the simulation time step and the number of simulation steps, $\mathbf{G}^*\big(g(\mathbf{m}^j;\mathbf{s_i}) - \mathbf{d_i}\big)$, *i.e.* $\nabla E(\mathbf{m}^j)$, can be calculated for any location $\mathbf{r_d}$ as:

$$\begin{aligned} \mathbf{G}^*\big(g(\mathbf{m}^j;\mathbf{s_i}) - \mathbf{d_i}\big)\Big|_{\mathbf{r_d}} = \frac{2}{m_j^3(\mathbf{r_d})} \sum_{i=1}^{2N} \sum_{l=2}^{L-1} \big(q_i(\mathbf{r_d}, T - l\Delta t)(p_i(\mathbf{r_d}, (l+1)\Delta t) \\ -2p_i(\mathbf{r_d}, l\Delta t) + p_i(\mathbf{r_d}, (l-1)\Delta t))\big)/\Delta t^2, \end{aligned} \tag{6.3}$$

where $T = L\Delta t$ is the time duration of the simulation. $p_i(\mathbf{r}, t)$ is the simulated pressure field obtained from the acoustic wave propagation modeling operator g, at location $\mathbf{r}$, time t, and the i^{th} transmit element. $q_i(\mathbf{r}, t)$ is the adjoint pressure field obtained by the same underlying acoustic wave propagation modeling for g, except the source is replaced by the "time-reversed" version of $\big(g(\mathbf{m}^j;\mathbf{s_i}) - \mathbf{d_i}\big)$ and initial conditions $q_i(\mathbf{r}, t) = 0$ and $\partial/\partial t q_i(\mathbf{r}, t) = 0$. Note that for the adjoint field computation, waves propagate out of all receive transducer elements instead of one transmit transducer element, by the same underlying acoustic wave propagation modeling for g, except the source is replaced by the $\big(g(\mathbf{m}^j;\mathbf{s_i}) - \mathbf{d_i}\big)$.

It is important to note that for each iteration, at least 2 wavefield simulations are needed for each transmit element (or 3 if the line-search algorithm is used to determine the step length α): one for the calculation of $g(m)$ and another for the adjoint wavefield simulation. As a result, the image reconstruction problem based on the general least-square optimization requires $2(2N)$ wavefield simulations per iteration. It can be seen that this reconstruction approach is very time consuming and may prevent its current use in the clinic.

6.2.2.2 Least-square optimization problem with source encoding

Instead of directly minimizing the objective function in Equation 6.1, it is possible to minimize the expectation of the objective function [22], [127]–[129]. To illustrate why this is possible, consider the following objective function [130]:

$$E_{\mathbf{W}}(\mathbf{m}) = \frac{1}{K}\sum_{k=1}^{K} \| \big(g(\mathbf{m};\mathbf{s}_{\mathbf{w_k}}) - \mathbf{d}_{\mathbf{w_k}}\big)\|_2^2, \tag{6.4}$$

where

$$\mathbf{d}_{\mathbf{w_k}} = \sum_{i=1}^{2N} w_{ik}\mathbf{d_i}, \quad g(\mathbf{m};\mathbf{s}_{\mathbf{w_k}}) = g(\mathbf{m};\sum_{i=1}^{2N} w_{ik}\mathbf{s_i}) = \sum_{i=1}^{2N} w_{ik} g(\mathbf{m};\mathbf{s_i}) \tag{6.5}$$

and $\mathbf{W} = \begin{bmatrix}\mathbf{w_1}, \mathbf{w_2}, \dots, \mathbf{w_K}\end{bmatrix}$ denotes the $2N \times K$ matrix consisting of K column vectors, whose elements are drawn from the distribution that has zero mean and unit variance, *i.e.* $\mathbb{E}[w_{ik}] = 0$ and $\mathrm{Var}[w_{ik}] = 1$. $\mathbf{s}_{\mathbf{w_k}}$ and $\mathbf{d}_{\mathbf{w_k}}$ are called encoded source and encoded recorded pressure field, with respect to the encoding vector $\mathbf{w_k}$. Throughout all studies performed in this work, the elements in the encoding vector were drawn from the Rademacher distribution, where +1 and -1 are drawn with equally 50% chance.

To simplify the expression in Equation 6.4, we combine all the simulated and recorded pressure fields into 2 separate matrices as:

$$\mathbf{P} = \begin{bmatrix} g_{11} & g_{21} & \dots & g_{(2N)1} \\ g_{12} & g_{22} & \dots & g_{(2N)2} \\ \vdots & \vdots & \ddots & \vdots \\ g_{1(2N)} & g_{2(2N)} & \dots & g_{(2N)(2N)} \end{bmatrix}, \quad \mathbf{D} = \begin{bmatrix} d_{11} & d_{21} & \dots & d_{(2N)1} \\ d_{12} & d_{22} & \dots & d_{(2N)2} \\ \vdots & \vdots & \ddots & \vdots \\ d_{1(2N)} & d_{2(2N)} & \dots & d_{(2N)(2N)} \end{bmatrix},$$

where g_{ij} and d_{ij} are the $L \times 1$ vectors of simulated and recorded pressure traces, transmitted by the i^{th} element and received by the j^{th} element. Applying matrices $\mathbf{P}$, $\mathbf{D}$, $\mathbf{W}$ to Equation 6.5, we can rewrite Equation 6.4 as:

$$\begin{aligned} E_{\mathbf{W}}(\mathbf{m}) &= \frac{1}{K}\sum_{k=1}^{K} \|(\mathbf{P}\mathbf{w_k} - \mathbf{D}\mathbf{w_k})\|_2^2 \\ &= \frac{1}{K}\sum_{k=1}^{K} \|(\mathbf{P} - \mathbf{D})\mathbf{w_k}\|_2^2 \\ &= \frac{1}{K}\sum_{k=1}^{K} [(\mathbf{P} - \mathbf{D})\mathbf{w_k}]^T[(\mathbf{P} - \mathbf{D})\mathbf{w_k}] \\ &= \frac{1}{K}\sum_{k=1}^{K} \mathbf{w_k}^T(\mathbf{P} - \mathbf{D})^T(\mathbf{P} - \mathbf{D})\mathbf{w_k}. \end{aligned} \tag{6.6}$$

Now, if we compute the expectation of $E_{\mathbf{w}}(\mathbf{m})$ with respect to $\mathbf{W}$, we can see that:

$$\begin{aligned} \mathbb{E}[E_{\mathbf{W}}(\mathbf{m})] &= \mathbb{E}\left[\frac{1}{K}\sum_{k=1}^{K} \mathbf{w_k}^T(\mathbf{P} - \mathbf{D})^T(\mathbf{P} - \mathbf{D})\mathbf{w_k}\right] \\ &= \frac{1}{K}\sum_{k=1}^{K} \mathbb{E}[\mathbf{w_k}^T(\mathbf{P} - \mathbf{D})^T(\mathbf{P} - \mathbf{D})\mathbf{w_k}]. \end{aligned} \tag{6.7}$$

If we define $\mathbf{h_j} = \begin{bmatrix} g_{1j} - d_{1j} & g_{2j} - d_{2j} & \dots & g_{(2N)j} - d_{(2N)j} \end{bmatrix}$ and use it to replace $\mathbf{P} - \mathbf{D}$, then, from Equation 6.6, we have:

$$\begin{aligned}\mathbb{E}[E_{\mathbf{W}}(\mathbf{m})] &= \frac{1}{K}\sum_{k=1}^{K}\mathbb{E}\left[\mathbf{w_k}^T\left(\sum_{j=1}^{2N}\mathbf{h_j}^T\mathbf{h_j}\right)\mathbf{w_k}\right] \\ &= \frac{1}{K}\sum_{k=1}^{K}\mathbb{E}\left[\sum_{j=1}^{2N}(\mathbf{w_k}^T\mathbf{h_j}^T\mathbf{h_j}\mathbf{w_k})\right].\end{aligned} \tag{6.8}$$

Using the fact that the elements in $\mathbf{w_k}$ are all independent, we have $\mathbb{E}[w_{ik}w_{jk}] = 0$ for $i \neq j$. Also, $\mathbb{E}[w_{ik}^2] = \mathrm{Var}[w_{ik}] - \mathbb{E}[w_{ik}]\mathbb{E}[w_{ik}] = 1 - 0 = 1$. Finally, we have:

$$\begin{aligned}\mathbb{E}[E_{\mathbf{W}}(\mathbf{m})] &= \frac{1}{K}\sum_{k=1}^{K}\mathbb{E}\left[\sum_{j=1}^{2N}\sum_{i=1}^{2N} w_{ik}\|g_{ij} - d_{ij}\|_2^2 w_{ik}\right] \\ &= \frac{1}{K}\sum_{k=1}^{K}\sum_{j=1}^{2N}\sum_{i=1}^{2N}\left(\|g_{ij} - d_{ij}\|_2^2\mathbb{E}[w_{ik}^2]\right) \\ &= \frac{1}{K}\sum_{k=1}^{K}\sum_{j=1}^{2N}\sum_{i=1}^{2N}\left(\|g_{ij} - d_{ij}\|_2^2\right) \\ &= \sum_{j=1}^{2N}\sum_{i=1}^{2N}\left(\|g_{ij} - d_{ij}\|_2^2\right) \\ &= \sum_{i=1}^{2N}\left(\|g_{i1} - d_{i1}\|_2^2 + \cdots + \|g_{i(2N)} - d_{i(2N)}\|_2^2\right) \\ &= \sum_{i=1}^{2N}\|g(\mathbf{m};\mathbf{s_i}) - \mathbf{d_i}\|_2^2 \\ &= E(\mathbf{m}),\end{aligned} \tag{6.9}$$

which is equivalent to Equation 6.1, meaning that $E_{\mathbf{W}}(\mathbf{m})$ can be used as the estimator of $E(\mathbf{m})$. Therefore, one can use K encoding vectors $\mathbf{w_1}, \mathbf{w_2}, \ldots, \mathbf{w_k}$ to obtain K differently encoded sources and recorded pressure fields based on Equation 6.5. Because minimizing $E_{\mathbf{W}}(\mathbf{m})$ is done on K encoded sources, it requires $2K$ wavefield simulations per iteration as opposed to $2(2N)$ when minimizing $E(\mathbf{m})$. In addition, since K can be any positive integer from 1 to $2N$, it is possible to choose a small

K to reduce the computational demand. However, using greater K will lead to the greater estimate of $E(\mathbf{m})$.

There has also been another technique similar to source encoding, called sketching, that appears in recent literature and allows the objective function to be approximated by the dimensionally-reduced data space. This dimensionality reduction in turn helps in reducing the computational burden in calculating the update direction. Interested readers should refer to [137] and [138] for example of uses of the sketching approach.

6.2.2.3 Compressed sensing

We described the source encoding technique in Section 6.2.2.2 to drastically reduce the computational demand. However, source encoding has 2 major drawbacks. First, since the encoded source and recorded pressure field are results of linear combinations of individual original sources and recorded pressure fields with different weights, the encoded source is prone to interference among signals transmitted from multiple original sources. This later results in strong image artifacts. Second, the source encoding technique does not reduce the size of the acquired signal dataset. The dataset size in both general and source encoding techniques is $(2N)^2$, which could require enormous storage when the number of elements on each transducer array increases. It is possible to use only a subset of the acquired signal dataset to reconstruct the image, but this might also result in the image artifacts due to the limited input dataset.

For this reason, the compressed sensing technique is applied in this work to reduce image artifacts resulting from both speeding up the image reconstruction using source encoding and by reducing the size of the dataset [133], [134], [139], [140]. The objective function in Equation 6.4 that incorporates compressed sensing penalty terms is then modified as [97], [135], [136]:

$$E_{\mathbf{W}}(\mathbf{m}) = \frac{1}{K}\sum_{k=1}^{K}\|\big(g(\mathbf{m};\mathbf{s}_{\mathbf{w_k}}) - \mathbf{d}_{\mathbf{w_k}}\big)\|_2^2 + \alpha\|\nabla\mathbf{m}\|_1 + \beta\|W\mathbf{m}\|_1, \tag{6.10}$$

where $\|\nabla\mathbf{m}\|_1$ is called the total-variation regularizer and W is the Haar wavelet regularizer. $\|\nabla\mathbf{m}\|_1$ and $\|W\mathbf{m}\|_1$ should be sparse in general, but sensitive to the image artifacts. Both penalty terms are likely to increase when image artifacts increase. As such, this optimization problem will choose $\mathbf{m}$ such that it balances the contribution between the data term (the term with the L2 norm) and the penalty terms. α and β control the strength of penalization, and the greater those values are, the stronger the enforcement on artifact suppression is. However, note that if those values are too high, they will also remove desirable image features.

With compressed sensing techniques, one can use only a subset of elements for signal transmission to acquire a smaller signal dataset and still achieve reconstruction quality comparable to that obtained from a full dataset. Let $\mathbb{M}$ be the subset consisting of indices of elements used for transmission. The encoded source and recorded pressure field are now written as:

$$\mathbf{s}_{\mathbf{w_k}} = \sum_{i\in\mathbb{M}} w_{ik}\mathbf{s}_{\mathbf{i}}, \quad \mathbf{d}_{\mathbf{w_k}} = \sum_{i\in\mathbb{M}} w_{ik}\mathbf{d}_{\mathbf{i}} \tag{6.11}$$

and the dataset size is reduced to $|\mathbb{M}|(2N)$.

To minimize the objective function in Equation 6.10 without directly computing the gradients of the L1 regularizers, we first add the auxiliary variable $\mathbf{u}$ and another convex L2 regularizer $\lambda\|\mathbf{m}-\mathbf{u}\|_2^2$ to the objective function and then modify the objective function as follow:

$$E_{\mathbf{W}}(\mathbf{m},\mathbf{u}) = \frac{1}{K}\sum_{k=1}^{K}\|\big(g(\mathbf{m};\mathbf{s}_{\mathbf{w_k}}) - \mathbf{d}_{\mathbf{w_k}}\big)\|_2^2 + \lambda\|\mathbf{m}-\mathbf{u}\|_2^2 + \alpha\|\nabla\mathbf{u}\|_1 + \beta\|W\mathbf{u}\|_1 \tag{6.12}$$

and decouple the objective function into two sub-problems [9], [95], [96]

$$E_{\mathbf{W},1}(\mathbf{m}) = \frac{1}{K}\sum_{k=1}^{K}\|\left(g(\mathbf{m};\mathbf{s}_{\mathbf{w_k}}) - \mathbf{d}_{\mathbf{w_k}}\right)\|_2^2 + \lambda\|\mathbf{m}-\mathbf{u}\|_2^2 \tag{6.13a}$$

$$E_{\mathbf{W},2}(\mathbf{u}) = \lambda\|\mathbf{m}-\mathbf{u}\|_2^2 + \alpha\|\nabla\mathbf{u}\|_1 + \beta\|W\mathbf{u}\|_1 \tag{6.13b}$$

Equation 6.13a minimizes $E_{\mathbf{W},1}(\mathbf{m})$ with respect to $\mathbf{m}$ and treats $\mathbf{u}$ as the constant. A conjugate-gradient method was employed to minimize $E_{\mathbf{W},1}(\mathbf{m})$. Similarly, Equation 6.13b minimizes $E_{\mathbf{W},2}(\mathbf{u})$ with respect to $\mathbf{u}$ and treats $\mathbf{m}$ as the constant. These two sub-problems are solved alternatively until they converge. Note that, since $E_{\mathbf{W},2}(\mathbf{u})$ is in the form of $\Phi(\mathbf{u}) + \alpha\|H_1(\mathbf{u})\|_1 + \beta\|H_2(\mathbf{u})\|_1$, where $\Phi(\mathbf{u})$ is convex, the Split-Bregman method can be employed to minimize $E_{\mathbf{W},2}(\mathbf{u})$ without directly computing the gradient of $\alpha\|\nabla\mathbf{u}\|_1 + \beta\|W\mathbf{u}\|_1$ [97].

In theory, the regularization parameter λ should be large because $\mathbf{m} \rightarrow \mathbf{u}$ as $\lambda \rightarrow \infty$, making Equation 6.12 resemble Equation 6.10. However, after splitting the objective function into 2 sub-problems, we found empirically that setting too large λ will induce a large penalty on the L2 regularizer and thus oversmooth the image. In fact, a small value of λ helps both decoupled sub-problems converge to the desired solution more easily. In addition, since $\mathbf{m}$ in Equation 6.13a is reinitialized by $\mathbf{u}$ from Equation 6.13b before minimization begins, and since the least square data term in Equation 6.13a is highly non-convex, it is likely that the resultant $\mathbf{m}$ will still preserve the features in $\mathbf{u}$.

6.2.3 Simulation Studies

6.2.3.1 Numerical phantoms

Image reconstructions are investigated on two phantoms with different complexities. The phantom size is 6 cm × 4 cm with a simulation grid spacing of 0.3125 mm. The first phantom shown in Figure 6.2(a) consisted of two cylinders with different sizes, where the larger cylinder acoustically shadowed the smaller cylinder. The second phantom shown in Figure 6.7(a) consisted of the breast tissue-mimicking structures (Madsen, Madison, WI) whose acoustic properties are similar to those found in the female breast. Acoustic properties of all regions in the first and second phantoms are given in Table 6.1 and 6.2, respectively. In addition, the attenuation coefficient of both phantoms is set to 0.75 dB/cm/MHz$^{1.5}$.

Table 6.1: Acoustic properties for individual regions in cylindrical phantom shown in Figure 6.1. Refer to the same figure for region number.

Region	1	2	3
Sound Speed (m/s)	1460	1570	1515
Mass Density (kg/m^3)	900	1200	1000

Table 6.2: Acoustic properties for individual regions in breast tissue-mimicking phantom shown in Figure 6.1. Refer to the same figure for region number.

Region	1	2	3	4	5	6
Sound speed (m/s)	1409	1461	1421	1537	1552	1452
Mass density (kg/m^3)	1000	1000	1000	1200	1200	1000

6.2.3.2 Input data generation

Input pressure traces were generated as if they were acquired from the ultrasound scanner described in Section 6.2.1. Two linear transducers with 4-cm wide apertures, 40 point-like elements on each, and 0.5 MHz center frequency, were modeled for the ultrasound scanner to enable imaging in transmission and reflection modes. The k-Wave toolbox [109] was utilized in this work to simulate the input pressure traces based on the *k*-space pseudospectral method [100], [101]. Each pressure trace consists of 1,878 pressure samples, reflecting a 17.1 MHz sampling rate. Numerical phantoms with true acoustic distribution (sound speed, mass density, and attenuation) maps were also used for generating the input pressure traces.

6.2.3.3 Reconstruction settings

The input pressure traces generated according to Section 6.2.3.2 will be used as the input for the image reconstruction algorithm. The reconstruction was initialized by the sound speed image, obtained from a bent-ray inversion technique described in [7], via the $\mathbf{u}$ term in Equation 6.13a.

The overall reconstruction algorithm was configured so that the vectorized sound speed image $\mathbf{m}$ was updated 20 times in total, as it was observed that at 20th iterations, the magnitude of the gradient in Equation 6.2b was within 5% of the magnitude of the gradient at the first iteration. If compressed sensing was disabled, minimizing $E_{\mathbf{W},1}(\mathbf{m})$ was just executed for 20 iterations. Otherwise, minimizing $E_{\mathbf{W},1}(\mathbf{m})$ and $E_{\mathbf{W},2}(\mathbf{u})$ were performed alternately for 4 times, where minimizing $E_{\mathbf{W},1}(\mathbf{m})$ was executed for 5 iterations before subsequently minimizing $E_{\mathbf{W},2}(\mathbf{u})$.

The same k-Wave toolbox in Section 6.2.3.2 was utilized for acoustic wave propagation modeling to compute the simulated pressure field and the adjoint pressure field in each reconstruction iteration, as described by Equation 6.3. The medium mass density and attenuation coefficient were set to 1000 kg/m^3 and 0.75 dB/cm/MHz$^{1.5}$, respectively.

Parameters α and β were both set to 10^{-4}. λ was set to 10^{-12}. Note that changing these parameters will affect the reconstruction results, and this might be worthwhile to investigate in the future.

6.2.3.4 Case studies

1. *Study 1: Performance comparison between original technique and source encoding technique with single randomization.* Images of the cylinder phantom were reconstructed with a full dataset (size $2N = 80$) using the bent-ray inversion technique outlined in [7], the original waveform inversion technique via minimizing the objective function in Equation 6.1, and the waveform inversion

with source encoding via minimizing the objective function in Equation 6.4. K was set to 1 to represent single randomization of the encoding vector, and this was equivalent to a source encoding technique presented in various preliminary studies [22], [127]–[129].

2. *Study 2: Comparison of images reconstructed by the source encoding technique with different randomization numbers and dataset sizes.* Images of the cylinder phantom were reconstructed using the source encoding technique with different combinations of $K \in \{1, 2, \ldots, 8\}$ and $N \in \{1, 2, 4, 5, 8, 10, 20, 40\}$ (or $2, 4, 8, \ldots, 80$ active transmit elements). Both reconstructions, with and without compressed sensing, were obtained. For each reconstruction case, the root-mean-square-error (RMSE) was calculated for both cylindrical regions, and the standard deviation (STD) was calculated for the background region. Then, two types of plots were generated: 1) plots showing average RMSE and STD values across different number of randomizations for a given number of transmit elements, and 2) plots showing average RMSE and STD values across different number of transmit elements for a given number of randomizations.

   A subset of the active transmit elements was chosen based on the bin-based approach described in [141]. Specifically, to activate M active transmit elements, all $2N$ element indices were divided into M equal-sized bins, and one element index was chosen for each bin as a representative of all transmit elements in that bin. Note that reconstruction results also depend on the chosen set of active transmit elements. As such, to obtain more precise RMSE and STD values, the whole reconstruction process (with different randomization numbers and dataset sizes, and compressed sensing enabled) were repeated for 4 more times, and the averages of RMSE and STD values across 5 different realizations were calculated and displayed on 3D surface plots as functions of number of randomizations and transmit elements.

3. *Study 3: Image reconstructions of the breast tissue-mimicking phantom.* Images of the breast tissue phantom were reconstructed using the original waveform inversion technique with a full dataset (size $2N = 80$) and total-variation regularization, as well as the waveform inversion with the $K = 1$ source encoding technique, using a partial dataset (size $2N = 8$), and compressed sensing. Note that the sound speed of fatty layers in region 1 was fixed to 1409 m/s, as ultrasound limited-angle tomography systems typically cannot resolve sound speed distributions in layers that are parallel to the transducer apertures.

6.3 Results and Discussion

6.3.1 Analysis of Computational Complexity and Dataset Size

Table 6.3 summarizes the computational complexity and dataset size of each reconstruction approach, as a function of number of active transmit elements ($M \leq N$) and number of randomizations ($K \leq N$). Note that for simplicity, the total number of transducer elements for these analyses is denoted by N instead of $2N$ that was used previously.

Table 6.3: Computational complexity and dataset size of each reconstruction approach, as a function of number of active transmit elements (M) and number of randomizations (K). Note that here N is the total number of physical transmit-receive elements, previously written as $2N$.

Reconstruction approach	WI	SE	SE + CS
Computational complexity	$O(N)$	$O(K)$	$O(K)$
Dataset size	$O(N^2)$	$O(MN)$	$O(MN)$

The reason that the source encoding technique decreases the computation from $O(N)$ to $O(K)$ is because the optimization is done on K pairs of encoded source and encoded recorded pressure, rather than N pairs of original source and original recorded pressure, and the computational demand scales linearly with the number of pairs. It is straightforward to see that the dataset size also scales linearly with the number of active transmit elements. Compressed sensing can be done in negligible time with the Split-Bregman method [97], and it does not require any additional dataset either.

6.3.2 Study 1: Original and Source Encoding Techniques

Figure 6.2 shows the reconstruction results of the simple cylindrical phantom using different reconstruction techniques. Although the bent-ray approach is much faster than the original waveform inversion counterpart ($\approx 160x$), it fails to recover the cylindrical structures from the signals acquired by the dual-sided ultrasound scanner with limited acquisition direction as it lacks the ability to account for diffraction and scattering effects. The waveform inversion technique with single randomization source encoding ($K = 1$) achieves a $80x$ speedup compared to the original waveform inversion. However, the image reconstructed by this technique clearly shows stronger artifacts, as the encoded source and recorded pressure field are calculated as linear combinations of weighted individual original sources and recorded pressure fields. This process can therefore lead to the signal cross-talk.

In the next two studies, we will demonstrate that by breaking the $K = 1$ rule in most of the existing source encoding techniques, and applying the compressed sensing technique, we can obtain reconstructed images that are very close to the ground truth (*i.e.*, close to the original waveform inversion approach).

6.3.3 Study 2: Source Encoding Technique with Compressed Sensing

Figure 6.3 shows images reconstructed by employing source encoding technique with different numbers of randomizations and active transmit elements. Reconstruction results without (panel (a)) and with (panel (b)) compressed sensing are compared side-by-side. As can be seen, applying compressed sensing techniques by adding total-variation and Harr wavelet regularizers to the original least-square objective function,

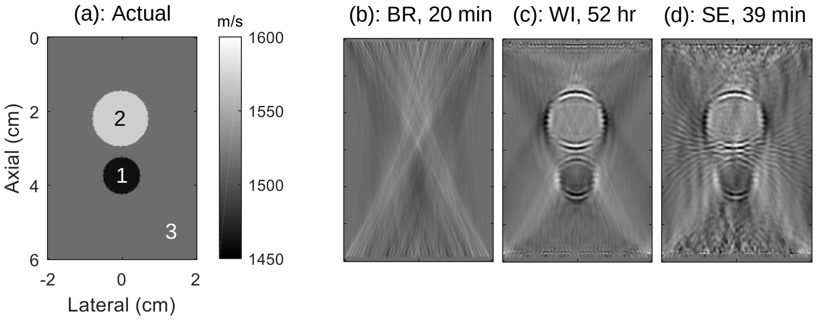

Figure 6.2: (a) Actual sound speed distribution of a phantom with two simple cylinders. (b)-(d) Corresponding reconstructed images using bent-ray, original waveform inversion, and waveform inversion with source encoding (with $K = 1$) approaches, respectively. All images were reconstructed with a full dataset size and without any regularizer embedded in the objective function. The single-thread runtimes for bent-ray (BR), original waveform inversion (WI), and waveform inversion with source encoding (SE) are approximately 20 minutes, 52 hours, and 39 minutes, respectively.

helps to reduce artifacts. Increasing the number of randomizations (K) from 1 to 2 further helps in artifact reduction too, even though the improvements of using higher K on the reconstructed images are less clear once compressed sensing has already been applied. However, using more than 2 randomizations for source encoding ($K > 2$) does not seem to give any further improvement, suggesting that $K = 2$ is sufficient to achieve a reconstruction quality comparable to that of the original waveform inversion approach.

To explain why increasing the number of randomizations helps improve the reconstruction quality, at the expense of computational increase, we have constructed two types of maps shown in Figure 6.4. They measure the completeness of the dataset and the energy leak due to cross-talk arising from the source encoding technique. This representation is adopted from [130]. Maps in panel (a) are for the original waveform inversion using the dataset generated by K active transmit elements (requires K acquisitions to acquire the dataset). These are constructed by assigning ones to the diagonal elements, whose indices correspond to the indices of active transmit ele-

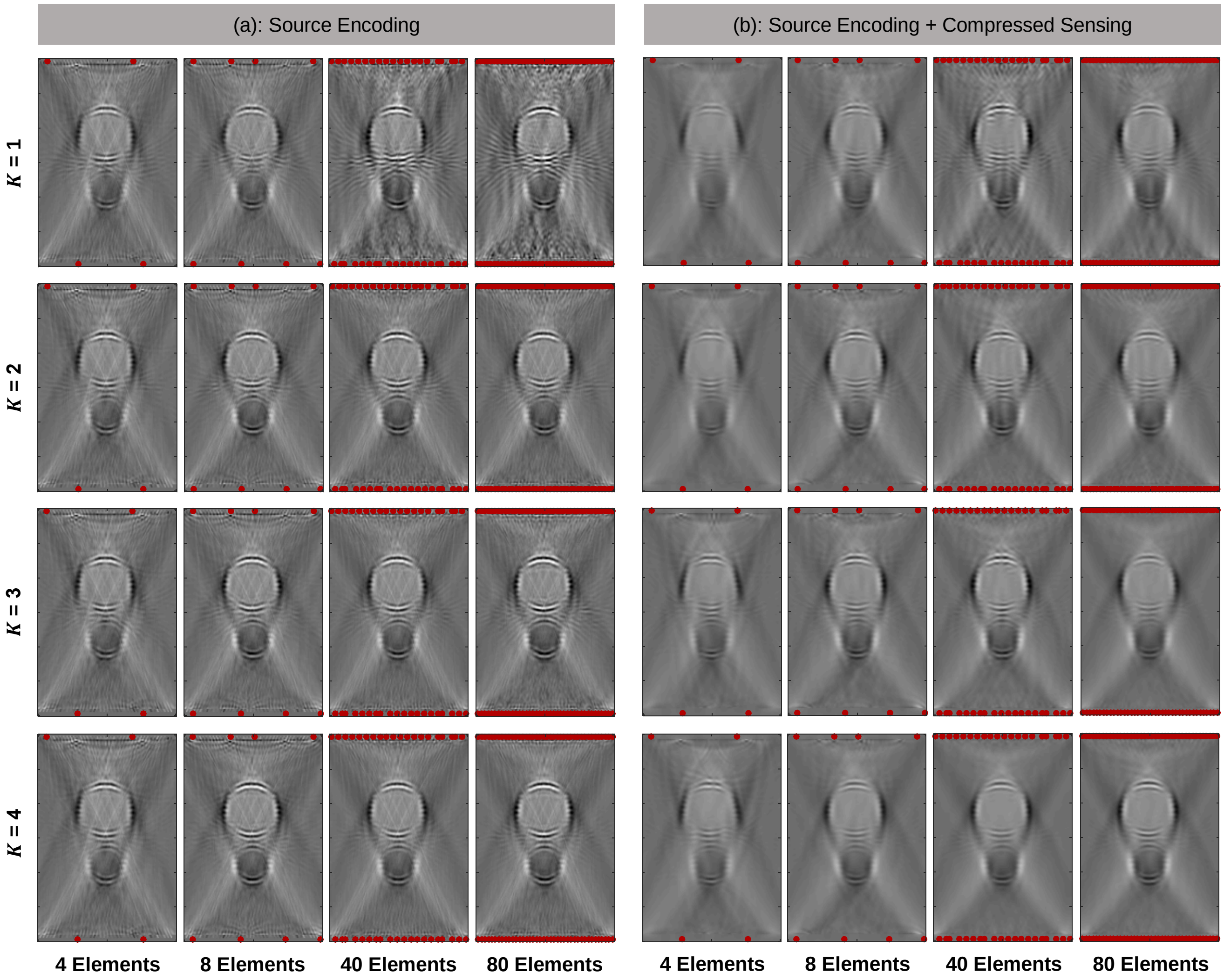

Figure 6.3: Reconstructed images of the phantom shown in Figure 6.2(a), using different reconstruction techniques, randomization numbers, and active transmit elements. Panels (a) and (b) show images reconstructed by source encoding technique without and with compressed sensing, respectively. Red dots in the images represent the chosen active elements. Note that the listed number of elements encompasses both apertures.

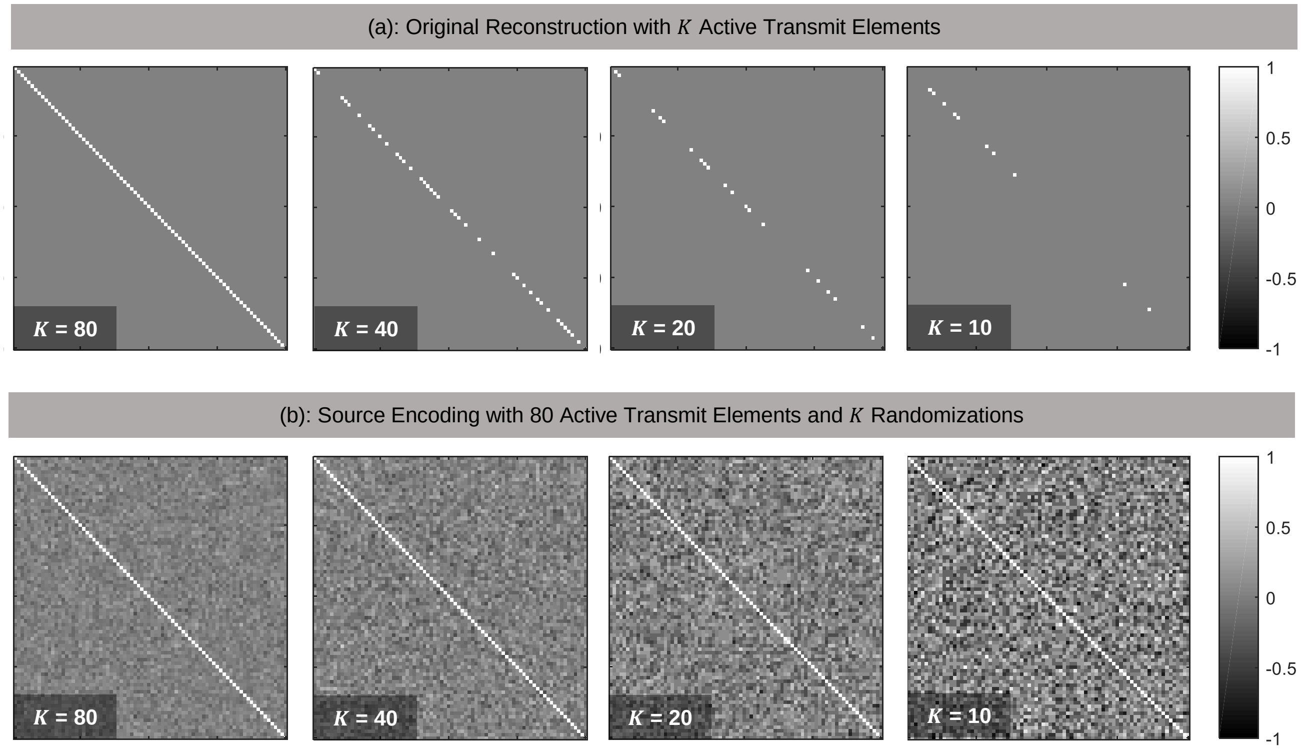

Figure 6.4: (a) Map of $\mathbf{W}\mathbf{W}^T$, where $\mathbf{W}$ is a $2N \times K$ matrix whose k^{th} column vector dictates an index of the transmit element at the k^{th} signal acquisition. The row vector has an element value of 1 at the transmit element index and 0 elsewhere. (b) Map of $\frac{1}{K}\mathbf{W}\mathbf{W}^T$, where $\mathbf{W}$ is a $2N \times K$ matrix whose k^{th} column vector corresponds to the $\mathbf{w_k}$ encoding vector for k^{th} randomization. Both (a) and (b) require the same computation. Note that in theory, $\mathbb{E}[\mathbf{W}\mathbf{W}^T] = \text{Cov}[\mathbf{W}\mathbf{W}^T] + \mathbb{E}[\mathbf{W}]\mathbb{E}[\mathbf{W}^T] = \mathbf{I} + \mathbf{0} = \mathbf{I}$, so the closer $\mathbf{W}\mathbf{W}^T$ to the identity matrix, the more complete the image reconstruction process and the less interference.

ments, on a zero-valued matrix. Maps in panel (b) are for the waveform inversion with source encoding and K randomizations on a full-size dataset. These are calculated as $\mathbf{W}\mathbf{W}^T$, where $\mathbf{W}$ consists of K columns of encoding vectors. The resulting map that is close to the identity matrix is likely to yield a good quality reconstruction. Note that both reconstruction methods require the same amount of computation, but their behaviors toward the final results are different. As can be seen from the maps, using only a subset of active transmit elements and the original waveform inversion approach does not cause the energy to leak, but causes some diagonal elements to become zero. On the other hand, the source encoding approach with a full-size dataset is more prone to diagonal elements being zero, but suffers from the energy leak outside the diagonal as the randomization number decreases. This suggests that it could be worthwhile to spend slightly more computation, *i.e.* by increasing the number of randomizations, to eliminate more cross-talk, especially when the dataset size is large. Such would achieve comparable results to the original waveform inversion approach while maintaining superior performance.

Referring back to Figure 6.3, it is also interesting to see that reducing the number of active transmit elements by up to a factor of 10 (from 80 elements down to 8) affects the reconstruction results only slightly. This suggests that there is a lot of redundant information contained in the full-size dataset. This phenomenon has also been reported in [142]. When only 8 elements are activated, the artifacts near the transducer aperture start to appear in the images reconstructed without compressed sensing. However, if compressed sensing is applied, those artifacts are barely visible and the final results look remarkably similar to those reconstructed with the full-size dataset. Further reducing the number of active transmit elements from 8 to 4 will cause distortions in the cylindrical structures that cannot be corrected by applying more regularization. This is the case since the regularizers used here do not constraint the geometrical structures of the imaged region. Preliminary studies in [7], [9], [64] utilize the covariance-based regularization technique that can account for geometrical information, but it requires segmentation on images from other modalities and thus is not considered here.

Figure 6.5 shows the average values of RMSE and STD, calculated across different number of (a) randomizations and (b) active transmit elements (smaller values indicate better reconstruction quality). It appears that the averaged root-mean-square error is more sensitive to the number of active transmit elements than the STD. A similar trend can be seen in for the STD, though less pronounced. A more detailed RMSE of the object regions and STD of the background region, as a function of number of randomizations and number of active transmit elements, is shown in Figure 6.6. Note that, as mentioned earlier in Section 6.2.3.4, the RMSE and STD values shown in this figure are averages of 5 different RMSEs and STDs corresponding to 5 different sets of active transmit elements.

It is interesting to mention that there is a trade-off between the RMSE and the STD when it comes to choosing the optimal number of active transmit elements. This is also observed in Figure 6.6, where the optimal RMSEs are achieved when the number of transmit elements is at least 8, but the optimal STD is achieved when the least number of transmit elements is used. Even though using less transmit elements can lower down the STD, it also lowers down the root-mean-square errors, meaning that the calculated sound speed is less accurate. This happens because of the cross-talk artifact, caused by source encoding, is more likely to occur when the number of transmit elements increases, and it subsequently overwhelms the artifacts due to the limited dataset size that increases ill-posedness of the reconstruction problem.

Furthermore, note that with compressed sensing applied, the RMSE does not seem to be more accurate, but the STD noticeably is. This is expected because applying compressed sensing should help in reducing the artifact level, but this does not necessarily mean that the inherent bias in the sound speed image is also eliminated.

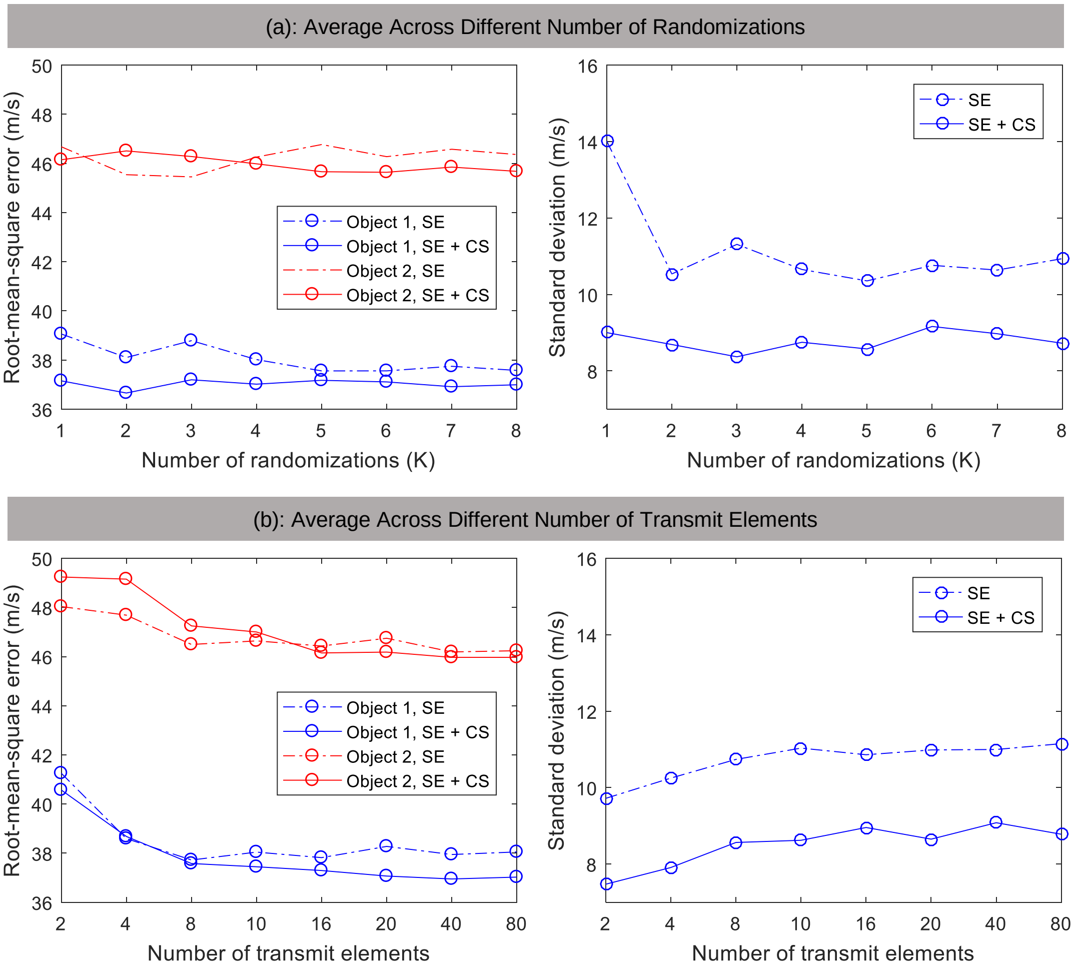

Figure 6.5: Average of RMSE and STD across (a) different number of randomizations K and (b) different number of transmit elements. RMSE and STD are calculated for cylindrical and background regions, respectively, for both reconstructions with and without compressed sensing. Smaller values indicate better performance. Note: SE = waveform inversion with source encoding and CS = compressed sensing (total-variation + Haar wavelet regularizers).

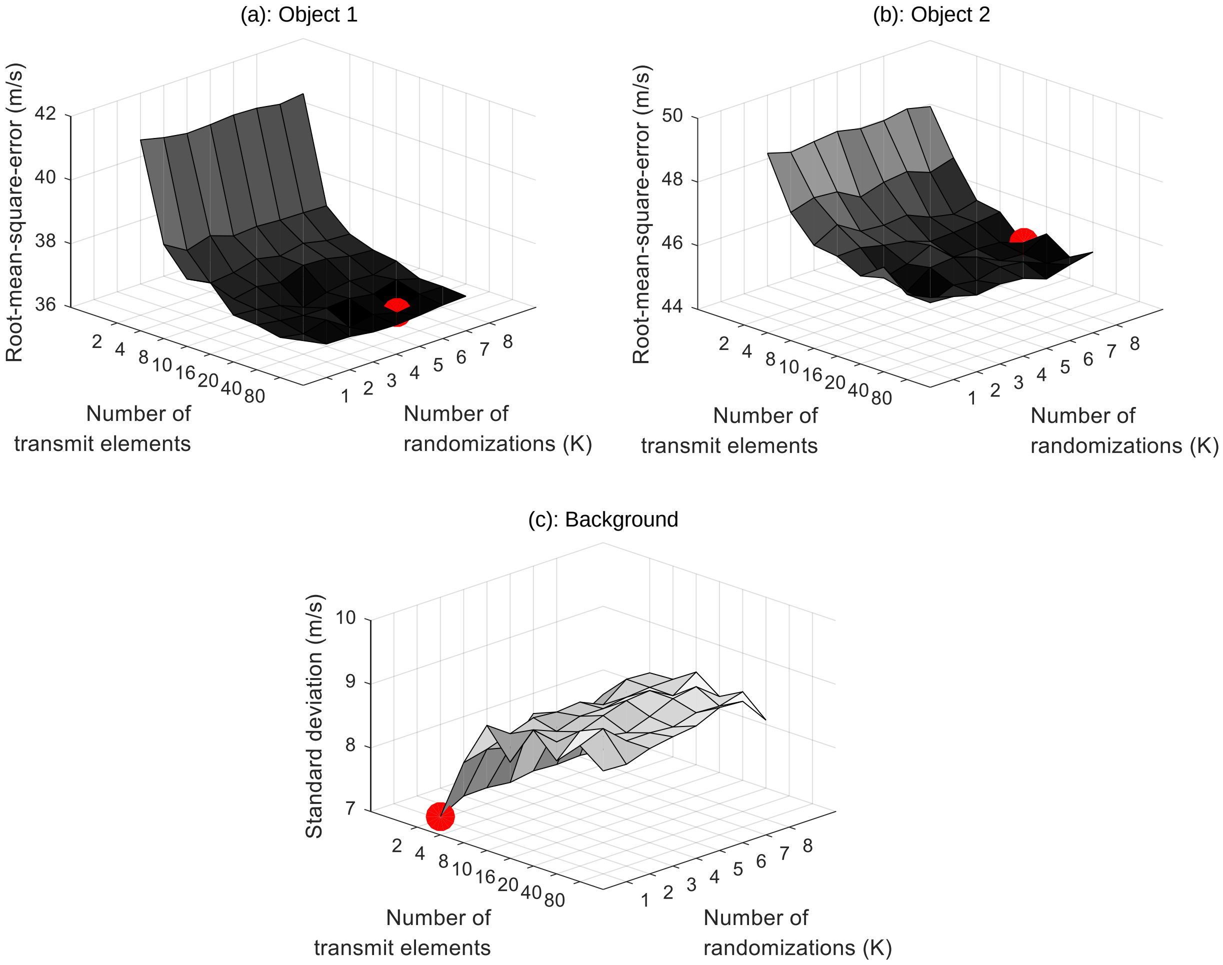

Figure 6.6: RMSE and STD as a function of number of randomizations K and number of transmit elements, for (a) object 1 and (b) object 2. Compressed sensing was applied to all reconstructions. The RMSE and STD shown here are averages of 5 different RMSEs and STDs corresponding to 5 different sets of active transmit elements. Reconstruction cases that yield the lowest RMSE or STD are marked in red.

According to Figures 6.5 and 6.6, although increasing the number of randomizations K might not help much in improving root-mean-square error, it should help in reducing image artifacts. This is especially obvious when increasing K from 1 to 2, as the STD at $K = 2$ in the top-right panel of Figure 6.5 appears to be less than the STD at $K = 1$ for the non-compressed sensing case, even though this becomes less obvious if compressed sensing is applied. Still, the artifact reduction can be observed directly in the reconstructed image, and such findings are also in agreement with Figure 6.3.

6.3.4 Study 3: Reconstructions of the Breast Tissue-Mimicking Phantom

Figure 6.7 shows reconstruction results of the breast tissue-mimicking phantom using different waveform inversion approaches. The original waveform inversion approach utilizes only total-variation regularization, as including an additional Haar wavelet regularizer otherwise does not result in any observable change. As can be seen, the reconstructed image with $K = 2$ source encoding, 8 transmit elements, and compressed sensing, appears remarkably similar to the image reconstructed using the original approach. This, together with other previous studies, suggests that it is possible to decrease both dataset size and the amount of computation, while maintaining a similar reconstruction quality compared to the original approach.

6.4 Conclusions

The original waveform inversion approach, which requires a huge amount of computation and memory resources, has been drastically optimized in this work via the use of source encoding and compressed sensing techniques. Source encoding allows for the image reconstruction to perform on one single encoded source as well as on one recorded pressure field instead of multiple original sources and multiple recorded pressure fields. The required computational amount is thus as little as that for a

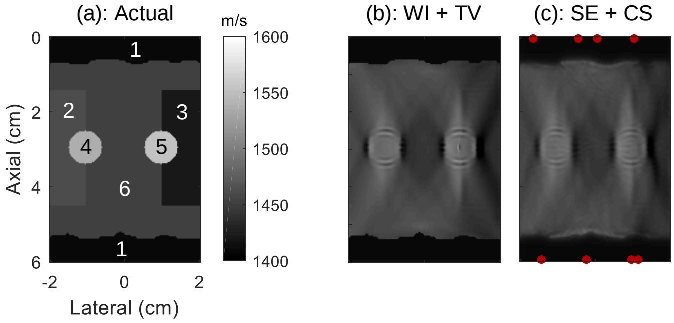

Figure 6.7: (a) Actual sound speed distribution within the breast-tissue mimicking phantom. (b) Corresponding reconstructed image using a waveform inversion approach using total-variation regularization and a full-size dataset. (c) Corresponding reconstructed image using a waveform inversion approach with $K = 2$ source encoding, partial dataset size, and compressed sensing. Red dots in the image represent the chosen active elements. The single-thread runtimes for original waveform inversion with total-variation regularization (WI + TV) and waveform inversion with source encoding and compressed sensing (SE + CS) are approximately 52 hours and 78 minutes, respectively. Note: WI = waveform inversion, SE = waveform inversion with source encoding, TV = total-variation regularizer, and CS = compressed sensing (TV + Haar wavelet regularizers).

single transmit element. It has been also demonstrated that using one additional encoding vector per iteration, *i.e.*, two randomizations, yields reconstruction results comparable to those of the original waveform inversion approach, particularly on large pressure datasets that are prone to cross-talk artifacts caused by the source encoding technique. In addition, the applied compressed sensing technique, through the use of total-variation and Haar wave regularizers, allows for the mitigation of various artifact types, including those related to the limited number of active transmit elements. As a result, the dataset size can be reduced by up to one order of magnitude without noticeable image degradation. However, further dataset size decrease will result in structural distortions in the image that exceed the ability of compressed sensing.

Although this work has demonstrated striking performance improvements in terms of computational and memory aspects as well as showed great promise in efficiently handing the huge amount of clinical datasets, further investigations are still encouraged. First, the dataset batching approach described in [122], [130] does not result in the cross-talk artifacts but still helps in reducing the computational demand (though not as much as source encoding). It would be worthwhile to compare the performance of this approach to the source encoding technique. Second, while numerical investigations show that compressed sensing can help reducing the dataset size, a formal mathematical proof still needs to be done for further performance improvements. One of the possible ways to do so is to measure the coherence of the operator that maps the designed sparse space (*e.g.*, total-regularization or Haar wavelet space), to the data space (pressure field). Such coherence measurement allows us to come up with the most effective set of regularizers that extract the most information out of the pressure field dataset. Most importantly, the proposed acceleration and data reduction approach needs to be validated experimentally on either physical phantoms or human subjects to ensure seamless clinical translation.

CHAPTER VII

Full-Wave Photoacoustic Tomography with Handheld Ultrasound and *A Priori* Information

7.1 Introduction

Photoacoustic imaging combines the benefits of high optical contrast from optical imaging and deep penetration from ultrasound imaging ($\approx 3 - 30$ mm) [143]–[146]. Pure optical imaging techniques while achieving microscopic resolution (0.1-100 µm), typically suffer from strong light scattering when imaging regions deeper than 1 mm. One of the potential photoacoustic applications that directly take advantage of absorption-based contrast is breast cancer detection. Angiogenesis increases tumor vascularization to support its growth [147]. Intra tumor hemoglobin concentration is likely to be higher than in benign regions ($\approx 1.5 - 2$x) and will thus increase light absorbtion. This appealing feature provides imaging contrast between malignant and benign tissues and has been previously demonstrated.[148]–[154]

The sensitivity of photoacoustics with respect to breast density changes [155] and the lack of ionizing radiation have drawn much attention to the development of clinical photoacoustic breast scanners. Three-D breast scanning systems for the prone and compressed breast have been proposed in [156], [157] and [148], [158], respectively. Similarly, Kitai et al. [159] and Xie et al. [12] designed a photoacoustic breast scanner in the mammographic geometry. Despite their promising results, they require the use of dedicated equipment, which hinders portability, cost-effectiveness, and most importantly, clinical potential. Such limitations could be overcome by using a handheld ultrasound transducer.

Commercial handheld ultrasound transducers are alternative solutions to facilitate portability and affortability, thus enabling clinical translation. Preliminary studies with regard to breast imaging exist [160], [161]. However, these techniques reconstruct optical absorption images by using back-projection or delay-and-sum beamforming techniques that neglect tissue acoustic heterogeneities that inturn affect the photoacoustic signals. Recently, several research groups have proposed photoacoustic tomography approaches based on circular or curved ultrasound arrays that aim to overcome artifacts caused by acoustic heterogeneities. Specifically, Deán-Ben, et al., Jose et al., Zhang et al., and Jin et al. [162]–[165] consider the time-of-flight change due to sound speed heterogeneity, and Huang et al., Arridge et al., and Javaherian et al. [166]–[168] utilize full-wave propagation modeling to accurately take acoustic heterogeneities into account. However, implementing those sophisticated algorithms for linear ultrasound arrays with limited directionality is non-trivial as the acquired photoacoustic signals are highly incomplete, and this will lead to undesirable limited-angle artifacts.

It is still possible to employ these techniques for handheld ultrasound, if the underlying reconstruction algorithm is well-constrained. Here, we present a full-wave photoacoustic tomography approach for the handheld ultrasound that allows inclusion of *a priori* information. Such information limits the reconstruction to a specific, informed, regions of interest (ROI). Note that in the clinic, the ROI location could be obtained from B-mode or B-flow segmentation. Intra-tissue regions should be moderately homogeneous. Therefore, a covariance-based probabilistic model can be setup to incorporate that homogeneity assumption into the reconstruction algorithm.

In addition, segmentation data could potentially also served to separate and mitigate heterogeneous tissue structures that would cause structural distortions in the reconstructed image. In summary, the added segmentation information will directly improve photoacoustic tomography imaging by means of the underlying full-wave modeling that offers superior reconstruction quality.

This work is organized as follows: Related background and details of the simulation studies are given in Section 7.2. Results, analyses and interpretation are given in Section 7.3. Section 7.4 provides summary of this work as well as potential future directions.

7.2 Materials and Methods

7.2.1 Photoacoustic Theory

Figure 7.1(a) shows the graphical representation of a typical photoacoustic scanning system. A short laser pulse is used to excite hemoglobin, an iron-containing metalloprotein, found in red blood cells to facilitate oxygen transport. Note that for the sake of generality, there is no exact location of the laser source, but in practice the laser source is setup in such a way that the light fluence is appreciably uniform across the imaged tissue region. Upon illumination, hemoglobin absorbs the photon energy and converts it to heat. This process is called thermalization and results in a sudden local physical expansion of the surrounding fluid. This in turn, induces the local initial broadband pressure p_0, which is linearly related to the optical absorption as described by the following equation [144]:

$$p_0 = \hat{\Gamma}\Phi\mu_a, \tag{7.1}$$

where $\hat{\Gamma}$ is the photoacoustic efficiency that is linearly related to the Grüneisen parameter, Φ is the laser fluence, and μ_a is the optical absorption coefficient. The Grüneisen parameter depends on the tissue type as different tissue types have different thermal coefficients of volume expansion, specific heats, and speeds of sound. However, for simplicity, most photoacoustic imaging applications treat it as constant [143], [145].

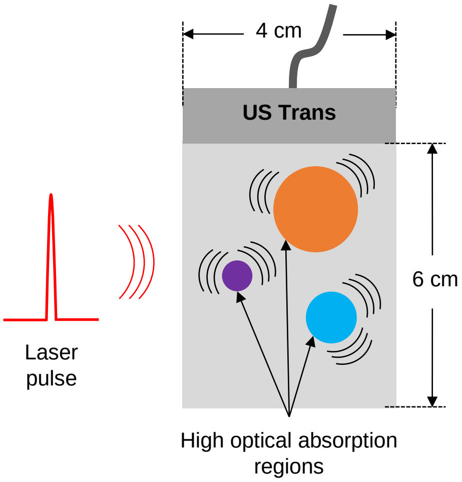

Figure 7.1: Graphical representation of a typical photoacoustic scanning system with a handheld ultrasound transducer capturing the acoustic signals emitted from the high optical absorption regions due to laser excitation.

The initial sudden expansion pressure rise will induce the then observable acoustic wave expanding from the site of illumination. The propagating wave pressure can be recorded by an ultrasound detector [143], [144] as $p(\mathbf{r}, t)$. Given $p(\mathbf{r}, t)$, the goal of the photoacoustic tomography is to recover p_0. Since p_0 is linearly proportional to μ_a, recovering p_0 is sufficient.

7.2.2 Modeling Acoustic Propagation

Given $p(\mathbf{r}, t) : \mathbb{R}^2 \times \mathbb{R}_0^+ \to [0, T]$ the recorded pressure field, where $[0, T]$ is the recorded time interval, and $p_0(\mathbf{r}) : \mathbb{R}^2 \to \mathbb{R}_0^+$ the initial pressure rise, the photoacoustic signal propagation in an acoustically heterogeneous tissue can be described by the following first-order coupled equations [14], [98], [99]:

$$\frac{\partial}{\partial t}\mathbf{u}(\mathbf{r}, t) = -\frac{1}{\rho_0(\mathbf{r})}\nabla p(\mathbf{r}, t) \tag{7.2a}$$

$$\frac{\partial}{\partial t}\rho(\mathbf{r},t) = -\rho_0(\mathbf{r})\nabla \cdot \mathbf{u}(\mathbf{r},t) \tag{7.2b}$$

$$p(\mathbf{r},t) = c^2(\mathbf{r})\left[1 - \tau(\mathbf{r})\frac{\partial(-\nabla^2)^{\frac{y}{2}-1}}{\partial t} - \eta(\mathbf{r}(-\nabla^2)^{\frac{y+1}{2}-1})\right]\rho(\mathbf{r},t), \tag{7.2c}$$

with initial conditions $p(\mathbf{r},0) = p_0(\mathbf{r})$ and $\mathbf{u}(\mathbf{r},0) = 0$. Particle velocity and acoustic density are represented as $\mathbf{u}(\mathbf{r},t)$ and $\rho(\mathbf{r},t)$, respectively. Ambient density and sound speed are given by $\rho_0(\mathbf{r})$ and $c(\mathbf{r})$, respectively. The terms τ and η, called absorption and dispersion proportionality coefficients, are defined through the acoustic attenuation coefficient $\alpha(\mathbf{r})$ and the power law exponent y by the following equations:

$$\tau(\mathbf{r}) = 2\alpha(\mathbf{r})c(\mathbf{r})^{y-1} \quad \text{and} \quad \eta(\mathbf{r}) = 2\alpha(\mathbf{r})c(\mathbf{r})^{y}\tan\big(\frac{\pi y}{2}\big). \tag{7.3}$$

7.2.3 Image Reconstruction

The reconstruction problem can be derived as minimizing the following objective function with respect to the vector of concatenated initial pressure values at all pixel locations, $\mathbf{p_0}$ [70]:

$$E(\mathbf{p_0}) = \big(\mathbf{d} - g(\mathbf{p_0})\big)^T\mathbf{C_D^{-1}}\big(\mathbf{d} - g(\mathbf{p_0})\big) + \big(\mathbf{p_0} - \mathbf{p_a}\big)^T\mathbf{C_M^{-1}}\big(\mathbf{p_0} - \mathbf{p_a}\big). \tag{7.4}$$

The recorded and simulated received pressure fields, $\mathbf{d}$ and $g(\mathbf{p_0})$, are represented by a collection of concatenated received pressure traces $\begin{bmatrix} p_1 & p_2 & \dots & p_N \end{bmatrix}^T$ by N transducer elements. Note that the operator g denotes the wave propagation modeling described in Equation 7.3. The data covariance matrix $\mathbf{C_D}$ can be used to adjust the contributions of individual pressure data samples. For simplicity, we assume that all pressure samples are independent and have equal variance σ_D^2, thus $\mathbf{C_D} = \sigma_D^2\mathbf{I}$, with $\mathbf{I}$ being the identity matrix.

The second term of the objective function, $\big(\mathbf{p_0} - \mathbf{p_a}\big)^T\mathbf{C_M^{-1}}\big(\mathbf{p_0} - \mathbf{p_a}\big)$, acts as a regularizer that constraints the reconstruction algorithm to converge to the desired solution. Note that by manipulating this term, *a priori* information can be incorporated. Specifically, the matrix $\mathbf{C_M}$ adjusts the variations of individual initial pressure pixels, as well as the assumed correlation strengths for all possible pixel pairs. Given σ as standard deviation of all pixels, $C_{M_{ii}} = \sigma^2$ for any pixel i, $C_{M_{ij}} = \rho\sigma^2$ for pixels i and j that are in the same tissue type and are assumed to correlate by a correlation coefficient $0 \leq \rho \leq 1$, and $C_{M_{ij}} = 0$ otherwise. Segmentation data originating from B-mode or B-flow can be used to provide a grouping mechanism for pixels from the same region, *i.e.*correlated pixels. The initial guess for a reconstructed image can be assigned through the term $\mathbf{p_a}$.

In this work, minimization of the objective function in Equation 7.4 is achieved by the conjugate gradient method. The minimization process starts with a steepest descent ($\gamma_{\mathbf{m}}$) computation which can be done analytically as [70]:

$$\gamma_{\mathbf{m}} = \mathbf{C_M}\mathbf{G}^*\big[\mathbf{C_D^{-1}}\big(g(\mathbf{p_0}) - \mathbf{d}\big)\big] + \big(\mathbf{p_0} - \mathbf{p_a}\big), \tag{7.5}$$

where $\mathbf{G}$ is the Fréchet derivative of g. In the continuous domain, it has been shown that the adjoint of $\mathbf{G}$, *i.e.* $\mathbf{G}^*$, is calculated as [167], [168]:

$$\mathbf{G}^*[h]\bigg|_{\mathbf{r}'} = \hat{\rho}(\mathbf{r}', T) \tag{7.6}$$

for any pressure trace $h(\mathbf{r}, t)$ acting as the adjoint source that induces the adjoint density $\hat{\rho}(\mathbf{r}, t)$. The adjoint density can be simulated using exactly the same set of coupled-equations listed in Equation 7.2, except Equation 7.2b is replaced by Equation 7.7 below, where the adjoint source term $h(\mathbf{r}, t)$ is injected to Equation 7.2b as a time-reversed additive mass source term, namely:

$$\frac{\partial}{\partial t}\hat{\rho}(\mathbf{r}, t) = -\rho_0(\mathbf{r})\nabla \cdot \hat{\mathbf{u}}(\mathbf{r}, t) + h(\mathbf{r}, T - t), \tag{7.7}$$

with the initial conditions $\hat{p}(\mathbf{r},0) = \hat{\mathbf{u}}(\mathbf{r},0) = 0$. The accent $\hat{}$ denotes the result from the adjoint acoustic propagation equations.

Now, if we take $h(\mathbf{r},t) = \sum_{j=1}^{N} \sigma_D^2 \big(p(\mathbf{r_{Rj}},t) - d(\mathbf{r_{Rj}},t)\big)$, where $p(\mathbf{r},t)$ and $d(\mathbf{r},t)$ are the simulated and recorded received pressure traces and $\mathbf{r_{Rj}}$ denotes the location of the j^{th} ultrasound receiver, one can show that:

$$\mathbf{G}^* \big[\mathbf{C_D^{-1}}\big(g(\mathbf{p_0}) - \mathbf{d}\big)\big]\bigg|_{\mathbf{r'}} = \hat{\rho}(\mathbf{r'},T)/\Delta t, \tag{7.8}$$

where Δt denotes the simulation step size, which is necessary to scale from the unit of time in the continuous domain to the unit of sample in the discrete domain.

After the steepest descent is computed, one can apply the conjugate gradient algorithm as follows to obtain the initial pressure image at the $(n+1)^{th}$ iteration, $\mathbf{p_0}^{n+1}$:

$$\mathbf{p_0}^{n+1} = \mathbf{p_0}^{n} - \alpha_{n+1}\mathbf{v}^{n+1} \tag{7.9a}$$

$$\mathbf{v}^{n+1} = \gamma_{\mathbf{m}}^{n} - \beta_{n+1}\mathbf{v}^{n}. \tag{7.9b}$$

The parameter β_n is chosen according to the Polak and Ribiére formula such that vectors $\mathbf{v}^i, i = 1, 2, ..., (n+1)$ form conjugate bases [106]:

$$\beta_{n+1} = \frac{< \mathbf{C_M^{-1}}(\gamma_{\mathbf{m}}^{n+1} - \gamma_{\mathbf{m}}^{n}), \gamma_{\mathbf{m}}^{n+1} >}{< \mathbf{C_M^{-1}}\gamma_{\mathbf{m}}^{n}, \gamma_{\mathbf{m}}^{n} >}. \tag{7.10}$$

The step length $\alpha_{\mathbf{n}}$ is determined by the optimal line search method that yields the greatest objective function decrease along the direction $\mathbf{v}^{n+1}$:

$$\alpha_{n+1} = \frac{(\mathbf{v}^{n+1})^T \mathbf{C_M^{-1}} \gamma_{\mathbf{m}}^{n+1}}{(\mathbf{G_m}\mathbf{v}^{n+1})^T \mathbf{C_D^{-1}} (\mathbf{G_m}\mathbf{v}^{n+1}) + (\mathbf{v}^{n+1})^T \mathbf{C_M^{-1}} \mathbf{v}^{n+1}}. \tag{7.11}$$

7.2.4 Simulation Setup Details

7.2.4.1 Input Data Generation

Figures 7.2(a) and 7.2(b) show the initial pressure (column 1), sound speed (column 2), and mass density (column 3) distributions of two numerical phantoms used in the simulation studies. The image of segmented regions used for generating *a priori* information is displayed in column 4. The phantom image size and pixel size are 6 cm × 4 cm and 0.0781 mm, respectively.

(a): Numerical Disc-Shaped Objects

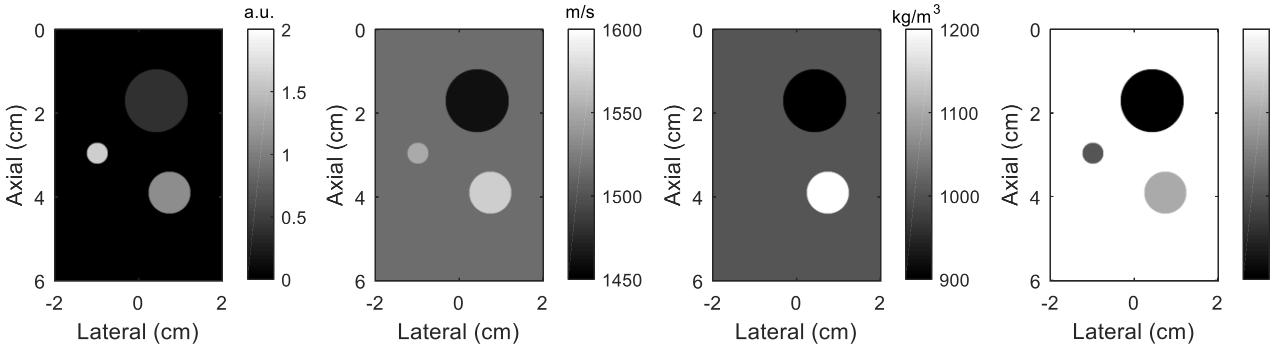

(b): Numerical Compressed Dense Breast

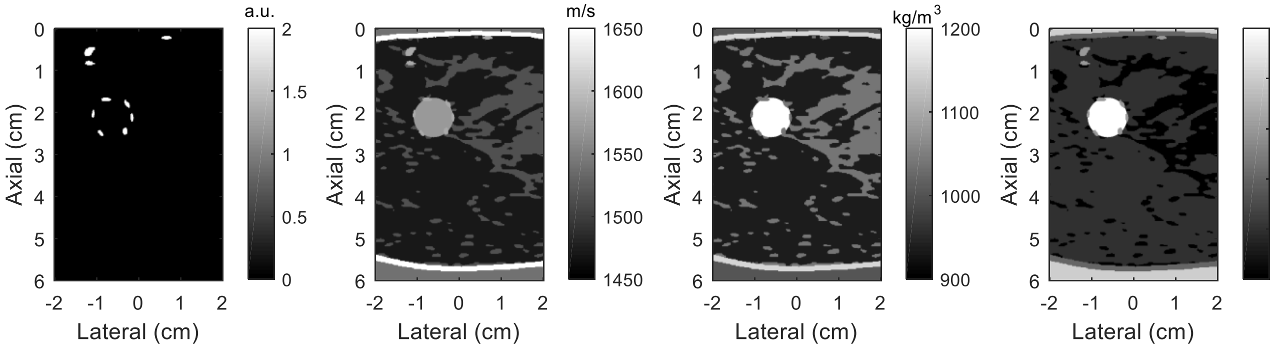

Figure 7.2: Two numerical phantoms used in this work, shown as (a) disc-shaped objects and (b) an anatomically realistic, compressed dense breast. Images on the columns 1, 2, 3, and 4 represent initial pressure, sound speed distribution, mass density distribution, and numbers labeling segmented regions, respectively.

The phantom shown in Figure 7.2(a) consists of 4 varying diameter disc-shaped

Table 7.1: The assigned initial pressure and acoustic properties of each region of the here employed numerical compressed dense breast. Sound speed and mass density values were obtained from [169]. The initial pressure was calculated by scaling down the optical absorption coefficient by a factor of 2/9. Refer to Figure 7.2(b), column 4 for region number.

Region	Initial pressure (a.u.)	Sound speed (m/s)	Mass density (kg/m^3)
Fibroglandular (1)	0.0089	1,515	1,040
Fat (2)	0.011	1,470	937
Skin (3)	0.018	1,650	1,150
Blood vessel(4)	2	1,584	1,040
Background (5)	0	1,500	1,000
Cancer (6)	0.009	1,570	1,100

objects. No acoustic attenuation was ascribed to this phantom. The disc-shaped structures were chosen as they resemble the cross-sections of spherical breast masses and cancers found in the clinic. The more complex phantom shown in Figure 7.2(b) was a 2D slice taken from an anatomically realistic, extremely dense 3D breast phantom [169]. The acoustic attenuation of this phantom was set to 0.75 dB/cm/MHz$^{1.5}$. Properties listed in Table 7.1 also apply to this phantom. The original breast phantom dimensions are 495, 615, and 752 voxels along the x, y, and z directions, respectively. However, in this work, we assumed that the breast was fixed and compressed along the axial (y) direction to mimic the compressed breast as found in x-ray mammography [6], [10]. Therefore, the original breast phantom was scaled by 0.55x and 1.2x along y and z directions, yielding the new dimensions of 495, 338, and 902 voxels along x, y, and z directions, respectively. One 2D slice was extracted along the y-axis from the compressed breast phantom at x = 400 and z = 200 to 452, and the extracted slice is shown in Figure 7.2(b). Note that since there is no cancer region in the original breast phantom, the cancer and its surrounding angiogenesis were generated artifically. This phantom should provide insight on the reconstruction performance in a more realistic case, and more importantly, in the case where regions of optical absorption are small and sparse.

The input pressure traces were generated with the actual initial pressure map, displayed in Figure 7.2. Such pressure traces were simulated based on Equation 7.2 using the k-Wave toolbox [109] that solves acoustic wave propagation based on a memory-efficient scheme called *k*-space pseudospectral method [100], [101]. The pressure trace was 75 µs long with 14 ns time step that corresponds to a 70.4 MHz sampling frequency.

The simulated transducer mimics the characteristics of a L7-4 linear array transducer (ATL/Philips, Bothell, WI). It has 128 elements on its approximately 4 cm wide aperture, and its frequency response was tapered using a Gaussian window with center frequency of 5 MHz and 70% bandwidth.

7.2.4.2 Reconstruction Settings

The reconstruction was accomplished by iteratively minimizing the objective function shown in Equation 7.4 and updating $\mathbf{p_0}$. The covariance matrix $\mathbf{C_D}$ was set to $\sigma_D^2\mathbf{I}$, where $\sigma_D = 0.01$ and $\mathbf{I}$ is the identity matrix. *A priori* information was setup by assigning the initial guess ($\mathbf{p_a}$) to zero-valued map, a non-negative correlation coefficient (ρ_k) and the standard deviation (σ) to 10 to allow a wide range of reconstructed pixel values. The reconstruction was run for 30 iterations. If $\rho > 0$ was used, the value of ρ will increase linearly, from 0 in the first iteration to the assigned value in the last iteration, as the iteration progresses.

Due to the band-limited transducer frequency response, the transducer receivers cannot accommodate all the frequency information from the broadband photoacoustic signals. Therefore, it is crucial to note that the received signals need to be first "recovered" before being entered into the reconstruction algorithm. The signal recovery process is called deconvolution that is achieved by the following relations [170]:

$$\mathcal{F}\{p(\mathbf{r},t)\} = H(f)\mathcal{F}\{\tilde{p}(\mathbf{r},t)\} \tag{7.12a}$$

$$\tilde{p}(\mathbf{r},t) \approx \mathcal{F}^{-1}\left\{ \frac{\mathcal{F}\{p(\mathbf{r},t)\}}{H(f)+\epsilon} W(f) \right\}, \tag{7.12b}$$

where $p(\mathbf{r},t)$ and $\tilde{p}(\mathbf{r},t)$ represent the band-limited received signal and recovered signal, respectively, and $H(f)$ refers to the transducer frequency response. $W(f)$ denotes the low-pass filter that suppresses the noise arising from deconvolution. Here, a Blackman filter with a frequency cutoff of 7.04 MHz was employed. The small positive parameter ϵ ensures that the denominator does not approach zero.

7.2.5 Simulation Studies

Three studies were performed on the two numerical phantoms shown in Figure 7.2:

1. Noiseless reconstructions

   Noiseless reconstructions were performed on both phantoms. Hereby we investigated the reconstruction accuracy obtained from 2 sets of sound speed and mass density distributions and 3 different correlation coefficients. The applied correlation coefficients ρ_k were 0, 0.0005, and 0.005. For each correlation coefficient value, initial pressure images were reconstructed based on heterogeneous (true) and homogeneous cases of sound speed and mass density distributions. The homogeneous acoustic distributions here represent the unknown sound speed and mass density maps, whose values were simply assigned by sound speed and mass density of the background. For reconstructions of the disc-shaped objects, the absolute percent errors of the reconstructed initial pressure value within each region was also calculated.

   Given the fact that it is difficult to segment small blood vessels in practice, additional reconstructions of numerical compressed dense breast phantom were also performed, where blood vessels are assumed as not identifiable. In these cases, blood vessels are lumped into the same segmented region as fat or cancer.

2. Noisy reconstructions

In this study, the amplitude and phase of the received signal was corrupted by Gaussian noise. The standard deviation of the Gaussian noise amplitude was calculates as 3% of the maximum absolute amplitude of all recovered pressure signals ($\tilde{p}(\mathbf{r}, t)$ in Equation 7.12b). The standard deviation of the Gaussian phase noise was calculated in units of the number of samples that corresponds to a 3% of the bandwidth of the transducer, *i.e.* $\approx 0.4\,\mu\mathrm{s}$ phase shift in the time domain. Effects of the received amplitude and phase errors on the reconstruction accuracy were investigated separately for each correlation coefficient ρ_k (0, 0.0005, and 0.005).

3. Effects of segmentation uncertainty on the reconstruction accuracy

   Performing segmentation on clinical B-mode or B-flow images can be much more challenging than the one performed here on simple disc-shaped phantoms, as aberration and low signal-to-noise ratio can cause ambiguous tissue boundaries and artifacts. For this reason, segmentation uncertainty was studied on a single 1-cm diameter disc placed in the center of the imaging field by imposing a boundary with zero correlation coefficient (uncertainty zone with $\rho_k = 0$) over the object boundary to generate the ambiguous boundary, as shown in Figure 7.3. The boundary thinkness was varied from 2 to 6 mm with 2 mm increments. Images were reconstructed with correlation coefficients ρ_k of 0.0005 and 0.005 in background and object regions, respectively. True sound speed and density distributions were utilized during the reconstruction. The true density was set to 1000 kg/m^3 throughout the image. The background's sound speed was set to 1515 m/s, and the object's sound speed was set to 1460 or 1570 m/s to reflect the negative and positive object's sound speed. For each reconstruction case, mean initial pressures were calculated from all the initial pressure pixels in the object region without uncertainty zone, and in the object region with uncertainty zone.

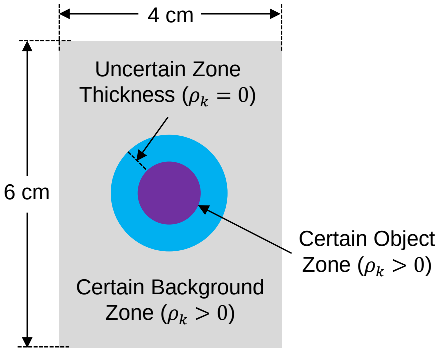

Figure 7.3: Inclusion of a segmentation uncertainty zone (zone with $\rho_k = 0$) between the certain object and background regions assigned with positive correlation coefficients.

7.3 Results and Discussion

7.3.1 Noiseless Reconstructions

7.3.1.1 Numerical Disc-Shaped Objects

Figure 7.4(a) shows the initial pressure reconstructions obtained with different correlation coefficients (ρ_k). Sound speed and mass density distributions were assumed to be heterogeneous and known. The calculated absolute percent errors of reconstructed initial pressure values of all discs are given in Table 7.2. As can be seen, using segmentation data as *a priori* information through applying positive correlation coefficients improves the reconstruction quality. Specifically, using higher correlation coefficients leads to more accurate reconstruction results and less limited-angle artifacts. This happens because, for any given set of pixels assumed to be correlated, $\mathbf{C_M}$ will promote the homogeneity across the corresponding elements in the steepest descent vector (Equation 7.5) that will be used later for updating that pixel group.

Figure 7.4(b) shows the reconstruction results equivalent to Figure 7.4(a), but with the unknown sound speed and mass density distributions, *i.e.* both were assigned to be homogeneous. For calculated absolute percent errors of reconstructed initial pres-

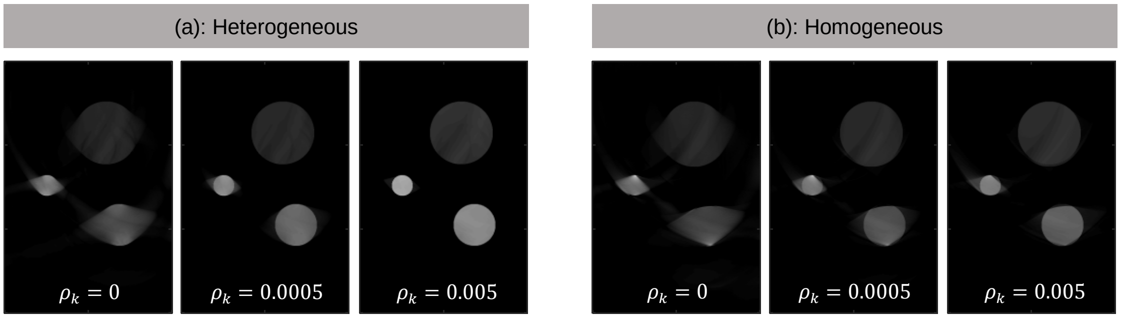

Figure 7.4: Reconstructed images of the numerical phantom containing disc-shaped objects, obtained from the indicated correlation coefficients (ρ_k) and sound speed distribution types (heterogeneous and homogeneous). The correlation coefficient value was increased linearly from 0 to the applied value as the reconstruction proceeds. Images are displayed in [0, 2] grayscale range.

sure values, see Table 7.2. It can be seen from both Figure 7.4(b) and Table 7.2 that using *a priori* information by enforcing a positive correlation coefficient helps in both, improving reconstruction accuracy and suppressing artifacts. However, unlike the reconstructions with heterogeneous distribution maps, the artifacts appearing in Figure 7.4(b) are the combined results of limited-angle artifacts and artifacts due to the wrong sound speed and mass density distribution assumption. Both types of artifacts start appearing during the early reconstruction iterations, where the correlation coefficient is low. However, when the correlation coefficient increases as the iteration proceeds, limited-angle artifacts can be suppressed effectively with a slight change of the objective value in Equation 7.4. This can be explained as suppressing the artifacts due to the wrong distribution assumption that will violate the homogeneity assumption made for the reconstruction algorithm and in turn detrimentally affect the objective value.

One can suppress the artifacts due to the wrong distribution assumption by setting fixed correlation coefficients to consistently enforce homogeneity within the groups of correlated pixels. However, this might lead to inaccurately reconstructed initial pressures in some other cases. For example, Figure 7.5 shows a comparison between (a) adaptive and (b) fixed correlation coefficients. The imaged phantom has true *homogeneous* (sound speed and mass density) distributions, but a truly *heterogeneous* optical absorption distribution. As can be seen from the reconstructions with fixed ρ_k, using higher ρ_k results in less accurate image, which is unexpected and opposite to the reconstructions with adaptive ρ_k. One of the possible reasons for this inaccuracy is because the steepest descent, shown in Equation 7.5, is a scaled version of the gradient by $\mathbf{C_M}$. The non-zero elements in the off-diagonal entries of $\mathbf{C_M}$, as a result of applying positive correlation coefficient, will cause the steepest descent vector pointing into a different direction than the original gradient vector. This directional difference could potentially add another complication when using the steepest descent vector to update the image that is farther from the true solution.

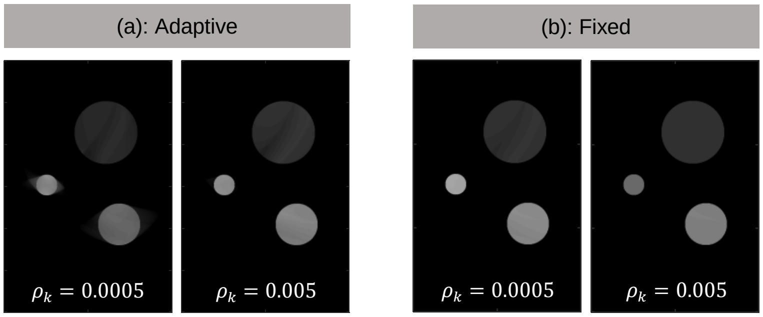

Figure 7.5: Reconstructed images of the numerical phantom for (a) adaptive and (b) fixed correlation coefficients (ρ_k). The sound speed and mass density distributions were assumed as homogeneous. Images are displayed on a [0, 2] grayscale range.

7.3.1.2 Numerical Compressed Dense Breast

Figures 7.6(a) and (b) show numerical compressed dense breast phantom images, reconstructed with heterogeneous and homogeneous sound speed and mass density, respectively. The attenuation coefficient was set as uniform and to 0.75

Table 7.2: Calculated percent error of the reconstructed initial pressure value ($\mathbf{p_0}$) within each region, obtained from reconstructions with different correlation coefficients (ρ_k). Refer to Figure 7.2(a), column 4 for region number.

Correlation (ρ_k) coefficient	Region number					
	Heterogeneous			Homogeneous		
	1	2	3	1	2	3
0	26.7	42.2	46.5	26.3	40.9	45.0
0.0005	20.1	34.9	28.0	20.3	36.1	29.0
0.005	3.65	19.8	3.36	4.97	32.4	9.65

dB/cm/MHz$^{1.5}$. It appears that when only small regions with high optical absorption are reconstructed, the original results with $\rho_k = 0$ are already similar to the true initial pressure given in Figure 7.2, structurally and quantitatively. In addition, using *a priori* information by applying positive correlation coefficient does not seem to give noticeable improvement. A similar effect is also demonstrated through the reconstructed images shown in Figures 7.6(c) and (d), obtained with the assumption that blood vessels are visually indistinguishable from fat and cancer regions and thus considered as parts of those surrounding tissues. This effect could be explained by the following facts. First, the smaller regions tend to generate less limited-angle artifacts than the larger ones. Second, from a mathematical point of view, adding *a priori* information, or in general, regularizing the optimization problem, will reduce an ill-posedness of the objective function [171]. Since the data term in Equation 7.4, $\big(\mathbf{d} - g(\mathbf{p_0})\big)^T \mathbf{C_D}^{-1} \big(\mathbf{d} - g(\mathbf{p_0})\big)$, is convex with respect to $\mathbf{p_0}$, this is already likely to facilitate convergence towards the true solution. Moreover, the regularization term $\big(\mathbf{p_0} - \mathbf{p_a}\big)^T \mathbf{C_M}^{-1} \big(\mathbf{p_0} - \mathbf{p_a}\big)$ does little help in reducing the ill-posedness when enforcing homogeneity in the small, high optical absorption regions. Nonetheless, for the same reason given to Figure 7.4, taking into account the heterogeneities of sound speed and mass density seems to slightly help in decreasing the reconstruction errors and artifacts. This suggests that small or granular regions can be omitted during segmentation for *a priori* information generation, and using the accurate distributions might be a more strict requirement to obtain accurate reconstructions.

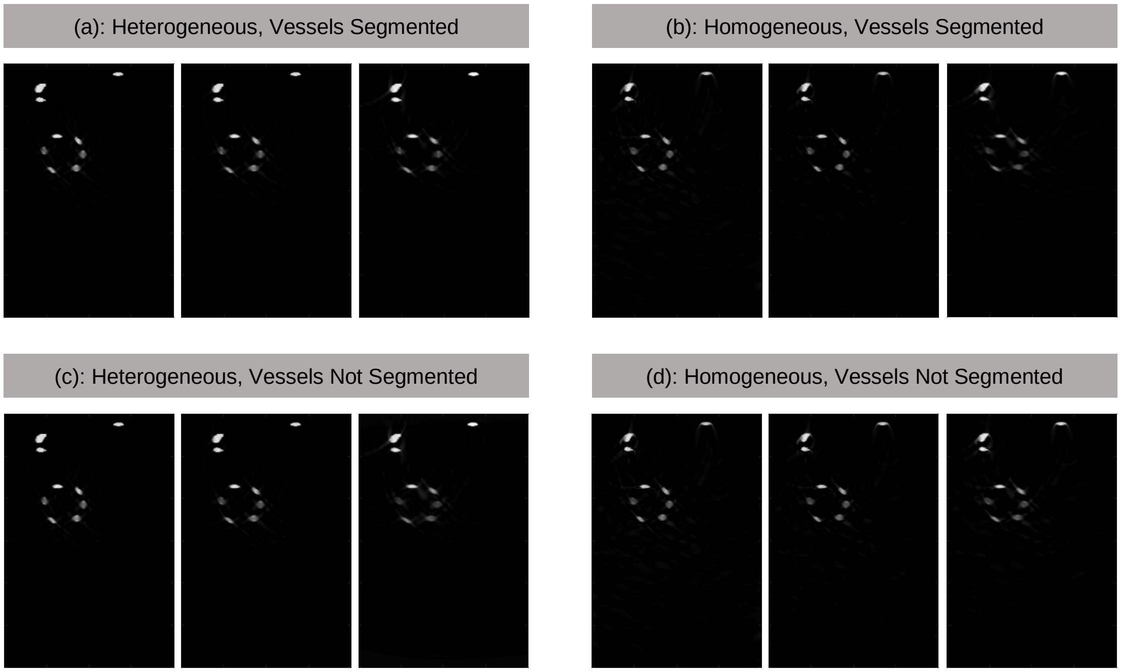

Figure 7.6: Reconstructed images of the numerical compressed dense breast phantom, obtained for different correlation coefficients ρ_k, distribution types, and segmentation structures. The correlation coefficient was increased linearly from 0 to the applied value as the reconstruction proceeds. Images are displayed on a [0, 2] grayscale range.

7.3.2 Noisy Reconstructions

Figures 7.7(a) and (b) show the reconstructed images obtained through repeating the noiseless reconstructions (Figure 7.4(a)) with heterogeneous sound speed and mass density distributions, except that here noisy received pressure traces were used as reconstruction inputs. The noiseless and corrupted signals received by the 100$^{\text{th}}$ transducer element (at 1.12 cm lateral position) are plotted in Figures 7.8(a) and (b)-(c), respectively. The calculated absolute percent errors of the reconstructed initial pressure values of all discs are given in Table 7.3 for all reconstruction cases. Visually, the zero-mean Gaussian phase noise induces amplitude variations in a lesser extent than compared to the zero-mean Gaussian amplitude noise that plays a more direct role in the amplitude variations. Therefore, the reconstruction results from the amplitude noise pressure dataset ($\rho = 0$ and 0.0005) look more grainy, than those from the phase noise.

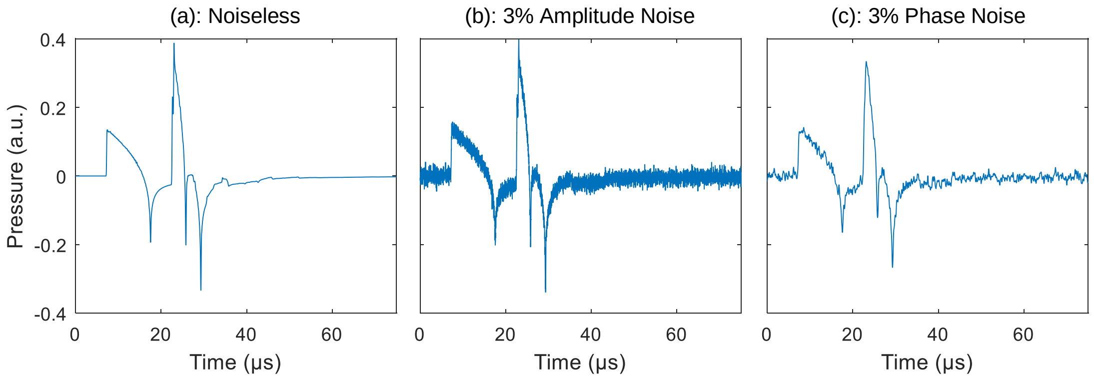

Figure 7.7: The (a) noiseless signal, (b) signal corrupted by 3% Gaussian amplitude noise, and (c) signal corrupted by 3% Gaussian phase noise, received by the 100th transducer element (at 1.12 cm lateral position). These signals are emitted from the numerical disc-shaped objects with a high optical absorption coefficient.

Nonetheless, it is clear that using *a priori* information does not only improve reconstruction accuracy, but also simultaneously suppresses limited-angle artifacts and noise. Also, as seen earlier in Section 7.3.1.1, applying higher spatial correlation enforces stronger homogeneity and thus reduces noise. This is because applying a positive correlation coefficient enforces the homogeneity within the pixels that belong to the same tissue type, *i.e.* same segmented group.

7.3.3 Effects of segmentation uncertainty on the reconstruction accuracy

Figure 7.9 shows the calculated initial pressure within the reconstructed object of interest, obtained at different uncertainty zone thicknesses, correlation coefficients, and types of sound speed contrast. According to Figures 7.9(a) and (c), it appears that the initial pressure calculated from pixels within the certain object region only

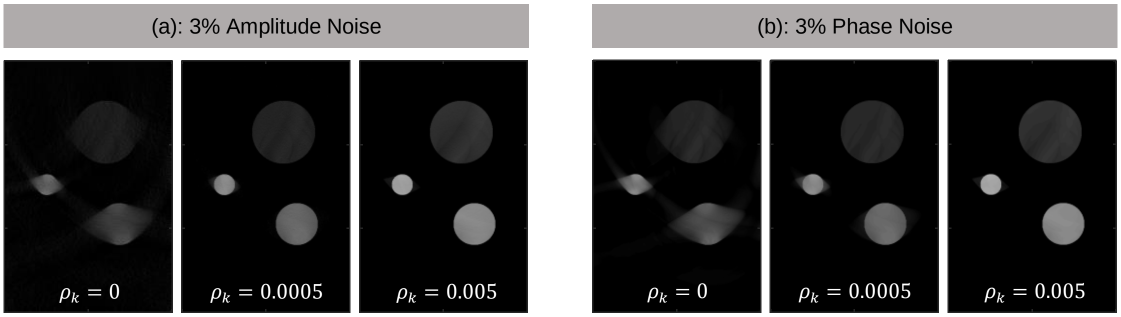

Figure 7.8: Reconstructed images of the numerical phantom containing numerical disc-shaped objects, obtained for different correlation coefficients (ρ_k) and received pressure input signals, corrupted by different types of transducer response noise. True (heterogeneous) sound speed and mass density distributions were used for reconstructions and the correlation coefficient was increased linearly from 0 to the indicated as the reconstruction proceeds. Images are displayed on a [0, 2] grayscale range.

Table 7.3: Calculated absolute percent error of the reconstructed initial pressure value ($\mathbf{p_0}$) within each region, obtained from reconstructions with different types of Gaussian noise. Refer to Figure 7.2(a), column 4 for region number.

Correlation (ρ_k) coefficient	Region number					
	3% amplitude noise			3% phase noise		
	1	2	3	1	2	3
0	45.5	54.7	58.1	26.7	42.2	46.5
0.0005	27.7	35.1	29.2	20.1	34.9	28.0
0.005	5.40	22.9	5.24	3.65	19.8	3.36

(uncertainty zone excluded) tends to be insensitive to the presence of the uncertainty zone. This could be attributed to the fact that zero correlation is assigned to the uncertainty zone that allows the pixels in that zone to variate easily, thus being able to absorb most of the reconstruction error. The reconstruction error in the uncertainty zone is further illustrated in Figures 7.9(b) and (d) that show the initial pressure calculated from pixels within the certain object region and the uncertainty zone. This suggests that it is still possible to utilize *a priori* information from segmentation data even though accurate segmentation cannot be achieved.

7.4 Conclusions

We have developed a full-wave photoacoustic tomography reconstruction, that allows inclusion of *a priori* information defined, for example, through segmentation of similar tissue types. Such segmentation can be done on images that are already available from other existing modes or modalities, such as B-mode and B-flow imaging techniques. We have shown that the use of *a priori* information can help in both improving reconstruction accuracy and reducing limited-angle artifacts as the additional *a priori* information will guide the reconstruction algorithm to approach the correct solution. This is especially helpful when handheld ultrasound arrays are used as they acquire less photoacoustic signal information compared to the ring ultrasound arrays. We have also demonstrated that, with deconvolution algorithms utilized, omitting the *a priori* information without degrading the reconstructed image quality is possible for small object sizes (Figure 7.6). However, this becomes more challenging for larger objects (approximately $\geq$ 5 mm diameter) as the limited-angle artifacts will show up more noticeably. So, even in the presence of recent deconvolution techniques, this is an example of the severe limitation of photoacoustics in the presence of limited bandwidth of sensitive ultrasound transducers. In addition, applying a positive correlation coefficient throughout all pixels belonging to the same tissue type will enforce

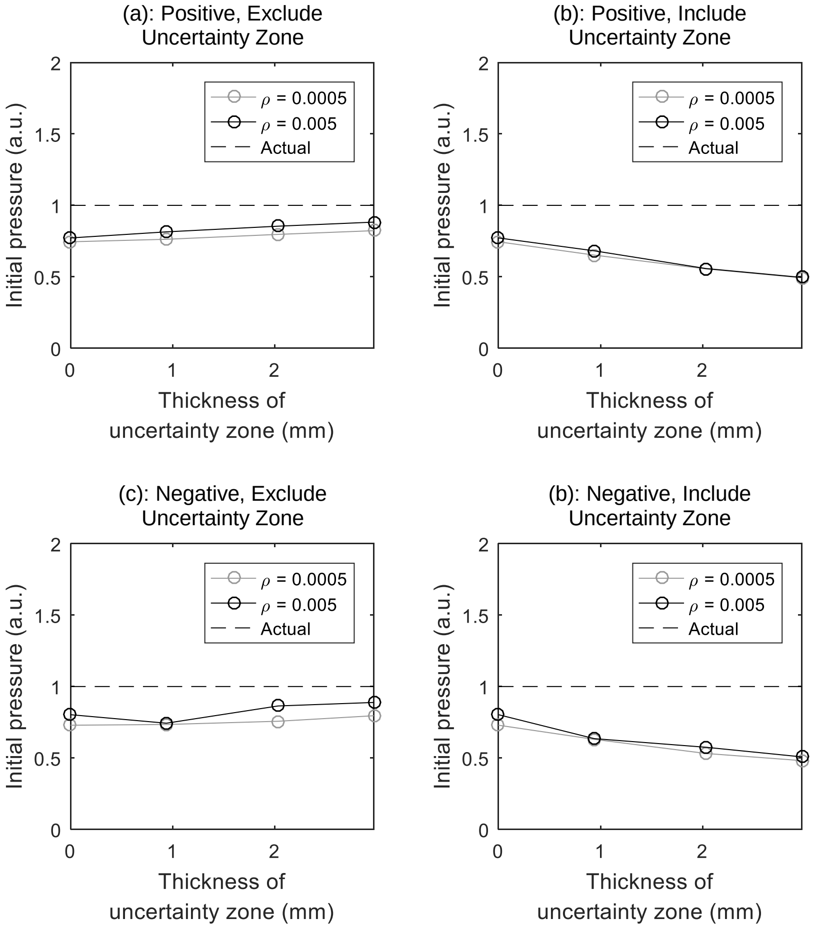

Figure 7.9: Initial pressure of a reconstructed disc-shaped object calculated from (a), (c) the initial pressure pixels within the certain object region only, and (b), (d) from the initial pressure pixels within the certain object region and uncertainty zone. Both positive and negative sound speed contrast objects were reconstructed under different correlation coefficient settings and uncertainty zone thicknesses.

more homogeneity within the segmented regions, and thus automatically reducing noise from the limited transducer response signal-to-noise ratio (SNR) (Figure 7.7) as well as some of the artifacts arising from the wrong sound speed and mass density distribution assumption (Figure 7.4).

Constructing *a priori* information based on segmentation and correlation coefficient assignment suggests several benefits. First, the segmentation process can be superficial, meaning that segmentation on small regions can be skipped to avoid an unnecessary and time-consuming task. For segmentation of larger regions, this can be successfully automated in many cases thanks to advances in segmentation techniques in the ultrasound field during the last decade [38], [60]. Second, the requirement of homogeneity within the segmented regions is flexible. Specifically, one can choose to apply a low correlation coefficient to segmented regions with ambiguous knowledge of optical heterogeneity. Third, noises from imperfect transducer response as well as artifacts due to the wrong acoustic distribution assumption can be suppressed via the heterogeneity constraint enforced by the positive correlation coefficient.

Even though the developed approach provides a proof-of-concept for a full-wave photoacoustic tomography reconstruction for handheld ultrasound arrays, it is still worthwhile for future work to investigate its performance on real datasets, for several reasons. Since real breast tissues are more heterogeneous and complex than the phantoms used in this work, segmentation can become difficult, and segmented regions may turn out to be acoustically and optically heterogeneous. Enforcing the homogeneity constraint on those regions thus no longer becomes effective. Furthermore, the noise models utilized in our simulation studies might not be realistic representations of all the actual noise types/sources found in physical experiments, such as laser light, imaged tissues, and signal acquisition hardware components. Most importantly, our simulation studies assume uniform laser fluence, which is mostly not the case in physical experiments. Both laser specifications and its placement play important role in the fluence, and accurate light transport modeling may be required to compensate any distorted fluence. Still, the developed photoacoustic image reconstruction approach and presented results shows potential clinical feasibility.

CHAPTER VIII

Conclusions

This dissertation primarily focuses on 1) investigating the accuracy and performance of our existing dual-sided ultrasound scanner, and 2) proposing various image reconstruction algorithms that can account for and correct complex acoustic phenomena. The latter utilizes pulse echo images as *a priori* information, but require a fair amount of computational resources and data storage.

Potential sources of error, which exist in the dual-sided ultrasound scanner and affect the accuracy of reconstructed images, were investigated in Chapters II and III. It has been shown that the most dominant error due to the transducer misplaced in the axial direction can be simply calibrated through a homogeneous transmission dataset. Less dominant mis-segmentations, which induce inaccuracies in *a priori* information of the reconstruction process, could potentially be minimized by using an appropriate ultrasound couplant or more advanced segmentation approaches specifically designed for breast images. Moreover, using an ultrasound couplant with acoustic properties similar to those of breast skin can help to reduce shadow area artifacts in B-mode imaging and potentially reveal important hidden structures.

Investigated image reconstruction approaches intended for dual-sided imaging, including sound speed, acoustic attenuation, and photoacoustic tomography. They are fully or partially based on full-wave modeling. This allows complex acoustic effects, such as reflection, diffraction, and scattering, to be modeled during data preprocessing (attenuation correction in Chapter V) or a reconstruction process (sound speed and photoacoustic tomography in Chapters IV, VI and VII). The ability to account for complex physics results in substantial improvements in image details. The original version of our sound speed waveform inversion algorithm, the most computationally and memory demanding, was also further optimized for drastic reduction in both computational and memory requirements. Moreover, the developed reconstruction algorithm is able to take advantage of existing pulse echo images as *a priori* information, allowing for further accuracy improvements. Also, note that photoacoustic tomography algorithms developed in this dissertation further demonstrate the potential combination of our dual-sided scanner to other modalities, at least to the optical imaging.

We believe that the rigorous investigations of the existing dual-sided ultrasound scanner as well as the development of advanced reconstruction algorithms suitable for this system could ultimately help improve the overall breast screening process in the clinic and bridge the gap between ultrasound and x-ray. However, there are some areas that still need to be considered in order to facilitate clinical translation in the future. Firstly, several simulation and reconstruction parameters do not accurately reflect imaging in realistic situations. Modeling the employed ultrasound transducer to have a low center frequency, an infinite-band frequency response, and a small number of point-like elements with omnidirectional sensitivity, is too optimistic. Such simplifications were done for reason of limited computing resources. Most of the simulation studies performed in Chapters III-VII also used the same grid spacing and acoustic propagation model for both input signal generation and image reconstruction procedures, making them susceptible to “inverse crime” [172] and perhaps leading to overly optimistic results.

Secondly, most of the investigated objects are based on a simple geometry. Even though they were modeled to mimic breast tissue or breast masses, their actual *in vivo* structure and acoustic properties can be much more complicated. Modeling *a priori* information, through segmentation of homogeneous regions in actual breast tissue on coresponding images (*e.g.*, B-mode, B-flow, or x-ray), will be challenging and prone to segmentation errors in many cases. This is very likely to occur due to the nature of breast tissue often being highly heterogeneous and due to ambiguous tissue boundaries. The compression force acting on the physical breast could also alter the acoustic distributions too, making it more difficult to evaluate the performance to preliminary techniques. With these two points in mind, applying the investigated findings and the developed reconstruction algorithms directly to the real scanning system and datasets can be extremely challenging. Nonetheless, all the work done in this dissertation should provide significant insight for further developments towards breast imaging in the clinic.

BIBLIOGRAPHY

BIBLIOGRAPHY

[1] R. L. Siegel, K. D. Miller, and A. Jemal, "Cancer statistics, 2018," *CA: A Cancer Journal for Clinicians*, vol. 68, no. 1, pp. 7–30, 2018, ISSN: 1542-4863. DOI: `10.3322/caac.21442`.

[2] N. R. Council *et al.*, *Saving women's lives: strategies for improving breast cancer detection and diagnosis*. National Academies Press, 2005.

[3] L. Watson, "Appropriate Use of Breast Imaging Modalities," *Radiologic Technology*, vol. 83, no. 4, pp. 371M–390M, 2012.

[4] E. M. Garcia, E. S. Storm, L. Atkinson, E. Kenny, and L. S. Mitchell, "Current Breast Imaging Modalities, Advances, and Impact on Breast Care," *Obstetrics and Gynecology Clinics of North America*, vol. 40, no. 3, pp. 429 –457, 2013, Breast Disorders, ISSN: 0889-8545. DOI: `https://doi.org/10.1016/j.ogc.2013.05.002`.

[5] M. L. Giger, M. F. Inciardi, A. Edwards, J. Papaioannou, K. Drukker, Y. Jiang, R. Brem, and J. B. Brown, "Automated Breast Ultrasound in Breast Cancer Screening of Women With Dense Breasts: Reader Study of Mammography-Negative and Mammography-Positive Cancers," *American Journal of Roentgenology*, vol. 206, no. 6, pp. 1341–1350, 2016, ISSN: 0361-803X. DOI: `10.2214/AJR.15.15367`. [Online]. Available: `https://doi.org/10.2214/AJR.15.15367`.

[6] P. L. Carson, F. Zafar, S. A. M. Verweij, W. M. Lee, M. M. Goodsitt, G. L. LeCarpentier, S. Sinha, F. M. Hooi, M. Roubidoux, and J. B. Fowlkes, "Dual sided automated ultrasound system in the mammographic geometry," in *2011 IEEE International Ultrasonics Symposium*, 2011, pp. 2134–2137. DOI: `10.1109/ULTSYM.2011.0529`.

[7] F. M. Hooi and P. L. Carson, "First-arrival traveltime sound speed inversion with a priori information," *Medical Physics*, vol. 41, no. 8Part1, 082 902–n/a, 2014, 082902, ISSN: 2473-4209. DOI: `10.1118/1.4885955`.

[8] F. M. Hooi, O. Kripfgans, and P. L. Carson, "Acoustic attenuation imaging of tissue bulk properties with a priori information," *The Journal of the Acoustical Society of America*, vol. 140, no. 3, pp. 2113–2122, 2016. DOI: `10.1121/1.4962983`.

[9] R. Jintamethasawat, Y. Zhu, O. D. Kripfgans, J. Yuan, M. M. Goodsitt, and P. L. Carson, "Limited Angle Breast Ultrasound Tomography with *A Priori* Information and Artifact Removal," in *Proc. SPIE*, vol. 10139, 2017, pp. 10139 –10139 –12. DOI: `10.1117/12.2253911`.

[10] E. D. Larson, W.-M. Lee, M. A. Roubidoux, M. M. Goodsitt, C. Lashbrook, F. Zafar, O. D. Kripfgans, K. Thomenius, and P. L. Carson, "Automated Breast Ultrasound: Dual-Sided Compared with Single-Sided Imaging," *Ultrasound in Medicine & Biology*, vol. 42, no. 9, pp. 2072 –2082, 2016, ISSN: 0301-5629. DOI: `https://doi.org/10.1016/j.ultrasmedbio.2016.05.001`.

[11] S. P. Sinha, M. A. Roubidoux, M. A. Helvie, A. V. Nees, M. M. Goodsitt, G. L. LeCarpentier, J. B. Fowlkes, C. L. Chalek, and P. L. Carson, "Multi-modality 3D breast imaging with X-Ray tomosynthesis and automated ultrasound," in *2007 29th Annual International Conference of the IEEE Engineering in Medicine and Biology Society*, 2007, pp. 1335–1338. DOI: `10.1109/IEMBS.2007.4352544`.

[12] Z. Xie, F. M. Hooi, J. B. Fowlkes, R. W. Pinsky, X. Wang, and P. L. Carson, "Combined Photoacoustic and Acoustic Imaging of Human Breast Specimens in the Mammographic Geometry," *Ultrasound in Medicine and Biology*, vol. 39, no. 11, pp. 2176 –2184, 2013, ISSN: 0301-5629. DOI: `https://doi.org/10.1016/j.ultrasmedbio.2013.05.018`.

[13] P. M. Morse and K. U. Ingard, *Theoretical Acoustics*. Princeton, NJ, USA: Princeton University Press, 1987, p. 949, ISBN: 9780691024011.

[14] A. D. Pierce, *Acoustics: An Introduction to Its Physical Principles and Applications*. Melville, NY, USA: Acoustical Society of America, 1989, p. 678, ISBN: 978-0883186121.

[15] P. Huthwaite, F. Simonetti, and N. Duric, "Combining time of flight and diffraction tomography for high resolution breast imaging: Initial invivo results (L)," *The Journal of the Acoustical Society of America*, vol. 132, no. 3, pp. 1249–1252, 2012. DOI: `10.1121/1.4742697`.

[16] C. Li, N. Duric, and L. Huang, "Breast Imaging Using Transmission Ultrasound: Reconstructing Tissue Parameters of Sound Speed and Attenuation," in *2008 International Conference on BioMedical Engineering and Informatics*, vol. 2, 2008, pp. 708–712. DOI: `10.1109/BMEI.2008.303`.

[17] C. Li, N. Duric, P. Littrup, and L. Huang, "In vivo Breast Sound-Speed Imaging with Ultrasound Tomography," *Ultrasound in Medicine & Biology*, vol. 35, no. 10, pp. 1615 –1628, 2009, ISSN: 0301-5629. DOI: `https://doi.org/10.1016/j.ultrasmedbio.2009.05.011`.

[18] P. Mojabi and J. LoVetri, "Ultrasound tomography for simultaneous reconstruction of acoustic density, attenuation, and compressibility profiles," *The Journal of the Acoustical Society of America*, vol. 137, no. 4, pp. 1813–1825, 2015. DOI: `10.1121/1.4913774`.

[19] R. G. Pratt, L. Huang, N. Duric, and P. Littrup, "Sound-speed and attenuation imaging of breast tissue using waveform tomography of transmission ultrasound data," in *Proc. SPIE*, vol. 6510, 2007, pp. 6510 –6510 –12. DOI: `10.1117/12.708789`.

[20] G. Y. Sandhu, C Li, O Roy, S Schmidt, and N Duric, "Frequency domain ultrasound waveform tomography: breast imaging using a ring transducer," *Physics in Medicine & Biology*, vol. 60, no. 14, p. 5381, 2015. DOI: `10.1088/0031-9155/60/14/5381`.

[21] J. Wiskin, D. T. Borup, S. A. Johnson, and M. Berggren, "Non-linear inverse scattering: High resolution quantitative breast tissue tomography," *The Journal of the Acoustical Society of America*, vol. 131, no. 5, pp. 3802–3813, 2012. DOI: `10.1121/1.3699240`.

[22] K. Wang, T. Matthews, F. Anis, C. Li, N. Duric, and M. A. Anastasio, "Waveform inversion with source encoding for breast sound speed reconstruction in ultrasound computed tomography," *IEEE Transactions on Ultrasonics, Ferroelectrics, and Frequency Control*, vol. 62, no. 3, pp. 475–493, 2015, ISSN: 0885-3010. DOI: `10.1109/TUFFC.2014.006788`.

[23] C. Calderon, D. Vilkomerson, R. Mezrich, K. F. Etzold, B. Kingsley, and M. Haskin, "Differences in the attenuation of ultrasound by normal, benign, and malignant breast tissue," *Journal of Clinical Ultrasound*, vol. 4, no. 4, pp. 249–254, 1976, ISSN: 1097-0096. DOI: `10.1002/jcu.1870040404`.

[24] R. Chivers and C. Hill, "Ultrasonic attenuation in human tissue," *Ultrasound in Medicine & Biology*, vol. 2, no. 1, pp. 25 –29, 1975, ISSN: 0301-5629. DOI: `https://doi.org/10.1016/0301-5629(75)90038-1`.

[25] S.-W. Huang and P.-C. Li, "Ultrasonic computed tomography reconstruction of the attenuation coefficient using a linear array," *IEEE Transactions on Ultrasonics, Ferroelectrics, and Frequency Control*, vol. 52, no. 11, pp. 2011–2022, 2005, ISSN: 0885-3010. DOI: `10.1109/TUFFC.2005.1561670`.

[26] R. J. Lavarello and M. L. Oelze, "Density imaging using inverse scattering," *The Journal of the Acoustical Society of America*, vol. 125, no. 2, pp. 793–802, 2009. DOI: `10.1121/1.3050249`.

[27] R. G. Barr, S. Destounis, L. B. Lackey, W. E. Svensson, C. Balleyguier, and C. Smith, "Evaluation of Breast Lesions Using Sonographic Elasticity Imaging," *Journal of Ultrasound in Medicine*, vol. 31, no. 2, pp. 281–287, 2012, ISSN: 1550-9613. DOI: `10.7863/jum.2012.31.2.281`.

[28] I. Cspedes, J. Ophir, H. Ponnekanti, and N. Maklad, "Elastography: Elasticity Imaging Using Ultrasound with Application to Muscle and Breast in Vivo," *Ultrasonic Imaging*, vol. 15, no. 2, pp. 73–88, 1993, PMID: 8346612. DOI: `10.1177/016173469301500201`.

[29] M. Tanter, J. Bercoff, A. Athanasiou, T. Deffieux, J.-L. Gennisson, G. Montaldo, M. Muller, A. Tardivon, and M. Fink, "Quantitative Assessment of Breast Lesion Viscoelasticity: Initial Clinical Results Using Supersonic Shear Imaging," *Ultrasound in Medicine and Biology*, vol. 34, no. 9, pp. 1373–1386, 2008. DOI: `10.1016/j.ultrasmedbio.2008.02.002`.

[30] M. André, C. Barker, N. Sekhon, J. Wiskin, D. Borup, and K. Callahan, "Pre-Clinical Experience with Full-Wave Inverse-Scattering for Breast Imaging," in *Acoustical Imaging*, I. Akiyama, Ed., Dordrecht: Springer Netherlands, 2009, pp. 73–80, ISBN: 978-1-4020-8823-0.

[31] N. Duric, P. Littrup, C. Li, O. Rama, L. Bey-Knight, S. Schmidt, and J. Lupinacci, "Detection and characterization of breast masses with ultrasound tomography: clinical results," in *Proc. SPIE*, vol. 7265, 2009, pp. 7265 –7265 –8. DOI: `10.1117/12.812994`.

[32] C. Li, G. Y. Sandhu, M. Boone, and N. Duric, "Breast imaging using waveform attenuation tomography," in *Proc. SPIE*, vol. 10139, 2017, pp. 10139 –10139 –9. DOI: `10.1117/12.2255569`.

[33] O. Roy, I. Jovanović, A. Hormati, R. Parhizkar, and M. Vetterli, "Sound speed estimation using wave-based ultrasound tomography: theory and GPU implementation," in *Proc. SPIE*, vol. 7629, 2010, pp. 7629 –7629 –12. DOI: `10.1117/12.844691`.

[34] N. V. Ruiter, M. Zapf, R. Dapp, T. Hopp, W. A. Kaiser, and H. Gemmeke, "First results of a clinical study with 3D ultrasound computer tomography," in *2013 IEEE International Ultrasonics Symposium (IUS)*, 2013, pp. 651–654. DOI: `10.1109/ULTSYM.2013.0168`.

[35] G. Y. S. Sandhu, C. Li, O. Roy, E. West, K. Montgomery, M. Boone, and N. Duric, "Frequency-domain ultrasound waveform tomography breast attenuation imaging," in *Proc. SPIE*, vol. 9790, 2016, pp. 9790 –9790 –12. DOI: `10.1117/12.2218374`.

[36] J. W. Wiskin, D. T. Borup, E. Iuanow, J. Klock, and M. W. Lenox, "3-D Nonlinear Acoustic Inverse Scattering: Algorithm and Quantitative Results," *IEEE Transactions on Ultrasonics, Ferroelectrics, and Frequency Control*, no. 8, pp. 1161–1174, 2017, ISSN: 0885-3010. DOI: `10.1109/TUFFC.2017.2706189`.

[37] T. Hopp, N. Duric, and N. Ruiter, "Image fusion of Ultrasound Computer Tomography volumes with X-ray mammograms using a biomechanical model based 2D/3D registration," *Computerized Medical Imaging and Graphics*, vol. 40, no. Supplement C, pp. 170 –181, 2015, ISSN: 0895-6111. DOI: `https://doi.org/10.1016/j.compmedimag.2014.10.005`.

[38] J. A. Noble and D. Boukerroui, "Ultrasound image segmentation: a survey," *IEEE Transactions on Medical Imaging*, vol. 25, no. 8, pp. 987–1010, 2006, ISSN: 0278-0062. DOI: `10.1109/TMI.2006.877092`.

[39] R. Jintamethasawat, X. Zhang, P. L. Carlson, M. A. Roubidoux, and O. D. Kripfgans, "Acoustic beam anomalies in automated breast imaging," *Journal of Medical Imaging*, vol. 4, pp. 4 –4 –10, 2017. DOI: `10.1117/1.JMI.4.4.045001`.

[40] R. Jintamethasawat, W.-M. Lee, P. L. Carson, F. M. Hooi, J. B. Fowlkes, M. M. Goodsitt, R. Sampson, T. F. Wenisch, S. Wei, J. Zhou, C. Chakrabarti, and O. D. Kripfgans, "Error Analysis of Speed of Sound Reconstruction in Ultrasound Limited Angle Transmission Tomography," *Ultrasonics*, In press.

[41] R. Jintamethasawat, O. D. Kripfgans, J. B. Fowlkes, and P. L. Carson, "3D Corrections for Reconstruction of Bulk Tissue Attenuation Coefficients," Submitted.

[42] R. L. Siegel, K. D. Miller, and A. Jemal, "Cancer statistics, 2016," *CA: A Cancer Journal for Clinicians*, vol. 66, no. 1, pp. 7–30, 2016, ISSN: 1542-4863. DOI: `10.3322/caac.21332`.

[43] P. B. Gordon and S. L. Goldenberg, "Malignant breast masses detected only by ultrasound. A retrospective review," *Cancer*, vol. 76, no. 4, pp. 626–630, 1995, ISSN: 1097-0142. DOI: `10.1002/1097-0142(19950815)76:4<626::AID-CNCR2820760413>3.0.CO;2-Z`.

[44] N. Cho, W. K. Moon, J. H. Cha, S. M. Kim, B.-K. Han, E.-K. Kim, M. H. Kim, S. Y. Chung, H.-Y. Choi, and J.-G. Im, "Differentiating Benign from Malignant Solid Breast Masses: Comparison of Two-dimensional and Three-dimensional US," *Radiology*, vol. 240, no. 1, pp. 26–32, 2006, PMID: 16684920. DOI: `10.1148/radiol.2401050743`.

[45] D. T. Blackstock, *Fundamentals of Physical Acoustics*, 1st ed. Hoboken, NJ, USA: John Wiley and Sons, Inc., 2000, p. 568, ISBN: 978-0-471-31979-5.

[46] F. Jensen, W. Kuperman, M. Porter, and H. Schmidt, *Computational Ocean Acoustics*, 2nd ed. New York, NY, USA: Springer-Verlag New York, 2011, p. 794, ISBN: 978-1-4419-8677-1.

[47] R. H. Randall, *An Introduction to Acoustics*. Mineola, NY, USA: Dover Publications, 2005, p. 368, ISBN: 9780486442518.

[48] S. Temkin, *Elements of Acoustics*. Melville, NY, USA: Acoustical Society of America, 2001, p. 515, ISBN: 978-1563969973.

[49] M. D. Lagios, E. A. Gates, P. R. Westdahl, V. Richards, and B. S. Alpert, "A guide to the frequency of nipple involvement in breast cancer: A study of 149 consecutive mastectomies using a serial subgross and correlated radiographic technique", journal = "The American Journal of Surgery," vol. 138, no. 1, pp. 135 –142, 1979, ISSN: 0002-9610. DOI: `https://doi.org/10.1016/0002-9610(79)90253-8`.

[50] C. Laronga, B. Kemp, D. Johnston, G. L. Robb, and S. E. Singletary, "The incidence of occult nipple-areola complex involvement in breast cancer patients receiving a skin-sparing mastectomy," *Annals of Surgical Oncology*, vol. 6, no. 6, pp. 609–613, 1999.

[51] T. Morimoto, K. Komaki, K. Inui, A. Umemoto, H. Yamamoto, K. Harada, and K. Inoue, "Involvement of nipple and areola in early breast cancer," *Cancer*, vol. 55, no. 10, pp. 2459–2463, 1985, ISSN: 1097-0142. DOI: `10.1002/1097-0142(19850515)55:10<2459::AID-CNCR2820551025>3.0.CO;2-L`.

[52] H. Ulger, N. Erdogan, S. Kumanlioglu, and E. Unur, "Effect of age, breast size, menopausal and hormonal status on mammographic skin thickness," *Skin Research and Technology*, vol. 9, no. 3, pp. 284–289, 2003, ISSN: 1600-0846. DOI: `10.1034/j.1600-0846.2003.00027.x`.

[53] S. Willson, E. Adam, and A. Tucker, "Patterns of breast skin thickness in normal mammograms," *Clinical Radiology*, vol. 33, no. 6, pp. 691 –693, 1982, ISSN: 0009-9260. DOI: `https://doi.org/10.1016/S0009-9260(82)80407-8`.

[54] J. F. Krucker, J. B. Fowlkes, and P. L. Carson, "Sound speed estimation using automatic ultrasound image registration," *IEEE Transactions on Ultrasonics, Ferroelectrics, and Frequency Control*, vol. 51, no. 9, pp. 1095–1106, 2004, ISSN: 0885-3010. DOI: `10.1109/TUFFC.2004.1334842`.

[55] A. F. Prokop, S. Vaezy, M. L. Noble, P. J. Kaczkowski, R. W. Martin, and L. A. Crum, "Polyacrylamide gel as an acoustic coupling medium for focused ultrasound therapy," *Ultrasound in Medicine & Biology*, vol. 29, no. 9, pp. 1351 –1358, 2003, ISSN: 0301-5629. DOI: `https://doi.org/10.1016/S0301-5629(03)00979-7`.

[56] F. Foster, M. Strban, and G. Austin, "The ultrasound macroscope: Initial studies of breast tissue,"

[57] J. F. Greenleaf and R. C. Bahn, "Clinical Imaging with Transmissive Ultrasonic Computerized Tomography," *IEEE Transactions on Biomedical Engineering*, vol. BME-28, no. 2, pp. 177–185, 1981, ISSN: 0018-9294. DOI: `10.1109/TBME.1981.324789`.

[58] A. L. Scherzinger, R. A. Belgam, P. L. Carson, C. R. Meyer, J. V. Sutherland, F. L. Bookstein, and T. M. Silver, "Assessment of ultrasonic computed tomography in symptomatic breast patients by discriminant analysis," *Ultrasound in Medicine & Biology*, vol. 15, no. 1, pp. 21 –28, 1989, ISSN: 0301-5629. DOI: `https://doi.org/10.1016/0301-5629(89)90128-2`.

[59] C. Glide, N. Duric, and P. Littrup, "Novel approach to evaluating breast density utilizing ultrasound tomography," *Medical Physics*, vol. 34, no. 2, pp. 744–753, 2007, ISSN: 2473-4209. DOI: `10.1118/1.2428408`.

[60] P. Gu, W.-M. Lee, M. A. Roubidoux, J. Yuan, X. Wang, and P. L. Carson, "Automated 3D ultrasound image segmentation to aid breast cancer image interpretation," *Ultrasonics*, vol. 65, no. Supplement C, pp. 51 –58, 2016, ISSN: 0041-624X. DOI: `https://doi.org/10.1016/j.ultras.2015.10.023`.

[61] S. Schmidt, N. Duric, C. Li, O. Roy, and Z.-F. Huang, "Modification of Kirchhoff migration with variable sound speed and attenuation for acoustic imaging of media and application to tomographic imaging of the breast," *Medical Physics*, vol. 38, no. 2, pp. 998–1007, 2011, ISSN: 2473-4209. DOI: `10.1118/1.3539552`.

[62] N. Duric, N. Boyd, P. Littrup, M. Sak, L. Myc, C. Li, E. West, S. Minkin, L. Martin, M. Yaffe, S. Schmidt, M. Faiz, J. Shen, O. Melnichouk, Q. Li, and T. Albrecht, "Breast density measurements with ultrasound tomography: A comparison with film and digital mammography," *Medical Physics*, vol. 40, no. 1, 013 501–n/a, 2013, 013501, ISSN: 2473-4209. DOI: `10.1118/1.4772057`.

[63] N. Duric, P. Littrup, L. Poulo, A. Babkin, R. Pevzner, E. Holsapple, O. Rama, and C. Glide, "Detection of breast cancer with ultrasound tomography: First results with the Computed Ultrasound Risk Evaluation (CURE) prototype," *Medical Physics*, vol. 34, no. 2, pp. 773–785, 2007, ISSN: 2473-4209. DOI: `10.1118/1.2432161`.

[64] M. Haynes and M. Moghaddam, "Large-Domain, Low-Contrast Acoustic Inverse Scattering for Ultrasound Breast Imaging," *IEEE Transactions on Biomedical Engineering*, vol. 57, no. 11, pp. 2712–2722, 2010, ISSN: 0018-9294. DOI: `10.1109/TBME.2010.2059023`.

[65] R. J. Lavarello and M. L. Oelze, "Density imaging using inverse scattering," *The Journal of the Acoustical Society of America*, vol. 125, no. 2, pp. 793–802, 2009. DOI: `10.1121/1.3050249`.

[66] Y. Levy, Y. Agnon, and H. Azhari, "Ultrasonic Speed of Sound Dispersion Imaging," *Ultrasound in Medicine & Biology*, vol. 33, no. 5, pp. 762 –767, 2007, ISSN: 0301-5629. DOI: `https://doi.org/10.1016/j.ultrasmedbio.2006.11.016`.

[67] M. Andr, J. Wiskin, D. Borup, S. Johnson, H. Ojeda-Fournier, and L. Olson, "Quantitative volumetric breast imaging with 3D inverse scatter computed tomography," in *2012 Annual International Conference of the IEEE Engineering in Medicine and Biology Society*, 2012, pp. 1110–1113. DOI: `10.1109/EMBC.2012.6346129`.

[68] J. Nebeker and T. R. Nelson, "Imaging of Sound Speed Using Reflection Ultrasound Tomography," *Journal of Ultrasound in Medicine*, vol. 31, no. 9, pp. 1389–1404, 2012, ISSN: 1550-9613. DOI: `10.7863/jum.2012.31.9.1389`.

[69] G. L. LeCarpentier, M. M. Goodsitt, S. Verweij, J. Li, F. R. Padilla, and P. L. Carson, "Acoustic Performance of Mesh Compression Paddles for a Multimodality Breast Imaging System," *Ultrasound in Medicine & Biology*, vol. 40, no. 7, pp. 1503 –1511, 2014, ISSN: 0301-5629. DOI: `https://doi.org/10.1016/j.ultrasmedbio.2013.03.014`.

[70] A. Tarantola, *Inverse problem theory and methods for model parameter estimation.* Philadelphia, PA, USA: Society for Industrial and Applied Mathematics, 2005, p. 342, ISBN: 0-89871-572-5.

[71] L. Huang, J. Shin, T. Chen, Y. Lin, K. Gao, M. Intrator, and K. Hanson, "Breast ultrasound tomography with two parallel transducer arrays," in *Proc. SPIE*, vol. 9783, 2016, pp. 9783 –9783 –12. DOI: `10.1117/12.2216531`.

[72] M. S. Hassouna and A. A. Farag, "MultiStencils Fast Marching Methods: A Highly Accurate Solution to the Eikonal Equation on Cartesian Domains," *IEEE Transactions on Pattern Analysis and Machine Intelligence*, vol. 29, no. 9, pp. 1563–1574, 2007, ISSN: 0162-8828. DOI: `10.1109/TPAMI.2007.1154`.

[73] V. Červený and I. Pšenčík, "Seismic, Ray Theory," in *Encyclopedia of Solid Earth Geophysics*, H. K. Gupta, Ed. Dordrecht: Springer Netherlands, 2011, pp. 1244–1258, ISBN: 978-90-481-8702-7. DOI: `10.1007/978-90-481-8702-7_53`.

[74] M. Haynes, S. A. M. Verweij, M. Moghaddam, and P. L. Carson, "Self-characterization of commercial ultrasound probes in transmission acoustic inverse scattering: transducer model and volume integral formulation," *IEEE Transactions on Ultrasonics, Ferroelectrics, and Frequency Control*, vol. 61, no. 3, pp. 467–480, 2014, ISSN: 0885-3010. DOI: `10.1109/TUFFC.2014.2931`.

[75] C. Li, L. Huang, N. Duric, H. Zhang, and C. Rowe, "An improved automatic time-of-flight picker for medical ultrasound tomography," *Ultrasonics*, vol. 49, no. 1, pp. 61 –72, 2009, ISSN: 0041-624X. DOI: `https://doi.org/10.1016/j.ultras.2008.05.005`.

[76] J. Tong, M. J. W. Povey, X. Zou, B. Ward, and C. P. Oates, "Speed of sound and density of ethanol-water mixture across the temperature range 10 to 50 degrees Celsius," *Journal of Physics: Conference Series*, vol. 279, no. 1, p. 012 023, 2011.

[77] A. Giacomini, "Ultrasonic Velocity in EthanolWater Mixtures," *The Journal of the Acoustical Society of America*, vol. 19, no. 4, pp. 701–702, 1947. DOI: `10.1121/1.1916541`.

[78] A. R. Selfridge, "Approximate Material Properties in Isotropic Materials," *IEEE Transactions on Sonics and Ultrasonics*, vol. 32, no. 3, pp. 381–394, 1985, ISSN: 0018-9537. DOI: `10.1109/T-SU.1985.31608`.

[79] D. Marioli, C. Narduzzi, C. Offelli, D. Petri, E. Sardini, and A. Taroni, "Digital time-of-flight measurement for ultrasonic sensors," *IEEE Transactions on Instrumentation and Measurement*, vol. 41, no. 1, pp. 93–97, 1992, ISSN: 0018-9456. DOI: `10.1109/19.126639`.

[80] B. Xu, L. Yu, and V. Giurgiutiu, "Advanced Methods for Time-Of-Flight Estimation with Application to Lamb Wave Structural Health Monitoring," in *7th International Workshop on Structural Health Monitoring*, 2009, 12021209.

[81] G. DArrigo and A. Paparelli, "Sound propagation in waterethanol mixtures at low temperatures. I. Ultrasonic velocity," *The Journal of Chemical Physics*, vol. 88, no. 1, pp. 405–415, 1988. DOI: `10.1063/1.454616`.

[82] B. Liu and A. B. Koc, "Ultrasonic Determination of Water Concentration in Ethanol Fuel Using Artificial Neural Networks," *Transactions of the ASABE*, vol. 55, no. 5, p. 1865, 2012, ISSN: 2151-0032.

[83] AlcoDens. (2018). Alcohol Gauging and Blending Calculations, [Online]. Available: `https://www.katmarsoftware.com/alcodens.htm` (visited on 02/25/2018).

[84] N. Osborne, E. McKelvy, and H. Bearce, "The density and thermal expansion of ethyl alcohol and its mixtures with water," *National Bureau of Standards*, vol. 9, pp. 327 –474, 1913. DOI: `https://doi.org/10.1016/S0016-0032(13)90867-X`.

[85] M. Birk, R. Dapp, N. Ruiter, and J. Becker, "GPU-based iterative transmission reconstruction in 3D ultrasound computer tomography," *Journal of Parallel and Distributed Computing*, vol. 74, no. 1, pp. 1730 –1743, 2014, ISSN: 0743-7315. DOI: `https://doi.org/10.1016/j.jpdc.2013.09.007`.

[86] F. Simonetti, L. Huang, N. Duric, and P. Littrup, "Diffraction and coherence in breast ultrasound tomography: A study with a toroidal array," *Medical Physics*, vol. 36, no. 7, pp. 2955–2965, ISSN: 2473-4209. DOI: `10.1118/1.3148533`. [Online]. Available: `http://dx.doi.org/10.1118/1.3148533`.

[87] B. Ranger, P. J. Littrup, N. Duric, P. Chandiwala-Mody, C. Li, S. Schmidt, and J. Lupinacci, "Breast Ultrasound Tomography Versus MRI for Clinical Display of Anatomy and Tumor Rendering: Preliminary Results," *American Journal of Roentgenology*, vol. 198, no. 1, pp. 233–239, 2012, ISSN: 0361-803X. DOI: `10.2214/AJR.11.6910`. [Online]. Available: `https://doi.org/10.2214/AJR.11.6910`.

[88] P. Huthwaite and F. Simonetti, "High-resolution imaging without iteration: a fast and robust method for breast ultrasound tomography," *The Journal of the Acoustical Society of America*, vol. 130, no. 3, pp. 1721–1734, 2011. DOI: `10.1121/1.3613936`.

[89] H. Gemmeke and N. Ruiter, "3D ultrasound computer tomography for medical imaging," *Nuclear Instruments and Methods in Physics Research Section A: Accelerators, Spectrometers, Detectors and Associated Equipment*, vol. 580, no. 2, pp. 1057 –1065, 2007, Imaging 2006, ISSN: 0168-9002. DOI: `https://doi.org/10.1016/j.nima.2007.06.116`.

[90] N. Ozmen, R. Dapp, M. Zapf, H. Gemmeke, N. V. Ruiter, and K. W. A. van Dongen, "Comparing different ultrasound imaging methods for breast cancer detection," *IEEE Transactions on Ultrasonics, Ferroelectrics, and Frequency Control*, vol. 62, no. 4, pp. 637–646, 2015, ISSN: 0885-3010. DOI: `10.1109/TUFFC.2014.006707`.

[91] M. K. Feldman, S. Katyal, and M. S. Blackwood, "US Artifacts," *RadioGraphics*, vol. 29, no. 4, pp. 1179–1189, 2009, PMID: 19605664. DOI: `10.1148/rg.294085199`.

[92] M. E. Anderson, M. S. McKeag, and G. E. Trahey, "The impact of sound speed errors on medical ultrasound imaging," *The Journal of the Acoustical Society of America*, vol. 107, no. 6, pp. 3540–3548, 2000. DOI: `10.1121/1.429422`.

[93] R. G. Barr, A. Rim, R. Graham, W. Berg, and J. R. Grajo, "Speed of Sound Imaging: Improved Image Quality in Breast Sonography," *Ultrasound Quarterly*, vol. 25, no. 3, 2009.

[94] J. A. Baker, M. S. Soo, and E. L. Rosen, "Artifacts and Pitfalls in Sonographic Imaging of the Breast," *American Journal of Roentgenology*, vol. 176, no. 5, pp. 1261–1266, 2001, ISSN: 0361-803X. DOI: `10.2214/ajr.176.5.1761261`.

[95] Y. Huang, M. K. Ng, and Y.-W. Wen, "A Fast Total Variation Minimization Method for Image Restoration," *Multiscale Modeling & Simulation*, vol. 7, no. 2, pp. 774–795, 2008. DOI: `10.1137/070703533`.

[96] Y. Lin and L. Huang, "Acoustic- and elastic-waveform inversion using a modified total-variation regularization scheme," *Geophysical Journal International*, vol. 200, no. 1, pp. 489–502, 2015. DOI: `10.1093/gji/ggu393`.

[97] T. Goldstein and S. Osher, "The Split Bregman Method for L1-Regularized Problems," *SIAM Journal on Imaging Sciences*, vol. 2, no. 2, pp. 323–343, 2009. DOI: `10.1137/080725891`.

[98] B. E. Treeby, J. Jaros, A. P. Rendell, and B. T. Cox, "Modeling nonlinear ultrasound propagation in heterogeneous media with power law absorption using a k-space pseudospectral method," *The Journal of the Acoustical Society of America*, vol. 131, no. 6, pp. 4324–4336, 2012. DOI: `10.1121/1.4712021`.

[99] B. E. Treeby and B. T. Cox, "Modeling power law absorption and dispersion for acoustic propagation using the fractional Laplacian," *The Journal of the Acoustical Society of America*, vol. 127, no. 5, pp. 2741–2748, 2010. DOI: `10.1121/1.3377056`.

[100] N. N. Bojarski, "The k-space formulation of the scattering problem in the time domain," *The Journal of the Acoustical Society of America*, vol. 72, no. 2, pp. 570–584, 1982. DOI: `10.1121/1.388038`.

[101] M. Tabei, T. D. Mast, and R. C. Waag, "A k-space method for coupled first-order acoustic propagation equations," *The Journal of the Acoustical Society of America*, vol. 111, no. 1, pp. 53–63, 2002. DOI: `10.1121/1.1421344`.

[102] Z. Tian, X. Jia, K. Yuan, T. Pan, and S. B. Jiang, "Low-dose CT reconstruction via edge-preserving total variation regularization," *Physics in Medicine and Biology*, vol. 56, no. 18, p. 5949, 2011.

[103] S. J. Norton, "Iterative inverse scattering algorithms: Methods of computing Fréchet derivatives," *The Journal of the Acoustical Society of America*, vol. 106, no. 5, pp. 2653–2660, 1999. DOI: `10.1121/1.428095`.

[104] R.-E. Plessix, “A review of the adjoint-state method for computing the gradient of a functional with geophysical applications,” *Geophysical Journal International*, vol. 167, no. 2, pp. 495–503, 2006. DOI: `10.1111/j.1365-246X.2006.02978.x`.

[105] J. Virieux and S. Operto, “An overview of full-waveform inversion in exploration geophysics,” *GEOPHYSICS*, vol. 74, no. 6, WCC1–WCC26, 2009. DOI: `10.1190/1.3238367`.

[106] J. R. Shewchuk, “An Introduction to the Conjugate Gradient Method Without the Agonizing Pain,” Pittsburgh, PA, USA, Tech. Rep., 1994.

[107] Y. Wang, J. Yang, W. Yin, and Y. Zhang, “A New Alternating Minimization Algorithm for Total Variation Image Reconstruction,” *SIAM Journal on Imaging Sciences*, vol. 1, no. 3, pp. 248–272, 2008. DOI: `10.1137/080724265`.

[108] T. Szabo, *Diagnostic Ultrasound Imaging: Inside Out*, 2nd ed. Cambridge, MA, USA: Academic Press, 2013, p. 832, ISBN: 9780123964878.

[109] B. T. C. Bradley E. Treeby, “k-Wave: MATLAB toolbox for the simulation and reconstruction of photoacoustic wave fields,” *Journal of Biomedical Optics*, vol. 15, pp. 15 –15 –12, 2010. DOI: `10.1117/1.3360308`.

[110] J. F. Greenleaf, S. A. Johnson, and R. C. Bahn, “Quantitative Cross-Sectional Imaging of Ultrasound Parameters,” in *1977 Ultrasonics Symposium*, 1977, pp. 989–995. DOI: `10.1109/ULTSYM.1977.196985`.

[111] S. Johnson, T. Abbott, R. Bell, M. Berggren, D. Borup, D. Robinson, J. Wiskin, S. Olsen, and B. Hanover, “Non-Invasive Breast Tissue Characterization Using Ultrasound Speed and Attenuation,” in *Acoustical Imaging*. Dordrecht: Springer Netherlands, 2007, pp. 147–154, ISBN: 978-1-4020-5721-2. DOI: `10.1007/1-4020-5721-0_17`.

[112] F. A. Duck, *Physical properties of tissues: a comprehensive reference book*. Cambridge, MA, USA: Academic press, 2013, p. 336, ISBN: 978-0122228001.

[113] D. H. Howry, D. A. Stott, and W. R. Bliss, “The ultrasonic visualization of carcinoma of the breast and other soft-tissue structures,” *Cancer*, vol. 7, no. 2, pp. 354–358, 1954, ISSN: 1097-0142. DOI: `10.1002/1097-0142(195403)7:2<354::AID-CNCR2820070220>3.0.CO;2-9`.

[114] T. Kobayashi, O. Takatani, N. Hattori, and K. Kimura, “Differential diagnosis of breast tumors. The sensitivity graded method of ultrasonotomography and clinical evaluation of its diagnostic accuracy,” *Cancer*, vol. 33, no. 4, pp. 940–951, 1974.

[115] J. J. Wild and J. M. Reid, “Echographic Visualization of Lesions of the Living Intact Human Breast,” *Cancer Research*, vol. 14, no. 4, pp. 277–283, 1954, ISSN: 0008-5472.

[116] C.-H. Chang, S.-W. Huang, H.-C. Yang, Y.-H. Chou, and P.-C. Li, "Reconstruction of Ultrasonic Sound Velocity and Attenuation Coefficient Using Linear Arrays: Clinical Assessment," *Ultrasound in Medicine & Biology*, vol. 33, no. 11, pp. 1681 –1687, 2007, ISSN: 0301-5629. DOI: `https://doi.org/10.1016/j.ultrasmedbio.2007.05.012`. [Online]. Available: `http://www.sciencedirect.com/science/article/pii/S0301562907002566`.

[117] R. Jirik, R. Stotzka, and T. Taxt, "Ultrasonic attenuation tomography based on log-spectrum analysis," in *Proc. SPIE*, vol. 5750, 2005, pp. 5750 –5750 –10. DOI: `10.1117/12.594474`.

[118] C. Li, N. Duric, and L. Huang, "Comparison of ultrasound attenuation tomography methods for breast imaging," in *Proc. SPIE*, vol. 6920, 2008, pp. 6920 –6920 –9. DOI: `10.1117/12.771433`.

[119] G. Y. Sandhu, E. West, C. Li, O. Roy, and N. Duric, "3D frequency-domain ultrasound waveform tomography breast imaging," in *Proc. SPIE*, vol. 10139, 2017, pp. 10139 –10139 –14. DOI: `10.1117/12.2254399`.

[120] F. Natterer, "An algorithm for 3D ultrasound tomography," in *Inverse Problems of Wave Propagation and Diffraction: Proceedings of the Conference Held in Aix-les-Bains, France, September 23–27, 1996*, G. Chavent and P. C. Sabatier, Eds. Berlin, Heidelberg: Springer Berlin Heidelberg, 1997, pp. 216–225, ISBN: 978-3-540-68713-9. DOI: `10.1007/BFb0105772`.

[121] A. V. Goncharsky and S. Y. Romanov, "Inverse problems of ultrasound tomography in models with attenuation," *Physics in Medicine & Biology*, vol. 59, no. 8, p. 1979, 2014. [Online]. Available: `http://stacks.iop.org/0031-9155/59/i=8/a=1979`.

[122] M. Pérez-Liva, J. L. Herraiz, J. M. Udas, E. Miller, B. T. Cox, and B. E. Treeby, "Time domain reconstruction of sound speed and attenuation in ultrasound computed tomography using full wave inversion," *The Journal of the Acoustical Society of America*, vol. 141, no. 3, pp. 1595–1604, 2017. DOI: `10.1121/1.4976688`.

[123] I. Céspedes and J. Ophir, "Diffraction correction methods for pulse-echo acoustic attenuation estimation," *Ultrasound in Medicine & Biology*, vol. 16, no. 7, pp. 707 –717, 1990, ISSN: 0301-5629. DOI: `https://doi.org/10.1016/0301-5629(90)90104-K`.

[124] W. Xu and J. J. Kaufman, "Diffraction correction methods for insertion ultrasound attenuation estimation," *IEEE Transactions on Biomedical Engineering*, vol. 40, no. 6, pp. 563–570, 1993, ISSN: 0018-9294. DOI: `10.1109/10.237676`.

[125] J. M. Hovem, "Ray Trace Modeling of Underwater Sound Propagation," in *Modeling and Measurement Methods for Acoustic Waves and for Acoustic Microdevices*, M. G. Beghi, Ed., Rijeka: InTech, 2013, ch. 23. DOI: `10.5772/55935`.

[126] T. P. Matthews, K. Wang, C. Li, N. Duric, and M. A. Anastasio, "Regularized Dual Averaging Image Reconstruction for Full-Wave Ultrasound Computed Tomography," *IEEE Transactions on Ultrasonics, Ferroelectrics, and Frequency Control*, vol. 64, no. 5, pp. 811–825, 2017, ISSN: 0885-3010. DOI: `10.1109/TUFFC.2017.2682061`.

[127] J. R. Krebs, J. E. Anderson, D. Hinkley, R. Neelamani, S. Lee, A. Baumstein, and M.-D. Lacasse, "Fast full-wavefield seismic inversion using encoded sources," *GEOPHYSICS*, vol. 74, no. 6, WCC177–WCC188, 2009. DOI: `10.1190/1.3230502`.

[128] Z. Zhang, L. Huang, and Y. Lin, "Efficient implementation of ultrasound waveform tomography using source encoding," in *Proc.SPIE*, vol. 8320, 2012, pp. 8320 –8320 –10.

[129] P. P. Moghaddam, H. Keers, F. J. Herrmann, and W. A. Mulder, "A new optimization approach for source-encoding full-waveform inversion," *GEOPHYSICS*, vol. 78, no. 3, R125–R132, 2013. DOI: `10.1190/geo2012-0090.1`.

[130] T. van Leeuwen and F. J. Herrmann, "Fast waveform inversion without source-encoding," *Geophysical Prospecting*, vol. 61, pp. 10–19, 2013, ISSN: 1365-2478. DOI: `10.1111/j.1365-2478.2012.01096.x`.

[131] B. Diarra, M. Robini, P. Tortoli, C. Cachard, and H. Liebgott, "Design of Optimal 2-D Nongrid Sparse Arrays for Medical Ultrasound," *IEEE Transactions on Biomedical Engineering*, vol. 60, no. 11, pp. 3093–3102, 2013, ISSN: 0018-9294. DOI: `10.1109/TBME.2013.2267742`.

[132] E. Roux, A. Ramalli, P. Tortoli, C. Cachard, M. C. Robini, and H. Liebgott, "2-D Ultrasound Sparse Arrays Multidepth Radiation Optimization Using Simulated Annealing and Spiral-Array Inspired Energy Functions," *IEEE Transactions on Ultrasonics, Ferroelectrics, and Frequency Control*, vol. 63, no. 12, pp. 2138–2149, 2016, ISSN: 0885-3010. DOI: `10.1109/TUFFC.2016.2602242`.

[133] X. Li, E. Esser, and F. J. Herrmann, "Modified Gauss-Newton full-waveform inversion explained Why sparsity-promoting updates do matter," *GEOPHYSICS*, vol. 81, no. 3, R125–R138, 2016. DOI: `10.1190/geo2015-0266.1`.

[134] A. Ramirez and G. R. Arce, "Seismic full waveform inversion from compressive measurements," in *Proc. SPIE*, vol. 9484, 2015, pp. 9484 –9484 –6. DOI: `10.1117/12.2178949`.

[135] D. L. Donoho, "Compressed sensing," *IEEE Transactions on Information Theory*, vol. 52, no. 4, pp. 1289–1306, 2006, ISSN: 0018-9448. DOI: `10.1109/TIT.2006.871582`.

[136] M. Lustig, D. Donoho, and J. M. Pauly, "Sparse MRI: The application of compressed sensing for rapid MR imaging," *Magnetic Resonance in Medicine*, vol. 58, no. 6, pp. 1182–1195, 2007, ISSN: 1522-2594. DOI: `10.1002/mrm.21391`. [Online]. Available: `http://dx.doi.org/10.1002/mrm.21391`.

[137] M. Pilanci and M. J. Wainwright, “Newton sketch: A near linear-time optimization algorithm with linear-quadratic convergence,” *SIAM Journal on Optimization*, vol. 27, no. 1, pp. 205–245, 2017. DOI: `10.1137/15M1021106`.

[138] E. Liberty, “Simple and deterministic matrix sketching,” in *Proceedings of the 19th ACM SIGKDD International Conference on Knowledge Discovery and Data Mining*, ser. KDD ’13, Chicago, Illinois, USA: ACM, 2013, pp. 581–588, ISBN: 978-1-4503-2174-7. DOI: `10.1145/2487575.2487623`.

[139] F. J. Herrmann, X. Li, A. Y. Aravkin, and T. van Leeuwen, “A modified, sparsity-promoting, Gauss-Newton algorithm for seismic waveform inversion,” in *Proc. SPIE*, vol. 8138, 2011, pp. 8138 –8138 –14. DOI: `10.1117/12.893861`.

[140] X. Li, A. Y. Aravkin, T. van Leeuwen, and F. J. Herrmann, “Fast randomized full-waveform inversion with compressive sensing,” *GEOPHYSICS*, vol. 77, no. 3, A13–A17, 2012. DOI: `10.1190/geo2011-0410.1`.

[141] J. Zhou, S. Wei, R. Sampson, R. Jintamethasawat, O. D. Kripfgans, J. B. Fowlkes, T. F. Wenisch, and C. Chakrabarti, “High volume rate 3D ultrasound imaging based on synthetic aperture sequential beamforming,” in *2017 IEEE International Ultrasonics Symposium (IUS)*, 2017, pp. 1–4. DOI: `10.1109/ULTSYM.2017.8091580`.

[142] T. P. Matthews and M. A. Anastasio, “Joint reconstruction of the initial pressure and speed of sound distributions from combined photoacoustic and ultrasound tomography measurements,” *Inverse Problems*, vol. 33, no. 12, p. 124 002, 2017.

[143] Y. Zhou, J. Yao, and L. V. Wang, “Tutorial on photoacoustic tomography,” *Journal of Biomedical Optics*, vol. 21, pp. 21 –21 –14, 2016. DOI: `10.1117/1.JBO.21.6.061007`.

[144] B. T. Cox, J. G. Laufer, P. C. Beard, and S. R. Arridge, “Quantitative spectroscopic photoacoustic imaging: a review,” *Journal of Biomedical Optics*, vol. 17, pp. 17 –17 –23, 2012. DOI: `10.1117/1.JBO.17.6.061202`.

[145] L. V. Wang, “Tutorial on Photoacoustic Microscopy and Computed Tomography,” *IEEE Journal of Selected Topics in Quantum Electronics*, vol. 14, no. 1, pp. 171–179, 2008, ISSN: 1077-260X. DOI: `10.1109/JSTQE.2007.913398`.

[146] M. Xu and L. V. Wang, “Photoacoustic imaging in biomedicine,” *Review of Scientific Instruments*, vol. 77, no. 4, p. 041 101, 2006. DOI: `10.1063/1.2195024`.

[147] D. Hanahan and R. Weinberg, “Hallmarks of Cancer: The Next Generation,” *Cell*, vol. 144, no. 5, pp. 646 –674, 2011, ISSN: 0092-8674. DOI: `https://doi.org/10.1016/j.cell.2011.02.013`.

[148] M. Heijblom, D. Piras, F. M. van den Engh, M. van der Schaaf, J. M. Klaase, W. Steenbergen, and S. Manohar, "The state of the art in breast imaging using the Twente Photoacoustic Mammoscope: results from 31 measurements on malignancies," *European Radiology*, vol. 26, no. 11, pp. 3874–3887, 2016, ISSN: 1432-1084. DOI: `10.1007/s00330-016-4240-7`.

[149] S. Fantini and A. Sassaroli, "Near-Infrared Optical Mammography for Breast Cancer Detection with Intrinsic Contrast", journal="Annals of Biomedical Engineering," vol. 40, no. 2, pp. 398–407, 2012, ISSN: 1573-9686. DOI: `10.1007/s10439-011-0404-4`.

[150] J. Wang, S. Jiang, Z. Li, R. M. diFlorio Alexander, R. J. Barth, P. A. Kaufman, B. W. Pogue, and K. D. Paulsen, "In vivo quantitative imaging of normal and cancerous breast tissue using broadband diffuse optical tomography," *Medical Physics*, vol. 37, no. 7Part1, pp. 3715–3724, 2010, ISSN: 2473-4209. DOI: `10.1118/1.3455702`.

[151] M. L. Flexman, M. A. Khalil, H. K. Kim, C. J. Fong, A. H. Hielscher, R. A. Abdi, R. L. Barbour, E. Desperito, and D. L. Hershman, "Digital optical tomography system for dynamic breast imaging," *Journal of Biomedical Optics*, vol. 16, pp. 16 –16 –17, 2011. DOI: `10.1117/1.3599955`.

[152] M. Heijblom, J. M. Klaase, F. M. van den Engh, T. G. van Leeuwen, L. W. Steenbergen, and S. Manohar, "Imaging Tumor Vascularization for Detection and Diagnosis of Breast Cancer, journal = Technology in Cancer Research & Treatment," vol. 10, no. 6, pp. 607–623, 2011, PMID: 22066601. DOI: `10.7785/tcrt.2012.500227`.

[153] J. Wang, B. W. Pogue, S. Jiang, and K. D. Paulsen, "Near-infrared tomography of breast cancer hemoglobin, water, lipid, and scattering using combined frequency domain and CW measurement," *Opt. Lett.*, vol. 35, no. 1, pp. 82–84, 2010. DOI: `10.1364/OL.35.000082`.

[154] J. Q. Brown, L. G. Wilke, J. Geradts, S. A. Kennedy, G. M. Palmer, and N. Ramanujam, "Quantitative Optical Spectroscopy: A Robust Tool for Direct Measurement of Breast Cancer Vascular Oxygenation and Total Hemoglobin Content In vivo," *Cancer Research*, vol. 69, no. 7, 2009, ISSN: 0008-5472. DOI: `10.1158/0008-5472.CAN-08-3370`. eprint: `http://cancerres.aacrjournals.org/content/69/7/2919.full.pdf`.

[155] K. E. Michaelsen, V. Krishnaswamy, L. Shi, S. Vedantham, A. Karellas, B. W. Pogue, K. D. Paulsen, and S. P. Poplack, "Effects of breast density and compression on normal breast tissue hemodynamics through breast tomosynthesis guided near-infrared spectral tomography," *Journal of Biomedical Optics*, vol. 21, pp. 21 –21 –8, 2016. DOI: `10.1117/1.JBO.21.9.091316`.

[156] R. A. Kruger, C. M. Kuzmiak, R. B. Lam, D. R. Reinecke, S. P. Del Rio, and D. Steed, "Dedicated 3D photoacoustic breast imaging," *Medical Physics*, vol. 40, no. 11, 113 301–n/a, 2013, 113301, ISSN: 2473-4209. DOI: `10.1118/1.4824317`.

[157] R. A. Kruger, R. B. Lam, D. R. Reinecke, S. P. Del Rio, and R. P. Doyle, "Photoacoustic angiography of the breast," *Medical Physics*, vol. 37, no. 11, pp. 6096–6100, 2010, ISSN: 2473-4209. DOI: `10.1118/1.3497677`.

[158] M. Pramanik, G. Ku, C. Li, and L. V. Wang, "Design and evaluation of a novel breast cancer detection system combining both thermoacoustic (TA) and photoacoustic (PA) tomography," *Medical Physics*, vol. 35, no. 6Part1, pp. 2218–2223, 2008, ISSN: 2473-4209. DOI: `10.1118/1.2911157`.

[159] T. Kitai, M. Torii, T. Sugie, S. Kanao, Y. Mikami, T. Shiina, and M. Toi, "Photoacoustic mammography: initial clinical results," *Breast Cancer*, vol. 21, no. 2, pp. 146–153, 2014, ISSN: 1880-4233. DOI: `10.1007/s12282-012-0363-0`.

[160] R. G. M. Kolkman, P. J. Brands, W. Steenbergen, and T. G. C. van Leeuwen, "Real-time in vivo photoacoustic and ultrasound imaging," *Journal of Biomedical Optics*, vol. 13, pp. 13 –13 –3, 2008. DOI: `10.1117/1.3005421`.

[161] S. A. Ermilov, M. P. Fronheiser, H.-P. Brecht, R. Su, A. Conjusteau, K. Mehta, P. Otto, and A. A. Oraevsky, "Development of laser optoacoustic and ultrasonic imaging system for breast cancer utilizing handheld array probes," in *Proc. SPIE*, vol. 7177, 2009, pp. 7177 –7177 –10. DOI: `10.1117/12.812192`.

[162] X. L. Deán-Ben, R. Ma, D. Razansky, and V. Ntziachristos, "Statistical Approach for Optoacoustic Image Reconstruction in the Presence of Strong Acoustic Heterogeneities," *IEEE Transactions on Medical Imaging*, vol. 30, no. 2, pp. 401–408, 2011, ISSN: 0278-0062. DOI: `10.1109/TMI.2010.2081683`.

[163] J. Jose, R. G. H. Willemink, W. Steenbergen, C. H. Slump, T. G. van Leeuwen, and S. Manohar, "Speed-of-sound compensated photoacoustic tomography for accurate imaging," *Medical Physics*, vol. 39, no. 12, pp. 7262–7271, 2012, ISSN: 2473-4209. DOI: `10.1118/1.4764911`.

[164] C. Zhang and Y. Wang, "A reconstruction algorithm for thermoacoustic tomography with compensation for acoustic speed heterogeneity," *Physics in Medicine and Biology*, vol. 53, no. 18, p. 4971, 2008.

[165] X. Jin and L. V. Wang, "Thermoacoustic tomography with correction for acoustic speed variations," *Physics in Medicine and Biology*, vol. 51, no. 24, p. 6437, 2006.

[166] C. Huang, K. Wang, L. Nie, L. V. Wang, and M. A. Anastasio, "Full-Wave Iterative Image Reconstruction in Photoacoustic Tomography With Acoustically Inhomogeneous Media," *IEEE Transactions on Medical Imaging*, vol. 32, no. 6, pp. 1097–1110, 2013, ISSN: 0278-0062. DOI: `10.1109/TMI.2013.2254496`.

[167] S. R. Arridge, M. M. Betcke, B. T. Cox, F. Lucka, and B. E. Treeby, "On the adjoint operator in photoacoustic tomography," *Inverse Problems*, vol. 32, no. 11, p. 115 012, 2016.

[168] A. Javaherian and S. Holman, "A Multi-Grid Iterative Method for Photoacoustic Tomography," *IEEE Transactions on Medical Imaging*, vol. 36, no. 3, pp. 696–706, 2017, ISSN: 0278-0062. DOI: `10.1109/TMI.2016.2625272`.

[169] Y. Lou, W. Zhou, T. P. Matthews, C. M. Appleton, and M. A. Anastasio, "Generation of anatomically realistic numerical phantoms for photoacoustic and ultrasonic breast imaging," *Journal of Biomedical Optics*, vol. 22, pp. 22 –22 –13, 2017. DOI: `10.1117/1.JBO.22.4.041015`.

[170] R. A. Kruger, D. R. Reinecke, and G. A. Kruger, "Thermoacoustic computed tomographytechnical considerations," *Medical Physics*, vol. 26, no. 9, pp. 1832–1837, 1999, ISSN: 2473-4209. DOI: `10.1118/1.598688`.

[171] S. I. Kabanikhin, "Definitions and examples of inverse and ill-posed problems," *Journal of Inverse and Ill-posed Problems*, vol. 16, no. 4, pp. 317–357, 2008, ISSN: 15693945. DOI: `10.1515/JIIP.2008.019`.

[172] A. Wirgin, "The inverse crime," *arXiv preprint math-ph/0401050*, 2004.